Swansea University
Prifysgol Abertawe

Wear and impact analysis of granular materials using Discrete Element Method simulations

by
James Thompson

A thesis submitted in partial fulfillment for the
degree of Doctor of Engineering

in the
Faculty of Science and Engineering

June 2023

Oh, Danny boy, the pipes, the pipes are calling

From glen to glen, and down the mountain side.

The summer's gone, and all the roses falling,

It's you, It's you must go and I must bide.

But come ye back when summer's in the meadow,

Or when the valley's hushed and white with snow,

It's I'll be here in sunshine or in shadow,

Oh, Danny boy, Oh Danny boy, I love you so!

Abstract

Wear models for abrasion, ductile erosion, brittle erosion and combined erosion are implemented into a Discrete Element Method program utilising the linear spring dashpot model. A linear damage model is developed, implemented and then applied to an industrial case study through which it is found to predict wear accurately and provide a good insight into the improvement based on material change using the abrasion models. Four methods of creating energy based modelling were created for specific use inside DEM and contrasted with known wear models to assess what mechanisms they may potentially replicate. Through use with DEM, this allows use with a Single Element Failure criteria which can rapidly assess a variety of material changes inside a system to take steps to de-risk potential industrial trials. Design changes were made to assess the effects on both wear/energy models and provide predictions for causes and possible side effects. The effect of particle kinetics were assessed with respect to angle of impact, mass flow rate and coefficient of restitution to determine how this impacts wear modelling in DEM.

Contents

Acknowledgements

This research was carried out at Swansea University under the Materials and Manufacturing Academy (M2A) project which is supported by the European Social Fund through the Welsh government

Firstly I would like to thank my academic supervisor Steve Brown for his help, support and advice over the past few years. I wish you a happy and relaxed retirement, I hope I was not too annoying as a final doctorate student!

I'd like to give thanks to my industrial sponsors, Wall Colmonoy and TATA Steel who have given me the opportunity to conduct this research. A special thank you to my industrial supervisors, Lewis Berry for the support he has provided over the years from Wall Colmonoy, and to Stuart Southern who provided the opportunities to apply my research in industry. Thank you as well to Derek Simons at Lloyd Walters industrial services who helped organise and monitor the industrial trial while the world appeared to be in chaos at the time.

I'd like to thank my parents Anthony and Stephanie Thompson, who have supported and guided me through life to make me into the person I am today. And a thank you to the Tobies who taught me everything I know!

An extra special thank you my grandparents, Maureen and Franz, for the support and vast amount of Sunday dinners which I have eaten over the last 9 years!

Thank you to Kate, for putting up with me through these past months using, occasionally extreme, levels of sass and for the complete lack of interest in DEM which has kept me sane! And thank you to Stanley for his consistent barking and critique of my work whilst I was writing this!

Finally I would like to thank my Nan. Sadly you are not here to see me finish this. So close yet so far. I love you and I miss you.

List of Figures

List of Tables

Abbreviations

CFD	**C**omputational **F**luid **D**ynamics
DEM	**D**iscrete **E**lement **M**ethod
FDM	**F**inite **D**ifference **M**ethod
FEM	**F**inite **E**lement **M**ethod
MEF	**M**ultiple **E**lement **F**ailure
SEF	**S**ingle **E**lement **F**ailure
Stl	**St**ereo**l**ithographic file

Symbols

Symbol	Definition	Unit
A	Area	m^2
a	Acceleration	ms^{-2}
C_1	Coefficient for Single Element Failure criterion model	[1]
C_2	Coefficient for hole acceleration model	[1]
C_d	Damage coefficient	[1]
c	Damping constant	kgs^{-1}
con	Denotes conveyor as subscript	[1]
D	Damage	[1]
d	Denoted damping as subscript	[1]
E	Energy	J
e	Coefficient of restitution	[1]
e	Denotes element number as subscript	[1]
F	Force	N
f	Penetration factor	[1]
G_k	Number of collisions (global collisions)	[1]
H	Hardness	Nm^{-2}
i	Denotes examined particle number as subscript	[1]
j	Denotes collided particle number as subscript	[1]
k	Spring Constant/Stiffness	Nm^{-1}
m	Particle mass	kg
N	Total number of timesteps	[1]
n	Current Timestep	[1]
n	Denotes normal direction as subscript	[1]
$\hat{n}$	Element unit normal	[1]

p	Denotes particle as a subscript	[1]
Q	Wear	m^3
R	Particle to element area ratio	[1]
r	Particle radius	m
t	Time	s
t	Denotes tangential direction as subscript	[1]
v	Velocity	ms^{-1}
$\hat{v}$	velocity unit vector	[1]
α	Angle of impact of a particle	rad
Δt	Timestep	s
δ	Overlap	m
ϵ	Specific energy due to brittle erosion	Jm^3
ω	Angular frequency	$rads^{-1}$
ζ	Damping ratio	[1]

Chapter 1

Introduction

1.1 Why?

Millions of tonnes of heavy, hard wearing material is processed through Tata Steel's Port Talbot heavy end each month. This impacts and wears upon every single surface it encounters including cranes, conveyors, chutes and other structures. Each structure suffers the effects of this consistent, repetitive impact of material. Inevitably they wear away and cause a shutdown of the local system which then costs thousands or even millions of pounds to repair. An additional cost is the time of personnel who must fix the systems and varying degrees of knock-on effect to the production of product.

Figure 1.1 shows a simplified layout of the process systems present at a steelmaking plant [1]. Each process surrounding the blast furnace, which creates the steel, requires granular materials such as iron ore, limestone, coal and coke. All of these materials must be transported both to and around a steel plant by ship, lorry, conveyor and chute system. At which point they are then processed to their required compositon, size and shape. With such a large amount of material being processed; enivitably an extremely large volume of wear will occur.

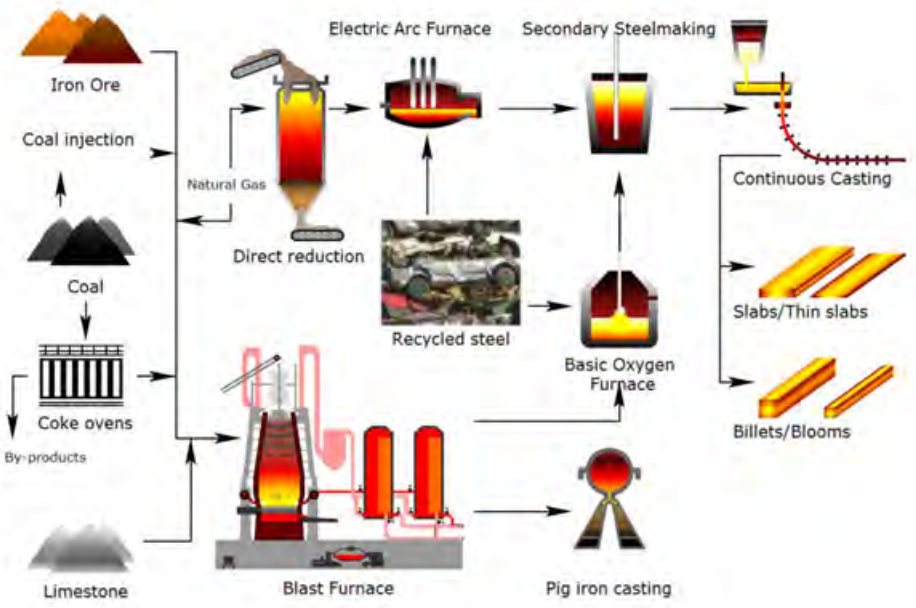

FIGURE 1.1: Schematic of the operation of a blast furnace and the surrounding systems [1]

For a long time, the effects of heavy impact and wear caused by the flow of granular materials were not considered either industrially or academically with serious scientific interest. This is a broad issue which affects many heavy industries but especially the steel making industry. This thesis aims to investigate how the use of the Discrete Element Method (DEM) can model wear and impacts to inform the choice of materials or design of structures. The work focusses solely on DEM, although other methods

will be highlighted, and case studies are presented to show the application of methods highlighting what is effective and what is not.

This thesis is separated into four parts. The first part is the Background which is comprised of 2 chapters: Chapter 2: The Discrete Element Method and Chapter 3: Wear Modelling. Chapter 2 is further split into two sections (i) the types of materials which are of interest and then (ii) details of how these are modelled using the Discrete Element Method. The second chapter of the background, Chapter 3, will look at wear modelling and models that have been established in the literature. A discussion of their uses and development is provided to introduce what is a large field of research.

The second major part of this thesis will look at how the Discrete Element Method can be used to provide analysis. Broken into two chapters (4 Wear and DEM, 5 Fluid Flow Implementation) this will describe the combination of DEM and wear models to simulate the damage caused by granular materials. I Chapter 4 a model will be developed which can assess the damage caused by any wear mechanism which calculates a volume of material removal. It will then shown how this model can be used in two methods to assess material and design changes in industrial systems. Chapter 5 will present a method of applying Computational Fluid Dynamics (CFD) steady-state velocity profiles to a full-scale DEM simualtion with negligible computational cost to DEM. This will then be applied to an industrial case study in the third section of this thesis.

The third major section (III Case Studies) deals with case studies which have been carried out during this work. The first concerns a coke screener, Chapter 6 situated in the heavy end at Port Talbot where an industrial trial was run and a series of wear models tested outside of a laboratory setting. The second, Chapter 7, looks at the coal injection lances on the blast furnace and how the velocity profile can be used to replicate and study the effects of changes in lance design and to assist in explaining why the wear occurs where it does. Finally, the last case study will look at the effects of parameter variation in wear and aims to identify key DEM parameters to provide further understand their effect.

Lastly the discussion and conclusion sections will review all of the findings and models presented, highlight areas of interest and possible conflict with other work, and identify areas for future research.

1.2 Project History

This project has a history as a collaborative project between TATA Steel and Swansea University beginning in 2006 with Bridgeman et al, this project ending in 2010. A 2D

version of DEM was developed, largely based on the original method created by Cundall and Strack [5][6]. Bridgeman took the 2D program and developed it to run in 3D, handling various physical calculations involving particle contacts and force modelling using the linear spring dashpot model. An overview of this will be discussed in the following section 2.2.2. They focussed on the inter particle dynamics of systems and replicating the bulk behaviour of material to better understand how particle systems work. It was also the initial implementation of numerous features in the program such as initial kinetic energy calculations, friction force and capillary forces related to moisture [5].

The second step for the DEM project was Holmes finishing in 2015. Holmes spent a large amount of time focussing on developing the efficiency of the program and expanding the scale of processes which it could simulate. Culminating in simulations of a scaled down version of the Tata Steel blast furnace. This included millions of particles (which at the time they noted was no small undertaking and it is still very much the same today) as shown in Figure 1.2. Holmes overhauled the contact detection algorithms, outputs and friction force calculation [7] and successfully developed the program so it could simulate 70 seconds of charging the blast furnace, with a radius of approximately 4 m radius, with 7.5 million particles in approximately 2 days on an 8 core PC [2].

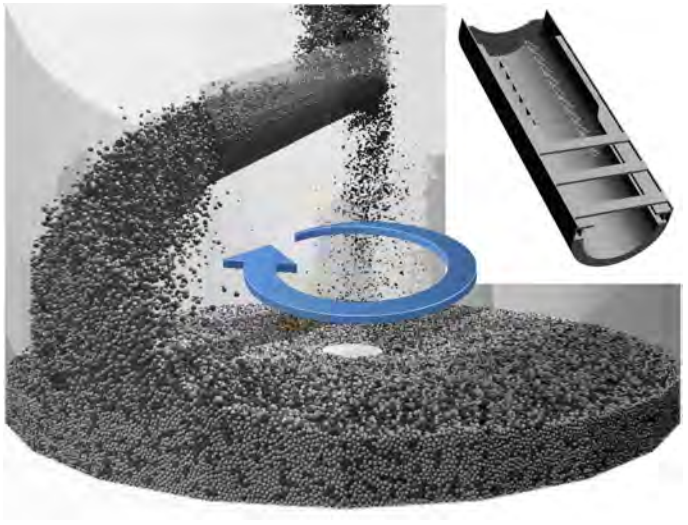

FIGURE 1.2: Blast furnace simulation carried out investigating chute design in Holmes' work [2]

The third project in this series involved the work of Carr, finishing in 2021, who from the basis laid out in Holmes' work began developing a non-spherical version of the DEM program. Polyhedral particles were used to model both irregular and angular particles requiring the development of a new contact algorithm [3]. The shapes of the regular particles simulated can be seen in Figure 1.3. This work would also introduce a simplified version of the Hertz-Mindlin force model and applied a non-linear volume

based method in contrast to the linear spring dashpot displacement based method used previously. The work would then investigate the effect of irregular particle shapes on the mixing of regular and irregular particles in the charging process.

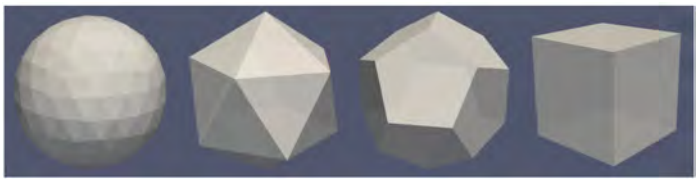

FIGURE 1.3: Regular shaped particles generated in Carr's work for validation [3]

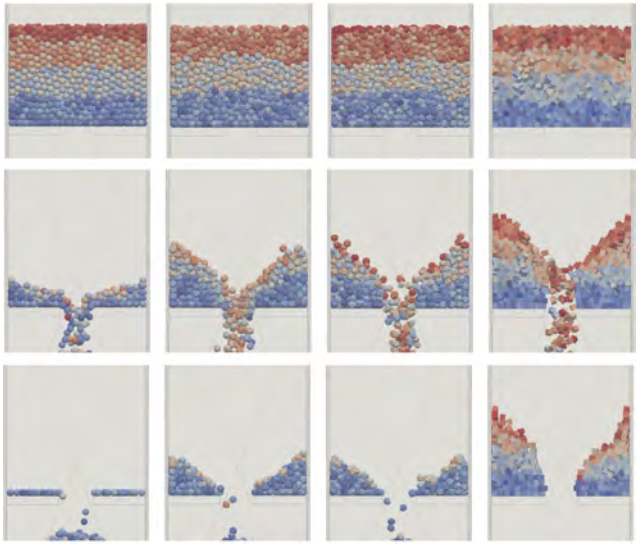

FIGURE 1.4: Hopper discharge simulations using spherical, icosahedral, dodecahedral, and cuboidal particles at t = 0.0s (top), t = 2.0s (middle) and t = 4.0s (bottom) [3]

The fourth project involving DEM was Walls finishing in 2022. Walls' work investigated size control in pelletisation focussing on the pelletisation of ferrous by products [8]. They did this by focussing on the kinetic behaviour of particles using the Discrete Element Method. During the work they formulated a theory based on Adhesion and Cohesion of particles to model agglomeration and implemented it into DEM to predict particle growth behaviour [9].

1.2.1 Bridgeman Application

Bridgeman primarily looked at the particle dynamics and flows of systems. One application did however take a preliminary look at the effect of particles on wall structures which they impacted. This was done by calculating the kinetic energy of a collision and summing these over the timescale of a simulation. This was done by dividing the wall boundary into multiple sections and recording the value [5]. Therefore, areas of high

kinetic energy transfer and areas of impact can be seen. Through his work the possibility of using this is clearly demonstrated and this is the work from which this thesis is based. A considerable portion of this application focussed on the effect of using various chute designs and attempting to quantify reduced disruption of particle kinematics. A suggestion noted in this work, and often suggested for chute systems, is the use of a curved chutes to smooth particles' transitional behaviour and maybe reduce wear. It is noted in his work that energy transfer is demonstrated to be remarkably similar to real world failure and impact zones.

1.2.2 Carr Application

For this application Carr focussed on the effect particle irregularity had on raw materials trajectory from the raw material delivery chute into the blast furnace. Trajectories of particles were tracked as they hit a 'deleter plane' positioned at the bottom of the blast furnace chute. This model investigated how particle geometry effected the flow of particles off the chute into the furnace and whether particle shape was a major factor. It was found with increasing particle irregularity in or with increasing irregular particle percentage in burdening material from the chute: 1. Max distance from furnace centre decreased 2. Spread of material from the principle point of contact decreases 3. The distribution of flow rate became smoother with respect to the distance from the centre [3].

A limitation of the work using irregular particles is the scale of simulations possible due to the greatly increased computational cost. In Carr's work the chute was scaled down by a factor of 2 which leaves a question as to the effect particle shape has on the whole top layer of the burden material which is mentioned. However, as pointed out by Carr, similar methods were used by Holmes when simulating the blast furnace in his work and Holmes was able to successfully investigate the burdening and layering of material using spherical particles. The question as to whether non-spherical particle simulations are worth the extra computational cost in this case remains mostly unanswered.

Overall the majority of applications which have been studied using the program thus far have all focussed on the inter-particle interactions in the systems, and little attention has generally been paid to their interactions with structures.

1.3 Aims and Objectives

The following are the overall objectvives of this work. These are to:

- Investigate the application of the Discrete Element Method in relation to impact and wear modelling
- Implement a method of assessing wear in industrial systems into DEM for both possible material and design changes
- Compare predictions from DEM to real world wear found at TATA Steel within a reasonable timeframe

Part I

Background

Chapter 2

The Discrete Element Method

The Discrete Element Method or DEM is a computational method which simulates the movement and interactions of granular materials. Unfortunately, there is no simple theory of how granular materials behave due to the complicated and varied behaviour they show. This led to a tool being developed which simulated individual interactions between particles to simulate the bulk behaviour of the material as a whole. The groundwork was laid by Cundall and Strack in 1979 after they constructed a program called BALL, which simulated the interactions between 2 dimensional discs [6]. The original mathematical models used have mostly been carried forward and improved, but the foundation of how DEM works remains similar today as it did in 1979. This has led to DEM becoming generally accepted as an effective tool for the simulation of granular materials. This background chapter aims to give an overview of what granular materials are, how they behave, why they are important, and to provide the fundamentals of how DEM works.

2.1 Granular Materials

A granular material is one which is made up of individual grains or particles [10]. Materials of this type make up the second most processed type of material in the world behind water [11]. These individual particles could be anything from coffee beans, peanuts, pharmaceutical pills, microscopic dust or anything in between. These materials are processed extensively in many heavy industries e.g. in Tata Steel Port Talbot granular material is transported from the harbour, to the sinter plant and onwards to other locations using all methods of conveying. The range of behaviours which granular materials can exhibit are numerous and may be property specific.

2.1.1 History

To understand the importance of granular materials it is interesting to first look at the role granular materials have played in the past. One of the first times these materials were looked at in detail was by Charles-Augustin de Coulomb who first stated the laws of sliding friction in reference to granular materials [12]. In more modern times the importance of their role cannot be understated, especially the development of our understanding of a very commonly used material, sand.

Several individuals explored the north African deserts throughout the early 1930s using the Ford Model T [13]. At the time people believed this to be an impossible task. However, Ralph Alger Bagnold and his companions did just this recording the first ever known east to west crossing of the Libyan desert in 1932 [14]. During this time techniques were developed to navigate sand in similar fashion to historic methods of travelling by sea using stars and Bagnold's own invention, the sun compass. Through this time, Bagnold became fascinated with the movement of sand and how it created dune 'cliff-like' structures. However, the importance of such knowledge was not appreciated at the time. In contrast, navigation skills across desert were soon to become extraordinarily valuable. In 1939 World War 2 would break out and from 1940 to 1943 the Allies campaign against Erwin Rommel's Afrika Korps would be in full effect.

In 1940, Bagnold saw an opportunity to use the navigation skills developed throughout his explorations of the early 1930s. He would get permission to form a unit called the Long Range Desert Group (LRDG). The main objective was to travel across the desert and commit acts of piracy against the Afrika Korps troops. The unit did this to great effect being instrumental in many operations. Bagnold passed command of the LRDG to his companion in explorations, Guy Pendergest. The LRDG would be especially instrumental in the success of a unit at the time known as 'L detachment' led by a

young officer called David Stirling [15]. This unit were instrumental in assaulting and raiding behind the enemy lines all across North Africa throughout the campaign. 'L Detachment' would later become known as the 1^{st} Special Air Service (SAS); however they would never have existed at all without the assistance of the LRDG and their desert navigation skills developed by Bagnold through his understanding of the movement of sand. He would publish his knowledge in a book called 'The Physics of Blown Sand and Desert' in 1941. This book laid the foundation of research into granular materials. It would be used by NASA to assist in understanding the terrain of Mars, and led to a Martian dune being named after Bagnold.

2.1.2 Types of Materials

Generally there are two classes of materials. Continuous and discontinuous. Continuous materials have been well researched and numerous theories surrounding them exist which combine what would commonly be thought of as different materials into a similar framework. The field of Continuum Mechanics does this as it looks at numerous materials such as water, metals, rubbers, ceramics etc. [16]. They all have one key property. Their bulk is one piece allowing the states of stress and strain (or other states) to vary continuously throughout the material. Figure 2.1(a) shows a wooden decking which is an example of this class of material.

(a) Continuous (b) Discontinuous

FIGURE 2.1: Demonstration of the classes of materials

A second type of material is the opposite of this where the material is made up of solids but their bulk is separated into individual entities usually of varying size, shape and properties. These are discontinuous materials or granular materials. Figure 2.1(b) shows coffee beans which is an example of this class of material. One key difference is that forces cannot propagate throughout a granular material without constant excitation [10]. This is logical with a simple thought experiment. Dropping a pebble in to water

creates a wave which then ripples and propagates outwards from the point of impact. However if you drop a pebble onto sand, the sand does not ripple outwards from the point of impact: it just lands. Mechanically it imparts the force of its impact onto the direct neighbours of the sand particles it landed on. The force of which is dissipated through further neighbouring particles unless it is excited again, or further force is applied to it.

2.1.3 Granular Materials and their properties

Naturally, individual particles in a granular material are subjected to all the same properties and forces as any other material. However, a discrete nature alters how external forces interact with in a discontinuous material influenced by particle volume, size, shape and strength [17]. For example, the diameter of an individual particle determines which forces are required to be considered. For particles at a molecular level, intermolecular forces would need to be considered such as Van der Waals or Brownian motion. As particle diameter increases so does the influence of other forces. For example, a simulation taking into account fluidised microscopic dust would have to consider forces which a conveyed flow of 1 cm diameter iron ore pellets could ignore and vice versa [18]. In situations where a granular material is heavily compacted a much greater importance would be placed on the stiffness and stress dependence of the material. When particle movement is involved dynamical effects, such as inertia, often outweigh other forces such as intermolecular forces or entropy [19].

This provides complications when selecting appropriate models for DEM from the wide variety of literature. Fortunately, even with some forces being varied depending on scale, simulations tend to have more in common with each other than not. It should be noted that many of the materials covered in this work could be considered as a 'broken solid' as most are greater than $3mm$ in diameter [20]. However, even though this upper diameter limit has been suggested the theories of granular materials have been successfully applied to one of the largest flowing materials in the world, ice mélange [21].

One of the challenges regarding granular material behaviour is their ability to exhibit both liquid and solid behaviours. For example, if you take a scoop of coffee beans, and pour them out it would behave like a liquid. However, on landing it reverts back to behaving fundamentally like a solid, bouncing and scattering away. This was observed by Lucretius in 55 BC "One can scoop up poppy seeds with a ladle as easily as if they were water and, when dipping the ladle, the seeds flow in a continuous stream".

Granular material also has the unique ability to create self-supporting structures through the existence of force chains. This can be seen in processes using hoppers where the material blocks chutes stopping the process. This ability arises from each particle's

macroscopic interaction with its neighbours, the phenomenon which allows the creation of sand dunes [14].

When granular materials are stored inside a silo they also show a unique behaviour. Janssen conducted a simplified analysis showing how the pressure exerted on the bottom of a silo follows the expected hydrostatic pressure equivalent until a characteristically small diameter is reached [22]. At this characteristic small diameter the force at the bottom of the silo becomes less than the equivalent hydrostatic pressure. This is why grain silos are tall and narrow whereas water towers have larger diameters and less height.

$$\sigma_{zz} = \rho g \lambda (1 - e^{-\frac{z}{\lambda}}) \tag{2.1}$$

Where λ represents a characteristic length which is shown in Equation 2.2

$$\lambda = \frac{D}{4K\mu_w} \tag{2.2}$$

Finally, the area of interest to this thesis is granular material handling. They must be processed and handled by machinery and, unlike materials such as water, they often require impacts of some variety to change direction in chute systems. This may be to alter their shape and size distributions in screening machinery or simply to move them through pipe work or on conveyor belts where they impact and slide along surfaces. All of these impacts induce wear in plant, create damage and incur financial penalties (both plant maintenance and down-time) which can be a considerable concern.

2.1.4 Quantifying their behaviour

2.1.4.1 Friction

The first property often used to quantify the friction behaviour inside granular materials is angle of repose. This can be considerably complicated if the effect of adding water to the material is also considered. Liquid/solid surface tension can alter the angle of repose and is an indication of the effect liquid content has on the friction properties of a granular material. Small levels of water may introduce an increase in friction as the material becomes more cohesive due to the surface tension of water. However, beyond a certain point it becomes water logged and the water acts like a lubricant, decreasing the friction coefficient. In this work the assumption is that all the granular materials

are dry. The friction models used incorporate sliding, rolling and twisting friction and are presented here [7].

2.1.4.2 Coefficient of Restitution

A second property which is used to characterise granular material is the coefficient of restitution as originally developed by Sir Isaac Newton in 1687. It is otherwise known as Newton's experimental law and it relates the initial velocity of an impacting body to its final velocity. The relation is quite simple in equation form as is shown in Equation 2.3

$$e = \frac{|v_{intial}|}{|v_{final}|} \tag{2.3}$$

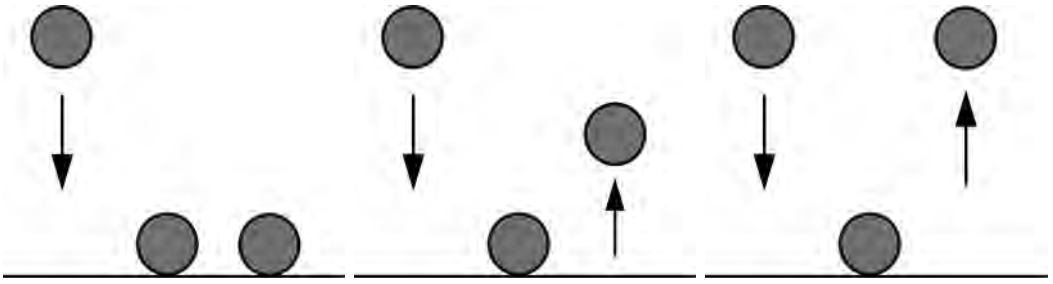

(a) $e = 0$ (b) $e = 0.5$ (c) $e = 1$

FIGURE 2.2: Effect of coefficient of restitution on a dropped particle

Four behaviours are possible at the values of this calculation, $e = 0$, $0 < e < 1$, $e = 1$ and $e > 1$. Situation 1, shown in Figure 2.2(a), is where the collision is entirely inelastic i.e., all energy is immediately dissipated upon collision and the velocity of a particle becomes 0. Situation 2, shown in Figure 2.2(b), is the realistic case where a particle dissipates a fraction of its energy into the impacted material. Situation 3, shown in Figure 2.2(c), is a purely elastic collision where the particle dissipates no energy and leaves the collision at exactly the same velocity as it started. Situation 4 is when the particle gains velocity from the collision and would require breaking the laws of physics. No accounts of these magical materials exist.

One problem with this is that the relative amount of energy lost during an impact can vary depending upon the velocity of the impact. This means it is not a material constant in the traditional sense, as it can be shown to be a function of the impact velocity [23][24]. For example in granular gases when considering the interactions between viscoelastic spheres using Hertz's contact laws, the coefficient of restitution is obtained as a function of the normal component of impact velocity [25]. Or when impacting rough materials

the coefficient can reduce as the rough surface assists in energy dissipation [26]. It is generally found to vary in higher coefficient values materials ($e > 0.5$) to a higher degree than low value materials [27]. However, in the case of the application of purely spherical particles in this work the coefficient of restitution is taken as a constant as the value will be set to replicate the nature of coke or coal for industrial application which requires a low value to ensure the correct post impact behaviour. Further reviews discussing the nature of the coefficient of restitution are available for various materials for example the study of ice particles [28].

2.1.4.3 Computational modelling of granular materials

Granular materials can be modelled in two distinct ways. The first is a Discrete based methodology where material is assumed to consist of separate particles or grains and contacts between these grains are modelled. This is the type of model which shall be used in this work. The second is a continuum based method where the separate grains of material are assumed to be a smaller part of a larger bulk whole, sometimes referred to as a system with a "body made of granular materials" [29]. An example of this is the Material Point Method (MPM) which utilises Lagrangian elements to simulate a material as a continuum body. Its use for granular materials has been demonstrated in rockfall and landslide conditions [30]. The Discrete based method is the one which shall be discussed next.

2.2 Discrete Element Method Preliminaries

2.2.1 Overview

The Discrete Element Method comprises two main components, the discrete elements themselves (i.e. the particles) and the structures which they can interact with. In the case of this thesis the individual particles are separate and not connected to each other and they are assigned the properties of a given material. The structures with which particles can interact represent features such as walls or plates.

DEM simulations are transient and simulate granular material behaviour over a given time, t. Time is subdivided into discrete parts called timesteps, Δt. The simulated time that has elapsed is the sum of the time steps completed, N. Therefore the time of a simulation can expressed as shown in Equation 2.4.

$$t = N\Delta t \tag{2.4}$$

When the simulation begins the initial positions of particles are defined in an input file. The initial definition may involve spawning a specific mass of particles in the first timestep or spawning a specific mass of particles per timestep. Either way particles are assigned position, initial velocity (usually 0 ms^{-1}), density, radius and any other properties required to represent the material and the system being simulated.

As the simulation progresses forces must be applied to the particles to create movement, and the positions of these are tracked individually using a Lagrangian method. There are two main approaches in DEM, hard sphere and soft sphere models. In hard sphere models particle forces are resolved instantaneously when contact is detected. The collision is defined to be at a single point and the forces can be calculated using the current impact velocities of the two particles [31]. Soft sphere models allow an overlap between the particles and calculate the force based on this overlap [6]. The forces generated can then be resolved to create movement. This is done using Newton's second law which, in its simplest form, is shown in Equation 2.5.

$$F = ma \tag{2.5}$$

In DEM this equation is solved for acceleration, a, using the particle's mass, m and force, F. The acceleration can then be used to determine a particle's velocity and therefore its position. The DEM simulation calculates the force section by splitting it up into parts which represent different mechanisms. Usually this is split into four general sections: the elastic component, F_c, the damping component, F_d, the gravitational component, $m_i g$, and finally an 'other' component, F_i, which can be used to represent any forces which the user wishes to apply. Therefore Newton's second law is written for particles as shown in Equation 2.6 for two particles which are represented as particle i and particle j [5][2][31][6].

$$m_i \frac{dv_i}{dt} = \sum (F_{c,ij} + F_{d,ij}) + m_i g + F_i \tag{2.6}$$

The rotation of the particles are also resolved using Newton's second law using the torques generated and transfer between particles and wall structures as shown in Equation 2.7.

$$I_x \ddot{\theta}_x = \sum M_x \tag{2.7}$$

Where I_x is the moment of inertia of a particle, $\ddot{\theta}_x$ is the angular acceleration and M_x is the torque/moment for the particle.

The use of these equations for the force calculation requires multiple components. The elastic component, F_c, is the part of the force which contains zero energy loss. For example if a particle was to collide with a surface at 1 ms^{-1} it would still have a velocity after the collision of 1 ms^{-1}. This is usually imagined as a spring. Naturally this is not representative of the real world. This is where the damping component, F_d, is introduced. It represents all the energy losses which can be experienced by a particle. It takes two forms in the calculation. One is derived from the coefficient of restitution which represents the loss of kinetic energy due to a collision and is generally a function of the material which was discussed previously section 2.1.4.2. Often this is imagined as a dashpot. The second is friction which is a function of the contact between two materials. Together this generally represents the energy dissipation of a collision. It should be noted that the method is by no means limited to just these factors. Additional factors can be included in this term as long as the effects can be characterised and modelled.

2.2.2 Force Models

For the forces to be calculated to create movement in the soft sphere model an overlap is required. This is shown for a 2D case in Figure 2.3 for particle i and particle j. Generally it is considered from the perspective of particle i i.e. it is impacting particle j.

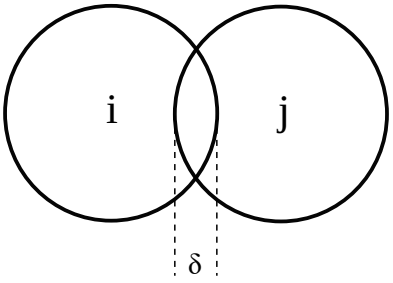

FIGURE 2.3: Demonstration of overlap, δ, between two impacting particles i and j

There are two main methods of calculating the contact or elastic force: Hooke's law and Hertz's contact theory. Each of these requires setting stiffness parameters for the material. However, due to the explicit time method (described below) used in the program it needs to be set carefully.

2.2.2.1 Time Integration

There are two types of time scheme when using computational models. Implicit and Explicit. Implicit methods solve an equation which involves both time steps of a simulation therefore $Q(t + \Delta t) = f(Q(t), Q(t + \Delta t))$.

Explicit methods use the information provided in the current timestep, t, to calculate the values for the next timestep, $t + \Delta t$. A key consideration when using the explicit method is the fact that it is only conditionally stable, especially when considering stiffness parameters.

The method implemented to calculate this in the DEM program is a Taylor Expansion. The first terms of which represent the Euler method, the secondary and tertiary terms reduce the total error of the expansion making a closer and more accurate approximation [2].

The general form of the Taylor Expansion is shown in Equation 2.8 [32]

$$f(a) + \frac{f'(a)}{1!}(x-a) + \frac{f''(a)}{2!}(x-a)^2 + \frac{f'''(a)}{3!}(x-a)^3 + ... \tag{2.8}$$

As the system deals with spring stiffness and its dynamic relations a critical time step can be obtained whereby the system would be at its naturally frequency. This was derived originally for DEM by Cundall and Strack although it is a well known phenomenon. For this case a 1D mass attached to a spring is imagined for the calculation and is shown in Equation 2.9 [6].

$$\Delta t_c = 2\sqrt{\frac{m}{k}} \tag{2.9}$$

Other authors have presented it in different forms for DEM as shown in Equation 2.10.

$$\Delta t_c = 2\pi\sqrt{\frac{m}{k}} \tag{2.10}$$

Equation 2.10 is the critical time step used by Bridgeman and Holmes [5][2]. Tsuji altered Cundall and Strack's original numerical model to create a suitable timestep for a system by looking at the convergence of particle behaviour in a plug flow [33].

From this it can be seen the timestep used in a simulation usually comes from a function of this critical time step $\Delta t = f(\Delta t_{crit})$ where so long as the timestep result in reliable simulation behaviour the exact method of determining it can vary. In general, it has become common practice to express the time step of a DEM model as shown in Equation 2.11.

$$\Delta t = C\sqrt{\frac{m}{k}} \tag{2.11}$$

Where C is regularly a fractional value. Malone carried out an investigation into the effects of the time step on the accuracy of a DEM model by investigating the energy error of a known system. They found that lower values of C were generally more accurate when assessing the relative error in energy conservation of a known perfectly elastic system which removed all forms of energy dissipation [34].

There has been criticism of this method of setting timesteps due to it being derived in a 1D system. Prior to Malone's 2008 paper, O'Sullivan 2008 suggested a smaller critical time step where $C = 0.17$ using a 3D system [35]. Through this they also stressed the importance of tracking the energy balance inside a system as a method of being able to detect potential numerical instabilities.

Generally, what can be determined from this is the more a timestep is reduced below the critical timestep value shown in Equation 2.9 the less effect it has on the results of the simulation [17].

2.2.2.2 Linear Spring Dashpot Model

The first method of creating an elastic force is to imagine the collision as a spring. For this Hooke's law is well known to describe the force required to compress a spring a certain amount. This compression can be thought of as the overlap, δ, shown in Figure 2.3, between two particles. The equation for this is shown in Equation 2.12.

$$F_c = k\delta \tag{2.12}$$

The second component is the energy dissipation. This is done using a dashpot which is calculated using the damping constant, c, which is a function of the material and the velocity of the impact, v as shown in Equation 2.13.

$$F_d = cv \tag{2.13}$$

Figure 2.4 shows how both a spring and dashpot is used in parallel to create the linear spring dashpot model. This is otherwise known as the Kelvin-Voight model. Two parts are considered, a normal component and tangential component, the values which are used to set both spring and damping constants shall be discussed in later sections.

Therefore, as shown in Equation 2.6, these two components can be summed to represent the impact force and be used to calculate the future velocity and position of the particles as shown in Equation 2.14.

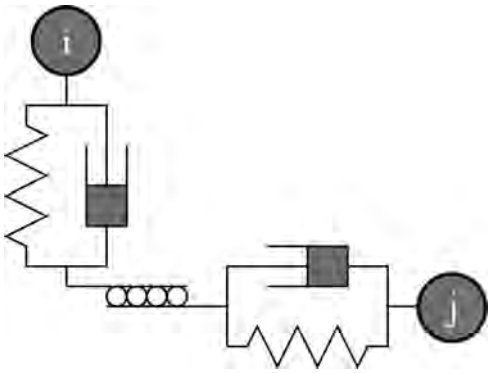

FIGURE 2.4: Linear spring dashpot model between two impacting particles i and j

$$F = k\delta + cv \tag{2.14}$$

2.2.2.3 Hertz Spring Model

Hertz's contact model is based on the contact mechanics work by Hertz in 1881 [36][37]. For DEM this is expressed as shown Equation 2.15.

$$F_c = k_h \delta^{3/2} \tag{2.15}$$

The difference between the force calculation of these methods can be seen in Figure 2.5 as a function of the overlap value. As can be seen the Hertzian model is a non-linear theory while the linear force model is clearly proven to be linear.

The damping of Hertz's contact theory was developed by Mindlin and Deresiewicz in 1953.

2.2.2.4 Hertz Mindlin Model

This model uses the loading history to model the contact force and account for the calculation of the tangential force displacement relationship which is not possible to using solely the models laid out by Hertz [37]. Mindlin and Deresiewicz laid out a series of rules for this impact and how it is to be calculated at varying positions on the load displacement path [38]. For example, there are considered to be cases, the first of which is where a tangential displacement of a contact is varying and the normal displacement is constant. The second where the tangential displacement is constant and normal displacement is varying. Both varying at the same time cannot occur. When the normal displacement is varying, the tangential spring constant can be calculated

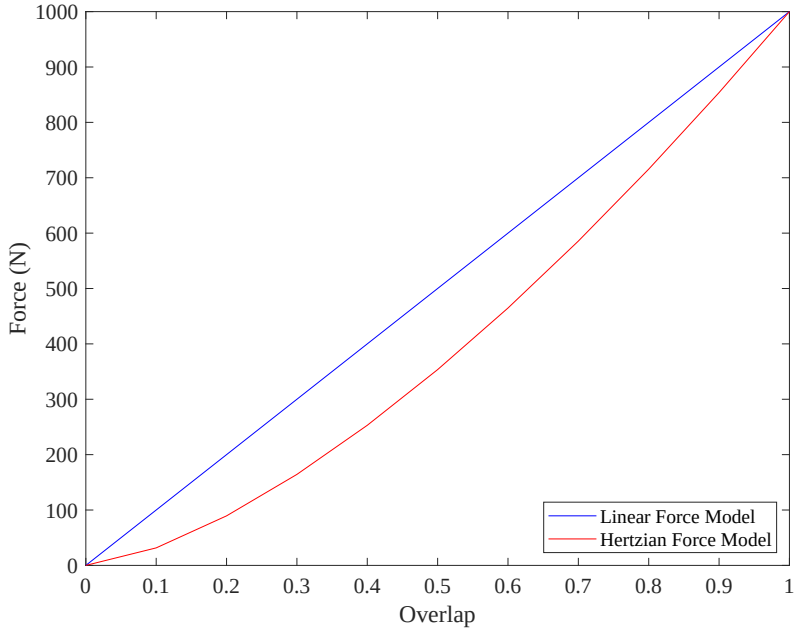

FIGURE 2.5: Spring force, F_c, comparison of linear and hertzian force models plotted against overlap, δ

depending on the contacts position on the load path i.e., it is either loading, unloading or reloading. This application of various rules and conditions allows the calculation to be much more physically correct, however it adds considerable complexity to the system. A full description of the process can be found in DiRenzo's work describing and comparing DEM contact models [39].

2.2.3 Spring Stiffness

In the contact models laid out, the spring stiffness value, expressed in Newtons per meter (N/m), of both the normal and tangential component plays a vital role and setting them is the initial starting point in DEM. With these values holding such an important role in the Discrete Element Method it is not surprising multiple methods of deriving them have been developed and presented however none are generally accepted and the spring stiffness value can vary depending on the contact model used.

2.2.3.1 Linear Force Model

Cundall and Strack defined two versions of spring stiffness for their linear model representing the normal and shear directions. In the literature these are now most commonly referred to as the normal spring constant, k_n, and the tangential spring constant, k_t. The values assigned by Cundall and Strack were in the range of 1.35 x10^9 and 1.56 x10^8

for the normal stiffness [6]. The tangential constant would then be a fraction of this. No detail was provided as to how these values were arrived at.

Often this spring stiffness value is set by the modeller and based on their experience of using their program. The other parameters are then used to affect the various properties and behaviours of the material. The main driving factor behind setting the spring stiffness value in the linear force model is to reduce the computational time, thereby beginning to overcome one of DEM's main limiting factors.

For example, in Malone's work mentioned previously, the spring stiffness value was derived as a function of the potential energy of the system as shown in Equation 2.16 [34].

$$k = \frac{2mgh_0}{\delta_{h_0}^2} \tag{2.16}$$

Another method was presented by Mishra and Murty. This used the kinetic energy of the highest velocity collision in the domain [40]. This is shown Equation 2.17.

$$k = f^2 \frac{mv_0^2}{d^2} \tag{2.17}$$

Where f is the penetration factor shown in Equation 2.18.

$$f = \frac{d}{\delta_{max}} \tag{2.18}$$

With the maximum overlap value allowed, δ_{max}, generally being set to 10 % of the particle diameter, d, for soft sphere DEM simulations. The purpose of this is to limit the force generated by the force equation to avoid unrealistic behaviour beause of an extremely large overlap.

Figure 2.4 shows the spring and dashpot system and it can be seen there is both a normal and tangential component to the model. To determine the tangential spring stiffness, k_t,a function of the normal spring and the material's Poisson ratio, υ, is used as shown in Equation 2.19.

$$k_t = \frac{k_n}{2(1+\upsilon)} \tag{2.19}$$

2.2.3.2 Hertz Stiffness

When compared to the previous model the Hertz models have an immediate benefit when calculating the spring stiffness value as they can be set based upon real world properties using their basis in contact mechanics. The calculation for the normal spring stiffness can be derived from the calculations of contact area, pressure and normal displacement between 2 spheres as is shown in Equation 2.20 [24].

$$k_{n,Hz} = \frac{4}{3} E^* \sqrt{r^*} \tag{2.20}$$

The tangential stiffness can also be calculated in a similar fashion and its calculation is shown in Equation 2.21.

$$k_t = 8G^* \sqrt{r^* \delta_n} \tag{2.21}$$

Where E^* is the effective Young's modulus of the materials in contact, r^* is the effective radius, G^* is the effective shear modulus, and δ_n is the normal overlap [39].

2.2.3.3 Selection of model

Hertz's spring constant is both a strength and weakness. As it is a set value based on material parameters, altering it invalidates its applicability. Using these material parameters often give rise to time step values between $\Delta t = 1\text{x}^{-6}$ and $\Delta t = 1\text{x}^{-9}$. This adds computational time to each DEM simulation being ran, in exchange for more accurate modelling of individual particle interactions.

However, when considering a particle and structural element interaction it generally gives a worse approximation than the linear model by assessing the impact angle of a collision with a structural element [39]. The reason for this is as the accounting for tangential displacement effects in the Hertz model can bring rise to errors which are often worse in scale than equivalent assumptions regarding setting the tangential stiffness in the linear model. This is further reinforced by the linear model showing good force exertion on boundaries for particle impacts on macroscopic scales [41].

In general, there is no consensus as to which model is best, and it is for the user to decide based upon their own needs. For this work, the linear spring dashpot model was chosen. This was because computational time was a priority and the linear spring dashpot model is capable of using a larger timestep value than the Hetrtz model, while retaining accuracy as discussed previously.

2.2.4 Damping

There are two main models for damping which are used in DEM. Kelvin-Voight and Hertz-Mindlin which was discussed previously [39]. The model used in the program is Kelvin-Voight so it shall be looked at here. This has a general equation of motion as shown in Equation 2.22, this is a combination of previous Equations 2.6, 2.12 and 2.13.

$$F = m\frac{d^2x}{dt^2} + c\frac{dx}{dt} + kx \tag{2.22}$$

Previous sections discussed calculating the spring constant, k for both normal and tangential components. To calculate damping, the damping constant, c, must also be determined. Cundall and Strack did this using a function of the normal and tangential spring constants, k_n and k_t. This was done through the use of a proportionally value titled β.

$$c_n = \beta k_n \tag{2.23}$$

$$c_t = \beta k_t \tag{2.24}$$

2.2.4.1 Coefficient of Restitution

The calculation of the damping has been altered over the years. One method is to calculate the damping using the materials coefficient of restitution, e, as mentioned previously in section 2.1.4.2. The coefficient is a description of the energy lost from a particle whist it impacts a surface. For cases where a bulk of particles is considered it has been shown that damping has little effect on the overall calculation when considering impact force [42].

As previously discussed, the values the coefficient of restitution represent whether a collision is inelastic, elastic or partially elastic. Therefore, it can represent the amount of damping present in each collision. There can be three states of damping: under damped, critically damped and over damped.

The state of damping is expressed using the damping ratio, ξ. Values greater than 1 would represent a system where it gains energy with each collision, as previously mentioned. A damping ratio equal to 1 would represent a critically damped system. Finally, values between 0 and 1 would be used for under damped systems. In DEM the system is under damped, physically representing the energy loss of a particle in system for each collision.

The damping coefficient can be calculated from the damping ratio using Equation 2.25.

$$c = c_c \xi \tag{2.25}$$

Where c_c is the critical damping coefficient ($\xi = 1$). For critical damping the coefficient is $c_c = 2\sqrt{km}$. Therefore, for an under damped system the damping coefficient is shown in Equation 2.26.

$$c^2 < 4km \tag{2.26}$$

This leaves the determination of the damping ratio value which is done using the coefficient of restitution as shown in Equation 2.27.

$$\xi = \frac{\ln(e)}{\sqrt{\pi^2 + ln(e)^2}} \tag{2.27}$$

From this the damping coefficient of the normal damper can be calculated using Equation 2.25 giving Equation 2.28 [43] [44].

$$c_n = \frac{2\sqrt{km}\ln(e)}{\sqrt{\pi^2 + ln(e)^2}} \tag{2.28}$$

Which can be simplified to the form shown in Equation 2.29.

$$c_n = 2\xi\sqrt{k_n m} \tag{2.29}$$

Once the normal damper is calculated it requires the calculation of the tangential damper. This uses the tangential spring in place of the normal spring and is calculated using the same method as shown in Equation 2.29, this is demonstrated in Equation 2.30

$$c_t = 2\xi\sqrt{k_t m} \tag{2.30}$$

2.2.5 Contact Detection

2.2.5.1 Overlap Calculation

The basis of how the DEM calculates forces has been set out in the previous section. This thesis is primarily interested in the interactions between the particle and the structural elements. Therefore, particular interest needs to be given to how the mesh elements interact with the particles. This is a key factor in the single largest downside and limiting factor for DEM which is the computational time it costs to run. The majority of which is used detecting interactions between two particles and particle to structure contacts. After which the extent of these interactions has to be determined. For example a simple case where particles are introduced at 1 kg/s onto a 2048 element 45° plate can take upwards of 10 minutes.

An initial consideration for how this is done is first needing to know how the elements are presented in the model. As DEM is a Lagrangian method each individual particle is tracked, this also holds true for the mesh [45].

The coordinates are presented in 3D using the Cartesian coordinates in x, y, and z. Therefore, each element is described by the three coordinates, either called nodes or vertices. The normal is then provided to give the element a direction which is often considered as "up". This is expressed as a 3D vector which represents a direction as shown in Figure 2.6.

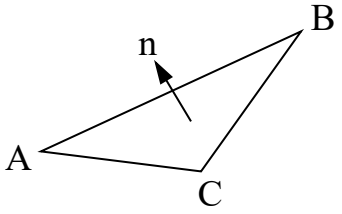

FIGURE 2.6: Element composed of coordinates, A, B and C showing the its normal, n

Therefore, any vertex/node (corner of a triangle), A, B or C is represented through its x, y, and z position as shown for vertex A in Equation 2.31.

$$A = \begin{Bmatrix} A_x \\ A_y \\ A_z \end{Bmatrix} \tag{2.31}$$

The normal is provided on creation of the model however it can be calculated using the 2 vectors derived from points A, B and C. These vectors would be vector $\vec{AB}$ and vector $\vec{AC}$. The cross product of which provides a vector 90 degrees to both, i.e. the normal of

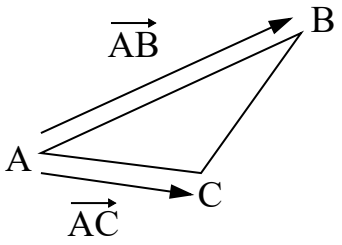

FIGURE 2.7: Element showing vectors $\vec{AB}$ and $\vec{AC}$ created using coordinates A, B and C

the element. Note in 3D there can be 2 answers for this, hence why the correct direction must be checked before use in a DEM program. The simplest method of which is the use of a program such as Blender [46].

The first routine searches through the elements using the parameters created by the element that is being looked at and the position of the particle. First a scalar parameter, D_e, is created using the dot product of the element normal unit vector and vertex A as shown in Equation 2.32. In this case the coordinate is treated as if it were a vector from the origin position of the simulation $[0, 0, 0]$.

$$D_e = \hat{n} \cdot A \tag{2.32}$$

The calculation of the magnitude of the element normal is also used as shown in Equation 2.33.

$$|\hat{n}| = \sqrt{\hat{n} \cdot \hat{n}} \tag{2.33}$$

An equivilant parameter to D_e is created using the particle position, D_p, as shown in Equation 2.34. This is a replication of Equation 2.32 is made using the particle position instead of the coordinate A.

$$D_p = \hat{n} \cdot P_i \tag{2.34}$$

These are then compared and used to calculate the distance between an element and particle using the magnitude of the element normal $|\hat{n}|$ as shown in Equation 2.35.

$$d_{p,e} = \frac{D_p + D_e}{|\hat{n}|} \tag{2.35}$$

The value $d_{p,e}$ gives the distance between the particle and the element. When compared with the particle radius, r, as shown in Equation 2.36

$$\delta = d_{p,e} - r \tag{2.36}$$

For a structural element, the overlap value is then doubled to create an effective overlap, δ, for the collision. This makes the collision equivalent to a single particle impacting an immovable particle of equal size and uses this for the force calculation as shown previously in Equation 2.12.

This demonstrates how the overlap value is created and collisions are detected. This is the basis of the initial routine set out [5].

This however does not provide all the information required when impacting with an element as pointed out by [2] as the position of the particle and the element will vary how much of the element is overlapped at any one time. It also means multiple elements can be overlapped as is demonstrated in Figure 2.8. Therefore, this value must be quantified to calculate the correct magnitude of force which should be applied. This is done using the theories set out for the field of game design. A brief summary of these will be shown to create an understanding, but more in depth versions can be found here [2] [47].

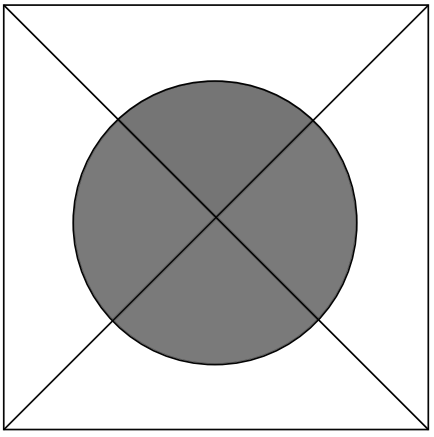

FIGURE 2.8: Particle impacting multiple elements in a single instance. Grey shaded area represents the total overlap area between the particle and elements

2.2.6 Voronoi

The complications arise when considering a single particle can impact a triangular element at any point and that if a particle is impacted it does not mean that an element is necessarily at the centre of a particles projected area.

To start this the orthogonal projection of the particle, $P_{i,p}$, first needs to be calculated. This is used to assess where this point is in relation to the element/triangle ABC. The orthogonal projection of the particle is calculated using the $d_{p,e}$ value and the unit normal of the element, $\hat{n}$. This calculates particle projection, $P_{i,p}$ as shown in Equation 2.37.

$$P_{i,p} = P_i + \hat{n}(d_{p,e}) \tag{2.37}$$

The element can then be split into sections which area created by the 3 vertices, where in a simple case there are three faces created from them. Face AB, AC and BC. Each vertex each has its own region also as shown in Figure 2.9.

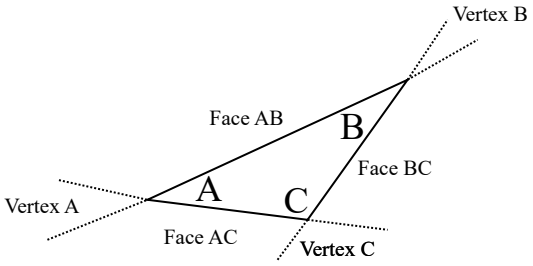

FIGURE 2.9: Element with vertex and face regions highlighted

This projected point will be in a position somewhere on the same plane as the element which is being looked at, in one of the zones highlighted or inside the element itself. The next step is to determine where it is. This can be done using a series of cases which compute and check possible positions by using the vectors created from the element coordinates ABC and the vectors created using the point $P_{i,p}$, $\vec{AP}$, $\vec{BP}$, and $\vec{CP}$. Then the dot products of various combinations can be used to check where the point is in relation to each coordinate [47]. For example, if P lay inside the vertex region of A then to dot products of $\vec{AB}$ and $\vec{AP}$ as well as $\vec{AC}$ and $\vec{AP}$ must both be negative or equal to zero. The angle created by both vectors is obtuse as can be seen in Figure 2.10.

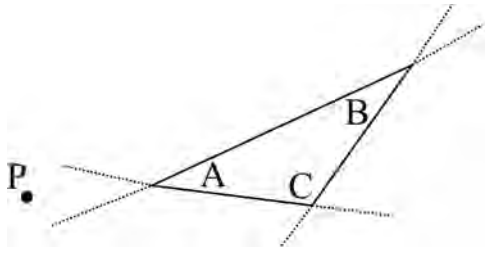

FIGURE 2.10: Element with a projected point, P, from a particle

The position can then be used to calculate the area of overlap between a particle and element area, as shown in Figure 2.6, using a series of cases which are highlighted in more detail here [2].

2.3 Summary

This chapter has reviewed the methodology used in DEM and briefly reviewed the types of materials it simulates. There are two main contact approaches which are taken in simulating granular materials; soft and hard sphere. In this work soft sphere will be used to calculate the required contact forces. It does this by allowing overlaps between both particle-particle contacts and particle-wall contacts. This is what ultimately provides DEM its difficulties as it does not replicate the system in a physically correct sense, i.e. particles do not actually overlap each other in the real world (excluding deformation). Therefore every subsequent parameter needs to be considered individually and assessed in terms of the applicability for any given situation (for example depending on the scale).

However, what is unexpected, is that in simulating forces between particles what could be considered the 'more physically correct' model of Hertz-Mindlin does not always provide a significant benefit and it comes with a considerable cost by reducing the timestep. Therefore, in this work, the linear-spring dashpot model will be used for particle-particle contacts and particle-wall contacts to limit the overall computational time required throughout.

Chapter 3

Wear

Wear, is a broad term and can by itself be extremely generic. It can vary massively depending on the system being studied, the conditions, materials, maintenance, design and so on. However, it can be thought of as one broad principle. A systems response to its operation resulting in damage and/or removal of material due to sustained use. Formally this was written as 'the progressive loss of material from the operating surface of a body occurring as a result of relative motion at its surface' [48].

It has far reaching consequences not only on a company but on the planet as a whole. Throughout the twentieth century the importance of this began to emerge and the term Tribology was coined for the field specialising in looking at the effects of friction and wear [49]. Studying wear is even more important in today's world as approximately 23% of the global energy consumption came from contacts between materials. The majority (20%) in attempting to overcome friction [50]. A possible reason for this is some equipment was designed before serious consideration was given to it. Leaving companies which have older structures generally having more issues with wear especially in the steel industry.

3.1 Overview

Wear taken to its logical conclusion results in the failure of a system. However, with the complexity of how wear can occur there are three different ways of looking at it. The first method looks at the wear scar which is produced and categorises from there. The second looks at the physical mechanism which causes wear and the third looks at the conditions surrounding the wear scenario [51]. Each method has its own uses and depending on the engineer's requirements each way of looking at wear can have its benefits and drawbacks.

To this end, as a mode of failure it requires categorisation to develop an understanding of how it occurs and what can be done to assist in its prevention. However, the exact categories have had some discussion over the years. In the mid twentieth century it was generally put into four categories [52] [53]; Adhesive, Abrasive, Corrosive and Fatigue. These categories are now usually expanded upon to six categories to include Erosive and Fretting wear. However, these can still vary depending on the author as shown in Figure 3.1.

Once the categories are established, it is important to look at how the contact can occur. Generally, these are considered to only be aesthetic categories and hold no real scientific use apart from understanding and conveying how the wear is carried out. These contacts are: Sliding, Rolling, Impact, Fretting and Slurry [54]. Impact and fretting are also considered to be their own form of wear.

From here, wear can be divided even further into plastic or elastic contacts. The type of wear occurring could depend upon how much stress is applied to a material. A materials elastic limit must be exceeded to wear due to abrasion for example. However, a material could wear from fatigue due to either plastic or elastic contacts showing low cycle or high cycle fatigue respectively.

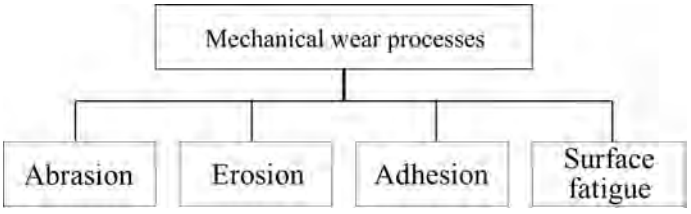

FIGURE 3.1: Recreated wear classifications as presented by Williams in 2005

To begin applying wear models for this thesis it is therefore important to understand the types of wear which could expected to be found in Tata Steel. The pieces of equipment studied in this work process granular materials at a high volume. These commonly involve repetitive impact and sliding of materials. Therefore, how these wear mechanisms

are modelled and how they may be applied needs to be discussed. Naturally, as they are to be applied in a computational model the ways of expressing them mathematically becomes important. As DEM will be used, types of wear commonly associated with the flow of granular material shall be looked at, namely: Abrasion and Erosion. Figure 3.2 shows illustrations of these wear mechanisms. Impact wear is also considered to a lesser degree, as the modelling of this phenomena is more recent and is generally concerned with more percussive impacts.

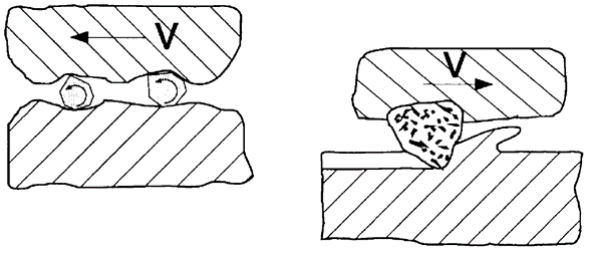

(a) Abrasion

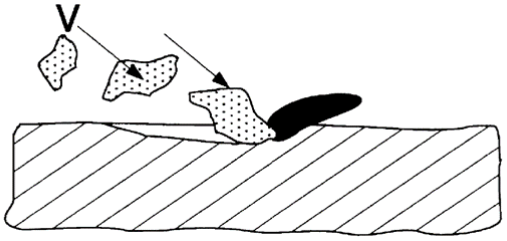

(b) Erosion

FIGURE 3.2: Illustration of abrasive and erosive wear mechanisms produced by Zum Gahr in 1998 [4]

3.2 Abrasion

Abrasion is probably the category which is most thought of when discussing wear however with it being so common its definition can be vague. Typically, it is considered to involve two sliding surfaces. Although this is not always the case, as situations often occur where only one sliding surface is present and asperities are involved in the form of particles. This could be thought of as a special form of abrasion or it could also be put into its own separate category as erosion.

As a form of sliding wear, two surfaces contact and one moves over the other. A difference in surface hardness then leads to the harder surface scratching/gouging material from the softer surface. There are two broad categories for Abrasion; two body and three body. Each looks at the effect of asperities trapped between the sliding materials. It is these asperities which dig in and abrade the softer material. Two body abrasion looks

at the sliding of the material, whereas three body looks at both the sliding and rolling of the asperities [51]. Two body abrasion has the potential to be worse although this is situation dependent [4].

Numerically abrasion is expressed by the Archard equation and is governed by the Reyes-Archard-Krushchov laws [55] [56]. It can also be referred to as the Rabinowicz or Preston equation depending on the field in which it is studied [48] .Here it shall be referred to as the abrasion equation for simplicity and it is shown in Equation 3.1.

$$Q = \frac{KWL}{H} \tag{3.1}$$

Where, K is the abrasive wear coefficient, Q is the material removed from a surface by the abrading surface, W is the total load of the asperity and L is the sliding distance of the asperity. H is the Vickers Hardness of the softest material.

The derivation for this equation shall be presented here as it is the most common equation considered and the generally most widely accepted wear equation.

First W needs to be understood as it is the local load provided by the asperity intruding on the abraded materials surface. An asperity is a piece of hard material between the two sliding surfaces. This could be from either of the materials, or from an outside source such as sand. The asperity is treated as a spherical object. Allowing the change in the local load on the asperity to be as shown in Equation 3.2.

$$\delta W = P\pi r^2 \tag{3.2}$$

Where P is the local pressure exerted by the asperity and r is the radius of the asperity.

Next the volume of material sheared off by an asperity is assumed to be in the shape of a hemisphere that has slid a distance of $2r$ or the asperities diameter.

The volume of the hemisphere is expressed in Equation 3.3.

$$\delta V = \frac{2}{3}\pi r^3 \tag{3.3}$$

When slid over the distance $2r$, it removes a volume as shown in Equation 3.4.

$$\delta Q = \frac{\delta V}{2r} \tag{3.4}$$

Therefore including the volume of the hemisphere, δV, this can be rewritten as Equation 3.5.

$$\delta Q = \frac{\pi r^2}{3} \tag{3.5}$$

Including the variation in load, W, this becomes as shown in Equation 3.6.

$$\delta Q = \frac{\delta W}{3P} = \frac{\delta W}{3H} \tag{3.6}$$

P is often expressed as the Vickers Hardness H. This allows the conclusion to be made for a slide over a distance $2r$, the material removed will be to the ratio of three times the Vickers hardness of the material for the total normal load applied.

This can be generalised for any sliding distance, L, as shown in Equation 3.7.

$$Q = \frac{KWL}{H} \tag{3.7}$$

The value of 3 has now been converted to a coefficient, K, which indicates the severity of the overall wear. Archard indicated in their research that this represented the probability of the asperity forming wear debris [55].

General values of K were presented for differing types of abrasion and erosion. A mild form of wear is indicated by values of approximately 10^{-8}. Severe wear is indicated by values of approximately 10^{-2}. In comparison erosion on this scale tends to sit between 10^{-4} and 10^{-1} [4]. The values of K are generally determined experimentally through a back calculation once the volume of material removed is known.

3.2.1 Abrasion and DEM

The abrasion equation has seen application in DEM, for example it was used to obtain a spatial distribution of wear on the bottom of hopper surfaces in the mining industry. It was found wear was grain shape sensitive which was measured by using clusters of spheres to represent particles. It was also determined the main stage of wear was during unloading of the hopper [57]. In a second application it was used to compare two and three body abrasion in the case of scraper conveyor chutes. It was found three body wear was approximately 33 times worse than the amount of two body abrasive wear for this application. It was also found abrasion rate increases with increases in Poisson's ratio, shear modulus and density of material [58].

DEM has also been coupled with the Finite Element Method (FEM) to study abrasion in attempts to scale up looking at wear from a small laboratory scale to a large industrial

one. This naturally always presents difficulties. In this case it was done for a tipper. Drum tests were used calibrate the wear model for the material. Then FEM was used to look at the tipper body and DEM was used to track the materials behaviours and contacts. The study showed good agreement between the simulation and field measurements [59]. From this it shows a real possibility of using field measurements to calibrate models against real world industrial processes.

3.3 Erosion

Most commonly erosion is thought of in respect to natural erosion, where water runs over rock gradually removing rock. Here however the impact of particles is considered. Complications quickly arise when investigating particle impacts as it is not easily determined what the main cause of erosion is driven by. This led to two main theories being devised for how a particle impinging upon surface causes the surface to wear: Ductile and Brittle. Typical wear curves are displayed for these for both mechanisms in figure 3.3 [60].

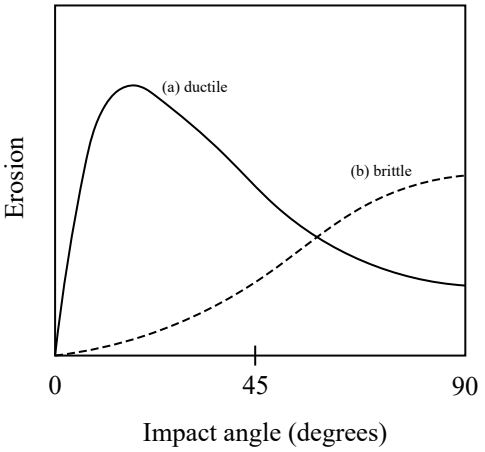

FIGURE 3.3: Curves displaying the variation between (a) ductile and (b) brittle erosion mechanisms with impact angle of particles as produced by Hutchings

3.3.1 Ductile Erosion

Ductile erosion is generally considered to occur via two mechanisms. The first is as a cutting mechanism, where the material is plastically deformed and removed during deformation. The material is pushed to the front of the eroding particle and removed as piece, in a similar manner to swarf when machining. The second mechanism is ploughing, this is when the eroding particle strikes the metal and pushes the excess material to either side of its path but no material is removed due to a single impact [61] [62]. After many impacts this will lead to material gathering and being removed.

A key parameter in ductile erosion is the impingement angle of the particle. It varies considerably with the angle with a maximum erosion occurring between 20 to 30 degrees as shown in figure 3.3. In a purely theoretical case where only ductile erosion acts; a 90 degrees or a 'normal' impact would produce little erosion in comparison. The mechanism which causes maximum erosion has been studied to determine which angle produces maximum erosion. In one case this was done by looking at the ratio of a material's fracture toughness and hardness and to use this to determine the erosion mechanism [63].

3.3.2 Brittle Erosion

In contrast to ductile, is at a maximum value when the impact angle is at 90 degrees. This is due to material's being worn by brittle mechanisms as they are less susceptible to the ductile erosion mechanisms of cutting or ploughing. Instead they tend to be more susceptible to cracking and fracture mechanisms [63]. In a very general sense this is due to an increased hardness of a material (there are exceptions) which makes it less susceptible to erosion at lower impact angles. This can be seen for the transitions between the wear of rubbers and tool steels which tend to erode mainly by ductile and brittle mechanisms respectively [64].

3.3.3 Identification of Erosion Mechanism

With two categories being present research has been carried out to find a way to determine which mechanism is occurring. This was called the erosion efficiency parameter and was aimed to determine the mechanism causing erosion: cutting and ploughing for example [65].

However following the identification of the erosion efficiency parameter there seems to be little work carried out in identifying the type of erosion mathematically until [66]. This paper was a start of categorising the types of erosion one may expect generally under certain conditions when the impact angle and particle velocities were varied. A number of interesting observations were made regarding erosion rate. They identified when particle velocity is low (36 ms^{-1}) the impacts of the particles measured in the study were generally elastic and did not contribute to the measured erosion rate. They stated this made erosion rate therefore almost independent of impact angle [66]. This is in direct contrast to work carried out by Johnson when looking at the impact velocity and elastic and plastic regime as will be discussed. From this it suggests even under elastic impact conditions there was a baseline erosion. Another interesting point raised was at that at high impact angle erosion rates are generally found to be lower due to some

phenomena: particle interference, particle embedding, and heavy plastic deformation of the surface but no actual material removal [66]. This leads to a question surrounding how the particle kinetics of a system affect wear modelling in general and if this can be quantified. Interestingly the erosion efficiency parameter identified is extremely similar to the parameter used to quantify the contact between materials identified by Johnson which will be discussed in section 3.3.3.2 [24] [65].

3.3.3.1 Ductile: Finnie's work

Of the two categories of erosion, the first to be looked at was Ductile by Iain Finnie in 1960. This concerned the cutting mechanism [67]. This is the model most often edited, critiqued and compared against in modern literature. Therefore, whilst not perfect it has stood the test of time.

Finnie expressed ductile erosion as shown in Equation 3.8. The derivation of this equation can be found here [68]. The work carried out is mainly in application to abrasive jet wear, i.e. high particle velocities and small particles. Ductile erosion is perhaps most commonly found in the form of slurry erosion.

$$Q = \frac{c}{\phi}\frac{mv^2}{2}f(\alpha) \tag{3.8}$$

Where m represents the mass of the particle. v represents the impact velocity. c represents a so-called cutting ratio and ϕ represent a flow stress. $f(\alpha)$ represents an angle function which is dependent upon the angle of impact α and the ratio of the horizontal and vertical force of impact, k. The cutting value, c, was generally taken as $1/2$ by Finnie through analogy to metal cutting experiments, however a review carried out by Shewmon and Sundarajan this found this to be invalid through the use of SEM [69]. In a review of fluid and particle systems and erosion modelling, it was stated these authors viewed Finnie's work as only of historical interest [70]. However, while many issues persist with the work, such as inaccurate calculation of wear at $0°$, and inaccuracy at higher impact angles, the model and derivatives still finds regular use in particle systems.

In 1972 Finnie published a paper regarding some observations about the erosion of ductile materials and the effect that each area had [71]. The factors listed as influencing erosion were:

1. Angle of impingement
2. Particle rotation at impingement

3. Particle velocity at impingement
4. Particle size
5. Surface properties
6. Shape of the surface
7. Stress level in the surface
8. Particle shape and strength
9. Particle concentration in fluid stream
10. Nature of carrier gas and its temperature

Generally, wear models take into account a selection of these parameters depending on their own application and needs. As will be demonstrated in the models presented here. For example, Finnie's work is concerned with the impact angle of a particle, size, and particle velocity at generally dilute levels of particle concentration.

The first limitation to this model is clear. It only models one aspect of erosion: ductile. It ignores any other types of erosion such as brittle. Another common issue which arises is when defining the constant parameters c and ϕ. An issue which was discussed by Finnie themselves in their final 1995 paper discussing their observations and opinions through their body of work [72]. Even though throughout the literature depending upon the application the methods of determining values for these values can vary. Leading to alterations to the equation which in some cases can make it nearly unrecognisable. An example of this is Equation 3.9

$$Q = \frac{Fm^2v^n}{\sigma_y} f(\alpha) \tag{3.9}$$

In this model F represents the fraction of particles which cut the surface ideally, a factor which was considered to be a one of the factors which affected erosion. σ_y represents the yield strength of a material [73]. This use this parameter contrasts with the usually quoted 'flow stress' which is generally a function of hardness [72]. Bousser used this version of the model to look at the effect of erosion on protective coatings for aerospace applications.

In general the value of the velocity exponent, n, has been shown to vary with the type of particle. It was noted by Bousser that values of $n = 2.2$ - 2.9 were seen in previous work carried out by Sheldon and Kanhere in 1972 [74]. They also stated that higher

velocity exponents were expected to exist in certain situations. For particles which are spherical, the model exponent can even be increased to 3 for example [60]. Also with increases in impact velocity, it can show a general trend of increasing [4]. Finnie made alterations to the equation depending on what factors were being considered [71]. However, Sheldon noted in their work, the experimental nature of the exponent variation is 'bothersome' and unknown and generally only an exponent value of $n = 2$ has been shown to fundamentally exist [67][74]. In short what can be surmised from this is the form of the equation can be altered depending on the parameters which are varying. The general outcome from this work is the conclusion that the erosion rate is proportional to the velocity with respect to an exponent ($Q \propto v^n$). In general, the value of ϕ is also set as a some function of hardness in more recent work. A secondary and unsurprising finding is the particle diameter also increases wear with respect to an exponent value of 3 [74]. This is accounted for via use of the mass calculation of a particle.

3.3.3.2 Brittle: Bitter's work

Starting in 1963, Bitter presented a two-part series which outlined a model for the deformation erosion mechanism which was excluded by Finnie. This considered the elastic and plastic stresses when a particle impinges upon a surface. An idea which is expanded upon greatly in the field of contact mechanics. Bitter outlined an energy balance for each particle interaction where the plastic energy absorbed by the material represented the amount of energy which went into creating the deformation for that impact. Leading to the creation of Equation 3.10, which describes the material removed from a single collision under a normal impact i.e. 90° [75].

$$Q = \frac{1}{2}\frac{m(v - v_y)^2}{\varepsilon} \tag{3.10}$$

The next step was to include the angle of impact as shown in Equation 3.11.

$$Q = \frac{1}{2}\frac{m(vsin\alpha - v_y)^2}{\varepsilon} \tag{3.11}$$

As can be seen Equation 3.11 fundamentally represents the ratio of plastic kinetic energy absorbed by the material and against ε. This factor, ε was called the deformation wear. It expresses the amount of energy required to remove a unit of material in this way. It was not immediately clear in Bitter's paper how the value was determined in their research. However, it was stated to be proportional to the elastic load limit, y, and the Young's

modulus of the material, in the form of y^2/E for both cement and glass[1]. However, the exact calculation of the specific energy value is not clear, and while the application of a combined ductile and brittle erosion equation is presented, and its application to metal is demonstrated its derivation is also not clear [76]. It was later surmised by the author the specific energy value is determined through back calculation from the measurement of material removal. A method was presented for its calculation using a Coriolis slurry tester. A note the author made in this work was the specific energy calculation is dependent upon the test condition carried out and is not an intrinsic material property [77]. Therefore, implying it is not applicable across applications. In more recent papers by other authors the value has also been presented [78]. The value is representative of the similar value used by Finnie in their description of ductile erosion, a factor used by Bitter in their combined ductile and brittle model.

The second value of interest is the value of v_y. It represents a so called 'threshold' velocity where as this value is reached the load applied to the material from the impact reached the elastic limit at this velocity. To derive this value Bitter used a schematic of a particle impacting a flat section. They used Hertz's contact theory to establish the stress distribution and derive Equation 3.12 [37].

$$v_y = \left(\frac{2\sigma_y}{3C}\right)^{5/2} - \frac{\pi^2}{2\sqrt{10}} y^{5/2} \left(\frac{1}{d}\right)^{\frac{1}{2}} \left[\frac{1-\nu_1^2}{E_1} - \frac{1-\nu_2^2}{E_2}\right] \tag{3.12}$$

The first term of which is often neglected resulting in the use of Equation 3.13

$$v_y = \frac{\pi^2}{2\sqrt{10}} y^{5/2} \left(\frac{1}{d}\right)^{1/2} \left[\frac{1-\nu_1^2}{E_1} - \frac{1-\nu_2^2}{E_2}\right] \tag{3.13}$$

Where y is the elastic load limit defined by Bitter using the cavity created from an impact in one case. Their work also used a value of $y = 1.59H_v/3.2$ where H_v was the Vicker's hardness of the material. When the velocity of impact is below this value, v_y, no erosion takes place using the model.

In contact mechanics this idea has been investigated further, most notably by Johnson who presented their model for an equivalent value. This effect was suggested to be captured using a non-dimensional parameter defined as $\rho v^2/\sigma_y$. A calculation using Hertz theory was also presented to determine the onset of yield for uniform spheres impacting the planar surface of a large body as shown through a rearrangement in Equation 3.14.

[1]It should be noted y and σ_y are not equivilant values although they do appear to be similar in definition

$$v_y^2 = \frac{26\sigma_y}{\rho}\left(\frac{\sigma_y}{E^*}\right)^4 \tag{3.14}$$

General values were given for the regime of the impact, the sections of interest of which are recreated in Table 3.1 [24]. It can be seen plastic impact is generally expected to begin occurring to some extent at low impact velocities and fully plastic impact would be expected at approximately 5 ms^{-1}, in contrast to work previously presented [66]. Therefore, between these impact velocity values a combination of both elastic and plastic mechanisms occur and quantifying and modelling the wear and impact at this point will likely be difficult.

TABLE 3.1: Regime for approximate impact velocities of metals recreated

Regime	$\rho v^2/\sigma_y$	Approx v_y (ms^{-1})
Elastic	$< 10^{-6}$	< 0.1
Fully Plastic	$\approx 10^{-3}$	≈ 5

Often this is for singular impact, and the effects of having a high mass flow rate of granular material is unclear.

In the second part of Bitter's 1963 series they began to look at the combination of what they termed deformation (brittle) and cutting (ductile) wear [76]. This investigation led to several erosion phenomena being explained especially regarding impingement angle.

Another consideration highlighted, is the work hardening of a material as it is deformed. In the first paper of his series, Bitter confirms results presented by Mulhearn and Tabor 1960 which displayed an increase in dynamic hardness of material when highly deformed while extremely ductile materials showed an even higher increase [79][75]. Possibly this is from the work hardening done when the material is impacted. This brings a new level of complexity into how to deal with the parameter ε for this model if in the real world it varies with work hardening.

3.3.3.3 Combined: Nielson and Gilchrist

An expansion of Bitter's combined erosion model was carried out by Nielson and Gilchrist in 1968. A key aspect to the combination of the two models is to generalise both models to output the same result. A second aspect was the creation of a critical angle which replaced Finnie's criteria [80].

$$Q = \frac{\frac{1}{2}M(V^2 cos^2\alpha - v_p^2)}{\phi} + \frac{\frac{1}{2}M(V sin\alpha - K)^2}{\varepsilon} \tag{3.15}$$

$$Q = \frac{\frac{1}{2}MV^2cos^2\alpha}{\phi} + \frac{\frac{1}{2}M(Vsin\alpha - K)^2}{\varepsilon} \tag{3.16}$$

Finnie's half of the equation uses a value of ϕ to represent the amount of energy required to remove one unit of material from the surface (note: this is not the same value as presented in Equation 3.8). In a similar fashion to ε from Bitter's equation. Equation 3.15 is for angle of impact below a critical angle, α_0. Equation 3.16 similarly represents when the angle of impact is above α_0. The critical angle, α_0 represents the angle at which a particle must impact so it leaves with no velocity parallel to the plate it impacted.

Interestingly Nielson and Gilchrist's equation has seen use in more recently when looking at the influence of impact angle on the erosion behaviour of cermet's [81]. Where it was found that an increase in impact angle switched the wear mechanism from damaging a binder phase, to both the ceramic and binder phases. With it generally being found erosion behaviour was considered to be worse at low impact angles for cermets, in line with all previous research carried out regarding ductile erosion, and the theoretical wear maps generated as shown in Figure 3.3.

A general limitation for these types of wear models is that it is assumed the mechanism is the sole driving factor in erosion, and the application of these in machining is both qualitatively and quantitatively accurate generally. However as was pointed out by Andrews, the models often ignore a number of factors similar to the factors presented by Finnie [71]. An example of this is the fact they do not account for cases where the particle impacts do not give rise to chips [82].

3.3.3.4 Combined: Clark and Wong

Clark and Wong took a similar approach to Neilson and Gilchrist in combining the models however their model was for the application slurry pot testing for 1% SiC by mass in a diesel oil [83]. They used a simple relationship for kinetic energy which would yield the expected theoretical values of erosion for both the ductile and brittle mechanism's. This created their brittle component as shown in Equation 3.17.

$$Q_{brittle} = \frac{m}{2}\frac{(v_n - v_y)^2}{\varepsilon} \tag{3.17}$$

Where v_n is the normal impact velocity, v_y, is the velocity required to initiate plastic flow, (although this was assumed to be zero for ductile materials) and ε is the specific energy required for brittle erosion. The ductile component is shown in Equation 3.18.

$$Q_{ductile} = \frac{m}{2}\frac{v_t^2 sin2\alpha}{\Phi} \tag{3.18}$$

Where v_t is the tangential velocity, in similar fashion to the abrasion model previously presented, Φ is the specific energy for ductile erosion and α is the impact angle. A key difference between this model and Neilson and Gilchrist's is the removal of the critical impact angle.

Combing both equations give the model which was presented as shown in Equation 3.19.

$$Q = \frac{m}{2}\left[\frac{(v_n - v_y)^2}{\varepsilon} + \frac{v_t^2 sin2\alpha}{\Phi}\right] \tag{3.19}$$

3.3.3.5 Erosion: Oka

A different approach to modelling erosion was carried out by Oka whom studied erosion using an angle function, $g(\alpha)$ in similar fashion to the work by Finnie. Using data obtained experimentally through the use of a 'blast erosion test rig' for sand erosion which used impact velocities of between 70 - 120 ms^{-1}. They were able to fit a model to the erosion expected per unit mass of particles at a 90 degree angle as shown in Equation 3.20 [84].

$$E(\alpha) = g(\alpha)E_{90} \tag{3.20}$$

The angle function was then determined to be a function of two exponents, n_1 and n_2, a sinusoidal function and the material hardness, H_v, expressed as Vicker's hardness in GPa. This is shown in Equation 3.21.

$$g(\alpha) = (sin\alpha)^{n_1}(1 + H_v(1 - sin\alpha))^{n_2} \tag{3.21}$$

The 90 degree erosion rate per unit mass, E_{90}, is then expressed as a function of the particle impact velocity, v_i, particle diameter, d_i, and the worn materials hardness. This is shown in Equation 3.22

$$E_{90} = K(H_v)^{k_1}(v_i)^{k_2}(d_i)^{k_3} \tag{3.22}$$

Exponents, k_1, k_2, and k_3 are used to fit the experimental data [85].

It can be seen in this model the complexity is not necessarily increased analytically, but it is increased experimentally as a large amount of data is required to obtain the relevant coefficients for effective use. When obtained it has been shown to be effective through the author's own work and others [86]. An issue with the model, is the dependence on high velocity impacts and use of non-standard testing equipment which makes it difficult to replicate [87].

3.3.3.6 Ductile: Shear Impact Energy Model

A later model developed in the field of erosion is the Shear Impact Energy Model, which uniquely was made with the application of DEM in mind. Drawing frequent comparison to Finnie's original works in ductile erosion. This model looked at the total tangential/shear impact energy of a collision as shown in Equation 3.24 [88].

$$E = F_t v_t dt \tag{3.23}$$

$$E_{shear} = -\int_{t_0}^{t_1} F_t v_t dt \tag{3.24}$$

Using a combination of the SIEM model and Finnie's original erosion model, the volume of removed material was expressed by Sun in 2022 as shown in Equation for application in a non-spherical particle screw conveyor [89]

$$Q = \frac{E_{shear}}{4p} \tag{3.25}$$

Where p was the 'flow' stress' stated in the original ductile erosion model presented by Finnie. A value which was generally taken as between 1 - 5x the hardness of a material [89]. This was a value of 4 for Zhao shown in Equation 3.25 [88]. In 2018 Xu, obtained a value of 4.2 using Finnie's adjusted 1972 equation [90] [71].

3.3.4 Erosion and DEM

For linking erosion and DEM Finnie's model has been shown to be implemented and can be accurate when careful calibration of the model is carried out for specific circumstances. The open source software LIGGGHTS for example implements Finnie's erosion model and details how it is done [91].

Bitter's model of brittle erosion has been used but is generally used in the form of being linked with Finnie's in a similar fashion to Nielson. Each paper appears to do it their own way or not provide any information regarding how the model was actually written into the code specifically [78].

Erosion equations are often more applied with the use of CFD modelling in combination with corrosion, where the particle-fluid interactions are modelled and then the particle tracks predicted. Work was carried out which developed these predictions for elbow and plugged geometries which showed good agreement [92][93]. With recent research in this field investigating and providing detailed approximations of the flow regime and wear pattern generated [94].

The velocity exponent used provides some concern to erosion modelling. A fundamental basis of $n = 2$ was developed in the original work derived for ductile erosion. This value holds a fundamental principle behind it being the kinetic energy of a collision and it is known to vary for single particle impacts with material strengths, and material combinations often with variations between $n = 2 - 3$.

3.4 Model Summary

Table 3.2 shows the wear models covered in this chapter with references of their uses, particle sizes and velocities associated with the testing. The wear modelling review carried out here is by no means exhaustive. Many other authors have carried out reviews with specific application to experimental wear modelling in mind, and/or their own application. Reviews of such models are found in the following: [69] [70] [95] [96] [97].

General trends can be seen in erosion such as the use of small particle sizes and high particle velocities. This would be in line with its prevalence in slurry erosion or combined fluid and particle modelling. Wear models found which operate at a slower velocity impact and sliding of material are general abrasion based models as opposed to erosion models. However, applications for this are limited and the application of it in DEM is not studied in depth. An interesting trend appears to be present, in the author's opinion, where the original models were generally mechanically simple, i.e. they were based off an analytical and measurable value such as kinetic energy or force. In the next decades models increased vastly in complexity as seen Equation 3.22, with the introduction of a number of exponents and coefficients which related to experiments in specific cases. Which increased the accuracy of individual equations to certain scenarios, but overall decreased their applicability to users other than the authors. An issue which was pointed out by Meng in their review "Unfortunately the available equations are so

TABLE 3.2: Wear model summary stating their mechanism, origin, known particle size uses and velocities ranked by particle velocity

Wear Mechanism	Author	Equation Form	Sizes	Velocities
Erosion	Zhao [88]	Impact Energy	0.127 mm (DEM particle)	152 ms^{-1}
Erosion	Neilson and Gilchrist	Kinetic Energy	210 μm (aluminium oxide) [80]	$\approx$ 80 ms^{-1}
Erosion	Hutching [98]	K.E based	212 - 600 μm (glass beads) 600 - 600 μm steel shot	64 ms^{-1}
Erosion	Shipway [99]	$f(H_p, H_t)$	125 - 150 μm	60 ms^{-1}
Erosion	Oka [84][85]	Experimentally derived	49 μm - 428 μm	$>$ 50 ms^{-1}
Erosion	Finnie [67]	Kinetic Energy	150 mm - 300 mm semi-rounded sand [78]	9 - 28 ms^{-1}
Erosion	Clark and Wong [83]	K.E based	125 - 830 μm (SiC) [83]	9 - 18 ms^{-1}
Abrasion	Archard [55]	Force Displacement	5 mm - 0.3 m [58][57]	0.7 - 1.1 ms^{-1}

confusing that few designers can use any of them to predict product life with confidence" [95]. In recent years however, models appear to have turned back to becoming simpler, and being based from the original principles which the models were established from.

3.5 Wear and Bulk Material Handling

The application of wear modelling has not been limited to looking at individual impacts of particles alone. In fact, wear has been studied with the application of a chute specifically, by the creation of an abrasive wear factor, shown in Equation 3.26 as a function of the chute conditions themselves [100]. This method is unique to wear modelling as it considers the flow of material as a continuous stream of a bulk solid.

$$K_c = \frac{\dot{m} v_s \tan\phi}{vB} N_{WR} \tag{3.26}$$

Where $\dot{m}$ is the mass flow rate of material, v_s is the rubbing velocity of the material on the bottom of the chute, v is the mean velocity of material at the section considered, ϕ_s is the friction angle on the chute surface, B is the chute width and N_{WR} is based

upon the design and conditions, accounting specifically for any curvature of the chute as shown in Equation 3.27.

$$N_{WR} = \frac{v^2}{R} + gsin(\theta) \tag{3.27}$$

Where R is the radius of the chute curvature and g is the gravitational acceleration.

3.6 Material Properties

3.6.1 Hardness

One property which is prevalent through out the majority of research regarding wear is hardness. It is generally defined as a materials resistance to permanent deformation. Subtle changes are made to the definition depending on the author such as "permanant deformation due to abrasion or erosion", or "permanent localised deformation" however the general theme is the same [101]. The reason for its consistent use is it is a material property which encapsulates both an elastic and plastic response from a material while being measurable. As ultimately hardness is a function of the load, F and a contact area, A, during an indenter test which is dependent upon the testing apparatus as shown in Equation 3.28.

$$H = \frac{F}{A} \tag{3.28}$$

Examples of these testing standards are: Brinell, Vickers and Rockwell etc. Generally, the value of hardness used in wear modelling is the Vicker's hardness of a material as it can be represented using the unit of N/mm^2 or MPa as shown in Equation 3.28. Using the tabor relationship, hardness can be established as a function of yield strength as shown in Equation 3.29 [79][53].

$$H = C\sigma_y \tag{3.29}$$

Where hardness, H, is expressed in Pascals, σ_y, is the yield stress and C is a constant with a value of 2.6 - 3 for metallic materials.

In some cases it alone provides a relatively good approximation of "wear resistance". For example, Oka's work found the relationship between surface hardness of a material and wear caused by multiple particle impacts was excellent for any material when considering

gas fired balls of approximately 1.59 - 3.18 mm in diameter at impact velocity of 150 ms^{-1} [102]. However, the hardness discussed is not the initial surface hardness, rather it is the hardness of the impacted surface during the erosion process which needs to be estimated due to the effects of work hardening and any thermal effects. However in other scenarios the erosion can be almost independent of the hardness of a material such as heat treated carbon steels [103]. Ratios between hardness and other material properties can also give an indication of a materials wear resistance. For coatings for instance there is good evidence suggesting that the ratio between hardness, H, and Young's modulus of the material, E, gives a good indication of the resistance to sliding wear [73] [104].

Therefore hardness and wear resistance are not interchangeable. Some applications call for the use of high hardness material to resist abrasion for example but others require a 'tougher' material to resist wear such as a tyre on a road. There have been attempts to create relations between hardness and fracture toughness [105]. A general ratio was presented by Moore which encompassed their conclusions regarding the role of hardness, H, and fracture toughness, K_c, in regard to the wear of brittle materials by defining the ratio between the two material properties as K_c/H. In general, they stated that high values will tend to have low wear. The result of this can be visualised as imagining an extremely high hardness material being too brittle to withstand an impact, glass for example. Whereas a material which is quite soft in nature i.e. low in hardness, but extremely tough such as rubber can withstand the rolling and abrasion of use in car and truck tyres. In this case the limitation of solely using hardness as a property to asses a material's wear resistance is demonstrated. A second method of assessing the erosion rate as function of particle and target surface hardness, H_p and H_t respectively, where $E \propto H_p/H_t$. This assessment was carried out by Shipway for brittle glass and ceramic materials [99]. In general, what can be determined from this is the material properties used to assess a materials wear resistance will be a function of the material itself (i.e. a metal, a ceramic, glass, rubber etc.) and the application it is used in (rolling on a road, impacts from a gas gun in an experimental lab, material handling systems etc.). Therefore, ultimately it appears to be up to the user to determine which parameters and functions are applicable to their application. Using only hardness to assess a material's wear resistance can be used so long as attention is paid to the applicability of such a model.

Wear testing itself is another consideration for the application of materials properties to quantify wear. The combinations of materials used and the scenario of the contacts will always be different [106]. This makes it extremely difficult to obtain generalised and consistent results in wear testing as scenarios will always change. If anything, this almost brings home the point of wear being difficult to quantify and why hardness is commonly used as an approximation.

3.7 Wear Testing Standards

Wear testing of materials is generally carried out to a standard depending on application. Once the wear of particular material is known in one environment it can then be compared and contrasted against others to determine the dominant wear mechanism and allow assessments of wear resistance in that same environment. Each standard aims to produce a ranking of materials by their "wear resistance" under a standards specificed conditions. Here three of these standars will be briefly discussed. It is noted in the standards that it should not be used to predict the exact resistance of a material in a particular environment as all the conditions are not acocunted for [107].

3.7.1 ASTM G65

ASTM G65 is the "Standard Test Method for Measuring Abrasion Using the Dry Sand/Rubber Wheel Apparatus" [108]. It is likely the most widely used test method for assessing the abrasion resistance of materials. It does this by measuring the mass/volume loss of a test material after subjecting it to a rotating abrasive wheel. A series of procedures are presented which aim to measure the wear of different types of materials depending on their expected abrasion resistance, in a similar fashion to hardness testing whereby harder/wear resistant material require harsher testing conditions as could reasaonably be expected.

Once the volume/mass loss of material is known, a wear coefficient can be calculated for that material under its specific test condition. For example in Archard's abrasion equation, shown in Equation 3.7. This could then be used in numerical analysis of systems.

3.7.2 ASTM G105

ASTM G105 is the "Standard Test Method for Conducting Wet Sand/Rubber Wheel Abrasion Tests" [107]. This is similar to the previous ASTM G65 test method, however in this case wet sand is introduced to the test material as slurry. This can greatly increase the wear and further the understanding of a materials behaviour under these conditions.

3.7.3 ASTM D968

ASTM D968 is the "Standard Test Methods for Abrasion Resistance of Organic Coatings by Falling Abrasive" [109]. In contrast to the previous standards ASTM G65 and G105, which used rotating abrasive wheels, D968 uses falling abrasive material. Generally either sand if a "less" abrasive material is required or silcon carbide, SiC if a "more" abrasive is requried. The procedure tests the resistance of organic coatings of materials, i.e. plant or animal coatings on materials which can protect a base material from corrosion for example. Therefore, the materials tested using this standard can be generally expected to be less hard-wearing than materials in the previous two standards. However the test methodology found here could be seen as more applicable to the granular material impacts studied in this work.

3.8 Summary

This chapter has reviewed the approaches to modelling the wear caused by particle impacts and slides which will be considered for application into DEM. There are two general fields which could be considered to be immediately applicable: abrasion and erosion. Abrasion is a well researched field, with one model supersedeing most others. However, its exact application is not that of particle impact, instead it consists of sliding components therefore when applied into to DEM for sliding and impacting bodies the bahaviour of it is not understood. It has seen application in DEM, however examples of this are limited.

Erosion, is perhaps what, on the surface could initially be considered the most applicable to DEM. It specifically attempts to model the effect of particle impacts, generally under the assumption of a single impact or via a dilute flow of material. Usually with small particles ($< 1mm$) and with high velocities ($> 10ms^{-1}$) as shown in table 3.2, two conditions which will not be true for this thesis. Therefore, it is difficult to know with certainty what the correct approach is. Determining an exact equation for erosion is extremely difficult, if not truthfully impossible, due to the complicated nature of the material itself and the variety of ways it can interact with the surrounding systems. Plus, the variety of materials and varying scenarios. Coupled with the addition of more wear mechanisms such as abrasion and corrosion. It is clear precisely predicting wear in this manner is always going to be difficult. An uncertainty the author believes surrounds the field of wear modelling as a whole due to its extremely complex and dynamic nature of the phenomena which is studied.

Part II

Discrete Element Method and Analysis

Chapter 4

Wear and DEM

This chapter will discuss the computational approach to modelling wear in the Discrete Element Method. This will include describing the differences between wear and damage and assessing the computational mesh sensitivity of predicted wear and damage quantities. A model is formulated using a linear damage rule which allows calculation of time to failure in systems using one of two failure criteria.

The original plan for this work included construction of an experimental rig to provide laboratory results assessing various materials at differing impact angles. However, due to a series of unfortunate circumstances this was not possible and so validation of models is done using industrial data. More detail on this can be found in appendix B.

4.1 Combining two fields

The fundamental issue which concerns this project is relatively simple. How to combine the wear equations demonstrated in Chapter 3 with the DEM methodology presented in Chapter 2? Attempts have been made in the literature including application of Archard's abrasion model, or Finnie's erosion model as covered in Sections 3.2 and 3.3. However, one frequently raised issue regarding wear modelling is the sheer variety and vagueness of the models. Meng et al in 1995 wrote "Unfortunately the available equations are so confusing that few designers can use any of them to predict product life with confidence". This lack of confidence manifests as models are often in the form of qualitative or limited quantitative modelling.

The following chapter is separated into sections. The first will discuss the application of known wear models to DEM and establish how these are calculated. The second section will focus on the mesh used inside a system to begin to understand the effect it has on wear calculation. This latter is an area where previous research is extremely limited.

The next section will look at damage prediction within a DEM computational framework and how this can be formulated to obtain time to failure predictions. Two criteria are established to allow assessment of systems for different purposes. These criteria introduce holes into underlying meshes in the DEM framework. A subsequent section investigates how the damage model behaves with respect to the mesh discretisation. The time to failure calculations generated by the damage model is assessed with varying impact angles for a known wear model while using a hole creation method.

After this the focus will shift by reversing the question of how wear modelling can be used in DEM, to how DEM can be used to model wear? The models will then be tested to understand their predictive outputs for varying angles of impact using both single particle impacts and a more realistic scenario where a mass flow rate of particles is spawned.

4.1.1 Wear Vs Damage

Before any discussion can begin surrounding wear in DEM, a distinction must be made between "wear" and "damage" as this can often lead to considerable confusion. For the case of this work, wear is considered to be the mechanism through which material is removed. For example, abrasion is a wear mechanism in that the sliding between surfaces causes asperities to remove material. Damage is the accumulation of the removal of this material over time and is expressed as a dimensionless number or could also be thought as a percentage. Wear itself is not expressed mathematically, but the material removed

due to wear is. This will be represented at all times by the letter, Q, with a unit of m^3 unless otherwise stated. Damage will be represented by the letter D and is dimensionless. A damage value of 0 can be thought of as undamaged, and a value of $D = 1$ can be thought of as completely damaged.

4.2 Wear in DEM

Chapter 3 presented a variety of wear models and discussed how they came about and demonstrates the variety of methods and approaches which can be used to model wear. Naturally these come from an experimental viewpoint, which while crucial to the accurate prediction of wear, often leads to equations becoming confusing and only applicable in a narrow range of cases. For this thesis, the interest lies on how DEM can be used to study the impact of granular material and the damage and wear caused by it. Therefore, the limitations applied by the DEM model must be understood and applied to the wear equations themselves. After which the use of DEM to investigate both the qualitative and quantitative predictions can be better understood.

Another consideration is that wear often occurs due to some plastic deformation which creates the removal of material. The contacts between materials in this this work are expected to generally be in a combined elastic and plastic region as was covered in Section 3.3.3.2 [24]. However, the models used here assume a linear contact approach and an elastic collision (although the majority of models will always calculate some wear even when impact is elastic in nature). There are several good reasons to use a linear approach.

The first is to limit the computational time for the simulations. An extremely large number of simulations have been carried in this project. The use of a material based non-linear contact model would have reduced the time step value considerably, severely curtailing the number of simulations possible in the project. The use of a linear model often provides very similar results in terms of behaviour of particles compared to non-linear methods and is sometimes even more accurate when considering the tangential component of the collision. This was covered in Section 2.2.3.3. This tangential component is a key parameter in many wear models and it can be the most complex component of the calculation for DEM. The 'simpler' linear model is often more accurate than more complicated or physically accurate models [39]. This is especially true concerning different impact angles of particles on material structures where impact angle is a key component in wear calculation, as will be seen later. Finally, all previous work regarding material behaviour was carried out using the linear spring dashpot model and the material models have been validated. Perhaps none of these reasons alone is enough to

justify the use of a linear model, however when taken together they make a strong case to use a linear approach.

The complexity of wear modelling is deep. It is a complicated field with many variations and additional factors, often relating to the combination of materials being worn and the mechanisms through which they interact. On top of this there are other industrial factors such as temperature, changing operators of machines and ambient conditions, and even the weather. Therefore, using precise wear modelling for one specific application was not deemed be a good initial approach to modelling wear in DEM. Instead, it was decided to identify the wear equations most commonly used in the literature. This was an effort to develop a more generalised approach for wear modelling in DEM. The number and variations of different wear scenarios, even at one steel plant, is significant and so the aim is to develop a model which is widely applicable across a range of problem types. The equations used to model various aspects of wear and some of their assumptions and limitations are now described.

4.2.1 Abrasion Model

The first wear model which is suitable for use in the Discrete Element Method is Archard's abrasion model which is shown in Equation 4.1. The derivation of this model can be found in Chapter 3.

$$Q = \frac{KWL}{H} \tag{4.1}$$

A key parameter in this equation is the slide distance value, L. This quantity (the distance through which a surface moves along another) requires knowledge of the end state of the system i.e. at the end of the current time step. However, in a simulation environment this distance is not known beforehand, therefore a projected slide distance is calculated for each time step. This is done using the tangential velocity, v_t, with respect to the impacted element and timestep value, Δt.

Since all other values will be known to the simulation Archard's equation can be written as shown in Equation 4.2.

$$Q = \frac{F_n v_t \Delta t}{H} \tag{4.2}$$

The Taylor expansion is used for the explicit time integration to calculate the amount of wear added due to the collision in the timestep. Note the assumption that the force value in the Archard equation above is assumed to be constant over the time step duration.

Also, notice from Equation 4.1 to 4.2, the removal of the wear coefficient term, K. This term is set experimentally and it represents the mechanism and nature of the wear taking place. For example, is material removed immediately from the system or, for sliding surfaces, is material being trapped between surfaces causing further wear? In DEM typical values of K were reported for an erosion process where a value of K in the range 0.01 - 0.001 represents a severe form of abrasive wear [4]. In this work a constant value of $K = 0.001$ is used. If there are alterations to DEM behaviour required for different scenarios then these are dealt with by changing the damage coefficient value, C_d, (which is defined later) instead of K.

An item of note for the abrasion model is that in contrast to the erosion models presented in Chapter 3, the impact angle is not directly required for its calculation. This is due to the use of normal force, F_n, and tangential velocity, v_t, in Equation 4.2 which inherently consider impact angle in their calculation. A similar concept was presented in relation to wear experimental models when looking at impact wear [110]. However even though impact angle is not required directly, a method to determine it for a collision is still necessary. This is done by considering it as a 2D problem. Where the normal of the element being impacted and the direction of the particle, derived using its velocity vector, are used. Using the dot product, which defines the angle between two vectors, the impact angle, α, can be calculated. This is shown in Equation 4.3 where $\hat{v}$ is the unit vector of the velocity and $\hat{n}$ is the unit vector of the normal of the element.

$$cos\alpha = \frac{\hat{v}.\hat{n}}{|\hat{v}|.|\hat{n}|} \tag{4.3}$$

4.2.2 Ductile Erosion

The second wear equation selected for application is Finnie's ductile erosion Equation 4.4.

$$E = \frac{c}{\phi}\frac{mv^2}{2}f(\alpha) \tag{4.4}$$

The cutting ratio, c, was set to general value of 2 in line with work carried out by Finnie on metal cutting work [67].

4.2.3 Brittle Erosion Model

Brittle erosion is the mechanism which has the fewest models concerning it. Often it is not applied in DEM simulations.

Bitter's original model shown in Equation 4.5 was implemented in a DEM program in its initial form, utilising the original threshold velocity derived.

$$Q = \frac{1}{2}\frac{M(vsin\alpha - v_y)^2)}{\varepsilon} \tag{4.5}$$

The threshold velocity, v_y, is set as the value calculated by Bitter in their work to determine the point at which plastic deformation begins [75][76].

4.2.4 Combined Erosion Model

Combining erosion models is not a common practice for simulating wear inside DEM. Neilson and Gilchrist were the first to create a combined wear model [80]. Here the Clark model created in 1995 is implemented as all parameters are readily available inside DEM [83]. Specifically it does not require the critical angle which was described in Neilsen and Gilchrist's model. The Clark model contains specific energy values for both brittle and ductile components, Φ and ε respectively, as shown in Equation 4.6.

$$Q = \frac{m}{2}\left[\frac{(v_n - v_y)^2}{\varepsilon} + \frac{v_t^2 sin2\alpha}{\Phi}\right] \tag{4.6}$$

4.3 Meshing

4.3.1 A meshes effect on wear

Normally in computer simulation work the first item to be investigated is how mesh discretisation affects the calculated values from the model. For DEM/wear simulations this is an area which has received little research attention as discussed in Chapter 2. Even though wear equations have been applied within the DEM framework, often little attention has been paid to mesh sensitivity.

4.3.2 Methodology

Four wear equations are considered: the abrasion equation by Archard, the ductile erosion model by Finnie, the brittle erosion equation of Bitter and the combined erosion model of Clark.

The methodology involved a simple simulation where a known quantity of material is spawned (i.e., continually introduced) and allowed to drop under gravity onto a 45°

TABLE 4.1: Particle and plate parameters used in the study of a 45 degree angled plate

Parameter	Value
Particle Hardness	1 GPa
Plate Hardness	1 GPa
Particle Poisson Ratio	0.3
Plate Poisson Ratio	0.3
Particle Young's Modulus	200 GPa
Plate Young's Modulus	200 GPa
Specific Energy due to Ductile Erosion	1 GPa
Specific Energy due to Brittle Erosion	1 GPa
Particle Diameter	0.01 m
Particle Density	8000 kg/m3
Particle Spring Stiffness	8000 N/m
Archard Wear Factor (K)	0.001
Damage Coefficient	1
Sliding Friction Coefficient	0.8
Twisting Friction Coefficient	0.3
Twisting Damping	1.5
Rolling Friction Coefficient	0.3
Rolling Damping	1.5

inclined plate at a rate of 1 kg/s. The mesh which represents the plate is then discretised more and more finely to study the effect of mesh discretisation on the wear calculation. The initial mesh comprises 8 elements. For subsequent simulations this is further refined to 32, 128, 512, 2048 and 8192 elements.

For the purpose of this study a set of generalised parameters were used, shown in Table 4.1.

4.3.3 Results

Figures 4.1, 4.2, 4.3 and 4.4 show the qualitative wear patterns generated by four different wear models and how the pattern changes with increasing discretisation of the mesh. One of the key differences in the wear models is shown by the qualitative wear prediction of the abrasion model versus the ductile erosion model. The abrasion model predicts the majority of wear occurring in the impact zone of the material, whereas the ductile erosion model predicts the most wear occurs in the 'run off' area of the plate, i.e. the area downstream of the impact zone.

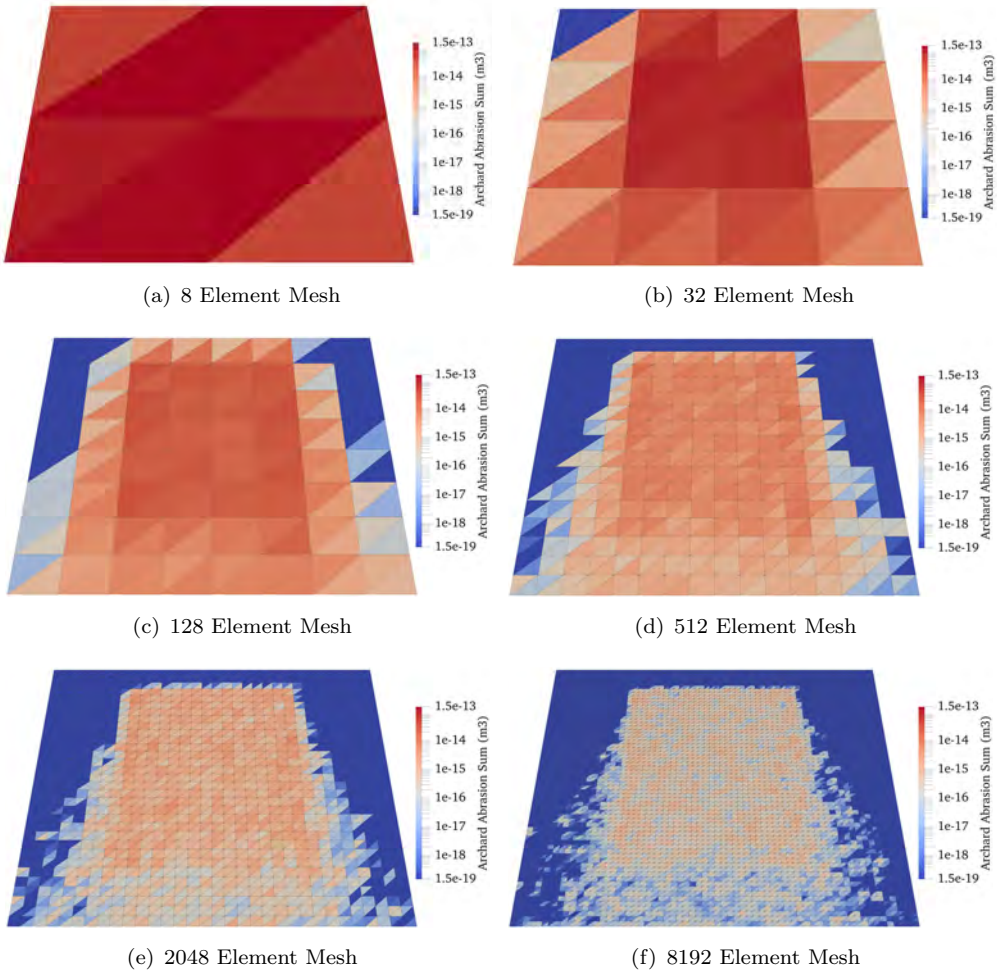

(a) 8 Element Mesh

(b) 32 Element Mesh

(c) 128 Element Mesh

(d) 512 Element Mesh

(e) 2048 Element Mesh

(f) 8192 Element Mesh

FIGURE 4.1: Qualitative wear predictions using Archard's abrasion model

Figure 4.5 shows the total amount of wear calculated for the 'most worn' element in the worn area i.e. the element with the highest total accumulation of wear based on the model used. This is shown for the four 'original' wear models used, Figure 4.5(a) shows Archard's abrasion model, Figure 4.5(b) shows the Finnie ductile erosion model, Figure 4.5(c) shows the combined erosion model created by Clark and Figure 4.5(d) shows the brittle erosion model made by Bitter. The key finding here was that the amount of wear on the 'most worn' element reduces as the mesh is discretised further, i.e. as it is refined more. This can be seen visually in Figures 4.1, 4.2, 4.3 and 4.4 where the qualitative distribution of wear changes and the total value can be seen to decrease via the colour. This creates an immediate question, if the wear per element changes depending on the discretisation of the mesh, how does the discretisation effect the total wear in the system as a whole.

Figure 4.7 shows the percentage difference in total wear calculated in the system between a mesh discretisation of interest and the coarsest discretisation of that wear model. Figures 4.7(a),(b),(c) and (d) show this for the abrasion, ductile erosion, combined

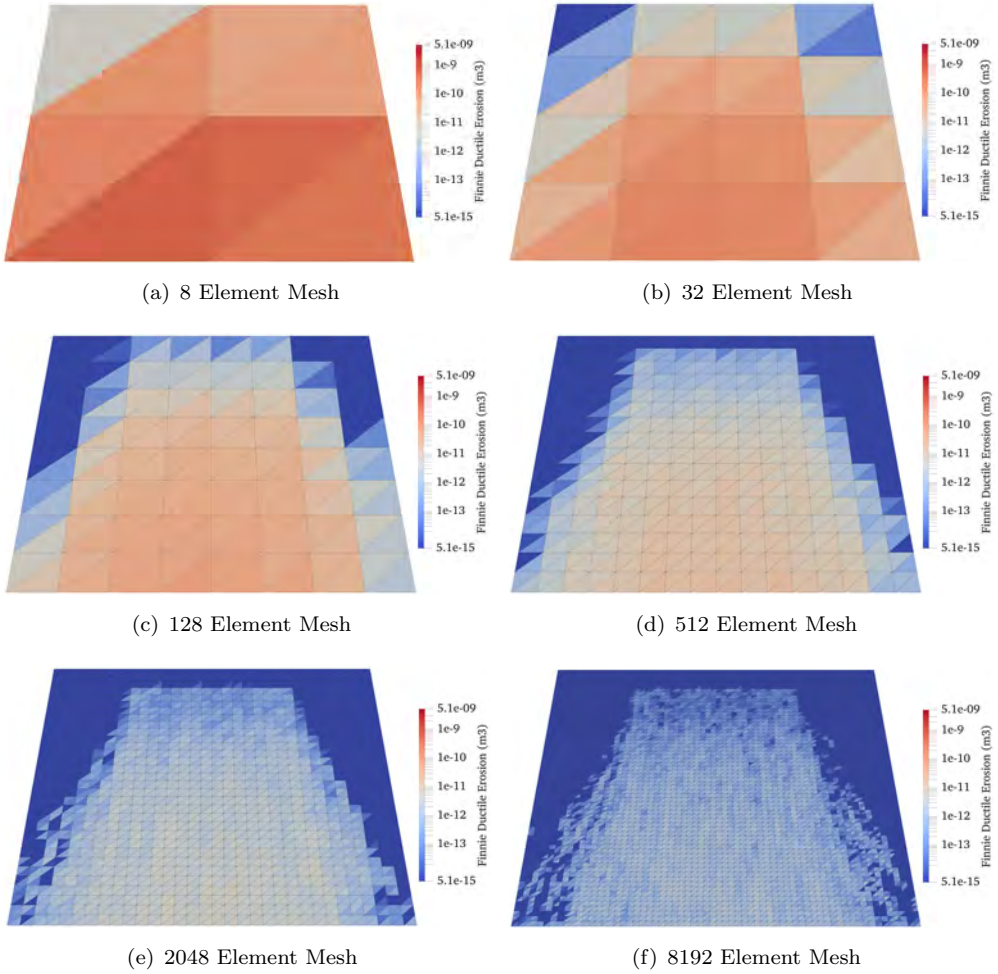

(a) 8 Element Mesh

(b) 32 Element Mesh

(c) 128 Element Mesh

(d) 512 Element Mesh

(e) 2048 Element Mesh

(f) 8192 Element Mesh

FIGURE 4.2: Qualitative wear predictions using Finnie's ductile erosion model

erosion and brittle erosion models respectively. As can be seen the variation in the total wear calculated in the system remains approximately constant with a variation of $1-4$ % for the abrasion model, $-3.5-0\%$ for the ductile erosion model, $0-3.5\%$ for the combined erosion model and $1-5\%$ for the brittle erosion model. This brings to light the fact when DEM calculates a wear value, its total value is approximately constant therefore it can be said that the global wear calculation is independent of the mesh discretisation.

4.3.4 Discussion

Figures 4.1, 4.2, 4.3 and 4.4 have shown the qualitative distribution in wear pattern generated by the 1 kg/s spawn of material. It can be seen that the two 'coarsest' meshes, 8 and 32 element, show a good initial general indication of the location of where the wear can be expected to be seen. For example, in Figure 4.1 the location of the wear is expected towards the impact area for the abrasion model whereas, Figure 4.2, using

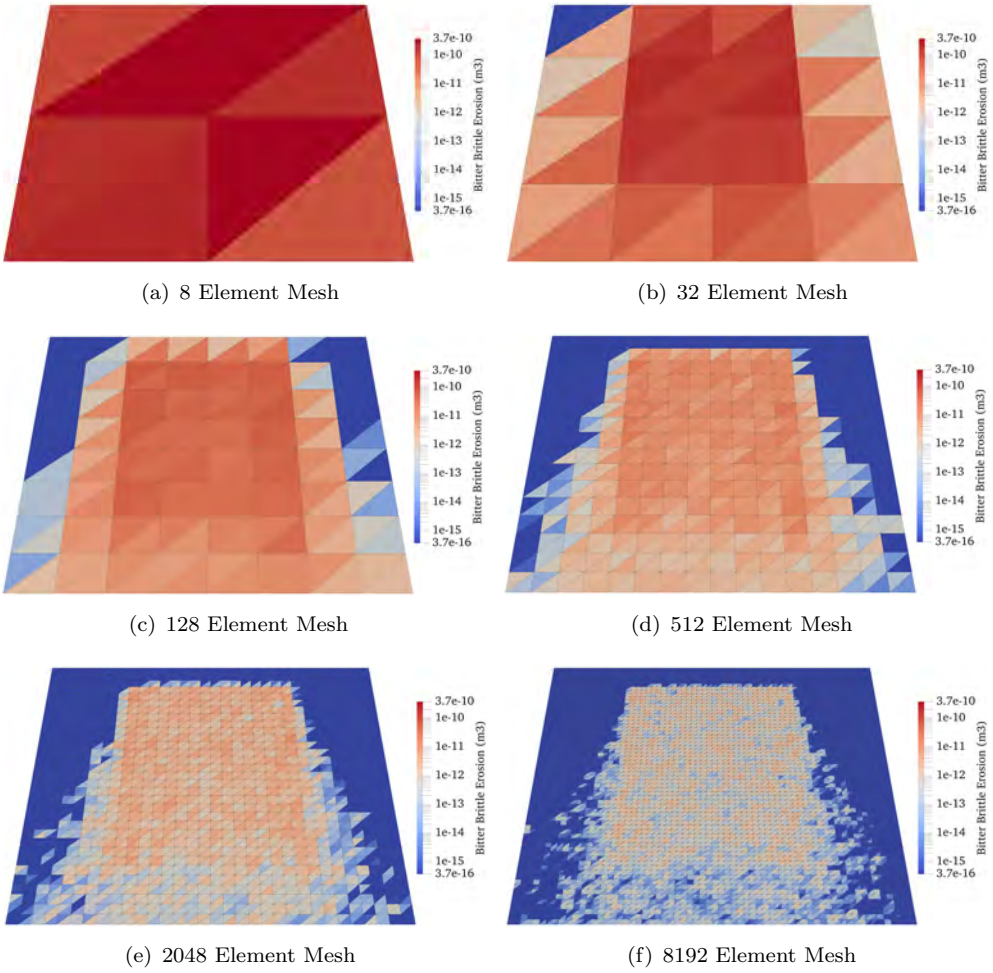

(a) 8 Element Mesh

(b) 32 Element Mesh

(c) 128 Element Mesh

(d) 512 Element Mesh

(e) 2048 Element Mesh

(f) 8192 Element Mesh

FIGURE 4.3: Qualitative wear predictions using Bitter's brittle erosion model

a ductile erosion model predicts the highest expected wear towards the 'run off' area for the particle i.e. the slide along the plate post impact. This shows a considerable difference in the two models predictions. The brittle erosion model predicts the highest wear in the impact zone also. Interestingly the combined erosion model also predicts wear in the impact zone, indicating that in this case and using equal parameters the model has a preference to which wear mechanism is dominant. In this case it is likely due to the effective normal and tangential velocities of the collisions.

As the meshes are refined further, i.e. the element size is reducing. More detail is seen from 128 and 512 elements. A narrowing of the impact zone is found as the element size is reduced, conforming to the shape of the particle spawn area. Coarser meshes will therefore tend to smear the predicted wear zone out more, showing a larger area affected by wear which might look more severe than it actually is.

Further refinement to 2048 and 8192 elements show even more detail in the wear pattern, to the point of being able to track individual particles on the plate. While possibly

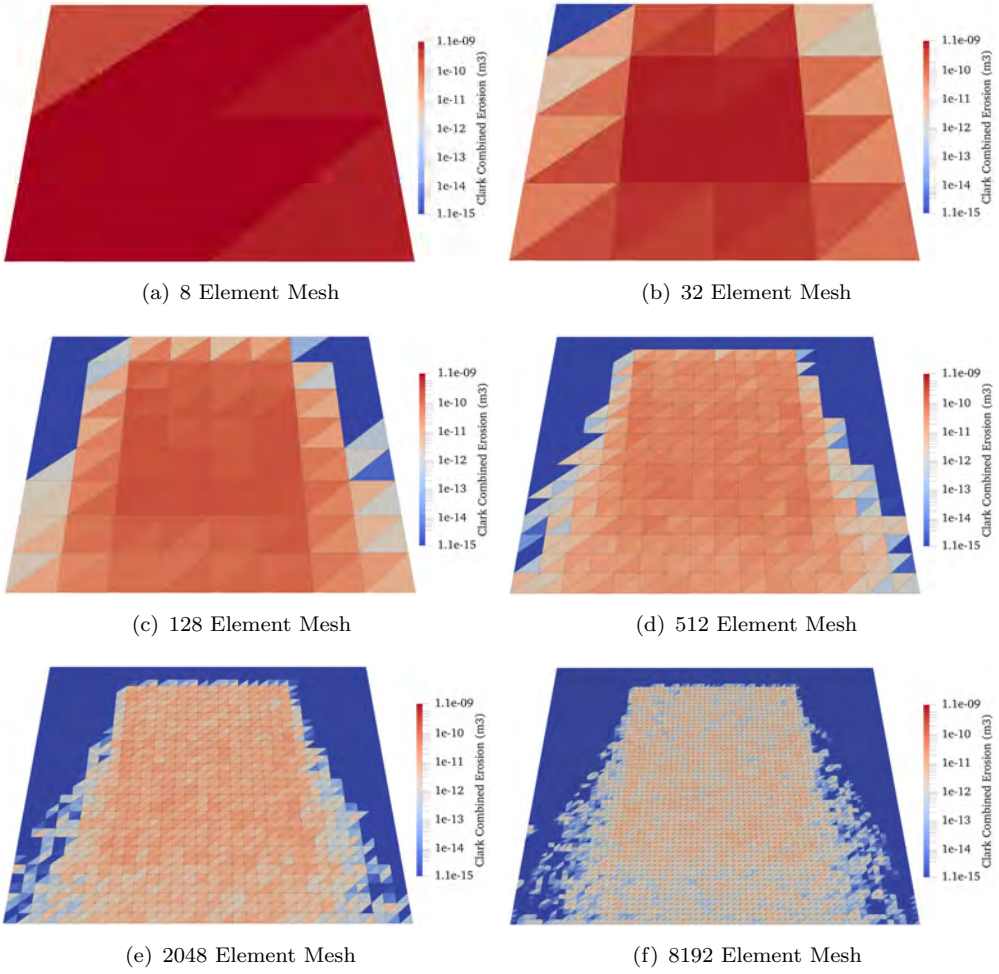

(a) 8 Element Mesh

(b) 32 Element Mesh

(c) 128 Element Mesh

(d) 512 Element Mesh

(e) 2048 Element Mesh

(f) 8192 Element Mesh

FIGURE 4.4: Qualitative wear predictions using Clark's combined erosion model

interesting in some scenarios, the increased computational time becomes expensive for not much greater detail in wear prediction.

Therefore a 512 element mesh in this case is considered to be a good starting point and a method of determining this point, pre-simulation, is required. A simple particle/element area ratio, R, can be used to define this point as shown in Equation 4.7 (where the projected or maximum cross-sectional area of the particle is used)[1].

$$R = \frac{A_p}{A_e} \tag{4.7}$$

The discretisation of 512 elements has a value of $R = 1$, meaning that when particle and element areas are approximately equal represents a good starting point for qualitative assessment, although other ratios may be better suited in different applications.

[1]It should be noted this is the inverse of the value presented in [111]. This was altered because it was found to be simpler comparing the particle to element size rather than the reverse

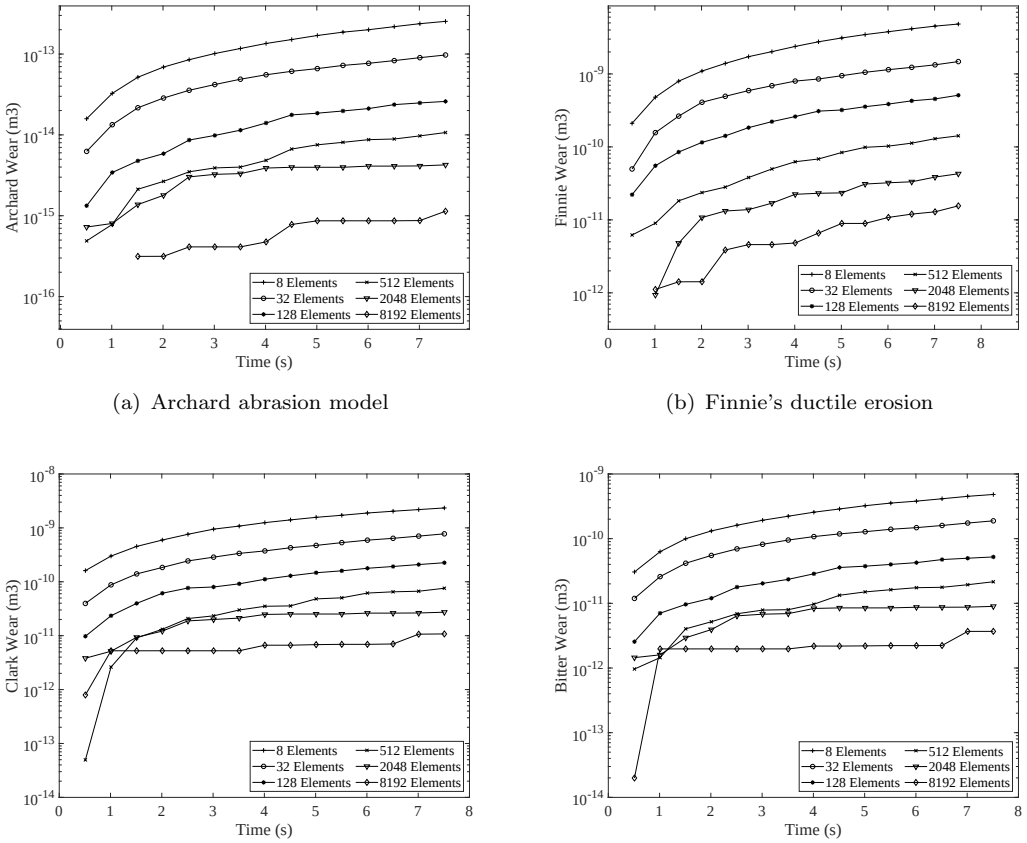

(a) Archard abrasion model

(b) Finnie's ductile erosion

(c) Clark's combined erosion model

(d) Bitter's brittle erosion model

FIGURE 4.5: Accumulation of wear over time on the 'most worn' element in the simulation by mesh discretisation

Figure 4.5 shows the accumulation of wear on the most worn element on the inclined plate. It is seen the most worn element suffers less wear as the mesh is refined. This reinforces what is seen in the changes of colour gradient in Figures 4.1, 4.2, 4.3 and 4.4. It is also a logical effect of DEM discretisation as when element size decreases the probability of a particle impacting across multiple elements is increased and the probability of a single element being impacted is decreased. Chapter 2 discussed the method which was used to assess particle and element impact which is consistent with the results above.

This also raises a question. If wear is assigned proportionally over elements as a function of mesh refinement, does the total amount of global wear in the simulation change with mesh refinement? Or in other words is the global calculation of wear in DEM mesh independent?

Figure 4.7 shows the difference in global wear calculated in simulations with different levels of mesh discretisation compared to the base 8 element simulation using Equation 4.8.

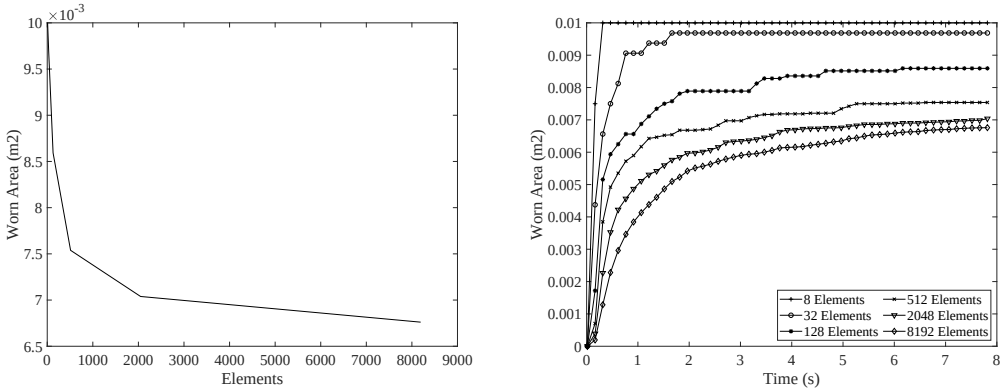

(a) Worn area by number of elements

(b) Worn area over time

FIGURE 4.6: Plots of the worn area predicted by number of elements over time

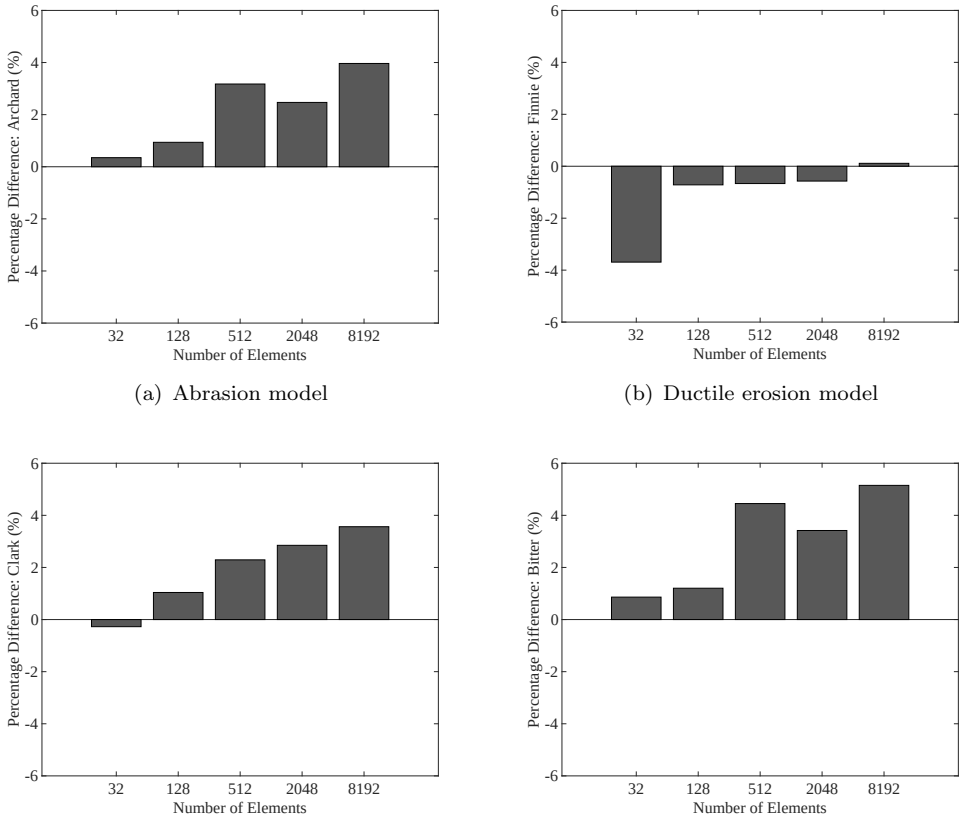

(a) Abrasion model

(b) Ductile erosion model

(c) Combined erosion model

(d) Brittle erosion model

FIGURE 4.7: Difference in total wear calculated between 8 element simulation and simulation of interest

$$P_a = \frac{\sum_{n=1}^{N} Q_{n,a} - \sum_{n=1}^{N} Q_{n,8}}{\sum_{n=1}^{N} Q_{n,8}} \tag{4.8}$$

As can be seen the difference between baseline 8 element and the 8192 element simulations for the abrasion model is 4 %. Similarly for the ductile erosion model the change is a reduction of 4 % for the 32 element discretisation, at which point further refinements have only minor effect. The combined erosion model shows an increase of 3.5 % in global wear and the brittle erosion model shows the highest change of 4.5 - 5 %.

From this data it can be concluded that the mesh has a negligible effect on the calculation of global wear. The differences in wear may also be slightly affected by small changes between simulations such as the random seed used for particle spawn positions. One variation of note is the reductions seen in the ductile erosion model compared to the increases seen in other models. It is unknown whether the location of wear in the modelled scenario is having any influence.

4.3.5 Key Findings

In summary, the main finding is that the calculation of wear inside a DEM simulation is mesh independent. Unsurprisingly, mesh discretisation affects the predicted wear pattern. However, a value of $R = 1$ is proposed as a good compromise for particle/element sizing which provides a balance between accuracy and computational time.

4.4 Damage in DEM

The previous section focussed on the wear calculation, both its qualitative and quantitative components. What is lacking with wear calculations is a method to translate results into a time to failure prediction inside DEM. The literature does not provide a method for doing this specifically in DEM (to the best of the author's knowledge) and therefore such a method was developed in this project.

Modelling damage is quite a common practice in other fields which deal with stress analysis of materials. Hertzian methods of force modelling in DEM might be suited to such an approach. However, the requirement for large simulations and the necessarily very small time steps required for Hertzian DEM models means they are not currently a practical solution.

Wear models generally provide outputs which have units of a volume. An obvious approach is to compare predicted volume losses to known volumes inside a simulation

to determine the extent of failure. The only volume parameter in the DEM simulation is the volume of each element on the mesh. This allows a simple model of wear damage to be devised which is then similarly assessed in terms of mesh discretisation sensitivity.

4.4.1 Methodology

Damage can be calculated by comparing the volume of an element, V, to the total amount of material that has been removed from it. Therefore, any wear value, Q, can be used to calculate a damage value, D, on any element, e, as shown in Equation 4.9.

$$D_e = \frac{Q_e}{V_e} \tag{4.9}$$

This can then be used over the course of a simulation in each timestep n as shown in Equation 4.10

$$D_{n,e} = \frac{Q_{n,e}}{V_e} \tag{4.10}$$

Using a linear damage rule (similar to the Palmgren-Miner fatigue rule) allows damage to be calculated in a simulation for all time steps, N [112].

$$D_{total,e} = \sum_{n=1}^{N} D_{n,e} \tag{4.11}$$

The damage rate can therefore be expressed as shown in Equation 4.12.

$$D_{r,e} = \frac{dD_{total,e}}{\Delta t} \tag{4.12}$$

Using this the total damage on an element $D_{total,e}$ and any time, t, can be calculated as shown in Equation 4.13.

$$D_{total,e} = D_{r,e}t \tag{4.13}$$

Now the damage can be calculated and tracked the next step is defining a point of failure.

4.4.2 Determination of Failure

The failure point of a simulation needs to be defined to determine a time to failure. The obvious method to define when a single element fails is that moment when all of its material has been removed, i.e. $D_{total,e} = 1$. This is the simplest method and is henceforth termed the Single Element Failure (SEF) criterion.

However, failure of a single element may not represent the failure of an entire system, some damage may be tolerable. Therefore a second scheme, termed the Multiple Element Failure (MEF) criteria, is introduced.

4.4.2.1 Single Element Failure Criterion

The first method of defining failure is the point at which a single element has a damage total equal to unity i.e. $D_{total,e} = 1$. At this point the simulation could be considered to have failed. This is the simplest method for defining a consistent definable point of failure. Using this a time to failure, $t_{failure}$, can be calculated for an element using Equation 4.14.

$$t_{failure,e} = \frac{D_{total,e}}{D_{r,e}} \tag{4.14}$$

The benefit of this method is the ability to rapidly assess numerous materials against a single DEM simulation. As has previously been discussed in Section 4.3.4, the determination of a wear value in DEM is deterministic. With consistent input parameters, approximately the same output values will be achieved minus any variation due to randomness in particle spawning. Therefore, it is possible to assess damage as a post process (and using multiple wear models and materials if models are equivalent). This will be demonstrated in the subsequent case study chapters. An expansion on this idea, factoring out the material properties, is also considered in greater detail in Section 4.6.

The ability to calculate failure times for different materials by post processing the results of a single simulation significantly reduces the greatest drawback of DEM, namely computational time. The ability to compare multiple wear models and materials using the data from a single simulation also provides a much more efficient design tool.

4.4.2.2 Multiple Element Failure Criterion

This criteria does not consider a system to have failed when a single element meets the condition $D_{total,e} = 1$. Instead, it tracks the total area of damaged elements with

$D_{total,e} = 1$ in the system. The user sets a maximum area of tolerable damage above which the system fails. This area must be a function of the plate/chute areas which are important in a given system and so will be application dependent. MEF is suitable for systems where design changes may be the key consideration or when more information is required regarding the failure. A natural result of using MEF is the ability to study simple hole development in DEM. Two methods have been used to determine the tolerable damage area, a particle independent method and a particle dependent method.

4.4.2.3 Particle Independent

This tracks the damaged areas of a system and defines failure when a certain percentage of the active wearing area has been removed. For example, if the total damaged area exceeds 15% of the impact area, then a failure is considered to have occurred. Often this is physically apparent in the real world when material falls through holes in handling systems. The point at which material begins to pass through a plate would be a good starting point for setting this value.

4.4.2.4 Particle Dependent

This criteria tracks failure in a similar way but defines the area based on particle size. This is expressed as a function of the projected particle area, A_p, as shown in Equation 4.15. Where n_{fail} is the factor used for the particle area (for example 2 for 200%) and A_{Fail} is the determined failure area.

$$A_{fail} = n_{fail} A_p \tag{4.15}$$

This method is useful when considering variable sized particles. It also provides a more consistent failure criterion when comparing across multiple simulations as it more closely correlates to what would be considered a real world failure i.e., material escaping through handling systems.

The MEF criterion also permits studying the effects of hole growth on particle flow and kinetics in a system. The particle dependent criteria also allows the comparison across simulations which use varying particle sizes and design changes.

4.4.3 Mesh effect on damage equation

Using the damage calculated from the respective wear values shown in Figures 4.1, 4.2, 4.4 and 4.3, the damage accumulation on the 'most worn' element (before any failure occurs due to either SEF or MEF in this case) is plotted for the various mesh discretisation's in Figure 4.8.

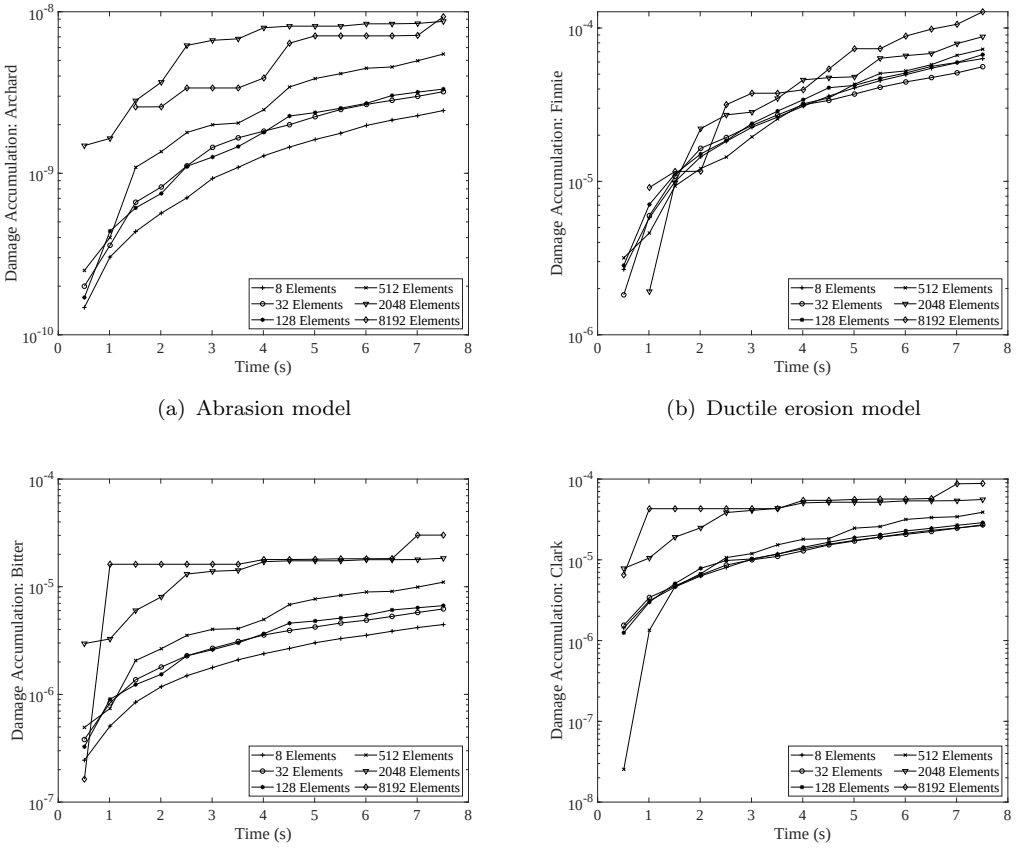

(a) Abrasion model

(b) Ductile erosion model

(c) Brittle erosion model

(d) Combined erosion model

FIGURE 4.8: Damage accumulation on 'most worn' element for each established wear model plotted against time for varying mesh discretisation

In general Figure 4.8 shows a trend where the total damage on the most worn elements increases as the mesh is refined. This is logical because the volume of elements reduces with mesh refinement and therefore the total proportion of damage is expected to be higher. An exception to this occurs in Figure 4.8(a) where it can be seen the damage accumulation is higher for the 2048 element simulation. The exact cause of this is unknown, however it is theorised this is possibly due to the variation in the spawn of particles however its exact cause is unknown.

Figure 4.9 shows the change in the global damage calculated, i.e. total damage summed across all elements on the plate, with respect to the mesh discretisation for each wear

model as calculated by Equation 4.8.

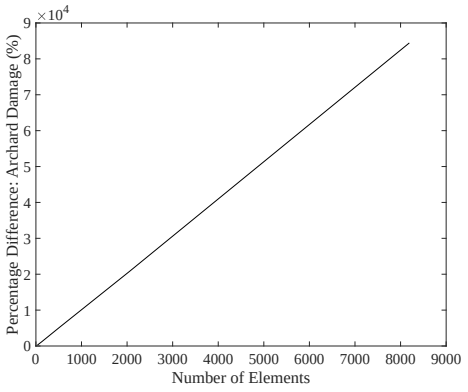

(a) Abrasion model

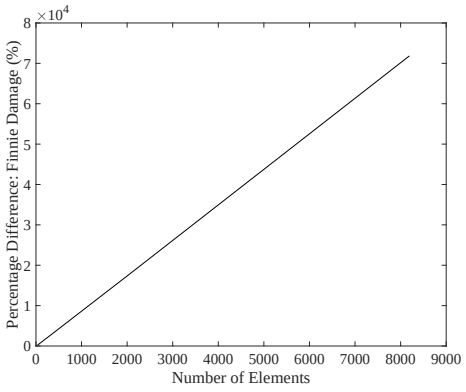

(b) Ductile erosion model

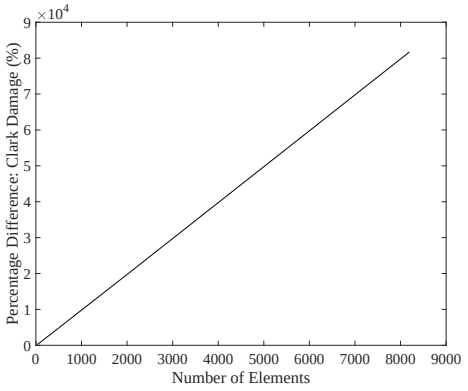

(c) Brittle erosion model model

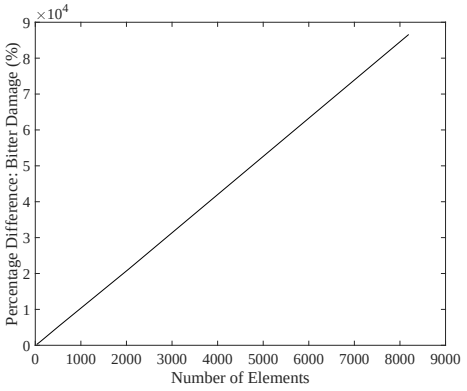

(d) Combined erosion model

FIGURE 4.9: Percentage difference plots for the total damage in the simulation against number of elements

Figure 4.10 shows the time failure plots, using the SEF criterion, against the number of elements in the system for abrasion, ductile erosion, brittle erosion and combined erosion. It can be seen a coarse mesh results in a long time to failure and a refined mesh results in a much shorter time to failure. The variation with the number of elements in the system is non-linear.

4.4.4 Findings

The first point to note is that damage calculation inside DEM using the SEF criterion is not purely deterministic like the calculation of wear. Damage is calculated using equation shown in Equation 4.9 which uses a single variable, the element volume. Therefore, calculated damage will vary as a function of mesh discretisation. Figure 4.10(a)(b)(c) and (d) shows the time to failure calculated from abrasion, ductile erosion, brittle erosion and combined erosion wear models. From this it is clear the system does not converge

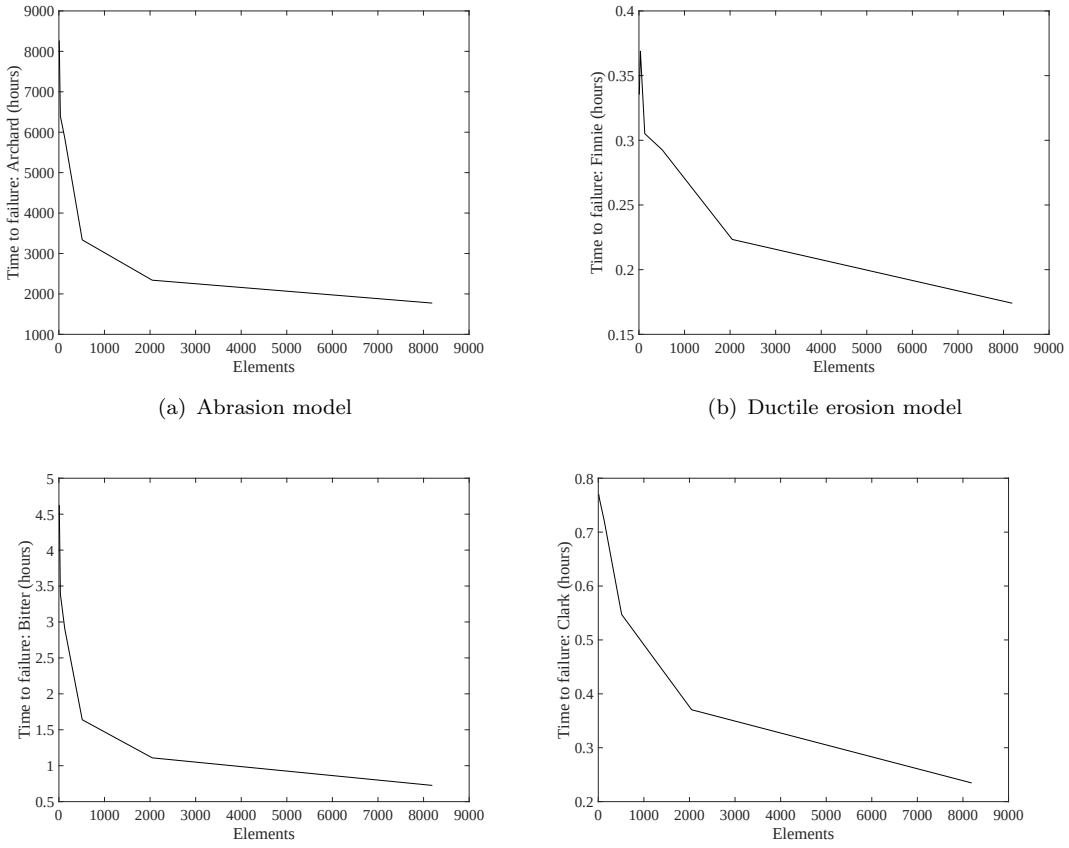

(a) Abrasion model

(b) Ductile erosion model

(c) Brittle erosion model

(d) Combined erosion model

FIGURE 4.10: Time to failure plots calculated using the SEF criterion against number of elements

to a single value and is dependent on element volume. Larger volume elements will take longer to fail while conversely very small elements may fail virtually instantaneously.

This highlights the importance of using consistent DEM simulation meshes for comparison as variation in the mesh will alter quantitative predictions. This will apply to both the SEF and MEF criterion as the MEF criteria requires satisfying the SEF criteria and then continuing the simulation.

One method of attempting to quantify this is using the particle to element ratio, R, presented in Equation 4.7. This is because any damage calculated is a function of both the impacting particle and the element. The impacting particle determines the total wear which would be calculated using the mass, velocity, and angle of impact of the particle. The element size determines how much there is to be worn away. Together they act as a function to assess the mesh as has been previously discussed in Section 4.3.4. It is theorised here the variation in time to failure prediction would be inversely proportional to the particle/element size ratio as shown in Equation 4.16.

$$t_{failure} \propto \frac{1}{R^n} \tag{4.16}$$

Where n represents an unknown exponent. Work was carried out exploring this further, in combination with particle sizing can be found in Chapter 8.

4.4.5 Key Findings

Damage calculation inside DEM is mesh dependent, which is a consequence of using the volume of an element inside the damage equation. The damage calculation is also not deterministic in contrast to the wear calculation. The variation in total wear is theorised to be some function of both the particle size and the element size.

4.5 Hole Creation

A feature which is possible to implement based on the failure criterion presented is the introduction of holes into the material. This is possible because the Lagrangian method used for the particles tracks each individual particle and obstacle element (including its nodes). This would also allow implementation of deformation based on wear as well, however hole creation was deemed more useful.

Each wall element is consists of three nodes as described in Section 2.2.5.1. A logical list of elements is created which states if an element is considered to be a hole or if it still contains solid i.e. $D < 1$. At the point of $D = 1$ an element is considered to be a hole and is flagged as such. All elements that are flagged as holes are ignored in the wall particle collision calculation.

An angled plate simulation is now studied where the failure point is determined by the particle dependent MEF criterion and holes may form in the plate which will alter the granular flow pattern. The simulation set up is similar to the one previously described in Section 4.3.2 however the plate is increased in size and refined further to increase resolution of the predicted wear pattern on the plate. The angle of the plate is varied in increments of 10 degrees creating simulations for 10, 20, 30, 40, 50, 60, 70, 80 and 90 degrees impact angle to assess the change in effect the impact angle has on the model as shown in Figure 4.11. A wear model also needs to be selected, and this was taken as the abrasion model. This is due to two reasons. The first is it being the most used wear model and so the most likely model to produce reliable results in industry. The second is only a single wear model can be used at a time when creating holes with the

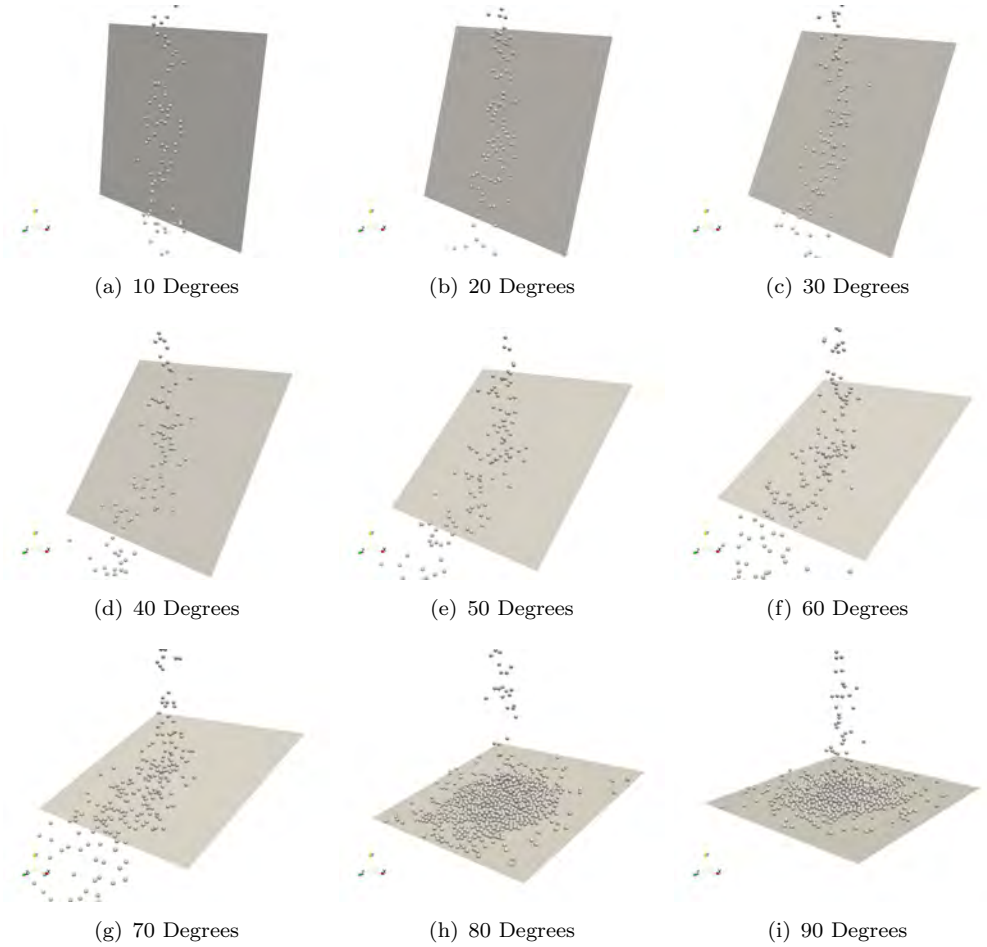

(a) 10 Degrees (b) 20 Degrees (c) 30 Degrees

(d) 40 Degrees (e) 50 Degrees (f) 60 Degrees

(g) 70 Degrees (h) 80 Degrees (i) 90 Degrees

FIGURE 4.11: Simulation image of a 1 kg/s spawn impacting a wear plate at varying angles

MEF criterion, and having a point of failure defined using the MEF criterion increases the computation time considerably. Therefore, limiting the number of simulations which can be run within a reasonable time frame.

4.5.1 Angled plate

Figure 4.11 shows the abrasive wear patterns created through the particle impacts at various impact angles on the plate[2]. The evolution of the wear pattern with the impact angle can be seen clearly looking from Figures 4.11(a) to (c) as the pattern goes from a long and thin wear pattern where particles have slid and skidded along the surface of the plate. By the 30 degree simulation, the pattern is shown to be smaller as particles begin to impact the closer to each other on the plate. The evolution of this can be seen through the particle impacts in Figure 4.11. From these Figures (c) through (g), a similar wear pattern can be seen where the highest wear is in the impact zone and a

[2]It should be noted Figures 4.11(a),(b),(h) and (i) have a differenct scale to the other subfigures

'run off' zone. The severity of this 'run off' zone is seen to increase as the impact angle increases.

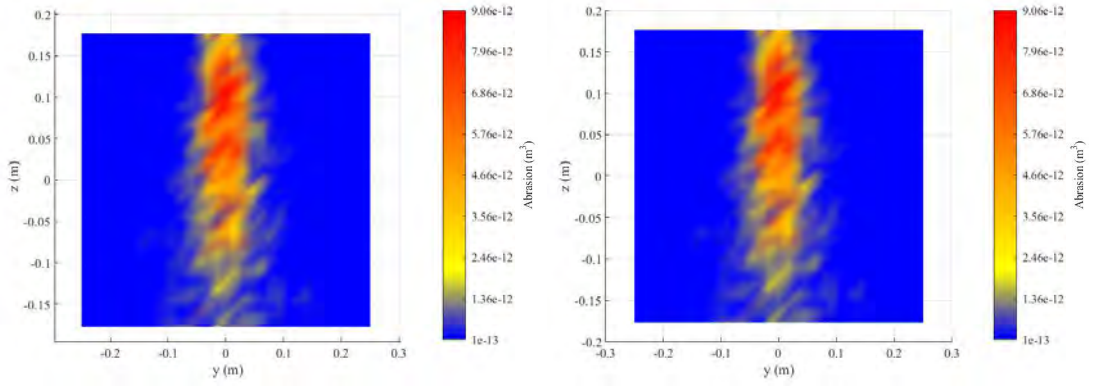

(a) 10° (b) 20°

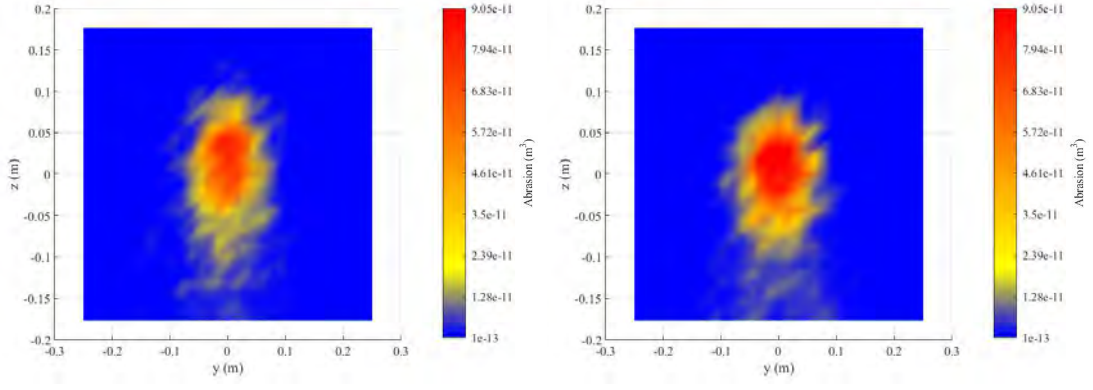

(c) 30° (d) 40°

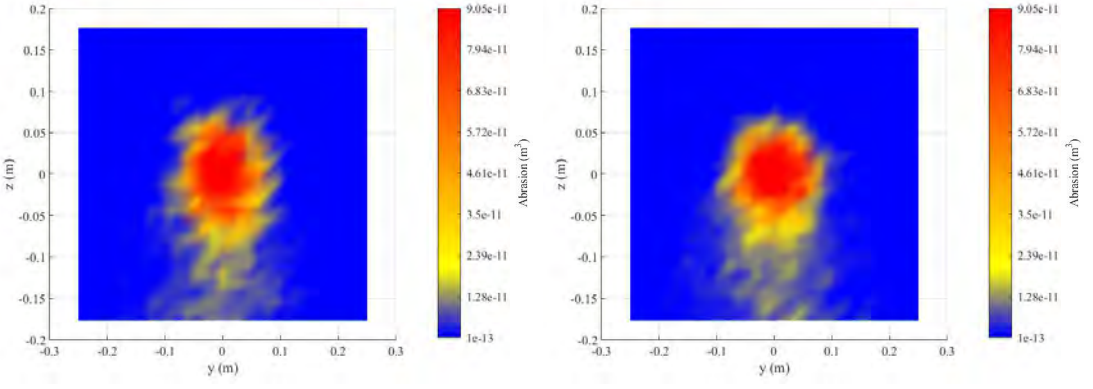

(e) 50° (f) 60°

Figure 4.12 shows the time to failure predictions generated, with only the angle of the plate varying as shown in Figure 4.11 for a constant particle spawn rate and constant damage coefficient. It can be seen the time to failure is approximately 47 seconds for a shallow angle of impact of 10 degrees. This is followed by a considerable reduction at 20 degrees to approximately 2 - 3 seconds. At which point it increases to 5 seconds for

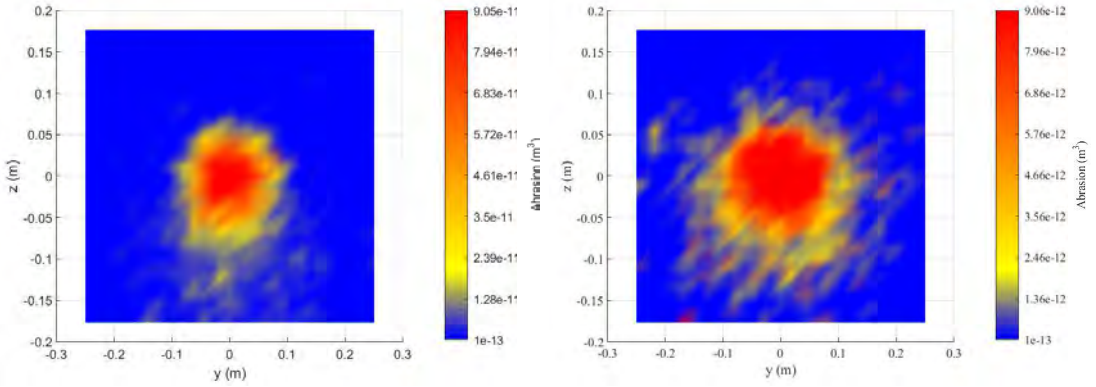

(g) 70° (h) 80°

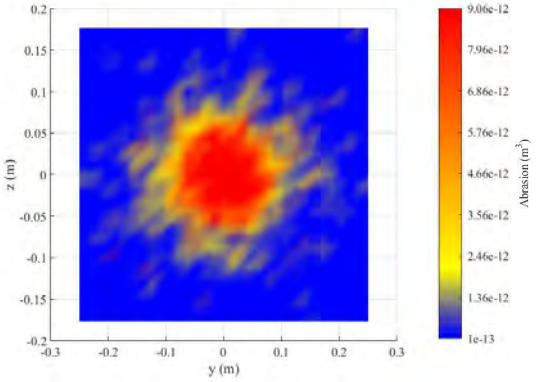

(i) 90°

FIGURE 4.11: Contour plots of wear pattern predicted by abrasion model with varying angle of impact for a multiple particle spawn

30 degrees and then shows a gradual decrease for the remaining angles until 70 degrees at which point the time to failure increases again at 90 degrees with a time to failure of 12 seconds.

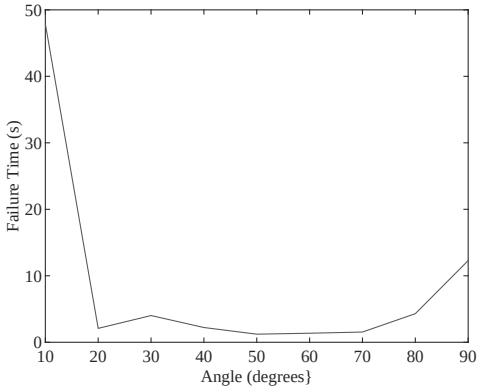

FIGURE 4.12: Time to failure using MEF criterion with particle dependent failure with varying angle of impact

The total abrasive wear in the system can be seen in Figure 4.12. It shows an interesting trend where the total wear is high for the shallow impact angle of 10 degrees followed by an immediate reduction towards 20 degrees. At which point an immediate increase is seen at 30 degrees, followed by another decrease from 40 through to 50 degrees. Then it begins to increase until the 90 degree simulation but does not exceed the total abrasive wear in the system shown in the 10 degree simulation.

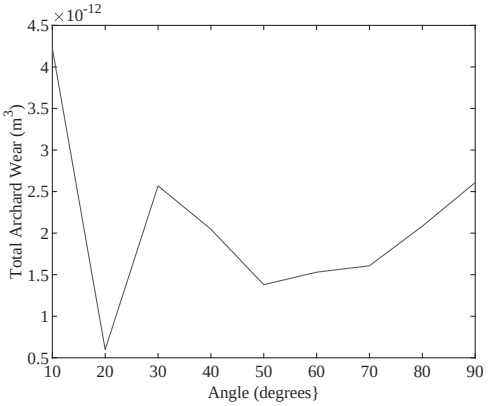

FIGURE 4.13: Total abrasive wear in system where failure occurs based on a particle dependent MEF criterion

The global/total number of collisions summary is shown in Figure 4.14. This shows an initial number of collisions across the plate of about 20k at 10 degrees. It then drops at a 20 degree angle of impact to about 2k collisions, after which is rises to about 5k collisions for 30 - 70 degree angles of impact. Then the number of collisions begins to increase considerably, about 25k at 80 degrees up to about 43k for a 90 degree impact angle.

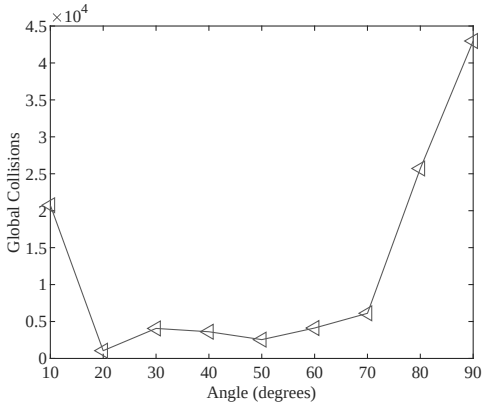

FIGURE 4.14: Number of collisions in system against angle of impact for particle dependent MEF criterion hole creation simulation

Figure 4.15 shows the normalised abrasive wear using Equation 4.17, where the wear value, Q, and the total number of collisions, G_k, is used. The normalisation shows a relatively low amount of wear per impact for the 10 degrees simulation. A rapid increase

in the amount of wear per impact is seen at 20 degrees and remains approximately consistent until 50 degrees at which point the wear per impact degrees to its lowest value at 90 degree angle of impact.

$$Q_{norm} = \frac{Q}{G_k} \tag{4.17}$$

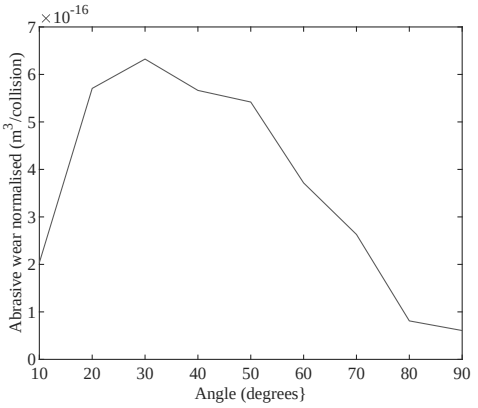

FIGURE 4.15: Normalised abrasive wear against angle of impact for particle dependent MEF criterion hole creation simulation

4.5.2 Summary of findings

It should be noted in this section that the end point of a simulation is defined by a MEF failure criteria rather than a time value. This means simulations varied in time considerably and differences when comparing to previous results are expected. The simulation set up used here utilised gravity as the driving force of the particles and used a constant stream of particles to create the wear.

When comparing failure times with consideration of both holes and failures it becomes clear that total wear in a system is not immediately associated with the most rapid failure as can be seen by comparing the 10 and 20 degree simulations from Figure 4.12 and 4.13. This is because as the angle of impact changes so do the kinematics of the particles as mentioned above. However in this case, the normalised wear appears to be at one of its lowest values at a 10 degree impact angle as shown in Figure 4.15 as opposed to when it was at its peak in Figure 4.24 even though the same simulation setup was used.

One possible reason for this is at a shallow impact angle the projected area of impact against the projected area of incoming particles, in this case from the spawn area, is larger as shown in Figure 4.16. As this projected crossover area is larger, there is more area for particles to impact over on the plate, so wear does not focus on one area as

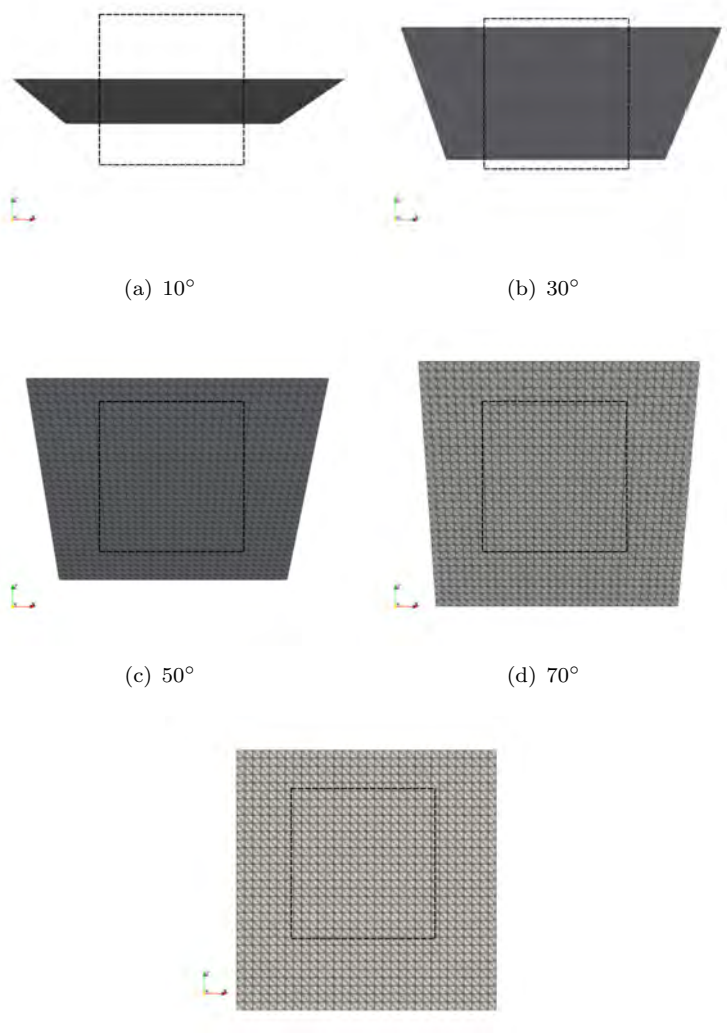

(a) 10° (b) 30°

(c) 50° (d) 70°

(e) 90°

FIGURE 4.16: Spawn area projected with a dashed line on a varying angled plate

strongly. This demonstrates a logical point, spreading the impact area of incoming particles on a plate decreases the local damage on an element even though the total wear on the plate is worse.

As the impact angle increases the time to failure decreases drastically, with an angle change of only 10 degrees causing a massive change in time to failure indicating an increase in the severity of the wear. Mechanistically this is likely due to the plate beginning to increasingly deflect particles creating a change in the velocity component being considered (tangential component in this case). Whereas previously in the 10 degree simulation while particles were dragging along the plate the change in velocity is not as significant for wear. For 20 and 30 degree impacts the particles are deflected along the plate causing increased areas of wear. But for less acute impact angles the

particles begin to bounce off the plate producing less subsequent impacts, although this effect is minor relative to other effects. At 50 degrees the time to failure becomes fairly constant, with a slight increase in the number of collisions and global abrasive wear. The particles post impact are beginning to roll as they no longer have enough velocity after the initial impact to impact again. This continues until particles remain on the plate, and the point at which particles begin to remain on the plate coincides with an increase in time to failure. Effectively creating a 'rockbox' on the plate whereby particles impact other particles instead of the plate, therefore insulating the plate from most of the damage. However, this predicts that while this effect 'insulates' the plate it does not appear to provide more life than compared to a shallow angle of impact.

4.5.3 Key Findings

Time to failures calculated in the system exhibit different behaviour from multiple particle impacts than would be expected from a wear model alone. This is a function of how the end of the simulation was defined using a failure criterion, instead of a set time value. Using the damage criteria, this allowed the wear to accumulate on the plate until a critical point was reached on a series of elements. Therefore, showing the effect of a larger worn area, but not a damaged area. This was demonstrated clearly in the 10 degree simulation where the time to failure was long, but the total abrasive wear was still relatively high, although not in comparison to the most rapid failures.

This section also shows two scenarios where damage is minimised, the first is a shallow skimming motion where particles are not entirely slowed down and therefore contribute very little to the damage of a surface. The second is where they are entirely stopped and begin to accumulate on the plate, at which point future particles impact the stationary particles and dissipate reduced force into the plate via force chains.

4.6 Energy Based Modelling in DEM

Using established wear models provides a good basis for assessing impacts in DEM but an idea arose in Section 4.4.3 when studying the SEF criterion. In this method material parameters were factored out to allow more rapid assessment when considering wear, essentially reducing the wear model to an energy calculation. So, how many ways could DEM be used to calculate a wear/energy value to capture all possible wear mechanisms in DEM? And then how to use real world information to inform the simulation which models are predicting the wear pattern accurately.

The first question is then raised as to how does one model wear in DEM usually? The methods presented in the literature are often energy based: either force displacement models or kinetic energy calculations. Therefore, a logical next step is to look at how many methods can be used in DEM to calculate energy, therefore in theory calculating all possible methods of assessing wear using energy transfer in DEM in a single simulation.

To begin looking at how DEM would approach this we need to understand which methods of calculating energy are available inside DEM. As discussed in Chapter 2 DEM is a force displacement based method. Therefore, it lends itself to energy calculation based from the initial soft sphere assumption using an overlap value. Using a contact mechanics approach and using the initial version of Hooke's law which expresses the force required to move 2 atoms apart as shown in Equation 4.18 [113].

$$F = kx \tag{4.18}$$

In this case where, F is the force required to move 2 atoms apart, k is the amount of force required to move an atom 1 meter i.e. stiffness and x is the distance an atom has moved. It should be noted this is also the method used to derive the elastic component of the force calculation in the linear spring dashpot model. The potential energy, or the total energy available here can be calculated by integrating F over the distance the atom has travelled as shown in Equation 4.19

$$W = \int kxdx \tag{4.19}$$

This integration results in a potential energy value as shown in Equation 4.20.

$$W = \frac{1}{2}kx^2 \tag{4.20}$$

Therefore, an initial model for looking at energies inside DEM could logically be based on this, assuming the distance an atom travelled is the overlap value found in soft sphere DEM. So for any collision, assuming a linear spring dashpot model is used, in DEM the total potential energy can be found using Equation 4.21.

$$E_{potential} = \frac{1}{2}k_{spring}\delta^2 \tag{4.21}$$

Any wear derived from energy values would theoretically be a fraction of this value and would naturally be expected to be highly dependent on the mechanism of wear. This

strain energy is an interesting first step for modelling impact energies however further steps would consider the component parts of a DEM calculation. The first step is to identify the component in DEM which is expected to be the component most responsible for wear, the energy dissipation.

4.6.1 Energy Dissipation through Damping

Determining wear based on the energy dissipation due to the damping is not a new idea to DEM, it has been used in ball milling scenarios [114] [115]. The idea of this method is to use the energy dissipated by the damping component of the system as this would reasonably represent the energy which would contribute to wear. This can then be used to calculate force as shown in Equation 4.22.

$$F_D = cv \tag{4.22}$$

This can be combined with the energy, E, calculation shown in Equation 4.23

$$E = Fd \tag{4.23}$$

Where d represents the distance moved. This represents all the theoretical energy which is dissipated by the damping component of the simulation, ignoring friction losses etc. The DEM spring damper system is composed of two components, as shown in Figure 2.4: the normal and tangential components. Using the relationship between velocity, v, and time the distance travelled in a single timestep, Δt, can be calculated using Equation 4.24

$$d = v\Delta t \tag{4.24}$$

Which can then be substituted into Equation 4.22 to give the general form for an energy dissipation due to the damping of the simulation.

$$E_{dissipated} = cv^2\Delta t \tag{4.25}$$

This general form can then give Equation 4.26 using the tangential component and Equation 4.27 using the normal component.

$$E_{tangential} = c_t v_t^2 \Delta t \tag{4.26}$$

The tangential form was shown to give good agreement by Boemer in ball mill applications [114].

$$E_{normal} = c_n v_n^2 \Delta t \tag{4.27}$$

This form presented by Boemer takes no account for the sign of the equation, i.e. whether the wear was caused through the acceleration or deceleration portion of the collision, and there is no clear indication in their work as to whether this was calculated at the initial impact condition or the relative velocity between wall and surface was calculated [114].

4.6.2 Energy transfer through kinetic energy

Kinetic energy is the second method of calculating the transfer, utilising the impact velocity of the particle. This is similar in fashion to the basic model created by Bridgeman in 2010. The kinetic energy equation is shown in Equation 4.28.

$$E = \frac{1}{2} m v^2 \tag{4.28}$$

As previously, this impact velocity can be split into two different components, normal and tangential. However, in this case the total impact velocity can also be considered where normal and tangential components are combined.

4.6.3 Energy transfer through total force x distance

The final method uses the force displacement assumption on which DEM is fundamentally based, by using the total force calculated by the spring and damper system as its force value as shown in Equation 4.29 for the normal component of the collision.

$$E = F_n v dt \tag{4.29}$$

For this method, the direction of the distance moved is altered as well so both normal and tangential components can be considered and a combined normal and tangential as well. This method forms the fundamental basis of Archard's abrasion model [55].

4.6.4 Summary of models

Table 4.2 shows possible equation forms which include values already calculated in a soft sphere DEM model which could be used to calculate a theoretical energy value. As can be seen energy models E_1 through E_4 use the energy dissipation through the dampers to model the energy loss. E_5 through E_8 use the force distance equation with normal and tangential components of the impact force calculated by the program. E_6 is an equivalent calculation to the one carried out by Archard, and is shown in Equation 3.7. E_9 through E_{11} use a simple strain energy calculation using the spring stiffness in both the normal and tangential directions as well as an effective spring stiffness which combines both directions. Finally, E_{12} through E_{14} use a kinetic energy calculation using the normal and tangential components of the impact velocity, as well as the total impact velocity. These equations are different ways energy transfer can be calculated inside DEM and therefore can be considered representative of all possible forms of wear which could occur. The list is by no means exhaustive but is a good starting point. The models are calculated in the program using a Taylor expansion to reduce errors [2]. These derivations are found in appendix A.

A possible benefit of assessing wear inside DEM using energy calculation is the methods are comparable quantitatively to each other. As opposed to traditional experimental/-analytical approaches, where each method is not necessarily quantitatively comparable as they come from different sources i.e. the equipment used is often different and testing equipment is often of a unique design [106]. Therefore, assessing which mechanism is likely to be dominant is difficult outside of a prediction based on material contacts and combinations. This could assist in giving a more complete analysis as to changing wear mechanisms as design changes are carried out in systems and highlight possible issues which could arise. Therefore, possibly de-risking many industrial projects which look at wear of material handling systems for example.

4.6.5 Behaviour of the Energy Models

4.6.5.1 Single Particle Runs

To investigate the behaviour of the energy models presented in Table 4.2, the first step was to study the effect of a single particle impact on a variably angled plate. This is to understand how the models behave with a comparable real world scenario, varying angles of impact are often an important factor in determining the mechanism of wear. The same simulation set up is used as was previously used to study the wear behaviour

TABLE 4.2: DEM possible energy models

Equation	**References**
$E_1 = c_n v_n v_n dt$	
$E_2 = c_n v_n v_t dt$	
$E_3 = c_t v_t v_n dt$	
$E_4 = c_t v_t v_t dt$	[115]
$E_5 = F_n v_n dt$	
$E_6 = F_n v_t dt$	[55]
$E_7 = F_t v_n dt$	
$E_8 = F_t v_t dt$	[88]
$E_9 = \frac{1}{2} k_n \delta^2$	
$E_{10} = \frac{1}{2} k_t \delta^2$	
$E_{11} = \frac{1}{2} k_{eff} \delta^2$	
$E_{12} = \frac{1}{2} m v_n^2$	
$E_{13} = \frac{1}{2} m v_t^2$	
$E_{14} = \frac{1}{2} m v^2$	

and hole creation in Section 4.3.2 and 4.5, however a single particle is now spawned instead of a mass flow rate of 1 kg/s.

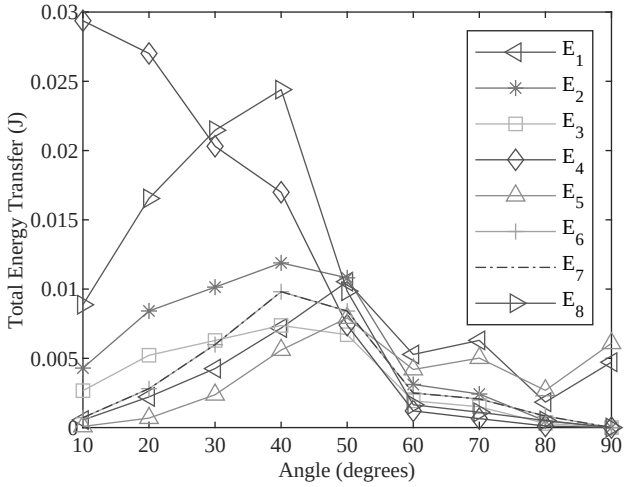

FIGURE 4.17: Energy models E_1 to E_8, as shown in Table 4.2, total energy transfer values for a single particle impact plotted against the angle of impact

Figure 4.17 shows models E_1 to E_8. This graph shows that for a single particle impact, all models are of a comparable scale. All the wear models tend to a peak energy transfer value between 10 and 50 degrees. Interestingly, this includes models which focus entirely on the normal component of the collision (E_1 and E_5) although these models have a tendency to peak towards the higher angles of impact approaching 50 degrees and also show an increase in energy transfer at the 90 degree angle. However, the result was unexpected. E_4 shows a pattern which has a peak at 10 degrees and a minimum and 90 degrees appearing to decrease as the impact angle becomes more obtuse. This behaviour is close to what would be expected of a purely ductile erosion mechanism.

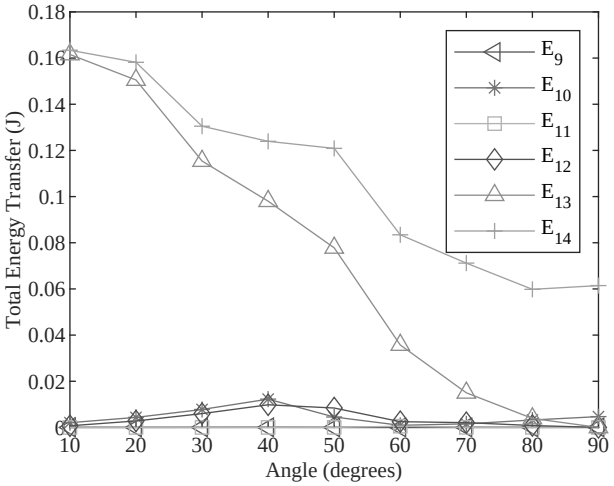

FIGURE 4.18: Energy models E_9 to E_{14}, as shown in Table 4.2, total energy transfer values for a single particle impact plotted against the angle of impact

Figure 4.18 show the energy models E_9 and E_{14} presented for a single particle impact by impact angle. What can immediately be noticed is the difference in scale between models E_{13} and E_{14} and all other models. Both models are approximately equal at 10 degrees and the reason for this is in a single impact the tangential component dominates the majority of the collision as the tangential and magnitude components are approximately equal at this point (i.e. the normal component is negligible). However, moving towards a 90 degree impact angle the E_{14} model, which utilises the impact velocity itself, remains high. This indicates in this case the transfer of energy to the plate is more efficient through a tangential collision.

4.6.5.2 Particle Spawn

The single particle impacts as shown in Section 4.6.5.1 gave a good initial indication of how the energy models behave compared to established wear models with varying impact angle. However, the issue with looking at wear models in this scenario is that it ignores a

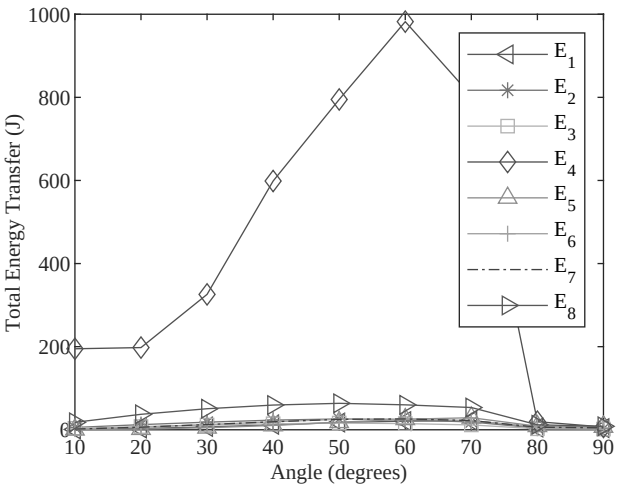

FIGURE 4.19: Energy models E_1 to E_8, as shown in Table 4.2, total energy transfer values for multiple particle impacts plotted against the angle of impact

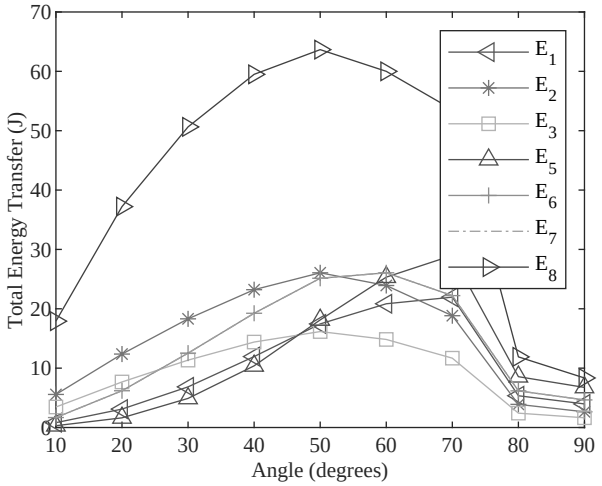

FIGURE 4.20: Energy models E_1 to E_8, as shown in Table 4.2, total energy transfer values for multiple particle impacts plotted against the angle of impact with E_4 removed

fundamental feature of industrial systems i.e., the sheer quantity of material processed. Therefore, a method was used to compare the energy models using a continuous stream of particles instead of a single impact. A constant flow rate of material of 1 kg/s was now introduced, in line with all previous simulation setups. The set up for this simulation can be seen in Figure 4.11.

Figure 4.19 shows the energy models E_1 to E_8. The scale of E_4 is considerably greater than the other models. For clarity, figure 4.20 was created without E_4.

The first feature of note in the energy transfer plots is the sudden decrease in energy transfer which is predicted towards the 80 to 90 degree impact simulations. The reason for this is demonstrated in Figures 4.11(h) and (i) where the particles can be seen

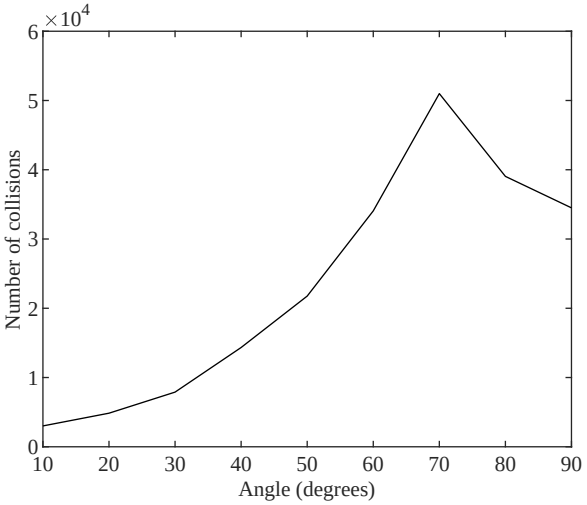

FIGURE 4.21: Number of collisions from a multiple particle simulation with respect to impact angle

remaining on the plate and thereby reducing the energy transfer. This is a well known property of granular materials meaning energy is dissipated as it travels through the layer of surface particles into the wear plate. This effect is often exploited in 'rock boxes' found in material handling systems for non-cohesive materials and used to dampen the effects of falling particles impacting on chute systems. DEM predicts this known phenomenon well as shown in Figures 4.19 and 4.20

For a single particle impact, the E_4 model predicted a maximum transfer at 10 degrees, however with multiple particle impacts it shows a peak at 60 degrees. This is indicative of a general trend which is seen across all the models where the peak is shifted towards higher angles of impact. This is because this simulation is a multi bodied problem, where overall behaviour is affected by particle-particle interactions.

To investigate this further the number of global collisions (all collisions across the plate where each collision is counted at the first instance of a new particle element impact, and stored on the cell data for the element) needs to be considered, as shown in Figure 4.21, to determine how the models are behaving with multiple particles.

It can be seen at higher angles the number of impacts increases, from a minimum at 10 degrees to a peak at 70 degrees. From 70 degrees it then decreases towards 90 degrees but remains considerably higher than at lower impact angles. This is due to the behaviour of the particles post collision. With the plate at high angles, particles can remain in the system and continue creating wear until they are removed. At more acute angles the chance of particles remaining in the system is reduced leading to less energy transfer and therefore less wear.

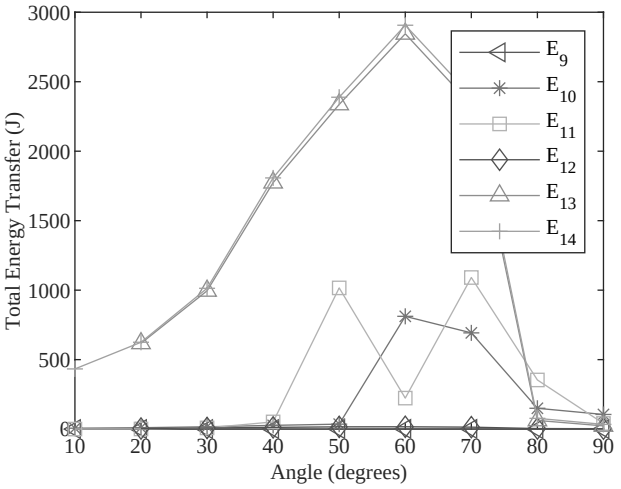

FIGURE 4.22: Energy models E_9 to E_{14} as shown in Table 4.2 total energy transfer values for multiple particle impacts plotted against the angle of impact

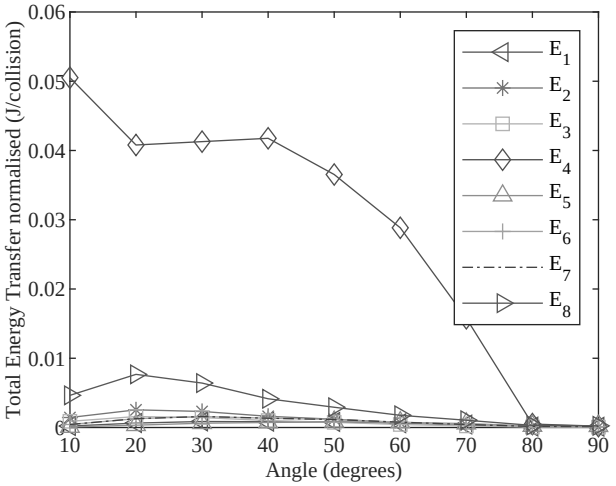

FIGURE 4.23: Energy models E_1 to E_8 as shown in Table 4.2 normalised total energy transfer values for multiple particle impacts plotted against the angle of impact

Figures 4.23 and 4.24 show the values calculated for the energy models when normalised against the number of collisions at each impact angle, as shown in Equation 4.30.

$$E_{norm} = \frac{E}{G_k} \tag{4.30}$$

Using this method the global effect of the impact angle, for a simulation with multiple particles in it can be established while factoring out the increased number of impacts.

Interestingly in Figure 4.24 when the energy transfer is normalised against the number of global collisions across the plate, the plate angles with most energy transfer move towards being more acute as opposed to maximum values being at higher impact angles

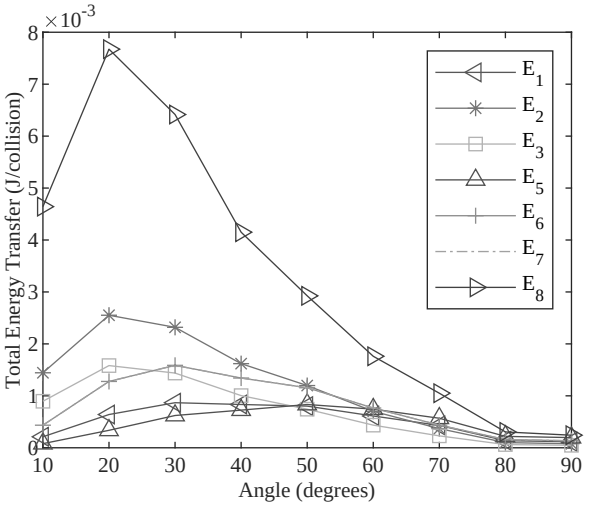

FIGURE 4.24: Energy models E_1 to E_8 as shown in Table 4.2 normalised total energy transfer values for multiple particle impacts plotted against the angle of impact with E_4 removed

as shown in Figure 4.19. This brings things closer to the energy transfer predicted by the single particle energy model, but it is not the same. It also brings the results into line with what would be expected in ductile erosion models where the highest wear occurs at shallower impact angles [60].

Once again, even models which are heavily normal dependent such as E_1 and E_5 show a normalised energy transfer which is greater at shallower impact angles than might be expected. Although they do show a decrease towards 20 and 10 degree impact angles as shown in Figure 4.24.

4.6.6 Findings

The models generally calculate higher energy transfers at impact angles between 10 and 50 degrees for single particle impacts. At the extremes (10 and 90 degrees) a general trend is seen where energy transfer decreases. E_4 is striking in that it creates a peak when the impact angle is 10 degrees.

By introducing a stream of particles the effects of a multi bodied problem can be seen where the kinematics and interactions of the particles in the system begin to affect how the models behave. This generally results in an increase in peak wear between 50 to 70 degrees. At higher angles the behaviour in the system changes as particles begin to remain on the plate. Even E_4 displays this behaviour with a complete switch from its behaviour using a single particle impact. This is thought to be a function of the number of collisions on the plate, as after normalising all models tend towards creating more wear through tangential impact, however the impact count is generally higher towards 70

degrees. Thus, it appears that particles are moving through the system more efficiently at shallow impact angles creating less energy transfer overall, even though individually a single impact at shallow angles creates more energy transfer.

Chapter 5

Fluid Flow Implementation

A useful development in a DEM program would be the ability to import fluid velocity profiles into DEM simulations. This would widen the field of possibilities for DEM application in industry as often granular materials are pneumatically conveyed along pipe systems, or injected. In these situations the particle/fluid interactions may significantly affect wear damage evolution. A good example at Tata Steel, which will be analysed later, is the coal injection lance in the blast furnace.

5.1 Overview

Particle interaction with fluids is a relatively well researched field. Probably the most famous historical contribution is Stokes law, developed by Professor George Stokes to describe the frictional effects exerted on spherical objects by a viscous fluid, in a low Reynolds number regime i.e. laminar flow [116]. The field of study where multiple phases are combined is also relatively well researched in the area of liquid fluid interaction. Gas solid interaction is the area of interest here, and while research is a little more limited it does exist [117]. Combined multiphase computational modelling is present within CFD codes such as ANSYS Fluent, where discrete phases can be introduced into the system. In some cases steps have been take to implement erosion predictions into these models [94].

Here we are concerned with the use of Discrete Element Method to assess wear and the extent to which a CFD profile could be implemented into DEM to improve predictions. This could be a tool for industrial scale systems to assess the effect of changes in design. No model for the application of forces using CFD profiles is currently included in the in-house program therefore one must be developed. This should be done without adding significantly to the computational run time of the model as this would reduce its attractiveness in an industrial setting.

5.1.1 Assumptions

An important initial assumption is made that the granular material does not affect the CFD profile implemented. This assumption is required to limit computational run time penalties. It is accepted this is a considerable simplification of multiphase flow behaviour. However, in cases where particles in gas streams are continuous and carried along with the flow it is expected that this assumption will be sufficient to replicate the wear experienced, especially in cases where two simulations are compared relative to each other to determine the effect of design changes. This will be demonstrated in a case study below.

Particles are assumed to be spherical during drag force calculation. It is well known that non-spherical shapes would affect drag coefficient values, for example, drag coefficient values and terminal velocities vary according to particle sphericity [118]. The assumption of spheres in this work is due solely to the complexity of computing non-spherical particle collisions inside DEM as outlined [3], not because of any problem with applying the drag coefficient force itself.

Particle collisions calculated through the use of DEM and velocity profile application are assumed to be the only driving forces inside the flow. All other interstitial effects such as moisture and other cohesive effects are ignored (although these effects inside DEM have been explored [8][9]). Thus, in the interests of practicality, the model here also assumes dry granular materials.

5.2 Implementation

As has previously been discussed in Chapter 2 DEM forces are applied by solving Newton's Second Law as shown in Equation 5.1. Theoretically any force could be applied so long as a force value can be calculated using the variables present in DEM. Therefore, if a velocity profile is imported it can also be used to move particles, using the same methods as those already successfully used to simulate conveyor belts.

$$m_i \frac{dv_i}{dt} = \sum (F_{c,ij} + F_{d,ij}) + m_i g + F_i \tag{5.1}$$

Initially this was done using a 'brute force' method which required considerable simulation time, but at least provided a proof of concept. This method consisted of looping through all particles in the system and all the velocity nodes present. The result of this is considerably longer computation times even with relatively small systems. Figure 5.1 shows an example where a velocity profile is introduced on a flat bed of particles, at which point it is moved along the bed.

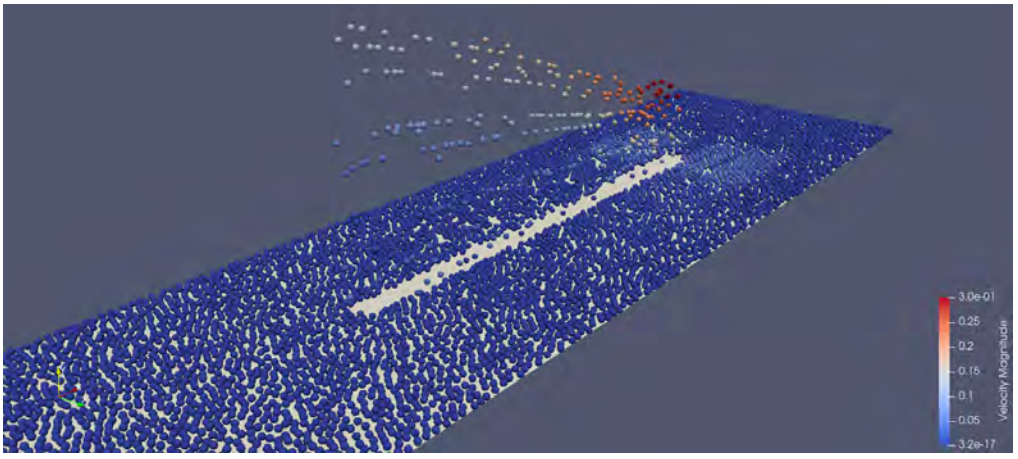

FIGURE 5.1: A flat bed of particles being effected by an applied velocity profile which moves along the surface

This was a good foundation but the computational time required to move the particles was unacceptable. Another method was required to reduce the simulation time. After testing a variety of methods a Finite Difference based method was selected to be implemented [119].

5.2.1 Application of Finite Different Method for Velocity Profiles

The Finite Difference approach works by creating a spatial framework in the DEM region where the velocity profile generated from a Computational Fluid Dynamics (CFD) simulation can be positioned and referenced. Effectively a structured orthogonal grid is located over the DEM simulation region and any element in this grid contains all of the local CFD characteristics. This is done by assigning each CFD node to each cell inside the FDM domain. Therefore allowing the DEM program to locate which FDM cell a particle is in, and therefore identify the correct CFD nodal data to apply. The force application is then carried out using the calculation of the drag force on a spherical particle which is then used to resolve Newton's second law as shown in Equation 5.7.

The first step of application is to create the FDM domain in the program. To create this the maximum and minimum coordinates of the FDM domain is specified using an xyz coordinated system, $FDM_{max,xyz}$ and $FDM_{min,xyz}$ respectively. This can be an equivilant size of the DEM domain or smaller. This region is then split into a number of cells of equal size. This cell size is expressed in the xyz coordinate system and is defined as the variable Δ_{xyx}. Δ_{xyz} can be defined by either specifying a Finite Difference cell size, or by specifying the number of cells required per axis of the domain as shown in Figure 5.2. This latter is the method used in the current DEM program, shown in Equation 5.2.

$$\Delta_{xyz} = \frac{FDM_{max,xyz} - FDM_{min,xyz}}{No.Cells_{xyz}} \tag{5.2}$$

The particle's local position in the domain can be found with respect to the FDM domain, L_{ijk}, in the terms of a local ijk coordinate system.

$$L_{ijk} = \frac{C_{xyz}}{\Delta_{xyz}} - O_{ijk} \tag{5.3}$$

Where the respective values shown in Equation 5.4.

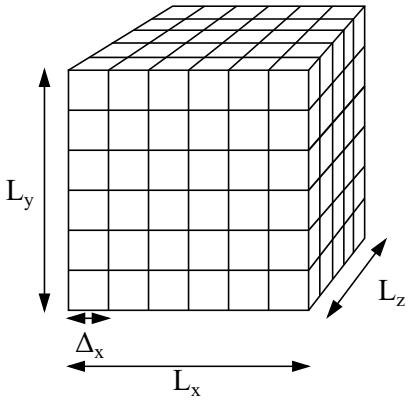

FIGURE 5.2: Finite Difference cube demonstration with length's, L_x, L_y and L_z highlighted with sub cube size, Δ_x

$$L = \begin{bmatrix} L_i \\ L_j \\ L_k \end{bmatrix} C = \begin{bmatrix} C_x \\ C_y \\ C_z \end{bmatrix} \Delta = \begin{bmatrix} \Delta_x \\ \Delta_y \\ \Delta_z \end{bmatrix} O = \begin{bmatrix} O_i \\ O_j \\ O_k \end{bmatrix} \tag{5.4}$$

Where C_{xyz} is the coordinate of the particle being assessed in the global xyz coordinate system, Δ_{xyz} is equal to the length, breadth and width of the sub FDM cube in its respective xyz directions and where O_{ijk} is the offset between the origin of the global coordinate system and the origin of the local coordinate system in the local coordinate ijk scheme.

Using Equation 5.3 the local coordinates, L_{xyz}, are found. These can then be inserted into the $3D$ matrix, Γ, which represents an FDM cube element mathematically after rounding down the ijk position of L_{ijk} to the nearest integer. These rounded down values are represented by i, j and k as shown in Equation 5.5.

$$\Gamma_{ijk} = W \tag{5.5}$$

Once the correct FD element, W, has been identified the list of relevant nodal numbers can be obtained as shown in Equation 5.6.

$$W = \begin{bmatrix} node_1 \\ node_2 \\ node_3 \end{bmatrix} \tag{5.6}$$

The length of this list is determined by the user, ideally it would use a single node per cube however this is highly dependent on the CFD mesh used in the simulation which will be discussed in a later Chapters 7 and 9. The nodal numbers obtained are then

used to find the relevant velocity values to be applied to the particles. This allows the program to simulate a material being moved in a fluid velocity profile such as a pipe flow.

5.2.2 Force Application

As shown in Chapter 2 the particle forces to be accounted for in Newton's second law are recreated in Equation 5.7.

$$m_i \frac{dv_i}{dt} = \sum (F_{c,ij} + F_{d,ij}) + m_i g + F_i \tag{5.7}$$

Where the value F_i is defined as any other force. This latter can be updated to include the all theoretical effects from a velocity flow profile, in this case the drag force on the particle, F_p, and the buoyancy force on the particle, F_b, can now be introduced into Equation 5.8.

$$m_i \frac{dv_i}{dt} = \sum (F_{c,ij} + F_{d,ij}) + m_i g + F_b + F_p + F_i \tag{5.8}$$

Therefore these two force components must be considered individually to determine their application inside DEM.

5.2.2.1 Buoyancy Force

Usually when a particle is suspended in a fluid, buoyancy forces, F_b must be considered. Buoyancy is a function of the density of the fluid, ρ_f, gravitational acceleration, g, and fluid volume, V_f, as shown in Equation 5.9. This is known as Archimedes' principle.

$$F_b = -\rho_f g V_f \tag{5.9}$$

In our case air provides relatively little buoyancy, if the air became stagnant the particle would drop due to gravity, therefore buoyancy force is assumed to be negligible. An update to the Newton's second law equation based on this assumption is shown in Equation 5.10.

$$m_i \frac{dv_i}{dt} = \sum (F_{c,ij} + F_{d,ij}) + m_i g + F_p + F_i \tag{5.10}$$

5.2.2.2 Drag Force

There are different types of drag force for a particle in a fluid, and other factors which could effect drag such as particle shape. For the purposes of this work profile drag is the type of drag considered.

As the particle is being driven by an air flow, the type of flow will affect how the drag force is calculated. In general there are three regions of flow, laminar, transition and turbulent [120]. These regions are differentiated and determined by the Reynold's number which is the ratio between inertial and viscous forces. The Reynolds number formulation is shown in Equation 5.11

$$Re = \frac{\rho_f v_f L}{\mu_f} \tag{5.11}$$

Where ρ_f is the density of the fluid, v_f is the velocity of the fluid, L is a characteristic length dependent upon the system, and μ_f is the dynamic viscosity of the fluid. At low Re values viscous forces dominate the flow, i.e. laminar flow, for a transitional region there is a balance between the two force types and at high Re numbers inertial forces dominate, i.e. turbulent flow [121].

Typical Reynold's number values determining the flow type for smooth pipes are $Re < 2000$ for laminar, $2000 < Re < 4000$ for a transitional region, and $Re > 4000$ for turbulent flow, however variations naturally exist depending on conditions and application [120]. For this application in DEM, the flow regime will always be turbulent in nature therefore the profile drag in this regime shall considered.

An initial profile force model was developed for the 'proof concept' where the drag coefficient of a particle was ignored and F_p was defined simply in terms of assuming the velocity acted over the area of a particle in and this generated an acceleration as shown in Equation 5.12

$$F_p = \rho_f A_p |v_i - v_f|^2 \tag{5.12}$$

This force was then be applied to the particle in the required direction using the unit vector of velocity node. For an initial proof of concept this was sufficient, as can be seen in Figure 5.1, however the model requires the use of a more accurate drag force model for actual application.

The first parameter to consider is the drag force of the fluid on the particle and this can be done by introducing the drag coefficient, C_P. The drag force equation is a well

established law from an experimental ideal relationship and is shown in Equation 5.13 [122].

$$F_P = \frac{1}{2} C_P \rho A v^2 \tag{5.13}$$

Generally in fluid mechanics the definition of velocity is solely the fluid velocity, v_f, as one body is assumed to be stationary. For use in DEM this will not be the case. Therefore the velocity must be altered to create an effective velocity which is the difference between the particle velocity, v_i, and fluid velocity, v_f. The magnitude of this value is then taken, as the direction of the flow is reapplied to the particle through the unit vector of the fluid flow.

Similar methods are used in commercial CFD codes when introducing discrete phases. The full equation for the drag force to be applied to the particle is calculated as shown in Equation 5.14.

$$F_p = \frac{1}{2} C_P \rho A |v_i - v_f|^2 \tag{5.14}$$

The variable to be defined is now the drag coefficient.

5.2.3 Drag Coefficient

The drag coefficient is a dimensionless value which represents the resistance of an object in a flow. It is generally considered to be a function of the shape of the object in question, however it also varies with the velocity of the fluid or in the case here, the effective velocity. As this case is assumed to deal with perfectly spherical particles, the drag coefficient can be established as a constant value. For $Re < 1000$ the drag coefficient is equal to 0.44.

However, the application in this case considers a flow which is turbulent. The behaviour of the drag coefficient of a sphere has been studied and determined to be a function of Reynold's number which when calculated for a particle in DEM is shown in Equation 5.15.

$$Re = \frac{\rho d_p |v_i - v_f|}{\mu} \tag{5.15}$$

When Reynold's number is greater than 1000 the drag coefficient is a function of Re as shown in Equation 5.16. This is the widely used Schiller-Naumann correlation, which is

a drag coefficient model for multiphase flow, although it should be noted it is only valid for isothermal conditions [123][124][125].

$$C_P = \begin{cases} \frac{24}{Re}(1 + 0.15Re^{0.687}), \text{if } Re > 1000 \\ 0.44, \text{if } Re < 1000 \end{cases} \tag{5.16}$$

This value can then be used in Equation 5.14 accounting for respective direction using the unit vector of the velocity node.

5.2.3.1 Drag Crisis

At approximately $Re = 30000$ a phenomenon know as the Eiffel Paradox or Drag Crisis occurs where the drag coefficient reduces from approximately constant at 0.5 to 0.2 for rounded bodies [120]. The cause of this is the boundary layer transitioning from laminar to turbulent. The approximate Reynolds number for this varies dependent upon the particle shape and roughness and when it occurs the application of the drag forces to the particles is no longer valid using the calculation previously presented in Equation 5.16. However, it is analytically simple to check if this number will be achieved prior to carrying out any simulation if the Reynolds number for the drag crisis is known.

5.2.3.2 Particle Shape

In this work the particle shape is assumed to be spherical and this assumption is now discussed. The shape of a particle has a pronounced effect on the drag forces acting on it in a flow. This can be seen in the general drag Equation 5.13 where the force is dependent on the area of the particle or shape . As this shape changes, so does the drag coefficient. For spheres, values between 0.44 - 0.47 are expected (depending on surface smoothness). In contrast, for flat plates perpendicular to a flow values such as 1.97 - 2 in 2D, or 1.18 in 3D [122] would be expected.

For common non-spherical shapes which have been simulated inside DEM [3], such as cubes, a drag coefficient of 1 - 1.2 could be expected in 3D [122], significantly different from a sphere. In this application we are concerned with coke material. The actual shape of coke varies and is difficult to predict, but it can be considered as an 'irregular shape'. For irregular shapes which are defined by sphericity there has been research quantifying drag coefficient effects [118]. This leads to a correction factor for the drag coefficient of 'irregular particles', the trend of which can be seen in Figure 5.3.

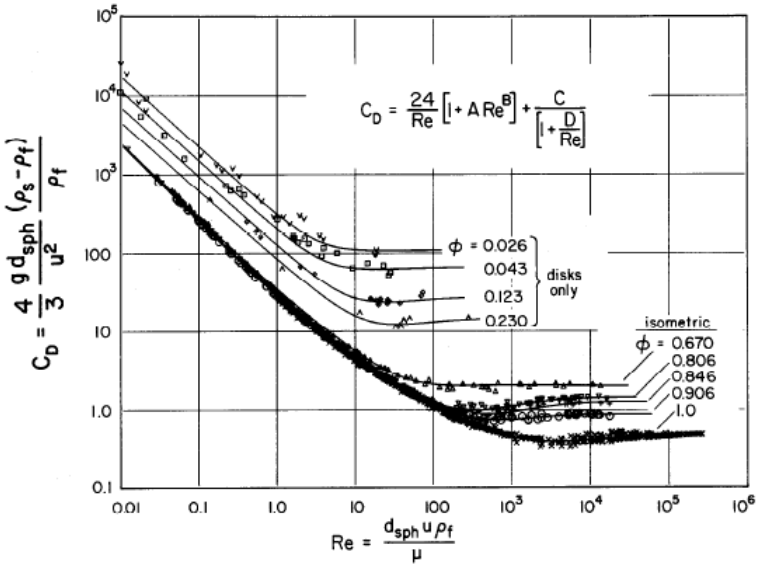

FIGURE 5.3: Effect of particle sphericity, Φ, and Reynold's number on drag coefficient produced by Haider and Levenspiel

Further work has been carried out by quantifying a value known as the Corey Shape factor and the associated changes with respect to drag coefficient, to create mathematical relations between the shape, effective Reynolds number and drag coefficient [126]. What can be seen is that a significant alteration in shape would have a pronounced effect. However, even minor changes in roughness or outcroppings (which could be expected in coke) could increase the drag coefficient by 3 - 4x which is significant. Even with this effect it was chosen to proceed with the modelling using perfectly spherical particles. The reasoning for this is two fold. This was the first development of using a CFD profile inside DEM in this way therefore this assumption is used to limit the complexity of the model. Secondly the DEM program only considers spherical particles, therefore the assumption also keeps it consistent with all stages of the modelling. The adaption of the DEM program would be a good future step for further development.

5.3 CFD Models

Computational Fluid Dynamics is a method which allows numerical simulation of fluid flow, where fluids are considered to be a continuous body, liquid or gas. For the applications here modelling of turbulence is required. An overview is provided of turbulence modelling, more information can be found in [127].

Generally all work carried out in CFD used Ansys FLUENT where the Navier-Stokes equations are solved, or the momentum equation using a RANS turbulence model, or a Reynold's Averaged Navier Stokes equation. This requires two main equations for

solution, the continuity equation and the momentum equation. However, the momentum (Navier-Stokes) equation cannot be solved alone and a model must be used to calculate the turbulence, which for the case of RANS calculates a so-called eddy viscosity term which can then be used to resolve the equations. There are two general models which are used for this which have separate applications, the k-ϵ and k-ω model. Further discussion regarding the selection of these model is present in Chapter 7.

5.4 Summary

This chapter has discussed the development of an algorhitm to apply a CFD steady state profile to DEM. Through this it has found and implemented an uncoupled method to rapidly determine the force applied to a particle from a fluid flow. While it currently assumes the particles are spherical, applying this to non-sperical or irregular shapes was also investigated. Shapes such as cubes could have a simple modification to allow their application inside this algorhithm through a modification of the drag coefficient value. However, much further invetsigation would be required to assess the effect of highly irregular particles such as coal or coke as their irregularity is much more unpredictable.

Part III

Case Studies

Chapter 6

Coke Screener

The initial application chosen for the project concerned the Coke Screeners located in the carbon management section of TATA Steel. These machines separate the different size fractions of material created in the coke ovens. Coke, by its very nature, is an extremely abrasive material which is known on plant for causing high wear areas. The coke screeners were no exception with sections of the machine surviving only days in certain conditions. This case study will cover the simulation of a known screener set up and compare this to the real world conditions. A second section will cover an industrial trial carried out using Wall Colmonoy's ColWear 62-1 wear plate and compare quantitative predictions calculated from the damage model presented in chapter 4 demonstrating the use of the SEF criteria. Finally, variations of system variables such as conveyor speed and angle will be investigated, as well as considering a classic curved plate option.

6.1 Operation

6.1.1 Overview and Methodology

The basic principle of a screening machine is similar to one which could be found in a laboratory setting but on a much larger scale. Material is inserted into a hopper at the rear of the machine by a front loader as seen in Figure 6.2. It is then transported up the machine using a conveyor belt, at which point it leaves the conveyor belt and impacts a top wear plate as can be seen in Figure 6.1. After impacting, it falls into the screening decks, where meshes are used to separate the size fractions of material. These are then transported outwards by three conveyors as can also be seen in Figure 6.2.

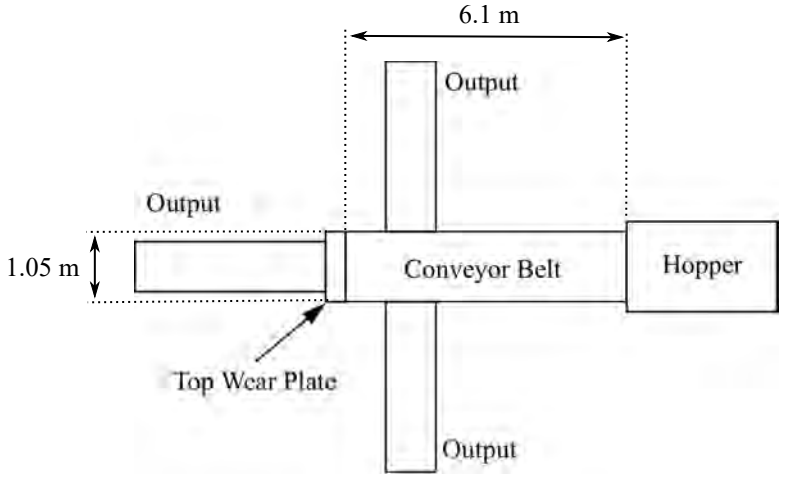

FIGURE 6.1: Basic schematic diagram of McCloskey S190 coke screener

FIGURE 6.2: McCloskey S190 coke screener operating at TATA Steel

There are three sets of factors which need to be taken into account when simulating the coke screener system. The first is the coke screener itself, the properties of which will be used to create the 3D models used for the simulation. The second is the coke material and the properties required to simulate its behaviour. Finally the properties of the worn material must be considered.

The relevant coke screener specifications are shown in Table 6.1, these were obtained from the operation and specification manuals provided by TATA Steel and Lloyd Walters Industrial Services who are in charge of machine operation [128] [129].

TABLE 6.1: Coke screener specification

Make	McColskey
Model	S190
Operation Angle	22.5
Conveyor Speed	160 rpm
Conveyor Width	1050 mm
Conveyor Drive Drum	285 mm
Conveyor Length	20 feet

A 3D model was created using the measurements provided in the manuals and by physically measuring the conveyor for values which are not present in the specification (such as the distance between the conveyor drum and the wear plate). The conveyor velocity was calculated using the speed of the motor and the diameter of the conveyor drive drum using the angular velocity Equation 6.1.

$$v_{con} = r_{con}\omega_{con} \tag{6.1}$$

Where v_{con} is the velocity of the conveyor, r_{con} is the radius of the drive drum and ω_{con} is the angular velocity of the drive drum. This is then calculated for the drive drums x and y velocity components using the angle of the conveyor.

The top wear plate was then discretised to show only the area which is of interest. Elements which represented the conveyor belt were used to apply a force to the material which would move the particles, replicating the action of a conveyor belt. Wear calculated on these elements is ignored for the entirety of the simulation. The 3D model created can be seen in Figure 6.3.

The SEF criteria is used to simulate the damage to the coke screener which allows comparison of a wide combination of plate materials. Table 6.2 shows the combinations of wear plate material properties used. Property set 2 and 11 represent the usual operation of the machine, whereas property set 5 and 14 represent the trial material properties used, although it should be noted it also utilises a 3 mm stainless steel base plate.

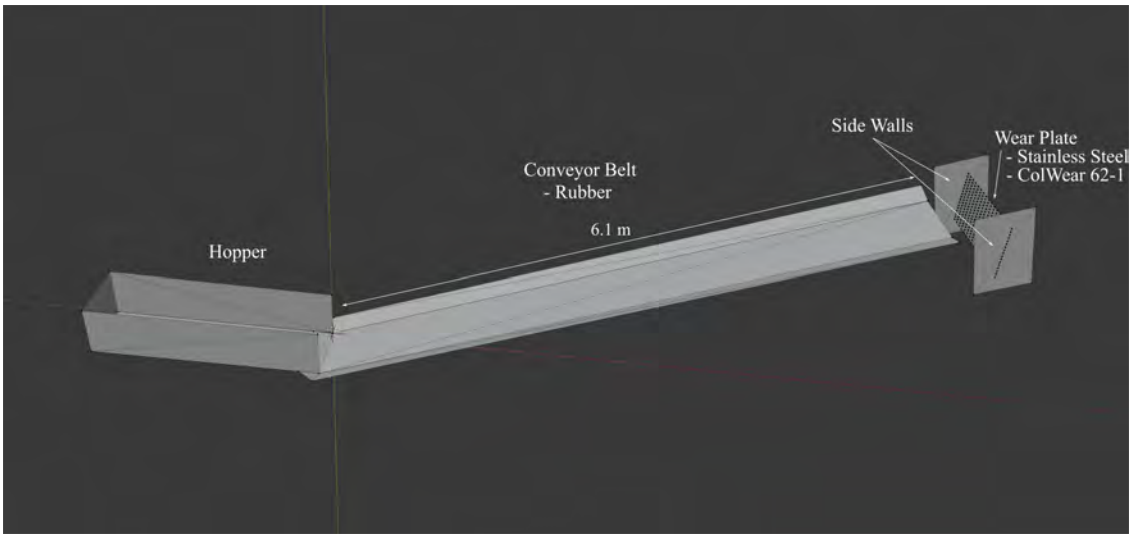

FIGURE 6.3: 3D model created to simulate the coke screener displayed in Blender

TABLE 6.2: Material parameters used for mild steel, stainless steel and ColWear for simulations of coke screener trial (* highlights the known material and industrial trial property sets)

Set	Material	Hardness, H	Thickness
1	Stainless Steel	94 HRB	1 mm
2*	Stainless Steel	94 HRB	3 mm
3	Stainless Steel	94 HRB	5 mm
4	ColWear	62 HRC	1 mm
5*	ColWear	62 HRC	3 mm
6	ColWear	62 HRC	5 mm
7	Mild Steel	71 HRB	1 mm
8	Mild Steel	71 HRB	3 mm
9	Mild Steel	71 HRB	5 mm

Set	Material	Tensile strength, σ	Thickness
10	Stainless Steel	679 MPa	1 mm
11*	Stainless Steel	679 MPa	1 mm
12	Stainless Steel	679 MPa	1 mm
13	ColWear	2653 MPa	1 mm
14*	ColWear	2653 MPa	3 mm
15	ColWear	2653 MPa	5 mm
16	Mild Steel	440 MPa	1 mm
17	Mild Steel	440 MPa	3 mm
18	Mild Steel	440 MPa	5mm

The final consideration is the material properties for DEM. Fortunately, previous work carried out by Holmes characterised coke as a material inside DEM and validated the parameters in simulations of blast furnace operations [2]. The validated parameter set used is shown in Table 6.3.

TABLE 6.3: DEM coke material parameters used

Parameter	Value
Spring Stiffness	16000 N/m
Particle Density	1150 kg/m^3
Coefficient of resititution	0.01
Particle Radius	0.015 m
Sliding friction coefficient	0.8
Rolling friction coefficient	0.3
Rolling damping coefficient	1.5
Twisting friction coefficient	0.3
Twisting damping coefficient	1.5

6.2 Known Wear

There were a number of areas considered for the application of DEM in the trial. These were the top wear plate, the bottom hopper and the mesh screens. The mesh screens were an interesting application. However, in discussion with Tata it was decided that the extra cost in simulation to simulate a screen would not provide meaningful results within an acceptable time frame. This was due to the nature of the mesh being on a very small scale which would result in an extremely high number of elements which, for a full scale simulation, would increase computational considerably. The bottom hopper would be the simplest application to model, however, its failure times are known to be longer than the length of this project. Therefore, the top wear plate was selected as it would provide a convenient trial duration, can be simulated relatively easily and would provide a good test to compare the DEM model to real world data.

6.2.1 Particle Sizing

The particle size distribution of the coke is not known as it was created on site, therefore it can vary massively from having extremely large pieces to a fine dust. This is the reason for screening. The material is screened to three size fractions; greater than 30 mm diameter, between 30 and 10 mm and less than 10 mm. Therefore, an initial approach using a constant particle size of 30 mm was used. This value gave a particle/element ratio of $R = 0.7$.

6.2.2 Failure

All the information gathered regarding wear and damage to coke screeners was only anecdotal in nature. The top wear plate is known to fail in approximately 2 - 4 weeks

of operation. This provided a range for comparison, therefore all predictions shall also be of a range comparing to the bottom limit of 2 weeks and the top limit of 4 weeks.

This information allows the calibration of the damage model to assess the system over time. Therefore, the calculation of the damage coefficient value, C_d, can be determined by taking a single simulation with the known material parameters and calculating its required damage coefficient, C_d, as shown in Equation 6.2.

$$C_d = \frac{t_{failure,real}}{t_{failure,simulation}} \tag{6.2}$$

The abrasion wear model was selected for use in the time to failure calculation for the purpose of this case study shown in Equation 4.2 (it is also equivalent to the E_6 energy model presented previously). Although a number of different wear and energy models have been presented for study in further sections of this case study, for application in industry a well established model was selected to provide information to operators.

6.3 Simulation Results

Figure 6.4 shows the simulation running using the conditions presented. The side walls of the plate have been hidden for clarity.

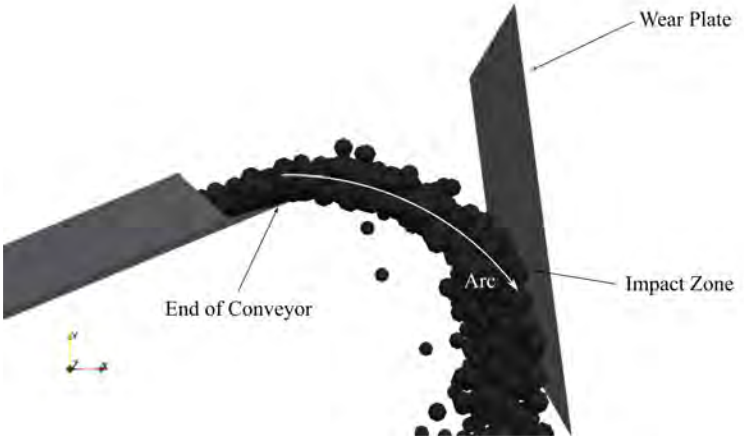

FIGURE 6.4: Simulation of coke screener showing impact of material on the top wear plate

Figure 6.5 shows the established wear models and the wear patterns they predicted. The abrasion model in (a) predicts wear in the impact zone with wear occurring in a crescent shape moving outwards. It also predicts a lesser extent of wear moving down

the plate towards the particle 'run off' zone, i.e. the area where the particles move to after impact. Using the abrasion model the hole created on the plate would be expected to be in the impact zone and spread horizontally and then downwards.

The brittle erosion model presented in Figure 6.5(b) predicts wear in a similar pattern to the abrasion model, suggesting that both an abrasive, cutting like mechanism would occur as well as one associated with a brittle type mechanism from crack propagation. Interestingly there are elements which show relatively little wear towards the run off of the particles, suggesting the plastic limit for the plate is not reached in these zones.

Ductile erosion is presented in Figure 6.5(c), and this shows a slight change in wear location with it being shifted down the plate towards the run off area for the particles.

The combined erosion model in Figure 6.5(d) shows a similar wear pattern when specific energy values are considered equal. These specific energy values were not known for this simulation therefore information provided by this model is for comparison only.

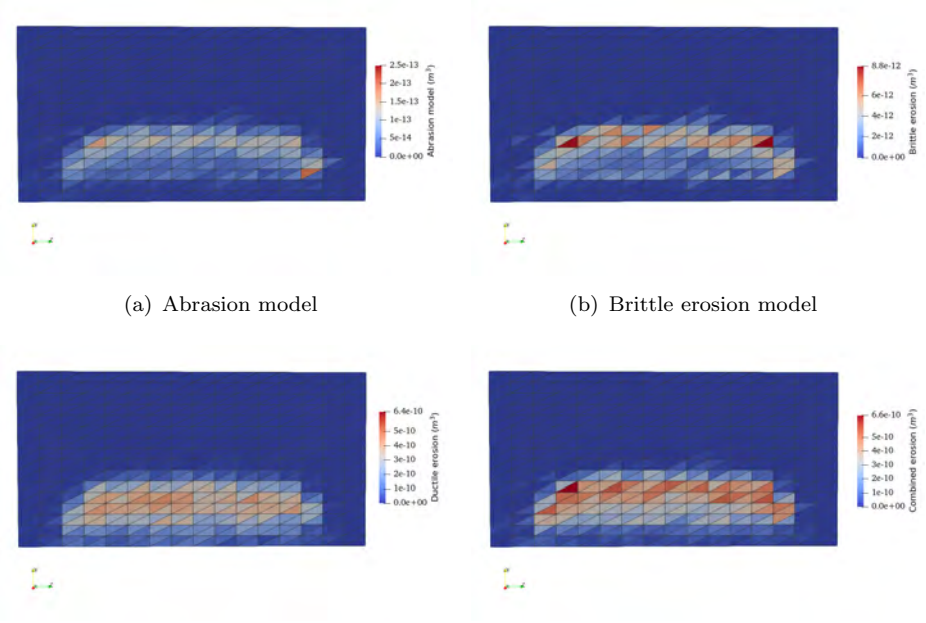

(a) Abrasion model

(b) Brittle erosion model

(c) Ductile erosion model

(d) Combined erosion model

FIGURE 6.5: Wear patterns generated using established wear models on the coke screener simulation

The damage model was calculated using the abrasion model as previously stated, however it also appears to show the most comparable wear patterns.

The predictions used the SEF criterion and are based on a single simulation with a value from the modified abrasion equation. This is shown in Equation 6.3, and is referred to as abrasion energy, or E_6 from the energy models presented in Table 4.2.

$$E_6 = F_n v_t \Delta t \tag{6.3}$$

This value can then be used in conjunction with materials parameters, the damage equation and damage coefficient, C_d to predict failure times for all of the other materials.

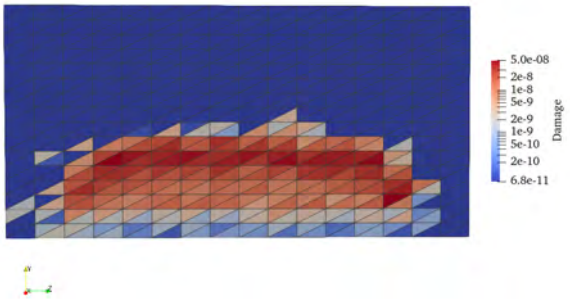

FIGURE 6.6: Damage pattern developed prediction using the abrasion model

Hardness is the main property used in combination with varying plate thicknesses as it is the most applicable for the metallic materials used and has shown good agreement to results found in the literature as described in Chapter 3. However, tensile strength has also been used to quantify the effect as well.

$$t_{failure} = C_d \frac{E/H}{V_e} \tag{6.4}$$

Table 6.4 shows the results provided by the SEF criterion model for failure of the different combinations of materials and thicknesses. The trial ColWear coating by itself is expected to provide a 3.5x life extension (property set 5). In the trial it shall also utilise a 3 mm stainess steel base plate similar to the original material analysed (property set 2). Therefore, in combination with the original materials life, a life extension of between 3.5 - 4.5x is predicted or approximately 14 - 18 weeks.

TABLE 6.4: Results from simulation using the SEF criterion (* highlights the known material and industrial trial property sets)

Set	Material	Time to failure (weeks)	Improvement based on Property set 2	Improvement based on Property set 11
1	Stainless Steel	1.3	0.3	1.0
2*	Stainless Steel	3.9	1.0	3.0
3	Stainless Steel	6.5	1.7	5.0
4	ColWear	4.6	1.2	3.5
5*	ColWear	13.7	3.5	10.5
6	ColWear	22.8	5.8	17.5
7	Mild Steel	0.7	0.2	0.5
8	Mild Steel	2.2	0.6	1.7
9	Mild Steel	3.6	0.9	2.8
10	Stainless Steel	0.4	0.1	0.3
11*	Stainless Steel	1.3	0.3	1.0
12	Stainless Steel	2.1	0.5	1.6
13	ColWear	1.6	0.4	1.2
14*	ColWear	4.9	1.3	3.8
15	ColWear	8.2	2.1	6.3
16	Mild Steel	0.3	0.1	0.2
17	Mild Steel	0.8	0.2	0.6
18	Mild Steel	1.4	0.4	1.1

6.4 Trial Results

Figure 6.7 shows the installation of the ColWear plate on the coke screener. At this point the plate is undamaged.

FIGURE 6.7: Coke Screener plate trial week 0

Figure 6.8 shows the top wear plate after 1 week of operation. At this point very little damage is present with some initial scratching of the surface and removal of surface marks. No indications of failure are present.

FIGURE 6.8: Coke Screener plate trial week 1

Figure 6.9 shows the wear plate after 4 weeks of service. This is the point at which a stainless steel plate would have been expected to fail or be close to failure. Wear can clearly be seen towards the centre of the plate in Figure 6.9(a) and gouges have created a rough surface to the plate. However, it does not appear to be at risk of failure.

Figure 6.10 shows the wear plate after 9 weeks of service. Surface delamination can clearly be seen in the centre of the impact zone. Wear is spreading outwards from there decreasing in severity going down the wear plate, through the 'run off' zone for the particles.

Figure 6.11 shows the wear plate after it had failed at 23 weeks of service. The hole created can be seen clearly and is in the same position of the delamination of the plate shown in Figure 6.10. Therefore, it is not due to any rapid changes in the system which caused a sudden failure. The delamination of the plate can be seen as a rusted colour around the hole. This colour is due to the oxidisation of the stainless steel base plate used. A clear arc shape to the wear can be seen.

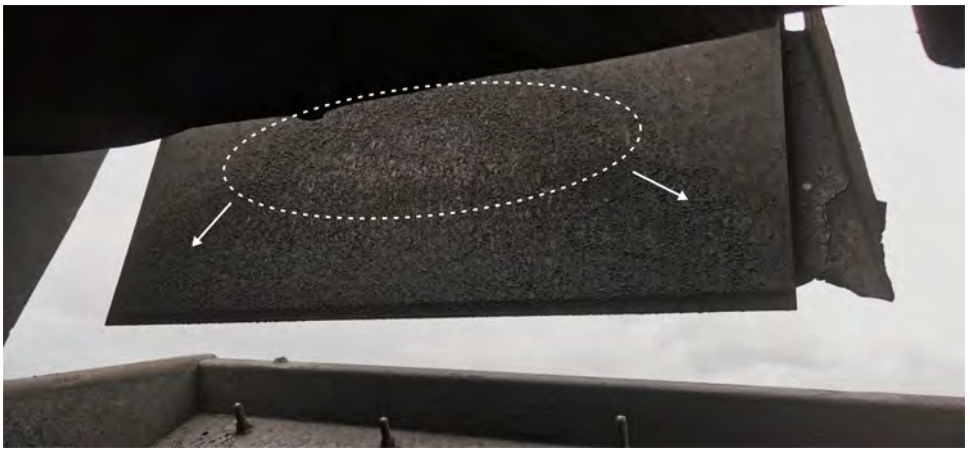

FIGURE 6.9: Coke Screener plate trial week 4

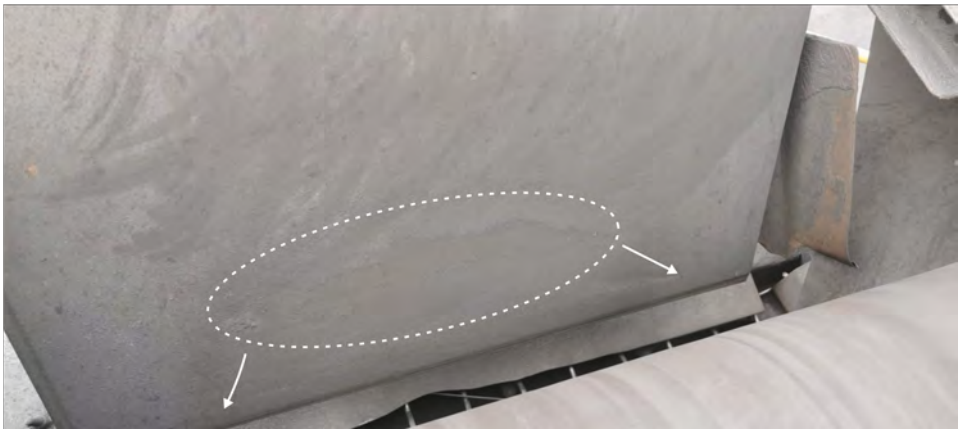

FIGURE 6.10: Coke Screener plate trial week 9

It should be noted failure of the plate was only considered once a hole large enough to impede operation of the machine was established. This was discussed as a failure mode in chapter 4 and this case study acts as a demonstration of this in the real world.

6.5 Findings

Figure 6.5 shows the wear patterns predicted by the established wear models implemented into DEM. When compared to the failure shown in Figure 6.11 the similarity between the pattern for the abrasion model, Figure 6.5(a), brittle erosion model, 6.5(b), and the combined erosion models, Figure 6.5(d), is immediately evident. The ductile erosion model is also relatively accurate, however the wear pattern is moved down towards the 'run off' area of the plate. An issue with comparing the models from this initial simulation is the scales are not comparable, as was highlighted previously in chapter 4. However this initial result does provide an qualitative validation of the model, and

FIGURE 6.11: Coke Screener plate failure after 23 weeks of service

has provided information regarding the mechanism which is most likely to be the main driver of damage i.e., the abrasion model.

Therefore the following damage model was based on the abrasion model, the results of which would be comparable to each other therefore providing a scale through which the expected time to failures could be predicted as shown in Table 6.4. As can be seen the prediction for the trial (set 5) was 13.7 weeks of service for solely the coating. With the addition of a stainless steel baseplate, this could be extrapolated to approximately 17.7 weeks, representing a 3.5x - 4.5x improvement in life. By looking at Figure 6.10 the coating can be seen to be damaged at week 9, however no oxidisation (which would be characteristic of an exposed steel base plate) is visible in the photos. This suggests at this point, the coating layer has not yet been worn through indicating the prediction has a good level of accuracy, although it is by no means precise. The prediction is also pessimistic, as the top wear plate lasted 23 weeks, or a 5.3x life improvement. This is regarded as a positive outcome, as a pessimistic prediction (bearing in mind the uncertainties in both DEM and wear modelling) is the safest option for providing information to industry.

Overall it is seen the abrasion model provides accurate qualitative predictions in this case, with pessimistic quantitative predictions but with a good level accuracy in the

damage model.

6.6 Conveyor Speed

6.6.1 Overview

A series of other variables are possible on the coke screener belt for further study of this application. The first is the simplest. Increasing the conveyor velocity and determining the effect on the wear and energy transfer predictions.

As was mentioned previously the conveyor speed is set via the RPM of the motor which drives it. Therefore this can be recalculated. The coke screener on plant ran at a constant speed however for the purpose of the case study it would be interesting to see the effects of varying the speed and how DEM predicts using the established wear models.

The increased speeds, 1.5x and 2x, will be compared to the velocity used in the previous simulations, shown in Table 6.1, which will be denoted as 1x. An initial plan considered a 0.5x speed but it was found material was unable to impact the wear plate at this lower speed. As conveyor speed is altered the speed at which material is processed will also be changed. Therefore a consistent mass of material must be processed to keep the simulations consistent and comparable, even though the time required for the material to be processed will be changed.

A numerical error in simulation was also found to occur when increasing the speed of the conveyor. High overlap values were created towards the edge of the wear plate as particles were trapped in this zone. This created an unrealistic area of wear. Here, for the purposes of this test, the sides of the wear plate were removed as this would only have a limited effect on the wear prediction itself. The original speed of the conveyor was also re-simulated to ensure all results were comparable.

Models often predict an increase in velocity will increase wear to some form of exponent n. However, changing velocity will also change the particle kinetics of the system i.e. impact angle etc. This could also include the rate at which material is processed. Higher velocities could decrease the density of particles impacting the wear plate or increase it if more particles are in the system at the same time. The purpose of this study is to find out what effects could be expected.

6.6.2 Results

An immediate consideration when increasing the speed of the conveyor is the altered particle kinetics as they impact the wear plate as shown in Figure 6.12. As can be seen at the original conveyor speed, Figure 6.12(a), the impact angle is relatively shallow at approximately 28°. Therefore based on observation it can be expected wear would occur due to higher cutting motions and therefore the dominant wear mechanism is more likely to be abrasion and ductile erosion based. As the conveyor speed increases, as shown in Figure 6.12(b), the impact angle becomes immediately steeper, approximately 64°, therefore a more deformation based model could be more dominant. Finally as the speed is increased again, Figure 6.12(c), the impact angle is steeper at approximately 83° and hardly shows any arc in the particles flight path.

Figure 6.13 shows the total accumulation of wear on the plate based using the established wear models for abrasion, ductile erosion, brittle erosion and a combined erosion model . An increase in total wear across the plate is found for the abrasive wear model between the original conveyor speed (1x) and the higher speed (1.5x), however it is not in line with the increase of speed of the conveyor. Moving to the highest speed there continues to be an increase, but it is once again not in line with the conveyor speed.

For ductile erosion, the original speed of wear is found to actually result in more global wear than the higher speed (1.5x). While the highest speed used is the most wearing, however once again it does not increase a large amount considering the speed of the conveyor.

Figure 6.14 shows the global collisions across the wear plate. An increase from 4k collisions to approximately 8k collisions is seen from the 1x to the 1.5x speed. A further increase of 3k collisions is seen from 1.5x to 2x speeds.

Figure 6.15 shows the wear normalised using the global collisions over time using Equation 6.5.

$$Q_{norm} = \frac{Q}{G_k} \tag{6.5}$$

This shows a spike in the global wear per collision for abrasion at the start of the impacts, shown in Figure 6.15. At which point it begins to become constant after the initial 0.5 seconds of impact for all conveyor speeds. The abrasive wear per collision for the original conveyor speed is higher than that of the increased conveyor speeds, with both higher speeds being approximately constant after the initial period. The normalised wear per

(a) Original conveyor speed

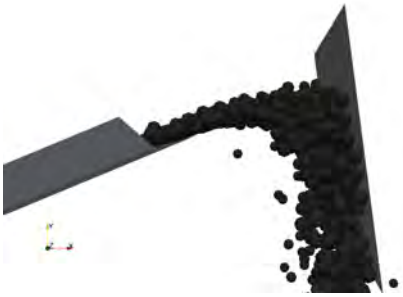

(b) 1.5x conveyor speed

(c) 2x conveyor speed

FIGURE 6.12: Particle trajectory when leaving the end of the conveyor belt and impacting the wear plate for varying particle speeds

collision being highest for the original conveyor speed is a trend throughout all the wear models, as is both higher conveyor speeds being approximately equal.

The largest difference of note is found in the ductile erosion model as it has no initial peak upon the beginning of impacts, instead the original conveyor speed's normalised wear per collision increases rapidly from the initial impacts and becomes constant after approximately 0.5 seconds. Both higher speeds remain constant throughout.

Figure 6.16 shows the total energy transfer calculated across the top wear plate for varying conveyor speed for the energy models established in chapter 4.

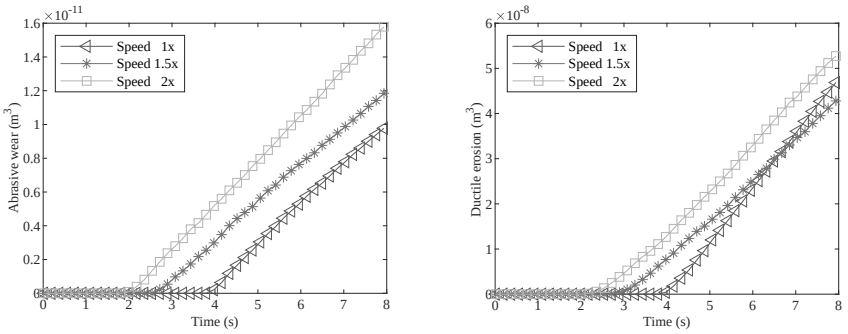

(a) Abrasive

(b) Ductile Erosion

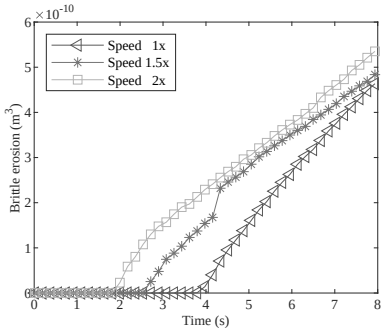

(c) Brittle Erosion

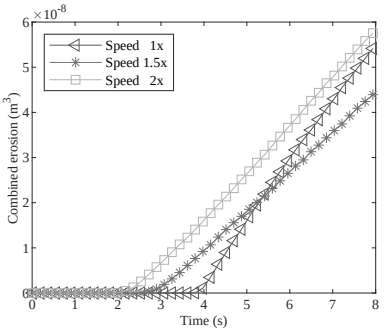

(d) Combined Erosion

FIGURE 6.13: Sum of wear calculated by established models over time for varying conveyor speed

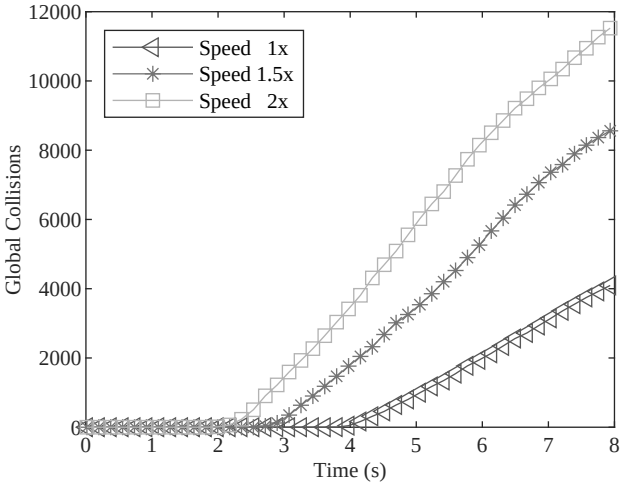

FIGURE 6.14: Global collisions against time for varying conveyor speeds

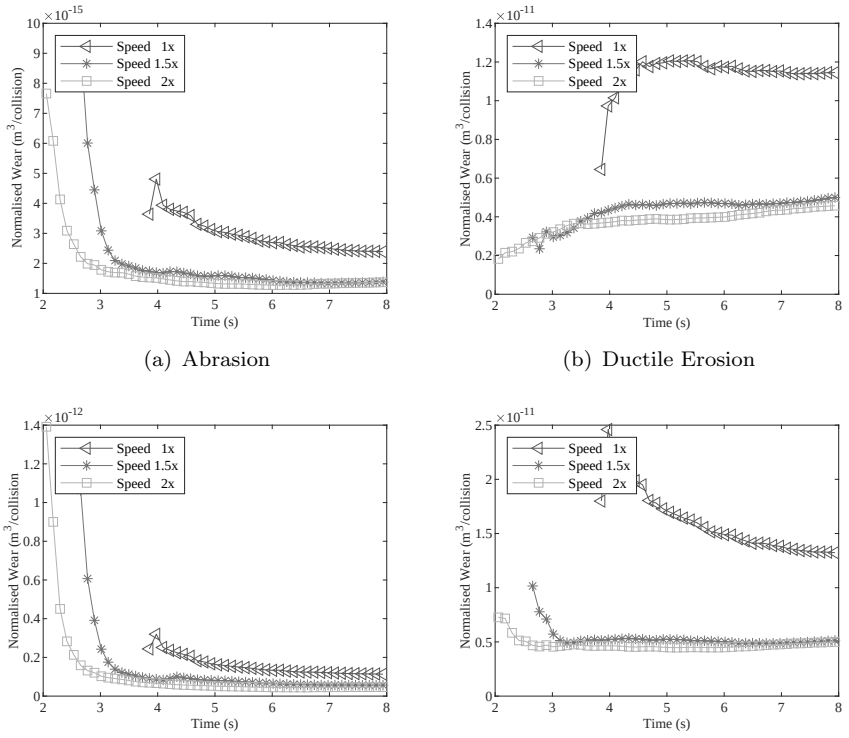

(a) Abrasion

(b) Ductile Erosion

(c) Brittle Erosion

(d) Combined Erosion

FIGURE 6.15: Normalised wear over time for varying conveyor speed

6.6.3 Findings

Figure 6.12 shows the trajectories of the particles impacting the plate at varying speeds. From this it is seen the impact angle becomes steeper as speed is increased. This, in general, shows an increase in wear and energy transfer as shown in Figures 6.13 and 6.16, except for the ductile erosion model. The reason for this is the change in impact angle from the increased particle velocity leaving the conveyor as the model is known to predict more wear at shallower impact angles characteristic of a ductile erosion mechanism. This is shown in Figure 6.12.

Figure 6.14 shows the global collisions across the top wear plate for varying conveyor speed. An interesting trend is apparent in this case as the particle collisions increase at a higher rate when moving from the original conveyor speed (1x) to the initial higher speed (1.5x), also increasing the number of global collisions overall. As the number of particles is identical in both systems the speed of the conveyor must be causing a higher rate of collisions as particles are impacting it faster. This is a fairly logical conclusion with higher conveyor speed, however the higher collision count itself is not as immediately clear. The cause of this can be seen by looking at Figure 6.12, where the trajectories of the particles can be seen. There is a large difference between the original conveyor speed, 6.12(a) and the higher speed (1.5x), 6.12(b). As the impact zone is higher up the

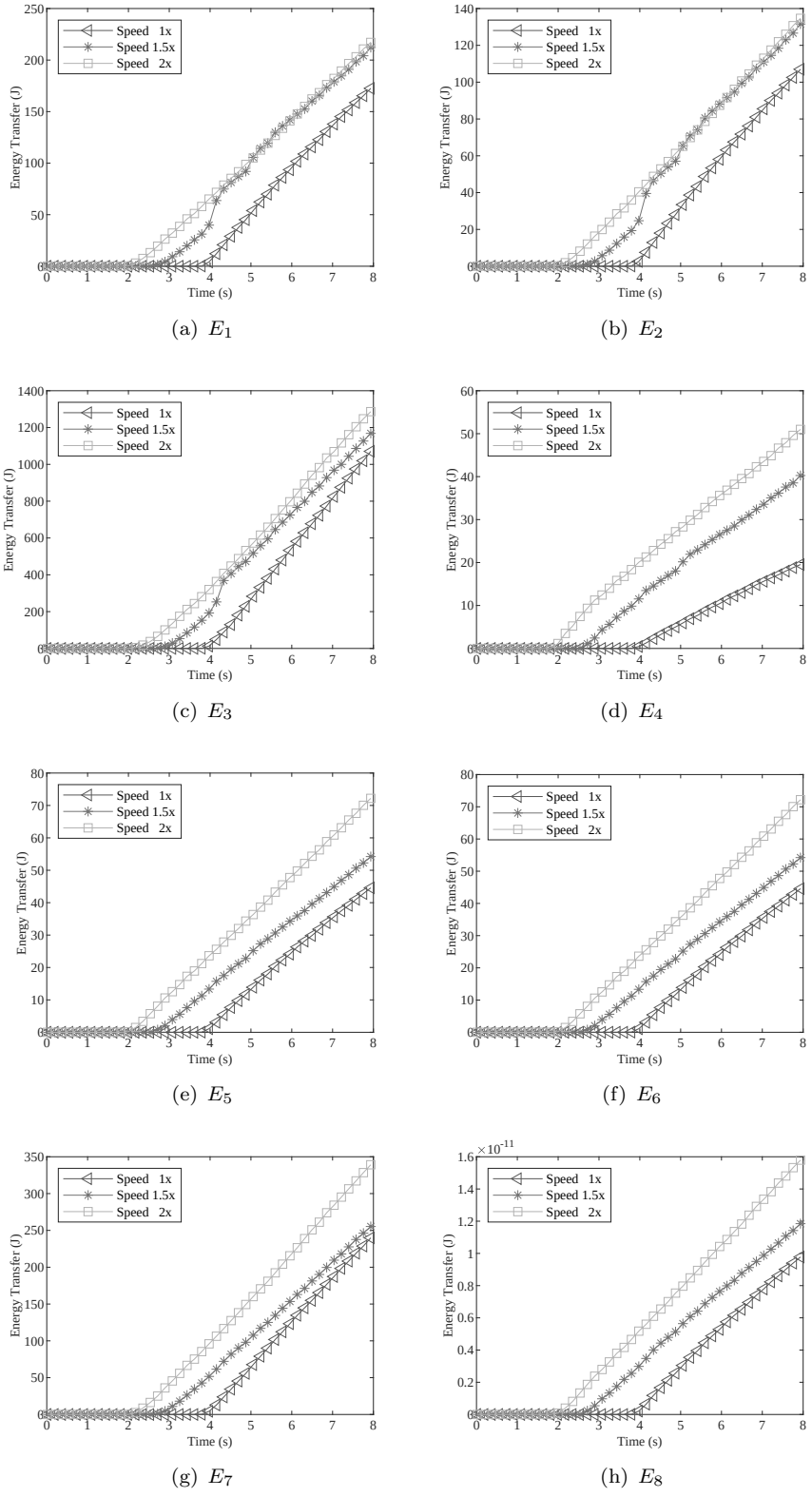

(a) E_1 (b) E_2

(c) E_3 (d) E_4

(e) E_5 (f) E_6

(g) E_7 (h) E_8

FIGURE 6.16: Energy transfer models over time for varying conveyor speed

TABLE 6.5: Conveyor velocity components for the x and y direction

Angle	**Velocity X**	**Velocity Y**
20	1.53	0.56
22.5	1.50	0.62
25	1.47	0.69
27.5	1.44	0.75
30	1.41	0.82

plate, a large area is available for impacts and therefore the number of global collisions across the plate is increased. A similar trend was seen in chapter 4 when the impact angle was varied for a multiple particle impact, in Figure 4.21 it could be seen as the impact angle increased a larger area was available for impact and the number of collisions increased (up until 70 degrees). In the case of the previous study this was due to the spawn area (the area where new partcles are introduced into the DEM system), however in the coke screener case the speed increases show a real world example of this effect. At the highest speed (2x) the number does increase but not proportionally, presumably because the impact area is not increasing as drastically.

6.7 Conveyor Angle

6.7.1 Overview

The second variable which can be altered is the conveyor angle. The conveyor is run at a set angle because the material can clog if the angle is too shallow. However, this provides an interesting first step towards minor design and parameter changes. These simulations will be carried out at angles the conveyor is capable of operating at. 22.5 degrees was used for the initial trial (the standard operating angle) but the machine can also run at 20, 25, 27.5 and 30 degrees. These require a recalculation of the conveyor velocities as shown in Table 6.5. The solid models were also altered to the required operating angles.

6.7.2 Results

Figure 6.17 shows the simulation running at the various set angles of the coke screener. The difference between the simulations is relatively small visually, however the impact zone can be seen to slowly move down the plate leading to a decrease in impact angle for the impacting particles.

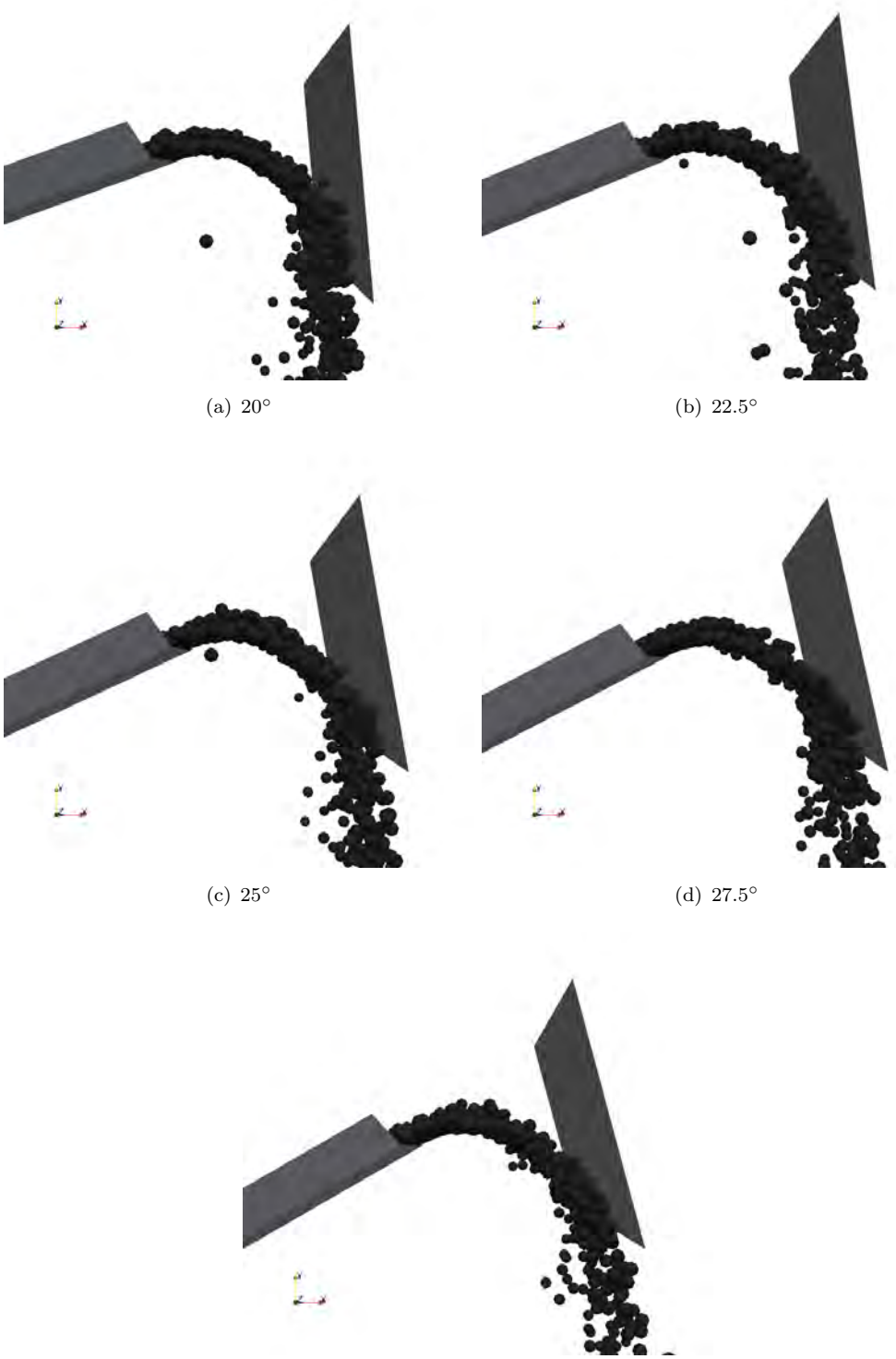

(a) 20°

(b) 22.5°

(c) 25°

(d) 27.5°

(e) 30°

FIGURE 6.17: Coke screener simulation running at the various set angles of the conveyor belt

Figure 6.18 shows the total wear across the top wear plate, for abrasion, ductile erosion, brittle erosion and combined erosion models respectively. It can be seen in Figure 6.18(a) abrasion is predicted to generally decrease as the angle of the conveyor is increased. Initially the change is not large between 20 - 25 degrees but a larger change is seen at 27.5 degrees and 30 degrees. For ductile erosion shown in Figure 6.18(b) the wear is seen to be approximately equal for the 20 and 30 degree simulations. While it is also approximately equal for the intermediate simulations of 22.5 - 27.5 degree simulations. It is generally lower for the extreme cases, however the difference is seen to be not particularly significant. For brittle erosion shown in Figure 6.18(c), the wear is approximately constant for the 20 and 22.5 degree simulations, with a slight decrease at 25 degrees. At which point the wear predicted decreases for the subsequent increases in angle. The combined erosion result, shown in Figure 6.18(d), shows a similar result to the one shown for ductile erosion.

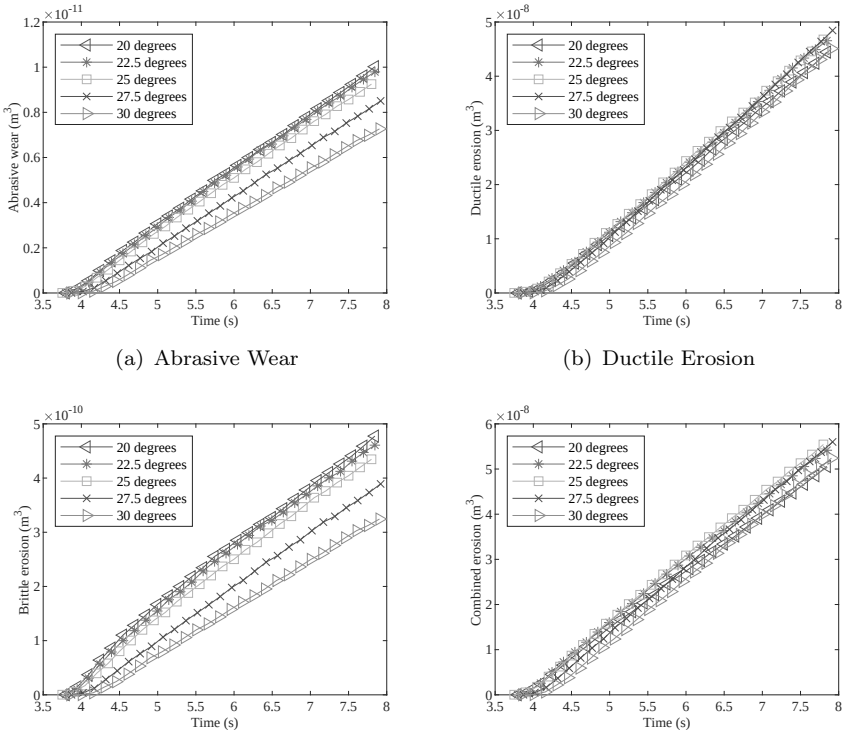

(a) Abrasive Wear

(b) Ductile Erosion

(c) Brittle Erosion

(d) Combined Erosion

FIGURE 6.18: Total wear across top wear plate over time with varying conveyor angle

Figure 6.19 shows the global collisions on the top wear plate with varying conveyor angle. It shows as the conveyor angle increases the total number of collisions on the plate decreases. With larger changes in global collisions as the conveyor angle is increased further.

Figure 6.20 shows the normalised wear calculation across the wear plate. An initial spike in wear per collision is seen for the abrasive wear model shown in Figure 6.20(a).

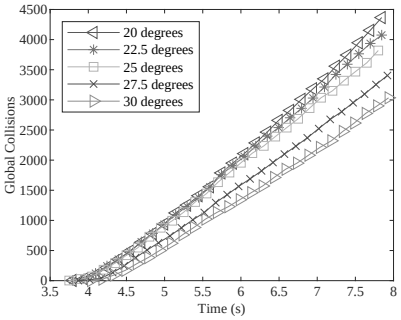

FIGURE 6.19: Global collisions across top wear plate over time with varying conveyor angle

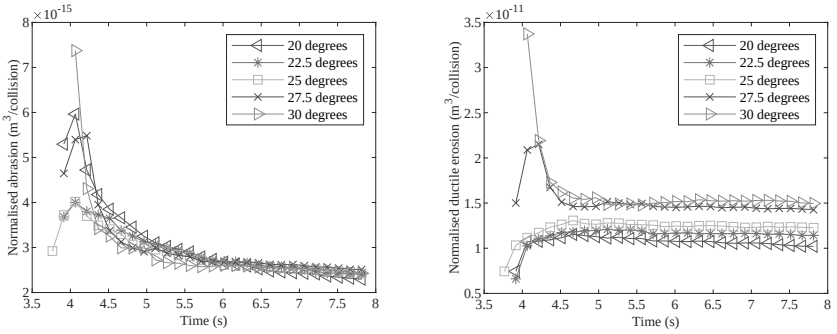

(a) Normalised abrasion

(b) Normalised ductile erosion

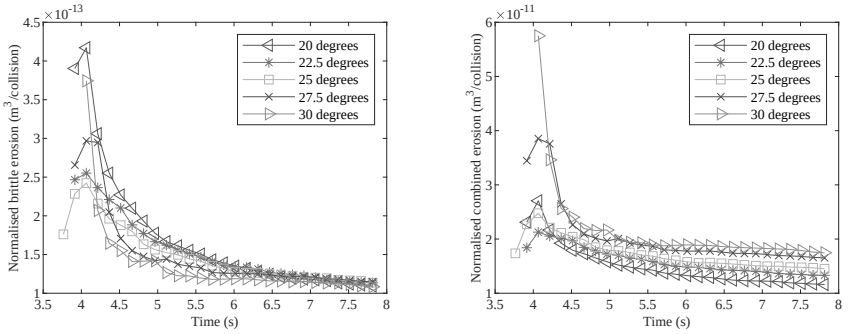

(c) Normalised brittle erosion

(d) Normalised combiner erosion

FIGURE 6.20: Normalised wear across top wear plate over time with varying conveyor angle

This is shown to decrease as the conveyor angle is increased until 25 degrees is reached. At this point it begins to increase again above that seen in the 20 degree simulation. After the initial spike the normalised wear becomes approximately constant for all the conveyor angles, with only small variations between them. For ductile erosion, shown in Figure 6.20(b) an initial spike in wear per collision is only seen for the 30 and 27.5 degree angles whereas all other simulations increase consistently until they become constant. This also continues as the angles of impact remain separate as the normalised wear per collision level off with the 30 degree simulation showing highest wear per collision, with each subsequent decrease in angle resulting in a decrease in wear per collision.

For brittle erosion, shown in Figure 6.20, a similar trend is seen as was shown for abrasion, in that there is a reduction in the spike from the 20 degree impact angle to the 25 degree angle. But an increase is seen after this point as impact angle is increased. The combined erosion model, shown in Figure 6.20 shows a similar trend to that seen in ductile erosion, with a spike for the 27.5 and 30 degree simulations. As the simulation progresses the normalised wear per collision becomes constant, but each value is different, showing the same trend as ductile erosion where as conveyor angle increases so does the normalised wear.

6.7.3 Findings

Altering the conveyor angle has shown using an abrasion or brittle erosion model that the wear would be expected to decrease overall with an increased conveyor angle. In theory this is likely a result of the shallower impact angle, as shown in Figure 6.17, therefore reducing the normal force component and tangential velocity. The ductile erosion is predicted to remain the same through changes in conveyor angle. This is a function of the particle kinetics as the total number of impacts decrease on the plate, however the ductile erosion per collision is increased resulting in the same volume of wear. This is likely a result of the decreased impact angle.

In contrast the normalised wear for abrasion and brittle erosion is expected to remain approximately constant, post the initial collision, therefore the reduction in global collisions is the cause of the decreased wear in these cases.

Overall the change in wear from the conveyor angle is not predicted to be dramatic with an overall reduction in the abrasion, but the ductile erosion is predicted to remain constant due to the resultant change in impact angle.

6.8 The Curved Plate Problem

An interesting case which is often brought up surrounding the wear and management of granular materials is the idea of using a curved plate to direct the flow of material. Previous work by Bridgeman used this curved plate to direct the flow and reduce the amount of rapid changes on the material leading to breakages [5]. It is a common idea inside material handling plants, however, practically it is not often implemented. This is mainly due to the increased complexity of manufacture and lack of evidence of its effectiveness. Work surrounding the design of curved chutes has been carried out in the literature, with abrasive wear factors even being created based on the design of a chute [100].

For this case, the effect of introducing a curve into the deflection plate of the coke screener is investigated to assess the effect it has on predicted wear. This is examined using the established wear models, energy transfer models and their resulting calculations.

6.8.1 Methodology

A curved chute section was created using a constant radius and placed at the top of the conveyor belt similar to the previous wear plate. The curve was designed to change the direction of the flow of material into the screening decks more gradually than the original flat plate therefore possibly decreasing wear. The design and model of the plate can be seen in Figure 6.21.

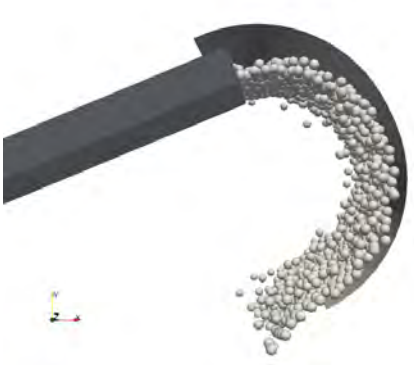

FIGURE 6.21: Constant radius curved plate processing material during simulation

The real operating conditions of the conveyor are used and compared with the previous data to determine if curved plates are a feasible wear reduction strategy. The mesh dicretisation and particle/element ratios are shown in Table 6.6 for both simulations.

TABLE 6.6: Property comparison for the original flat and curved plates

Parameter	Flat Plate	Curved Plate
Elements	512	1152
Particle/Element Ratio, R	0.724	0.755

6.8.2 Results

Figure 6.22 shows the wear patterns produced by the established wear models. Each one can be seen to be different showing the effect of each different mechanism. Figure 6.22(a) shows the abrasion model, which has an area of high wear towards the initial area of contact with the particles and then a consistent wear across the plate as the particles are redirected. Figure 6.22(b) shows the ductile erosion prediction. Immediately a high area of wear can be identified in the run off area of the plate which infers that particles would

be expected to cause higher wear as they are redirected. It also has a bias towards the positive z indicating a preference of direction of the particles which is most likely due to the design of the curve and its placement at the top of the conveyor in this case. This would be expected to be the same even if no bias was present. Figure 6.22(c) shows the brittle erosion prediction. This is the most unique patten of all models as the wear can be seen in the impact zone and along the edges of the plate. In the particle redirection area, very little wear is predicted, if any. Figure 6.22(d) shows the combined erosion model which predicts a relatively even distribution of wear across the plate with a slight increase in the impact zone.

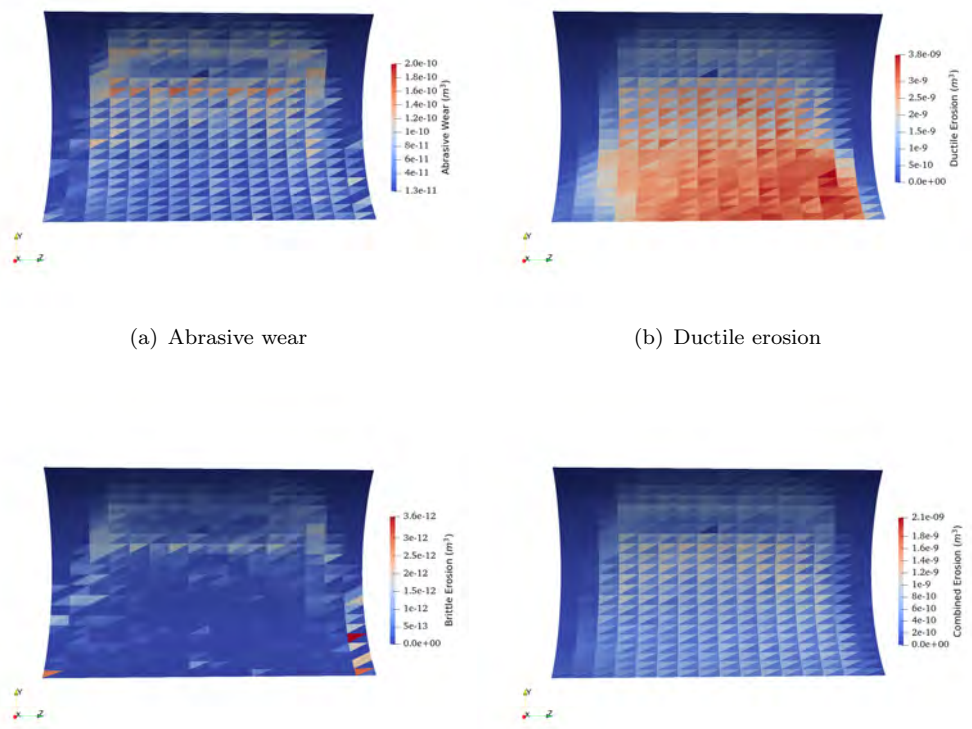

(a) Abrasive wear

(b) Ductile erosion

(c) Brittle erosion

(d) Combined erosion

FIGURE 6.22: Wear patterns predicted using established wear models on the curved plate design

Figure 6.23 shows the total wear across the wear plate for both the original and curved plate design for the established wear models. As DEM is deterministic this value is not affected by the mesh discretisation used. Figure 6.23(a) shows the total wear generated on the plate is predicted to be slightly increased for abrasion using the curved plate design. Figure 6.23(b) shows the total ductile erosion is predicted to be considerably increased using the curved plate. Figure 6.23(c) shows the total brittle erosion is predicted to be decreased across the plate. Figure 6.23(d) shows the total combined erosion

is predicted to also increase.

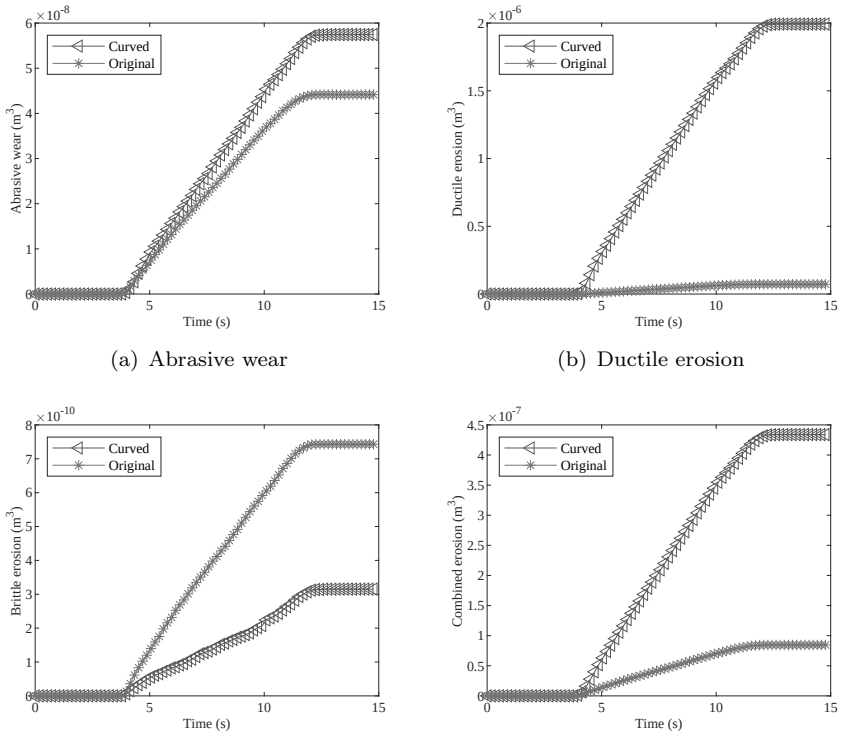

(a) Abrasive wear (b) Ductile erosion

(c) Brittle erosion (d) Combined erosion

FIGURE 6.23: Sum of wear across wear plate for both the new curved plate and the original flat plate

Figure 6.24(a) shows the total global collisions, G_k, counted across the curved and original wear plates. A considerable increase in collisions is seen for the curved plate to 144k collisions. This was increased from 7.2k collisions for the original plate design. For a comparison to be effective between the two different designs however the mesh must be comparable, at this time it is suggested to do this using the particle/element ratio. This correction is suggested using the value of the relevant simulation as shown in Equation 6.6 to create an effective global collision, G_k^*, value for a simulation where both have an effective value of $R = 1$. Using this the global effective collision count for the curved plate reduces to 109k effective collisions and the flat plate reduces to 5.3k effective collisions. Results using this recalculation are shown in Figure 6.24(b)

$$G_k^* = G_k R \tag{6.6}$$

In this way the wear can be normalised using the effective collisions count to assess whether, per collision, the curved plate is increasing the amount of wear overall. This is shown in Figure 6.25. All models show a similar trend in the initial instance of wear where a spike can be seen as particles begin to impact the respective plates. This then

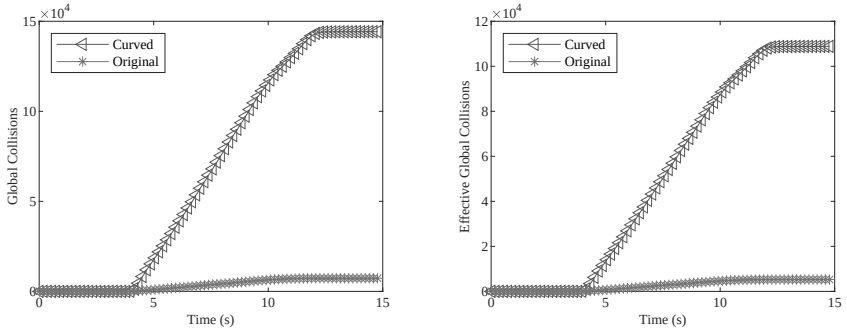

(a) Global Collisions (b) Effective Global Collisions

FIGURE 6.24: Global collisions across plate for both curved and original plate designs

continues until a constant value is reached for the simulations. The only model which this trend does not apply to is the ductile erosion model for the original plate design which does not have an initial spike, instead it increases from a lower value. Figure 6.25(a) shows the wear per collision for abrasion is decreased using the curved plate design. Figure 6.25(b) shows wear per collision for ductile erosion is increased using the curved plate design. Figures 6.25(c) and (d) show the wear per collision is decreased for brittle and the combined erosion models for the curved plate design.

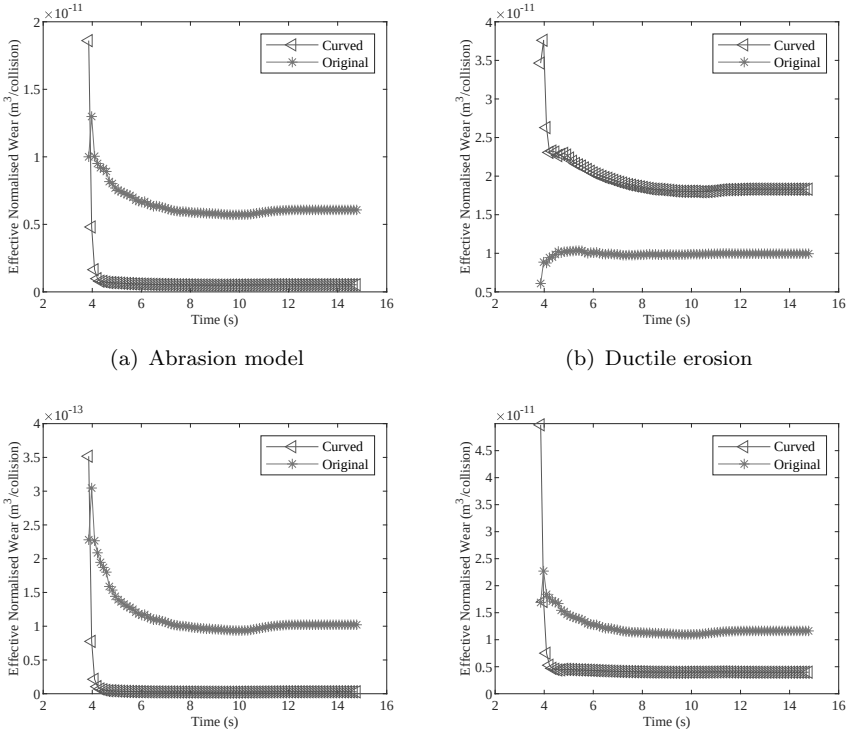

(a) Abrasion model (b) Ductile erosion

(c) Brittle erosion (d) Combined erosion

FIGURE 6.25: Effective normalised wear across the wear plate for both curved and original designs

Figure 6.26 shows the predicted energy transfer patterns for the first 8 energy models. E_1 and E_6 shows a similar wear patterns to the abrasion model E_6 which is to be expected as it is the energy version of the abrasion equation. Therefore suggesting E_1 creates a similar prediction to an abrasion model. E_2, E_3 and E_7 also show similar patterns to the abrasion equation where wear is expected in the impact zone, however now more energy transfer is expected to occur during the particle redirection similar to the combined erosion equation. E_4 shows a pattern similar to the ductile erosion model where high transfer is expected towards the run off zone of the particles, including a bias towards the positive z direction. E_8 also creates a similar pattern where the transfer is shown to be high in the run off zone of the particle but not to the same degree as E_4.

Figure 6.27 shows the energy models presented for DEM. An increased energy transfer can be seen for the curved design in all models except E_5 as shown in Figure 6.27(e). The largest increases in energy transfer can be seen in the E_2, E_3, E_4 and E_8 models.

Figure 6.28 shows the energy transfer models normalised using the effective global collisions calculated using Equation 6.6. This shows a decrease in the energy transfer per collision for all models using the curved plate design except for E_4 which shows an increase. All models show an approximately similar trend where a spike is present when the impacts begin except for the E_4 energy transfer model where it is seen to increase until it becomes constant. All models converge to an approximately constant value after a period of time inside the simulation.

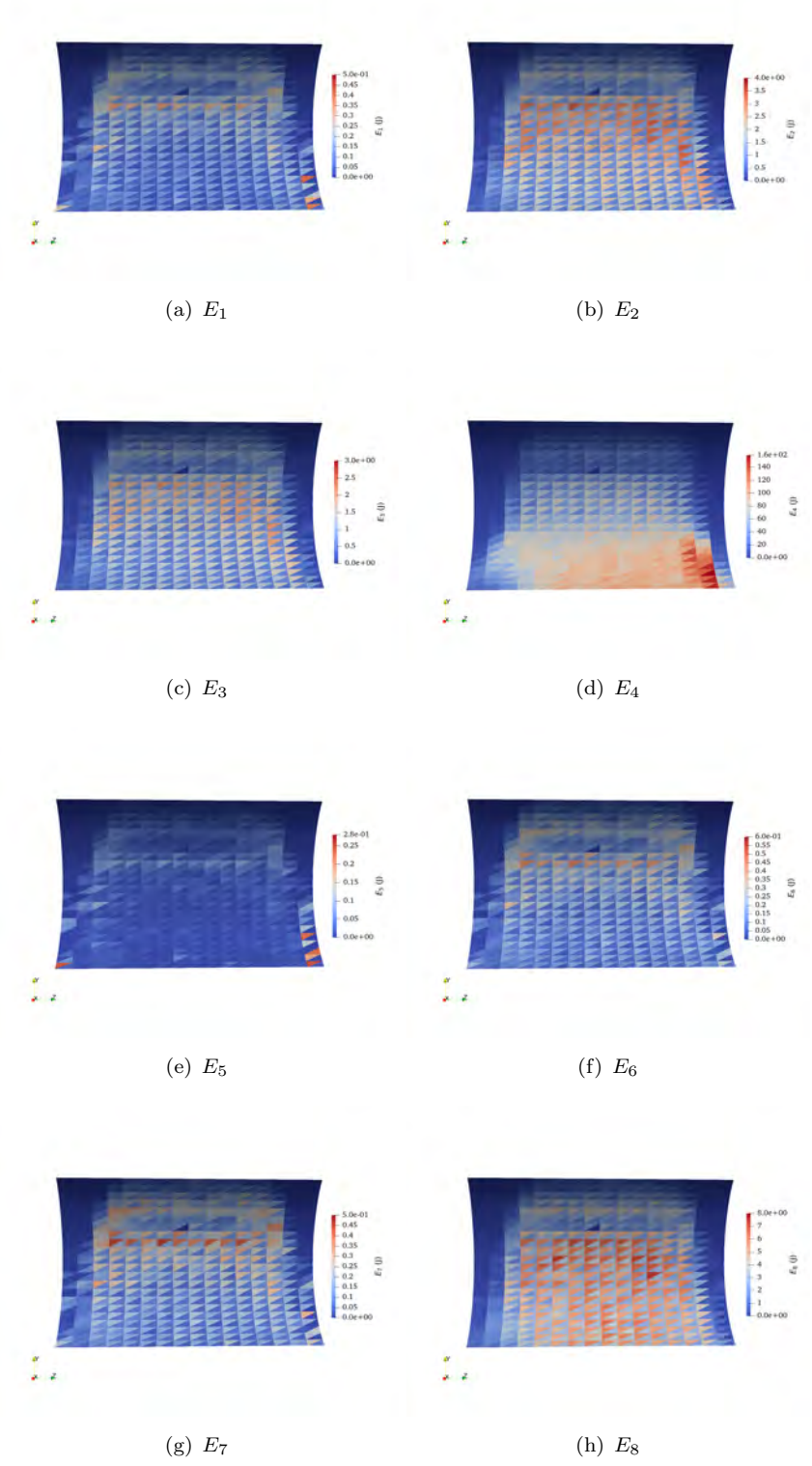

(a) E_1 (b) E_2

(c) E_3 (d) E_4

(e) E_5 (f) E_6

(g) E_7 (h) E_8

FIGURE 6.26: Predicted energy transfer model patterns on the curved plate design

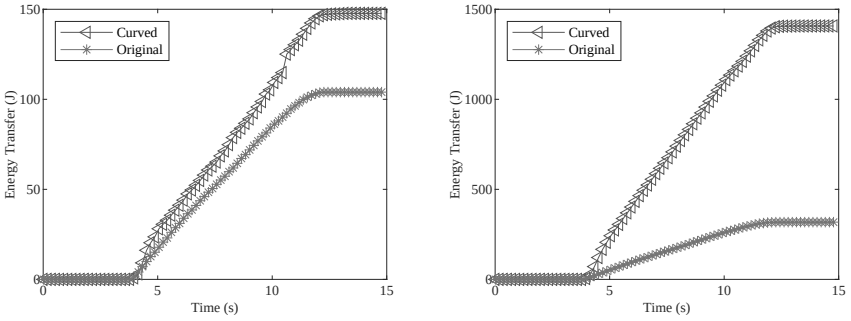

(a) E_1

(b) E_2

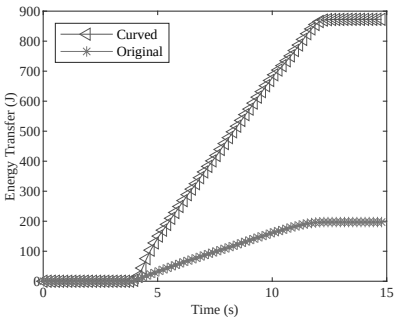

(c) E_3

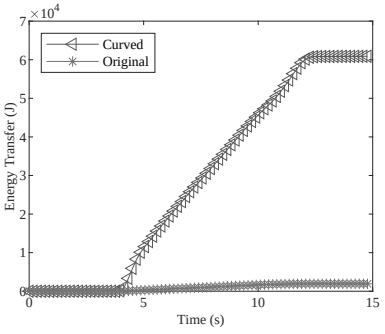

(d) E_4

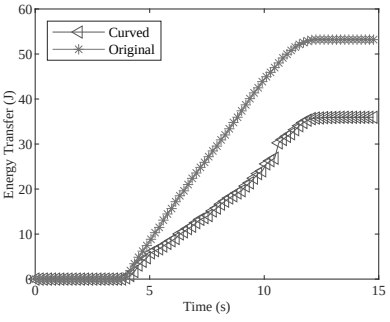

(e) E_5

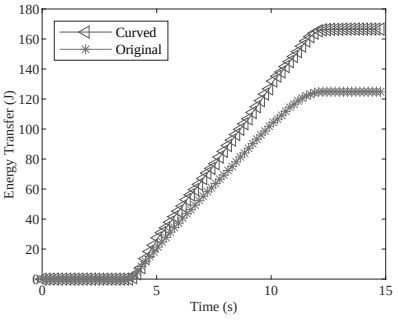

(f) E_6

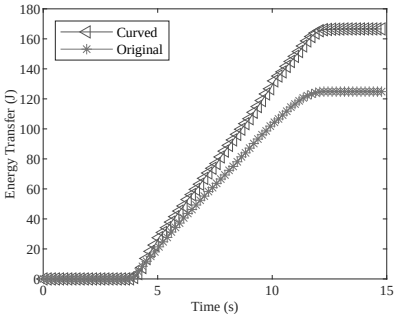

(g) E_7

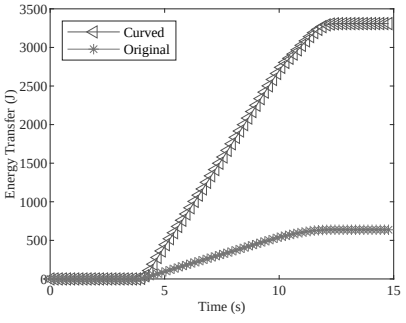

(h) E_8

FIGURE 6.27: Sum of energy transfer across the plate for both curved and original designs

6.8.3 Findings

The study of the effects of a constant radius curved plate design has been studied using both established wear models and the energy transfer models which were presented in

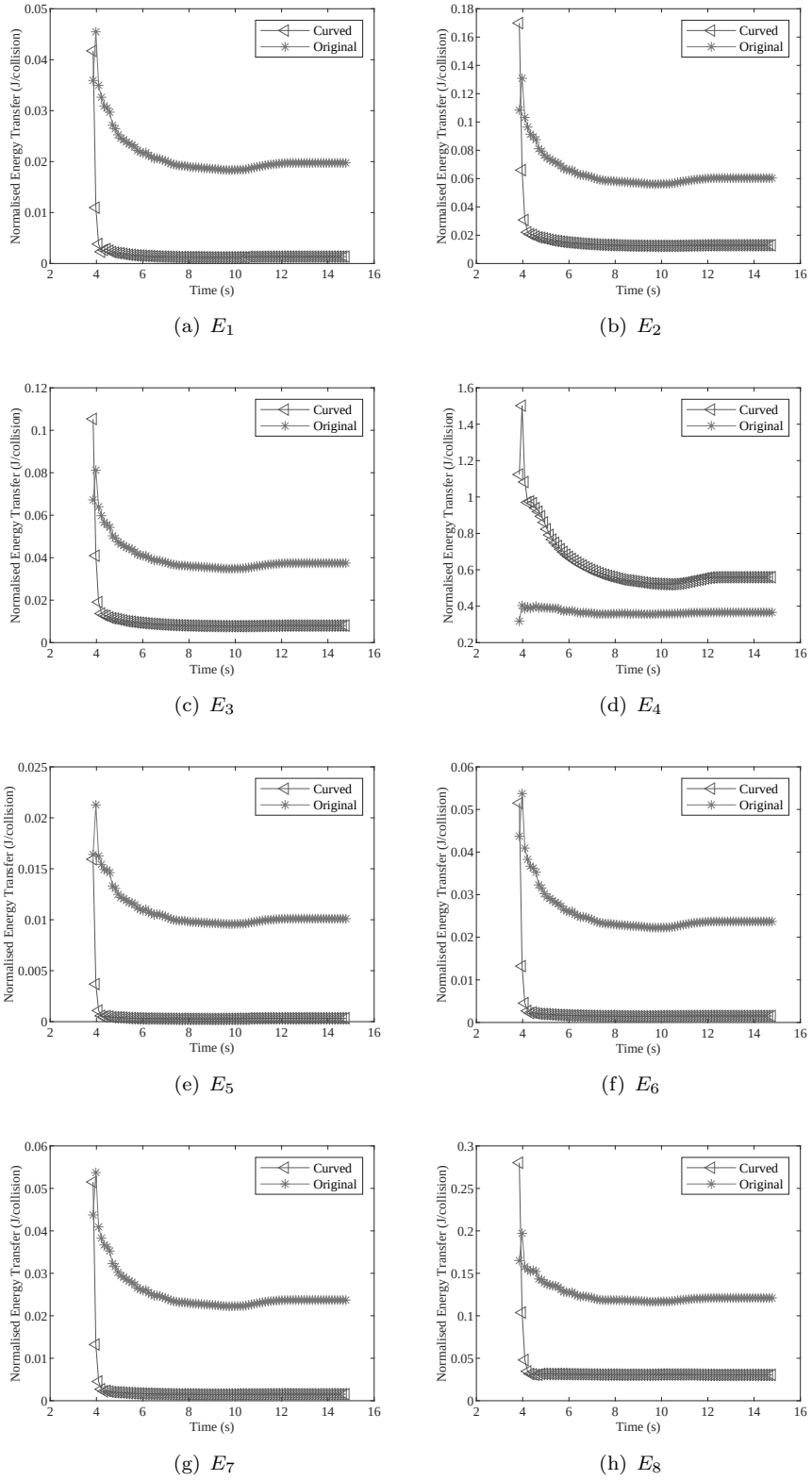

(a) E_1 (b) E_2

(c) E_3 (d) E_4

(e) E_5 (f) E_6

(g) E_7 (h) E_8

FIGURE 6.28: Effective normalised energy transfer for across the wear plate for both curved and original designs

Table 4.2. Predicted wear and energy transfer patterns can be seen in Figures 6.22

and 6.27 respectively. The first major finding is there is a general global increase in both wear and energy transfer which can be seen from Figures 6.23 and 6.27 with one exception, the brittle erosion model shown in Figure 6.23(c). A reason for this result can be determined by looking at the particle kinetics of the system shown in Figure 6.21 and comparing it to the original state of the particle kinetics shown in Figure 6.12(b). The overall impact of the collision is reduced as the particles are redirected gradually which considerably reduces the total brittle erosion calculated. The effect of this can be seen on the wear and energy transfer patterns in Figures 6.22(c) and 6.27(e). This redirection leads to a steady change in velocity across the plate, therefore leading to two possible outcomes. The plastic threshold velocity for the brittle erosion equation is not being met during redirection, and/or the redirection is not impactful enough to cause significant wear and energy transfer. For the energy transfer this can generally be seen in both pure normal component transfer equations Figures 6.27(a) and (e). This naturally leads to a logical conclusion that the ductile erosion would be expected to increase (i.e. tangential only transfer equations), and this can be seen to be the case as shown in Figure 6.23(b), where it is seen to increase considerably.

However while wear and energy transfer is generally shown to increase globally, the wear/energy transfer per collision is generally shown to decrease, with the exception of the ductile erosion model and energy model E_4. This energy model can be found in the literature also, where it was used to replicate the wear inside ball mills and represent ductile erosion [114]. Here it shows a very similar behaviour as the ductile erosion model, c.f. Figures 6.22(b) and 6.26(d).

The global collision count is also seen to increase considerably as shown in Figure 6.24. Part (a) shows the original global collision values where there is approximately 20x the number of collisions for the curved design. Part (b) shows the method which was theorised to make the simulations more comparable to each other as the particle/element ratios are not equivalent (although they are similar in this case). This method suggests using their respective ratios to create an effective collision value for an imaginary simulation of $R = 1$ to allow comparison. This showed the curved plate had an effective global collision value approximately 20.5x higher. This is quite a small difference as the element sizes were kept close in order to make the simulations as comparable as possible.

Overall it can be concluded a curved plate would generally decrease the abrasion per collision of a particle however it would increase the number of collisions considerably which would in turn cause greater wear than the original wear plate design. This would be especially true for wear and transfer mechanisms which are tangentially dominant such as ductile erosion. This could be improved by further study of curved plate designs. It also highlights how a different design may decrease the wear per collision but could

increase the number of collisions by an order of magnitude thereby introducing further wear and increasing the prevalence of a secondary wear mechanism, ductile erosion in this case. However, the reduction in the brittle erosion wear mechanism can also clearly be seen, curved chutes could be an effective design change for systems concerned primarily with brittle erosion.

Chapter 7

Coal Injection Lance

The coal injection lances are located on the blast furnace and were selected as the second industrial case study in this project. These experience regular wear due to the granulated coal which they process and the harsh conditions under which they operate. This application allowed assessment of how effective an uncoupled fluid flow implementation in a DEM framework can be. It also provided a good contrast of wear style from the previous case study. The effects of changing designs on predicted DEM wear also builds on the work in previous case studies.

7.1 Introduction

Blast furnaces are used to smelt material and produce metals, iron in this case, a schematic of which can be found in Figure 7.1(a) [130]. Granulated coal with an approximate 1 mm diameter is used and is injected at the bottom of the furnace as shown in Figure 7.1(b). This is done using preheated air between 900 - 1200°, which forces the granulated coal into the furnace. Naturally with the conditions of the coal injection lance wear is to be expected and it is the cause of this wear which is to be investigated here.

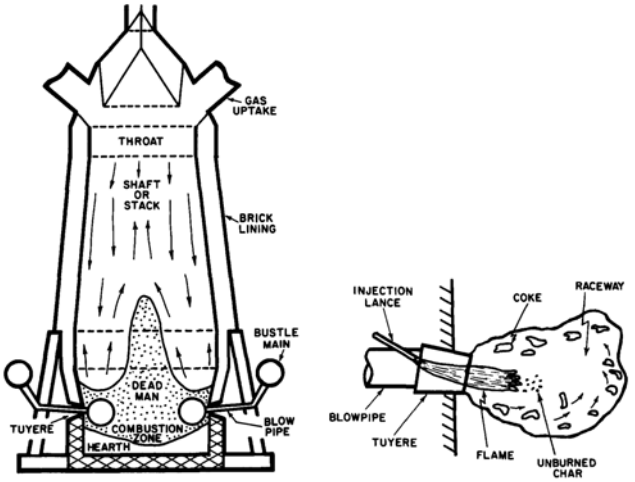

(a) Blast Furnce (b) Tuyere

FIGURE 7.1: Schematic of blast furnace and coal injection lance operation as presented by Hutny

7.1.1 Failures

Figure 7.2 shows the images provided of the lance failure which were to be investigated. Figure 7.2(a) shows failure 1, which is the area of interest. A worn area can be seen towards the threaded end of the lance. The aim was to determine the lance features which cause this wear and determine if changes in design would decrease it.

A second failure is also shown in Figure 7.2(b). It shows a split along the length of the lance, along the outside of a bend. The exact specification of this bend is unknown however the bend is thought to be the main cause of this failure.

7.1.2 Variables

In the lance there are a number of design variables which could alter flow, causing flow disruptions, and could be possible causes of wear. The two main variables are (i) the

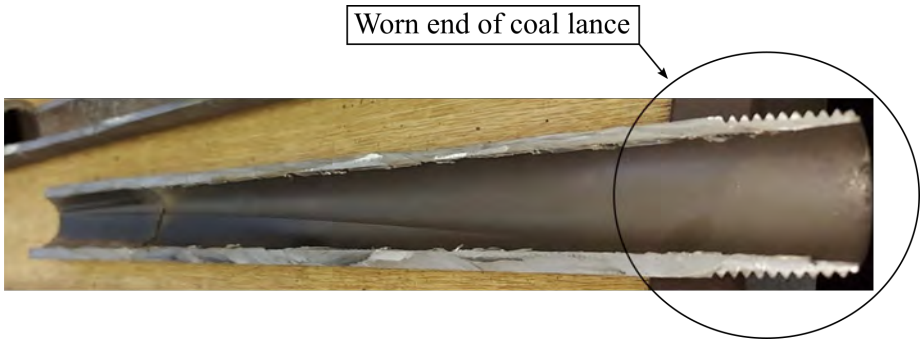

(a) Failure 1

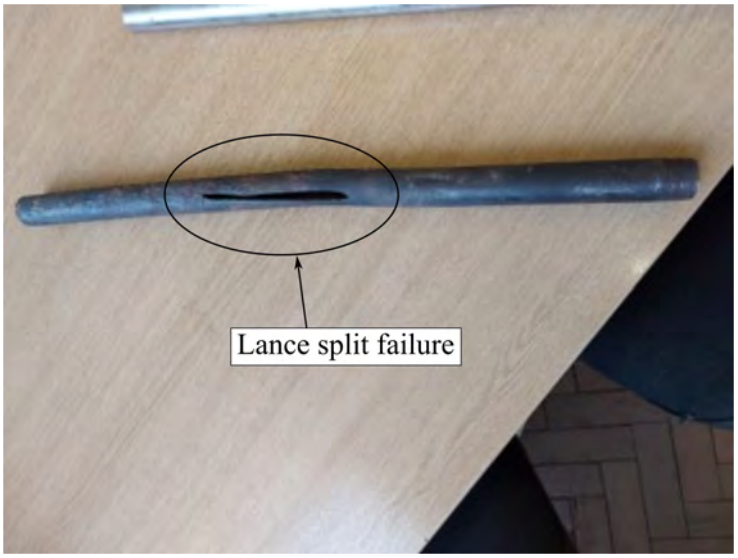

(b) Failure 2

FIGURE 7.2: Coal injection lance failure images

gap caused by the threading of the lance to the main body and (ii) the reduction in diameter from the main body to the lance.

These two variables were investigated and the effect of each individual change examined. This created three natural cases. Case 1 being the original case presented where there is a gap and reduction in diameter as shown in Figure 7.3(a). Case 2 being the removal of the gap created by the thread but keeping the reduction in diameter as shown in Figure 7.3(b), and case 3 being the removal of the reduction in diameter but retaining the gap as shown in Figure 7.3(c).

The failure time is generally measured in the amount of coal processed. The majority of failures occurring at approximately 3500 tonnes of coal. With 4000 tonnes being the expected mass of coal to be processed. However, the main aim of this work is to study the effect of design features on the wear, precise failure times are of less interest in this case.

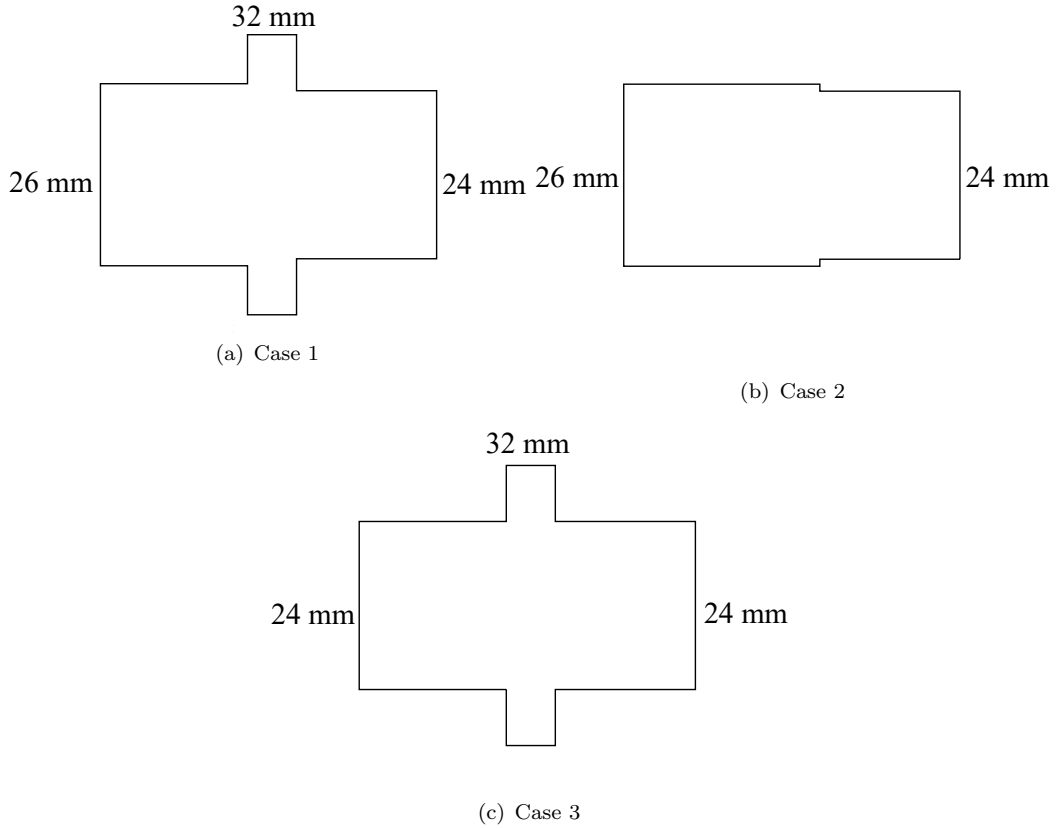

(a) Case 1

(b) Case 2

(c) Case 3

FIGURE 7.3: Coal injection lance cases 1, 2 and 3

Figure 7.2(b) shows a split along the lance. The cause of this is suspected to be the bend in lance, therefore a study shall also look at 2 cases with varying bends. The first shall be case 4 where a slight bend in the lance is introduced and the second shall be titled case 5 where a severe bend is introduced.

7.2 CFD

7.2.1 Operation

The operational parameters used for the lance can be seen in Table 7.1

TABLE 7.1: Coal injection lance operational parameters

Parameter	Value
Mass flow rate (gas)	3.33 m^3/min
Mass flow rate (coal)	20 kg/min
Particle diameter	1 - 2 mm

The first step to assess the causes of wear inside the coal injection lance was to create a CFD simulation of the system. To begin this the calculation of the Reynold's number

inside the flow is needed. The Reynolds number is a function of density and the dynamic viscosity of the gas flow. Each of these, in turn, is a function of temperature, therefore the temperature of the air flow is needed. However, the exact temperature is unknown, however a general range for preheated air on injection is between 900 - 1200°C. Therefore 1000 °C was chosen as value to be used in the calculation shown in Equation 5.11. This provided a Reynold's number of 15660, thus establishing a turbulent flow regime is expected. Note, this is below the values often quoted for the drag crisis for spherical and irregular particles. Furthermore, the effective Reynolds number for a particle laden flow will decrease, as discussed in Section 5.2.3.2 and demonstrated in Equation 5.15 [126][118].

Using this information the next step was to create a 2D model to provide a basic understanding of the flow behaviour in the lance. Following this a 3D simulation provided further details and and was introduced into the DEM model. The application of a velocity profile in DEM is discussed and the method is presented in chapter 5.

7.2.2 Models

For modelling turbulent flows a turbulence model needs to be selected. The k-ω model developed by Wilcox was selected for use here as it is considered strong in the case of internal flows such as this case study [127][131][132].

7.2.3 Mesh Sensitivity

As with all CFD studies a mesh sensitivity study needs to be carried out to understand the effect of the parameters and determine a point at which accuracy is no longer mesh dependent. However, in this case there is the secondary consideration importing the FE mesh into the DEM program in 3D. Unfortunately, this secondary consideration comes at the cost of reduced accuracy in the CFD simulation setup. The causes of this will be discussed further in chapter 9. The sensitivity study aims to limit this as much as possible.

7.2.3.1 Two Dimensions

The two dimensional version of the coal injection lance was created using SpaceClaim, the ANSYS internal model creator. A uniform mesh was created and refined based on real lance dimensions. The reason for using a uniform mesh is for easier importing into the DEM program, avoiding empty cells when using a more locally refined mesh. It is

accepted that this is a less efficient method of meshing this geometry. Figure 7.4 shows the meshes displayed in Table 7.2.

TABLE 7.2: 2D mesh sensitivity settings

Ref	Mesh Size	Nodes
1	5 mm	3882
2	2.5 mm	13312
3	1 mm	69248
4	0.5 mm	293625
5	0.25 mm	1163231

Figure 7.4 shows the velocity magnitudes and the y component of the velocity calculated using the mesh refinement. As can be seen the free stream velocity is calculated as approximately 122.05 ms^{-1} with a coarse 5 mm mesh and does not vary with mesh refinement. However, there is clearly variation in the y component of the velocity. This behaviour is picked up by the coarse mesh at 5 mm and with increased mesh refinement it is resolved more clearly while also showing increasing predicted y velocities. This appears to show that the restriction in the flow does not appear to converge to a final solution with mesh refinement, so this behaviour cannot be considered mesh independent at 0.25 mm.

7.2.3.2 Three Dimensions

Figure 7.5 shows the velocity profiles used for the three initial case studies of the coal injection lance.

7.3 DEM Set Up

Design drawings were obtained for the coal injection lance model for case 1, as shown in Figure 7.3(a). This model was then modified for the relevant cases as shown in Figure 7.3(b) and 7.3(c). The mesh along the lance Section of interest was discretised as shown in Figure 7.6 for the purpose of the DEM simulation. This discretisation was used across all the cases for the model used which resulted in a particle/element ratio of $R = 0.308$.

Figure 7.7 shows bent lance cases 4 and 5. They each used equivilant mesh sizing as was used for the three straight lance cases as shown in Figure 7.6. Case 4 shows a slight bend in lance, while case 5 represents a more severe bend.

The FDM cube for the velocity profile application was constructed using the values shown in Table 7.3. This application, with many elements, highlighted an issue using

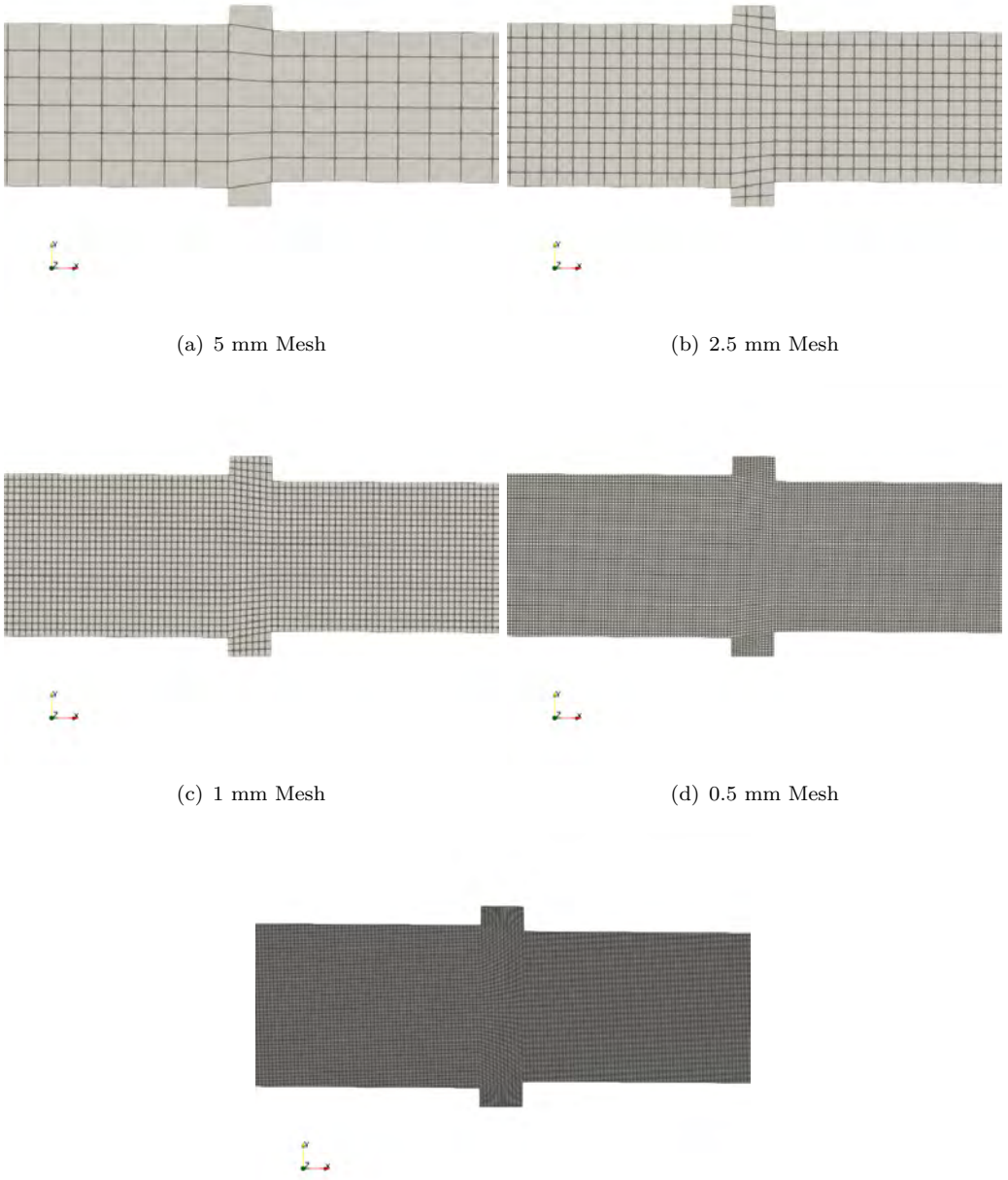

(a) 5 mm Mesh

(b) 2.5 mm Mesh

(c) 1 mm Mesh

(d) 0.5 mm Mesh

(e) 0.25 mm Mesh

FIGURE 7.4: Meshes used in the 2D mesh sensitivity study

the FDM method in this fashion, namely the time it took to generate the FDM cube list (1 - 3 days). This will be discussed in more detail in chapter 9 regarding the velocity profile implementation.

Gravity was ignored throughout the DEM simulation as the effect was determined to be negligible. There were some issues with force models due to the spawn location of particles inside the velocity profile. An issue which will also be discussed in chapter 9.

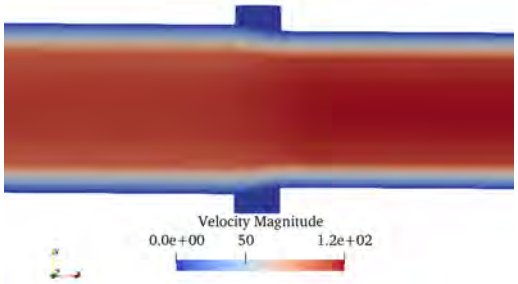

(a) 5 mm Mesh

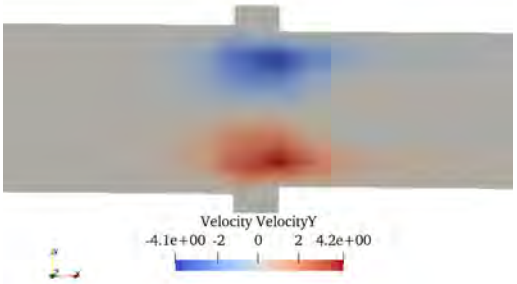

(b) 5 mm Mesh Y Component

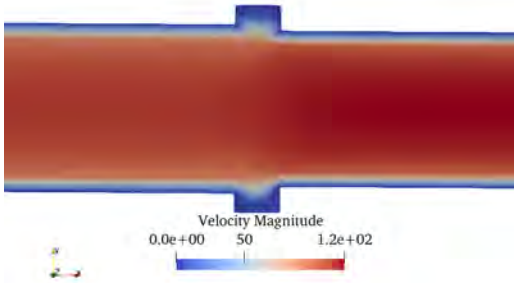

(c) 2.5 mm Mesh

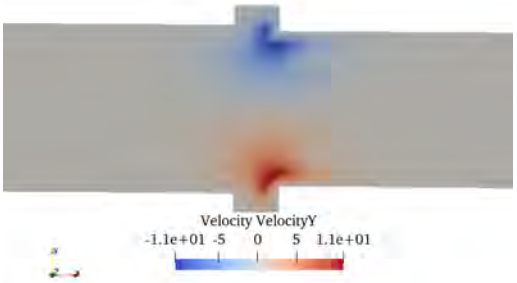

(d) 2.5 mm Mesh Y Component

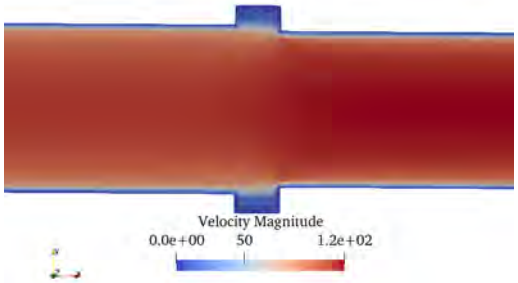

(e) 1 mm Mesh

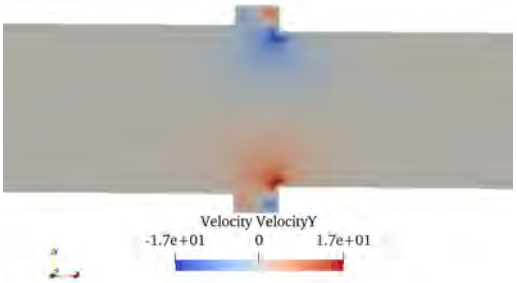

(f) 1 mm Mesh Y Component

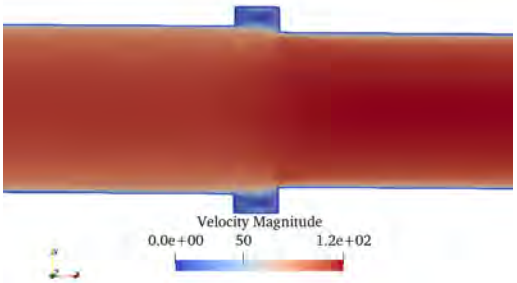

(g) 0.5 mm Mesh

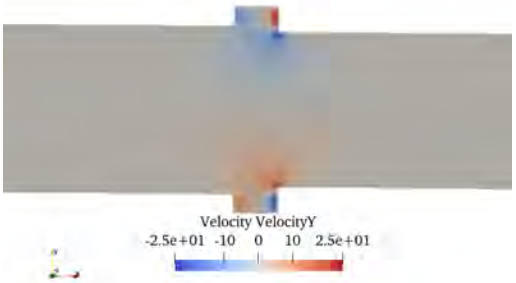

(h) 0.5 mm Mesh Y Component

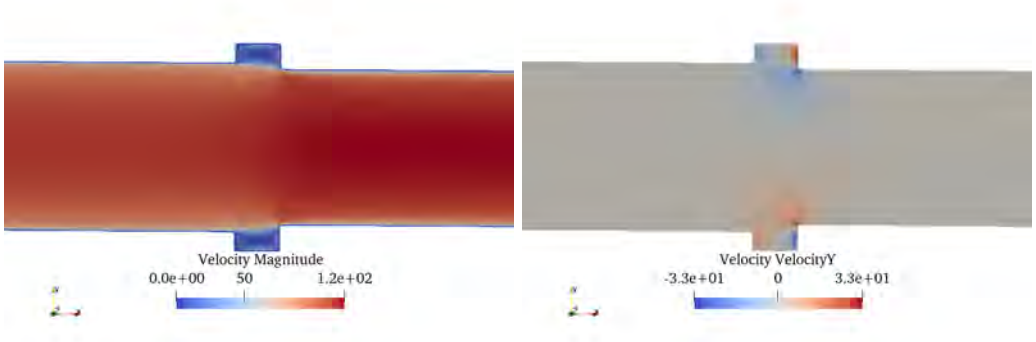

(i) 0.25 mm Mesh (j) 0.25 mm Mesh Y Component

FIGURE 7.4: Velocity magnitudes and Y component for each 2D mesh, note Y component scale bars are not identical

TABLE 7.3: FDM cube set up values

Parameter	Value
FDM Cube Length, $FDM_{max,x}$	0.020 m
FDM Cube Length, $FDM_{max,y}$	0.020 m
FDM Cube Length, $FDM_{max,z}$	0.70 m
FDM Cube Length, $FDM_{min,x}$	-0.020 m
FDM Cube Length, $FDM_{min,y}$	-0.020 m
FDM Cube Length, $FDM_{min,z}$	-2.250 m
Cubes, Δ_x	36
Cubes, Δ_y	36
Cubes, Δ_z	648
Number of cubes	839808

The DEM material parameters are shown in Table 7.4

7.4 DEM Wear Profiles Results

Figure 7.8 shows the simulation in progress for cases 1 to 3. One feature which is noted is the gap causing a disruption in the flow which appears to decrease the velocity of particles, in turn reducing the time it takes for the lance to process all the material spawned in the simulation. Case 3, shown in Figure 7.8(c), processes all the material in a shorter time than cases 1 or 2.

Figure 7.9 shows a cross-sectional view of the lance at the section which contains the features of interest. In general the velocity of the particles can be seen to increase in the flow in case 3 shown in Figure 7.9(c) in comparison to cases 1 and 2, shown in Figures 7.9(a) and (b).

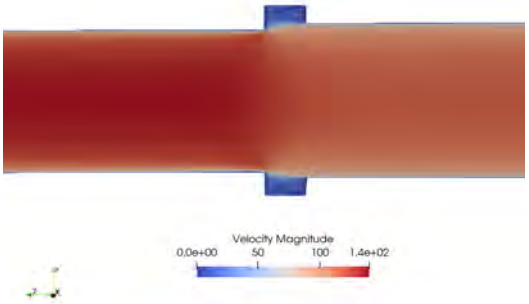

(k) Case 1

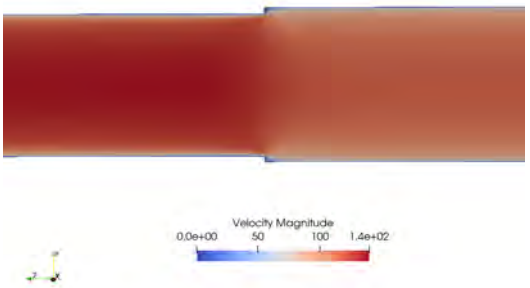

(l) Case 2

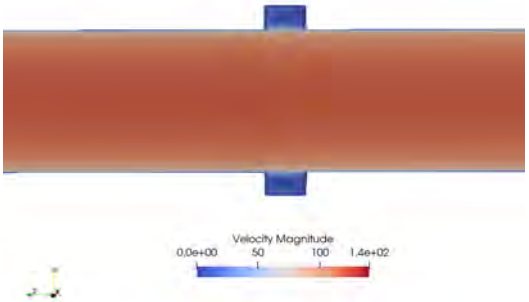

(m) Case 3

FIGURE 7.5: Velocity profiles for the coal injection lance cases

(a) Case 1

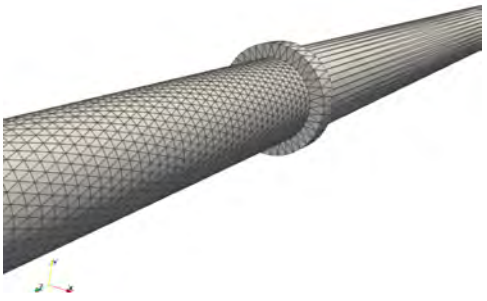

(b) Case 1 zoomed in

FIGURE 7.6: Coal injection lance mesh used on case 1

Figure 7.10 shows the wear profiles predicted using the abrasion model where particles travel in the positive z direction. Figure 7.10(a) shows in case 1 wear is predicted to occur at the threaded end of the lance and then decrease along the lance in the positive z direction. Qualitatively this matches the failure images provided in Figure 7.2(a). Case 2 shown in Figure 7.10(b) shows a similar wear profile however the wear appears to be

(a) Case 4 (b) Case 5

FIGURE 7.7: Models used inside DEM for bent lance case's 4 and 5

TABLE 7.4: Coal injection lance material parameters

Parameter	Value
Poisson Ratio	0.3
Particle Diameter	0.0005 m
Particle Density	1150 kg/m^3
Particle Spring Stiffness	16000 N/m
Coefficient of restitution	0.01
Archard Wear Factor (K)	0.001
Damage Coefficient	1
Sliding Friction Coefficient	0.8
Twisting Friction Coefficient	0.3
Twisting Damping	1.5
Rolling Friction Coefficient	0.3
Rolling Damping	1.5

increase in severity across the entire lance. Case 2 shown in Figure 7.10(c) shows an increased wear across the entire length, with a slightly more severe area at the threaded end.

Figure 7.11 shows the wear profiles predicted using the ductile erosion model. Figure 7.11(a) shows case 1 where wear is predicted to occur along the entire lance. Case 2 shown in Figure 7.11(b) shows an increased severity of wear along the entire lance, qualitatively more severe towards the end of the lance. Figure 7.11(c) shows case 3, which again shows wear across the entire lance, however, it appears considerably more severe towards the end of the lance.

Figure 7.12 shows the wear profiles predicted using the brittle erosion model. Figure

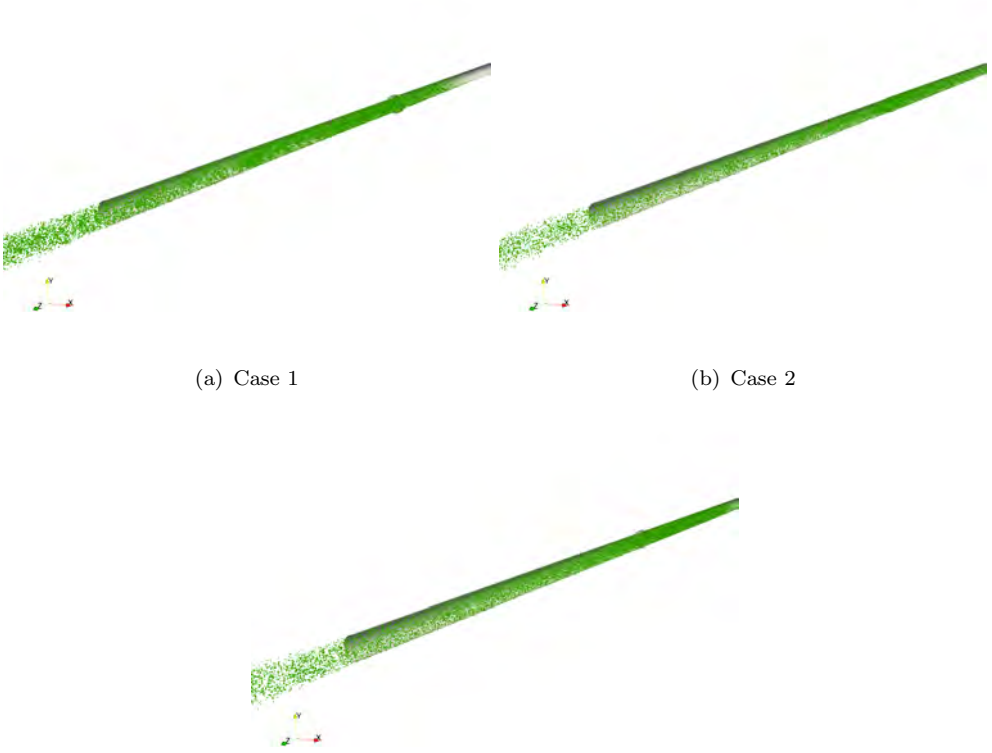

(a) Case 1

(b) Case 2

(c) Case 3

FIGURE 7.8: Full coal injection lance simulation showing particles in green

7.12(a) shows case 1 which predicts wear to occur towards the threaded end of the lance and decrease along the length in positive z direction until it is practically negligible. Case 2 shown in Figure 7.12(b) shows an increase in severity of the wear occurring at the threaded end of the lance and a slight increase along the length of the lance. Figure 7.12(c) shows case 3, which predicts wear along the entire length of the lance.

The energy transfer models can be found in appendix B where Figures B.3 - B.16 show the energy models E_1 - E_{14}.

Figure 7.14 shows the number of collisions on the lance for each of the cases. Figure 7.14 shows the number of collisions across the lance. Case 1, shown in Figure 7.14(a), predicts an increased number of collisions towards the threaded end of the lance with a reduction in the number of collisions in the positive z direction of the lance. Figure 7.14(b) for case 2 shows a similar pattern to case 1. Case 3, shown in Figure 7.14(c), shows an increased number of collisions along the length of the lance.

Figure 7.16 shows the mean wear of all elements for the circumference of the mesh plotted against the length of the lance. The abrasion model, case 1 (Figure 7.16(a)), shows a slight increase in wear in the initial elements from the threaded end at which

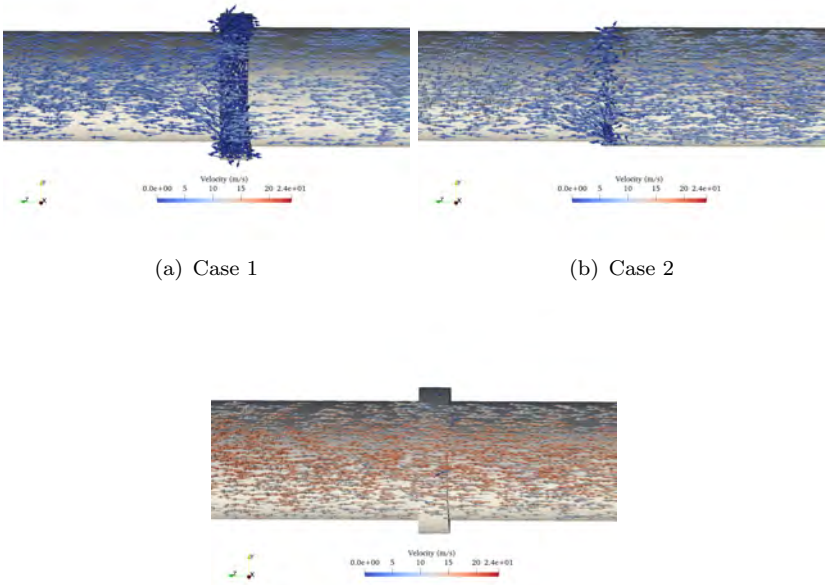

(a) Case 1 (b) Case 2

(c) Case 3

FIGURE 7.9: Cross section of lance at the investigated features where velocity vectors are represented through arrows which are orientated based on their direction

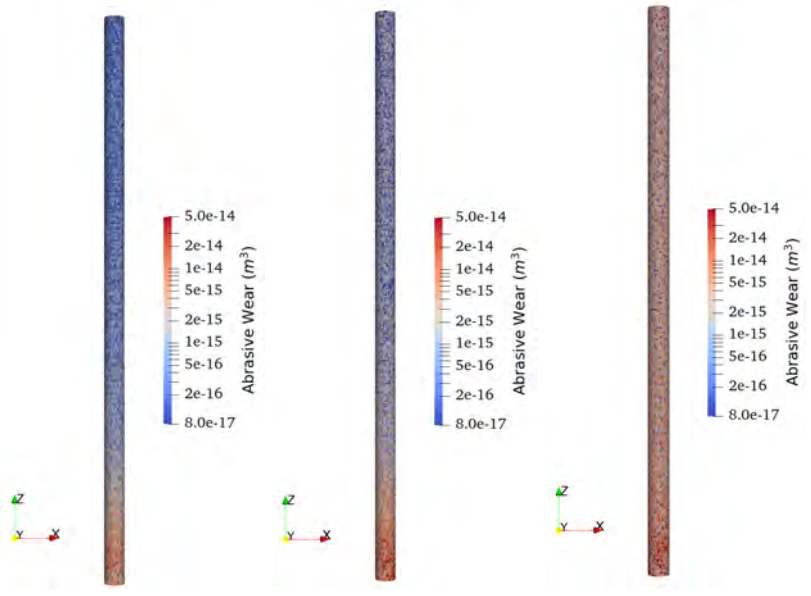

(a) Case 1 (b) Case 2 (c) Case 3

FIGURE 7.10: Abrasive wear pattern prediction on the cases for the coal injection lance with the bottom showing the threaded end and the top showing the tip of the lance

point the wear becomes close to constant along the length of the lance. This matches the qualitative result found in Figure 7.10(a). Case 2 shows an increased amount of wear at the threaded end of the lance, and this decreases gradually along the length of the

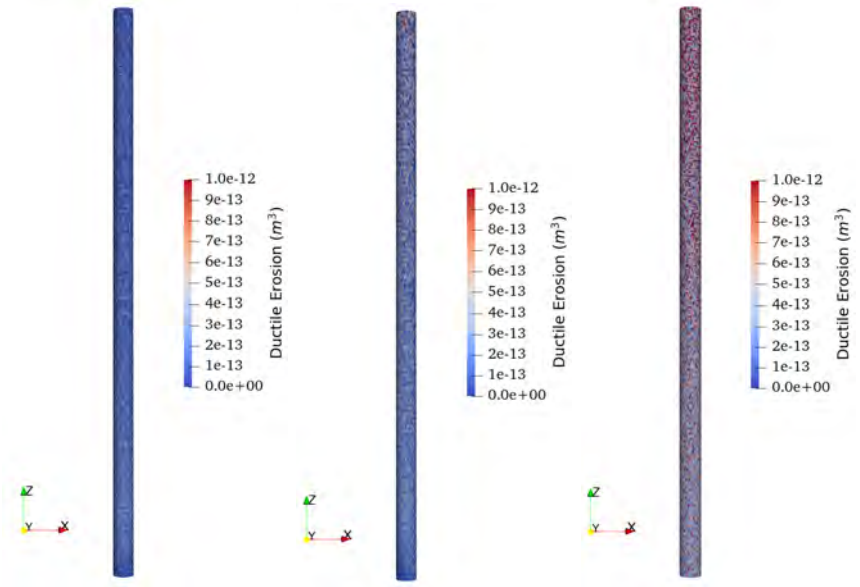

(a) Case 1 (b) Case 2 (c) Case 3

FIGURE 7.11: Ductile erosion wear pattern prediction on the cases for the coal injection lance with the bottom showing the threaded end and the top showing the tip of the lance

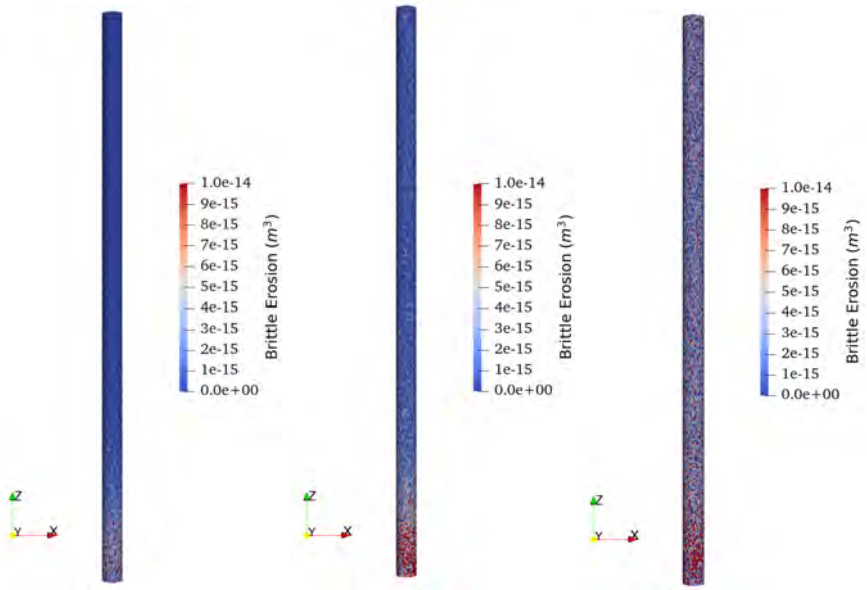

(a) Case 1 (b) Case 2 (c) Case 3

FIGURE 7.12: Brittle erosion wear pattern prediction on the cases for the coal injection lance with the bottom showing the threaded end and the top showing the tip of the lance

lance. Case 3 shows generally high wear across the entire length of the lance matching Figure 7.10.

Figure 7.16(b) shows the mean wear plotted for the ductile erosion model. Case 1 shows

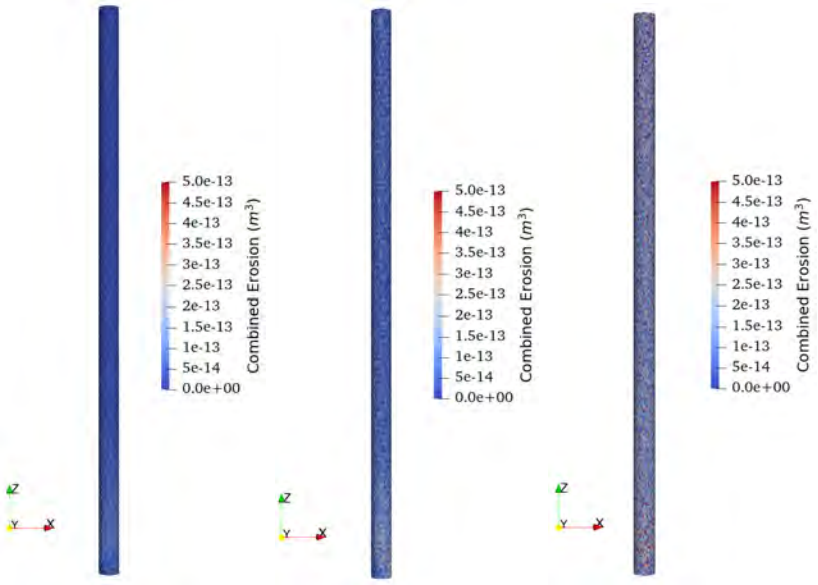

(a) Case 1 (b) Case 2 (c) Case 3

FIGURE 7.13: Combined erosion wear pattern prediction on the cases for the coal injection lance with the bottom showing the threaded end and the top showing the tip of the lance

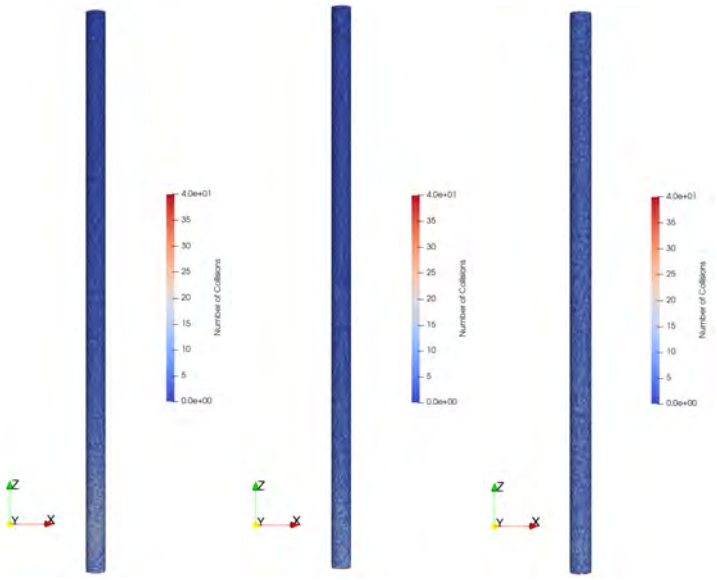

(a) Case 1 (b) Case 2 (c) Case 3

FIGURE 7.14: Number of collisions on the coal injection lance with the bottom showing the threaded end and the top showing the tip of the lance

a slight increase in wear towards the lance tip where particles leave the lance. Case 2 shows a further increase in wear at the lance tip. Case 3 shows a dramatic worsening of the wear along the entire length of the lance. These match the qualitative predictions found in Figure 7.11.

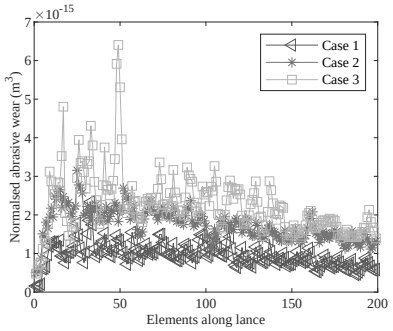

FIGURE 7.15: Mean number of collisions along the length of the coal injection from the left representing the threaded end, to the right representing the tip of the lance

Figure 7.16(c) shows the mean wear plotted for the brittle erosion model. In case 1 the wear at the threaded end of the lance is not considerable and remains approximately constant for the length of the lance. Case 2 shows a considerable increase in wear at the threaded end and then a gradual reduction along the length. Case 3 shows a similar pattern as seen in case 2.

Figure 7.16(d) shows the mean wear plotted for the combined erosion model. Mean wear is approximately constant along the length of the lance. Case 2 shows a general increase in wear, and case 3 shows another general increase in wear across the entire length of the lance.

Figure 7.17 shows the mean wear normalised against the mean number of collisions along the lance. For all models it can be seen the normalised/wear per collision increases from cases 1 to 2. This effect is largest for the brittle and combined erosion models while it is not significant for the ductile erosion model. From cases 2 to 3 an increase in normalised wear is seen for the ductile and brittle erosion models across the entire length. The abrasion and brittle erosion models show a slight increase but the increase does not appear as significant.

7.4.1 Extra cases

As an aside, the effect of a bend in the coal injection lance was also studied. This was done in an attempt to capture the effects of a large design change in the system. For the sake of brevity only the results are presented here.

Figure 7.18 shows the abrasion model prediction for cases 4 and 5. This shows an area of wear occurring on the back side of the bend in case 4, Figure 7.16(a). Case 5, Figure 7.16(b), shows a considerable worsening of this wear on the back side of the bend. This matches the failure seen in Figure 7.2(b). Figure 7.19 shows the ductile erosion models wear prediction. The pattern predicted is similar to the abrasion prediction, although

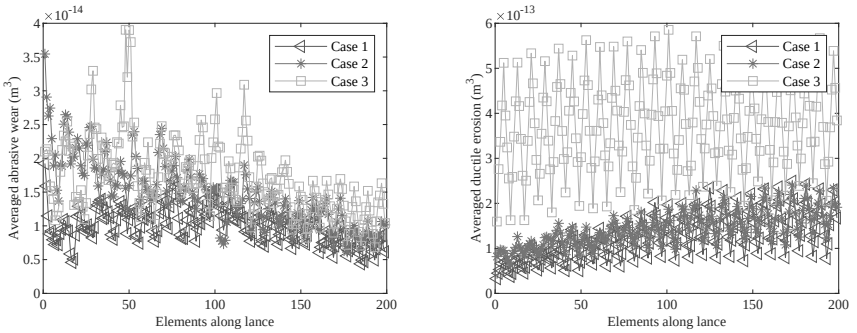

(a) Abrasion model

(b) Ductile erosion model

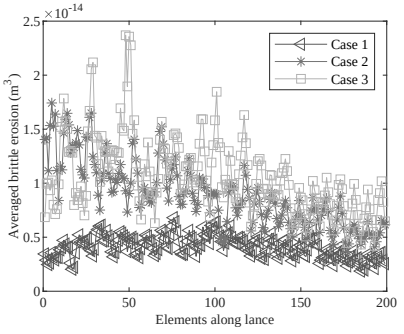

(c) Brittle erosion model

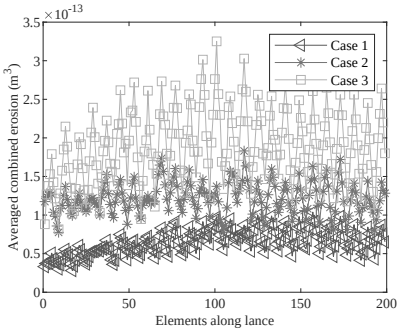

(d) Combined erosion model

FIGURE 7.16: Mean wear predicted using established models along the length of the coal injection from the left representing the threaded end, to the right representing the tip of the lance

there is a slight difference in the length of the wear zone, it being extended for the ductile erosion model. The brittle and combined erosion model, Figure 7.20 and Figure 7.21, shows a similar wear pattern predictions as well, with the brittle model being closer to the abrasion model and the combined model closer to the ductile model. Overall, each model predicts a same area for high wear. It is also predicted to be considerably worse than the wear towards the threaded end of the lance.

7.5 Findings

Figures 7.10, 7.11, 7.12 and 7.13 show the qualitative predictions from the wear models for the initial 3 cases studied. From these the mean wear was plotted along the length of the lance as shown in Figure 7.16, which were combined with an equivalent collision plot, Figure 7.15, to create a normalised mean wear along the lance to determine the effects of the design changes in these cases. The first finding is the abrasion and brittle erosion models predict wear which matches the real world industrial failures found in Figure 7.2(a). In contrast, the ductile erosion model predicted wear to occur toward the

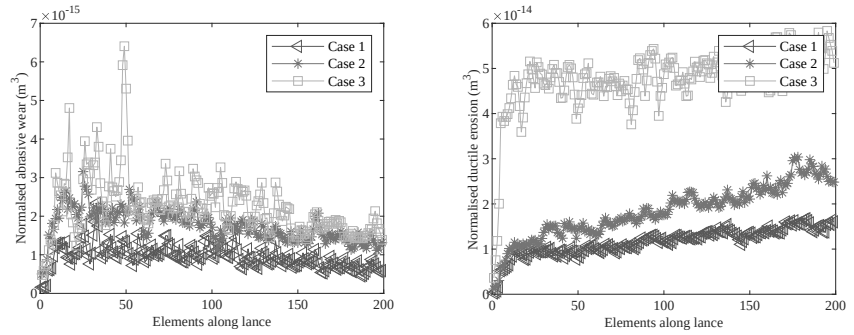

(a) Abrasion model

(b) Ducile erosion model

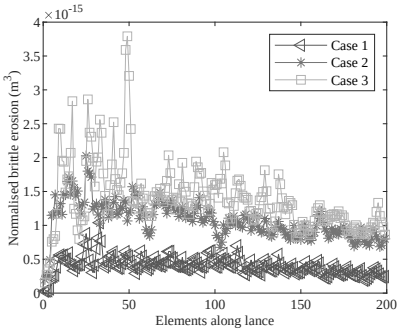

(c) Brittle erosion model

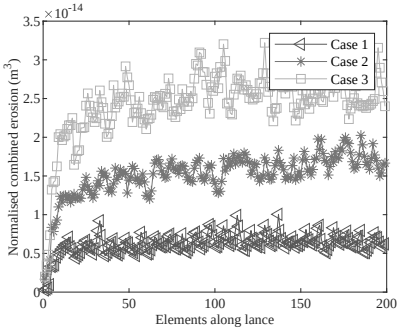

(d) Combined erosion model

FIGURE 7.17: Normalised wear predicted using the mean wear along the length of the coal injection from the left representing the threaded end, to the right representing the tip of the lance

lance tip where particles left the system. This does not mean the model is inaccurate, it means the wear occurring here is probably not due to ductile erosion mechanisms.

The cause of this wear in case 1 appears to be the impacting of particles after the gap created by the threads. This can be seen clearly in the qualitative collision plot in Figure 7.15. With the removal of this gap the effect is predicted to be worse. The gap and/or diameter reduction appears to cause a flow disturbance which picks particles up and places them into the free stream. This is theorised to reduce the abrasive wear when compared to case 2. However, it appears to come at the consequence of slowing the particles, which in of itself would also decrease the total wear. In case 2 this flow disturbance appears to be less dramatic as can be seen in Figure 7.9(a) and (b).

In case 3 the gap is still present however the diameter of the lance remains the same. This suggests the constriction is the cause of the flow disturbance and is causing the particles to be pushed into the free stream flow. Keeping diameter the same increases the particle velocity in the free stream, however it also appears to come at the cost of an increase in wear along the entirety of the lance and an increase in wear per collision as seen in Figures 7.9 and 7.17.

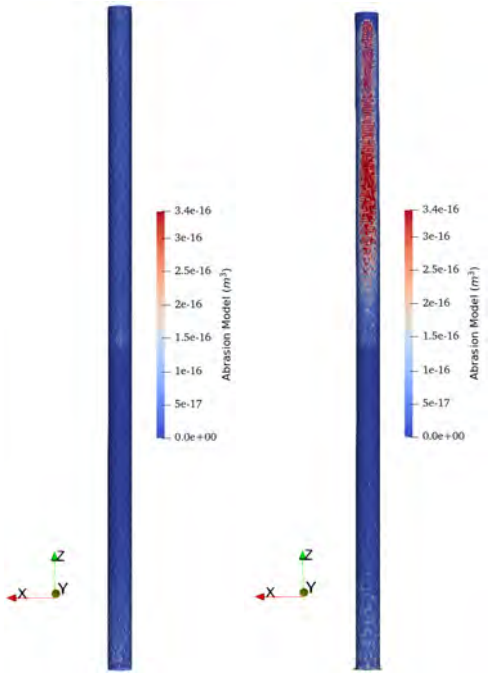

(a) Case 4 (b) Case 5

FIGURE 7.18: Wear pattern predicted by the abrasion model for the bent coal injection lance models

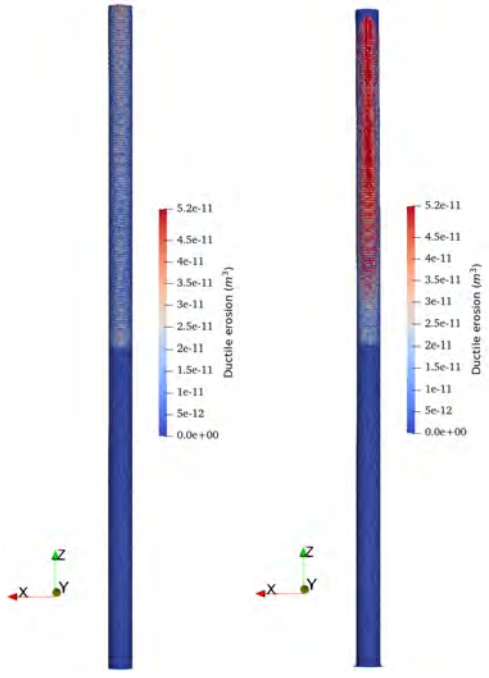

(a) Case 4 (b) Case 5

FIGURE 7.19: Wear pattern predicted by the ductile erosion model for the bent coal injection lance models

Two extra cases were simulated to assess the effect of a much larger design change to the lance and to test the FDM application. The qualitative results of this can be seen in

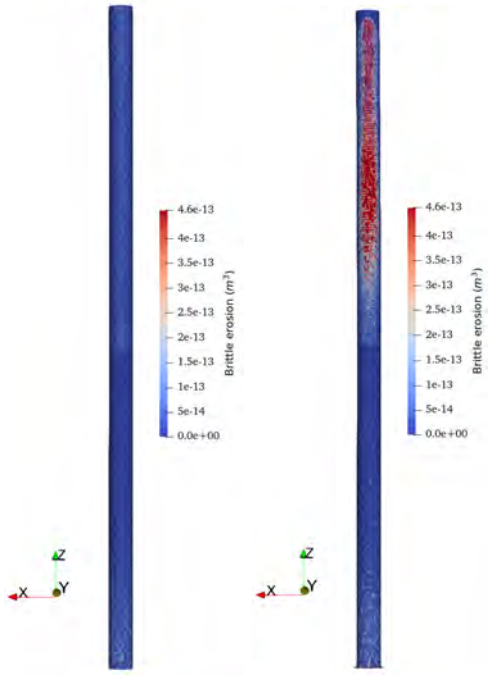

(a) Case 4 (b) Case 5

FIGURE 7.20: Wear pattern predicted by the brittle erosion model for the bent coal injection lance models

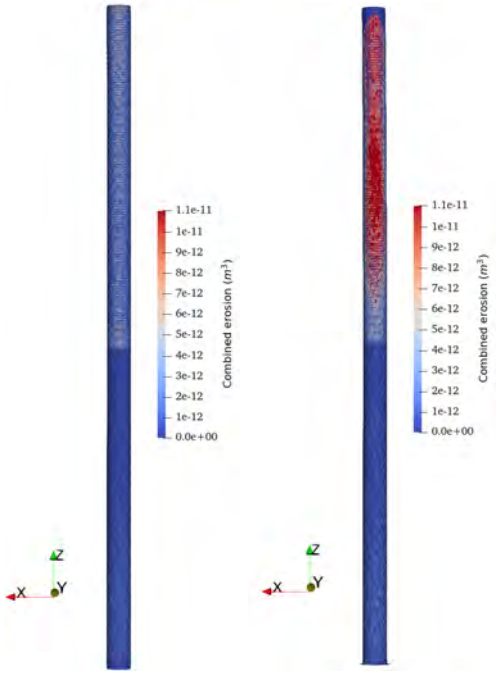

(a) Case 4 (b) Case 5

FIGURE 7.21: Wear pattern predicted by the combined erosion model for the bent coal injection lance models

Figures 7.18, 7.19, 7.20 and 7.21. An area of severe wear forms on the back side of a bent lance which increases in severity as the bend decreases in radius. Figure 7.2(b) shows this

failure on the industrial application, qualitatively predicted by DEM. All wear models predicted the form of this failure, with slight variations. This would suggest this mode of failure is extremely severe, with all wear mechanisms acting at the same time. This is confirmed by comparing the failure images, while there is wear at the threaded end it is not quite enough to cause failure, however once the bend is established it appears to failure rapidly.

Chapter 8

Parameters

The final case study chapter will investigate the effects of parameters on the energy transfer, wear, damage and time to failure predictions inside DEM. The first case is the effect of mass flow rate, as all previous studies have kept this constant. The second section will look at the variation of the coefficient of restitution. This parameter is a major part of the energy dissipation inside a DEM system therefore its effect on energy transfer and wear predictions is investigated. Finally when calculating the time to failure from wear calculations using an abrasion model or an E_6 transfer model, the damage rate has to be accelerated in order to assess a system based on the MEF criterion, however, what is the effect of increasing both damage coefficient and particle radius?

8.1 Mass Flow Rate

An interesting feature demonstrated in wear modelling and energy transfer inside DEM is the behaviour of multiple particles in a system. This has been seen in Chapter 4 when the wear and energy models were studied depending on impact angle. Different behaviours were seen for both a single particle impact and multiple particle impacts. This is the so-called multi-bodied effect and it begs the question how the variation in the number of particles being spawned in a model affects the outputs, or in other words how is the wear and energy transfer affected by the mass flow rate of material?

8.1.1 Methodology

For this study, an angled plate is used in line with previous studies in Chapter 4. Particles were spawned above the plate and allowed to drop under gravity at varying mass flow rates. The rates to be studied were: 1 kg/s, 2 kg/s, 3 kg/s, 4 kg/s, 8 kg/s, 16 kg/s and 24 kg/s. The material parameters used are shown in Table 8.1.

TABLE 8.1: DEM parameters used for studying the variation of mass flow rate

Parameter	Values
Spring stiffness	8000 N/m
Coefficient of restitution	0.3
Particle radius	0.005 m
Particle density	8000 kg/s
Sliding Friction Coefficient	0.8
Twisting Friction Coefficient	0.3
Twisting Damping	1.5
Rolling Friction Coefficient	0.3
Rolling Damping	1.5

Figure 8.1 shows the set up used for the simulation using the 4 kg/s spawn. A mesh discretisation of 2048 elements is used on a 0.5 m by 0.5 m square plate, leading to a particle/element ratio of $R = 0.64$. All other variables are kept constant throughout.

8.1.2 Results

Figure 8.2 shows the number of collisions across the plate. Figures 8.2(a) - (e), 1 - 8 kg/s, shows the development of the collisions increasing in the run off area for the particles. At 16 kg/s, Figure 8.2(f) the number of collisions in the impact zone increases considerably where it immediately begins to have a higher number of collisions than the run off area. This effect is increased with the final increase to 24 kg/s shown in Figure 8.2(g).

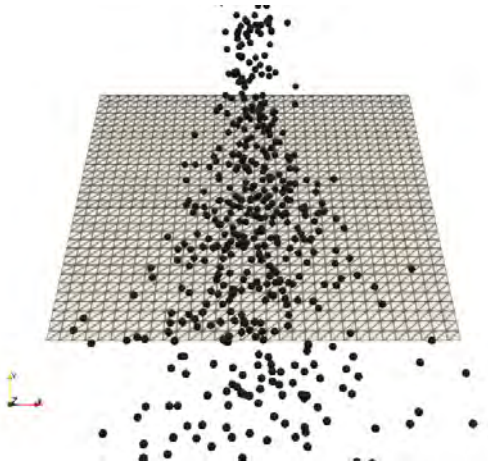

FIGURE 8.1: 45 degree plate simulation using a mass flow rate of 4 kg/s

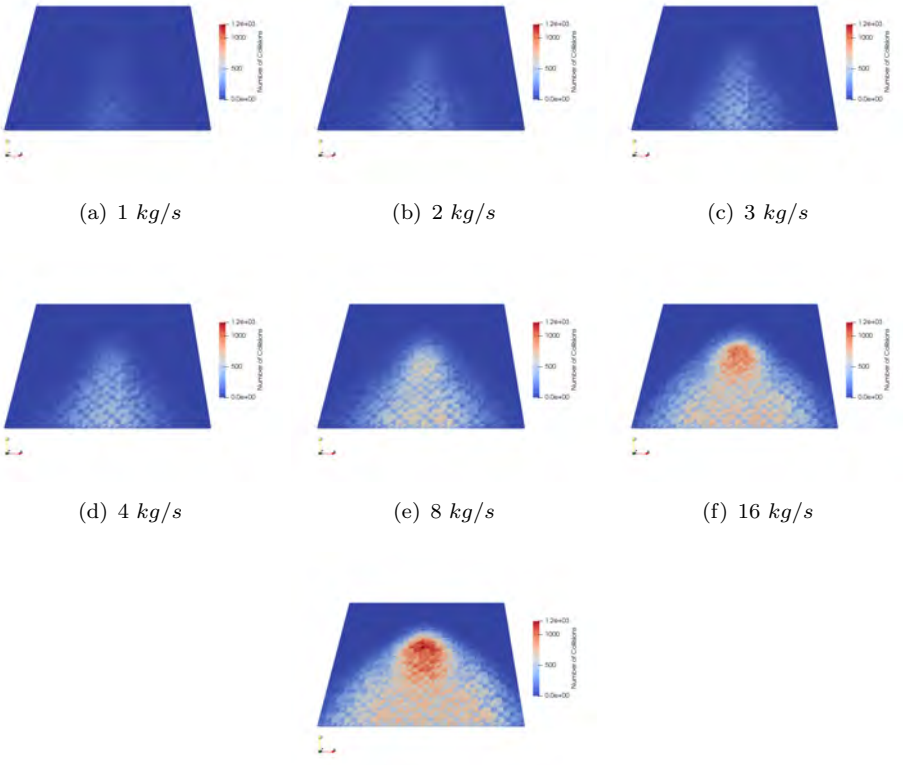

(a) 1 kg/s (b) 2 kg/s (c) 3 kg/s

(d) 4 kg/s (e) 8 kg/s (f) 16 kg/s

(g) 24 kg/s

FIGURE 8.2: Number of collisions across the plate predicted for varying mass flow rate

Figure 8.3 shows the wear patterns predicted using the abrasion model for varying mass flow rate. The initial wear can be seen to occur at the impact zone of the particles as shown in Figures 8.3(a) - (d). At an 8 kg/s rate, Figure 8.3(e), an arc can be seen to occur across the impact zone where the highest wear occurs. This is seen to increase in severity with further increases to mass flow.

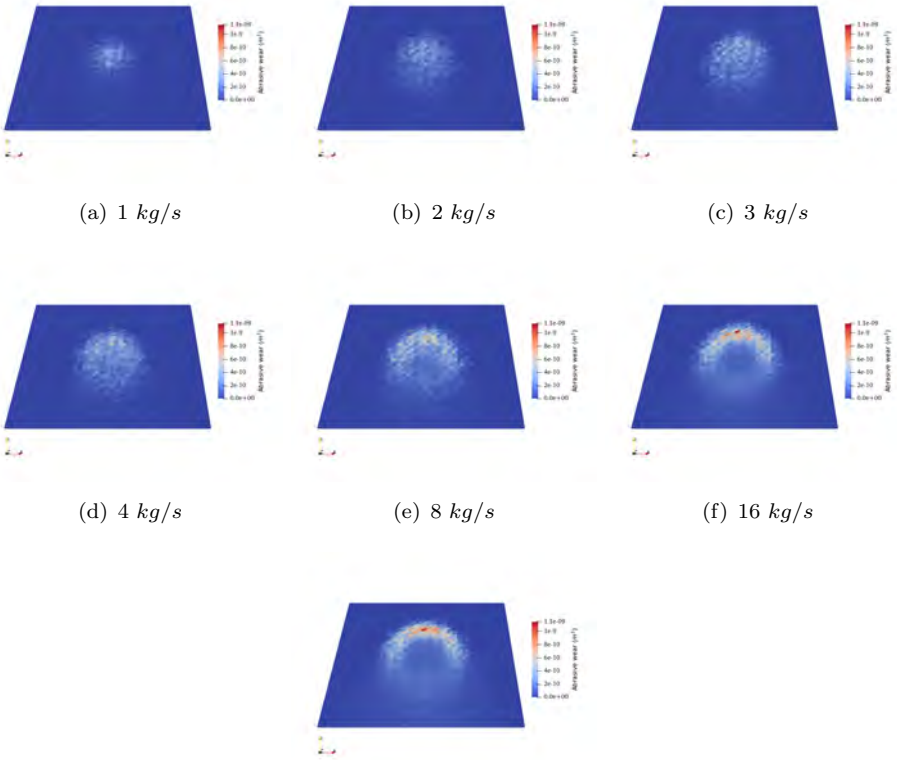

(a) 1 kg/s (b) 2 kg/s (c) 3 kg/s

(d) 4 kg/s (e) 8 kg/s (f) 16 kg/s

(g) 24 kg/s

FIGURE 8.3: Wear patterns predicted using the abrasion model for varying mass flow rate

Figure 8.4 shows the wear pattern predicted using the ductile erosion model. As has been shown previously with the ductile erosion model, wear is predicted to occur in the run off zone of the particles. It is predicted to increase in severity as the mass flow is increased, with the highest wear expected to occur at the lip of the plate. Interestingly at 16 kg/s it moves from a single severe wear area at the lip of the plate to two distinct zones as shown in Figure 8.4(f) and (g).

Figure 8.5 shows the wear pattern predicted by the brittle erosion model. The impact zone is the location of the highest wear for all mass flow rates in similar fashion to the abrasion model. The predicted wear can also be seen to become more severe as the mass flow increase. An arc can also be seen to develop in the wear from the 4 kg/s case, Figure 8.5(d), onwards until the final mass flow of 24 kg/s, Figure 8.5(g), where it can be seen clearly.

Figure 8.6 shows the wear pattern predicted by the combined erosion model. It can be seen from Figures 8.6(a) - (c) at flow rates between 1 - 3 kg/s the majority of the wear occurs in the impact zone. Progressing towards 8 kg/s, Figures 8.6 (d) - (e), it can be seen wear begins to emerge and become more severe in the run off area for the particles

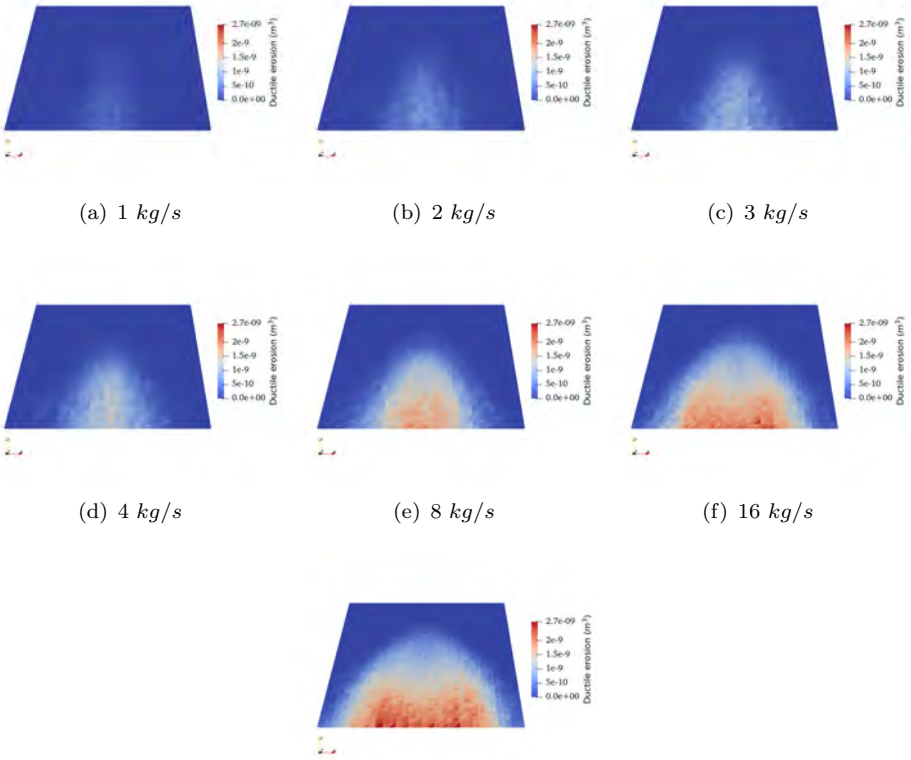

(a) 1 kg/s (b) 2 kg/s (c) 3 kg/s

(d) 4 kg/s (e) 8 kg/s (f) 16 kg/s

(g) 24 kg/s

FIGURE 8.4: Wear patterns predicted using the ductile erosion model for varying mass flow rate

although the impact zone is still more severe. At the highest mass flow rates of 16 - 24 kg/s this behaviour of wear occurring in both the impact zone and run off area is seen to be fully developed, generally being worse in the impact zone.

Figure 8.7 shows the accumulation of wear on the plate from the established wear models for each mass flow rate simulated. In general the total wear on the plate is increased for all models with increased mass flow. A notable exception to this is seen in the brittle erosion model shown in Figure 8.7(c) where the 16 kg/s and 24 kg/s are approximately equal. It should be noted the increase in total wear across the plate does not appear to be directly proportional to the increase in mass flow rate.

This is demonstrated further in Figure 8.8. Which shows as the mass flow is increased the total wear in the system appears to begin converging to a single value. This can be seen clearly for the brittle erosion model in Figure 8.8(c). It can also be seen in Figure 8.8(a), (b) and (d) but to a lesser extent where the curve is less severe, however this convergence is still clearly present.

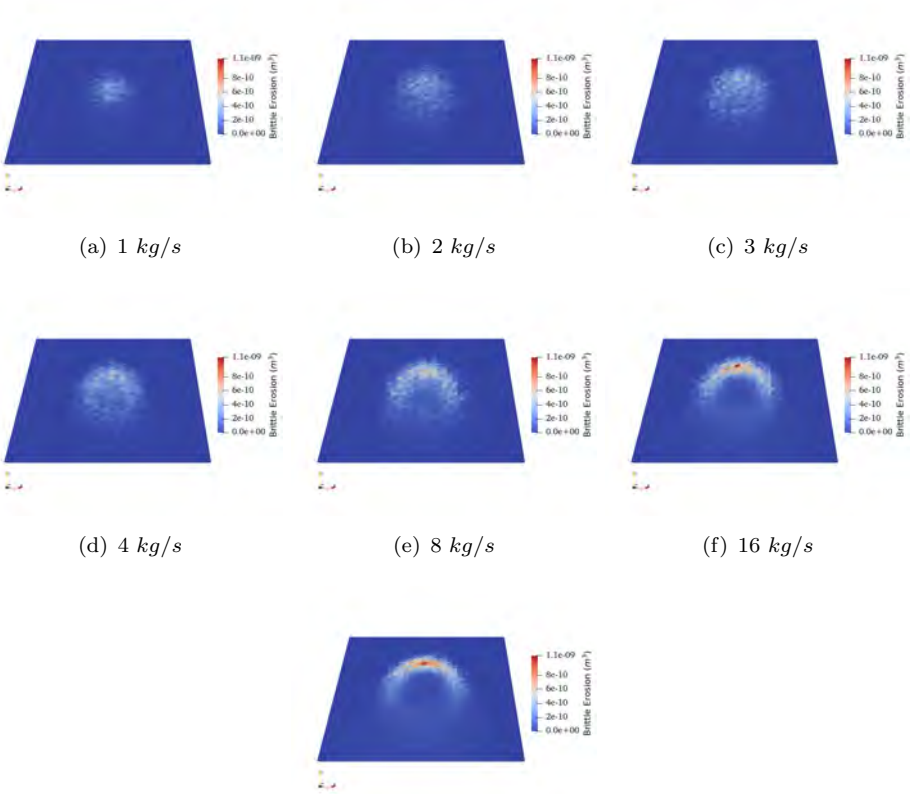

(a) 1 kg/s (b) 2 kg/s (c) 3 kg/s

(d) 4 kg/s (e) 8 kg/s (f) 16 kg/s

(g) 24 kg/s

FIGURE 8.5: Wear patterns predicted using the brittle erosion model for varying mass flow rate

Figure 8.9 shows the number of collisions with the plate in the simulation plotted against time, (a), and plotted against the mass flow used in the simulation, (b). It can be seen as the mass flow rate increases the number of collisions also increases. This increase is close to linear as shown in Figure 8.9 with a small curve showing a slight decrease, however it does not appear to be significant.

Figure 8.10 shows the normalised wear predicted by the established wear models. For the abrasion, brittle erosion and combined erosion models, Figures 8.10(a), (c) and (d), show that 1 kg/s has the highest normalised wear per collision, which becomes constant after an initial spike. Then the normalised wear rate decreases for each subsequent increase in mass flow rate. Figure 8.10(b) shows the ductile erosion model behaves differently. Each normalised wear rate increases from an initial low value after which they become approximately constant for the rest of the simulation for each mass flow rate. Mass flow rates 1 kg/s and 2 kg/s show spikes in the beginning. A small increase in normalised ductile erosion for is seen for each increase in mass flow rate until 4 kg/s,at 8 kg/s it begins to decrease. This decrease continues until the 24 kg/s simulation which shows

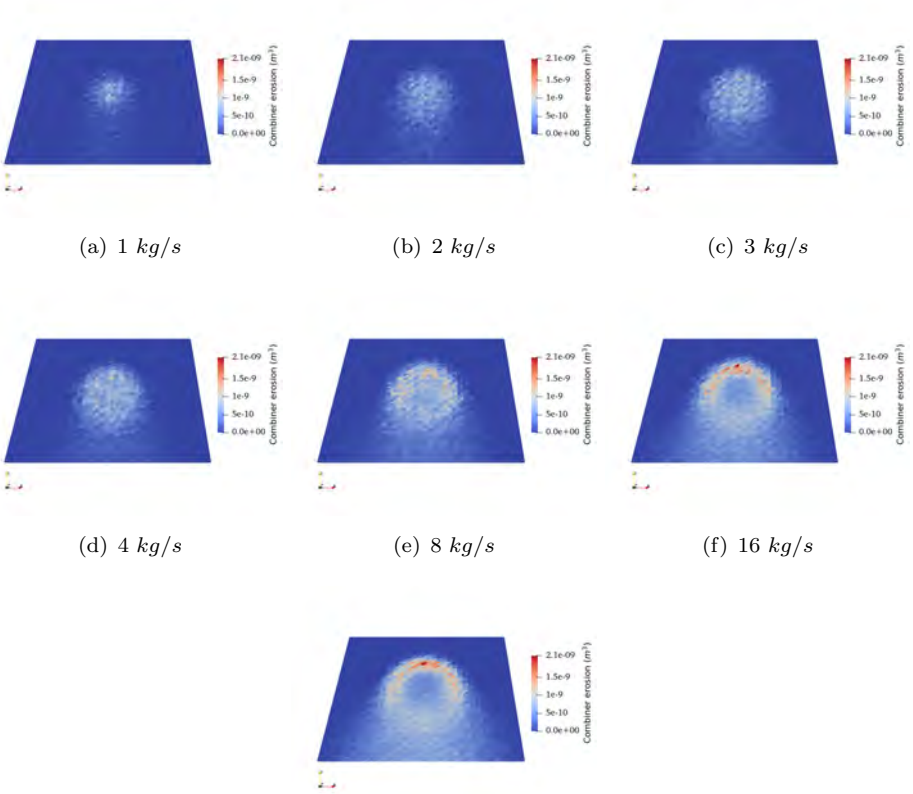

(a) 1 kg/s (b) 2 kg/s (c) 3 kg/s

(d) 4 kg/s (e) 8 kg/s (f) 16 kg/s

(g) 24 kg/s

FIGURE 8.6: Wear patterns predicted using the combined erosion model for varying mass flow rate

the lowest normalised ductile erosion for all mass flow rate simulations in similar fashion to all other models.

8.1.3 Findings

Overall, when increasing the mass flow rate of material, a general increase in the wear can be expected across the plate for all energy models. This finding is logical as with an increased mass of material a higher wear value would be expected. However, it does not appear to hold true past a certain value of mass flow. This effect can seen clearly with the brittle erosion model, Figure 8.5(c), where the total wear in the system can be seen to be approximately constant for the highest mass flow rates, 16 and 24 kg/s. This is also the case, to a lesser extent, for all other wear models. The abrasion model, shown in Figure 8.3(a), appears to be approaching a constant value for total wear while the ductile erosion and combined erosion models appear to require further mass flow rate increases to achieve this point. What is the cause of this?

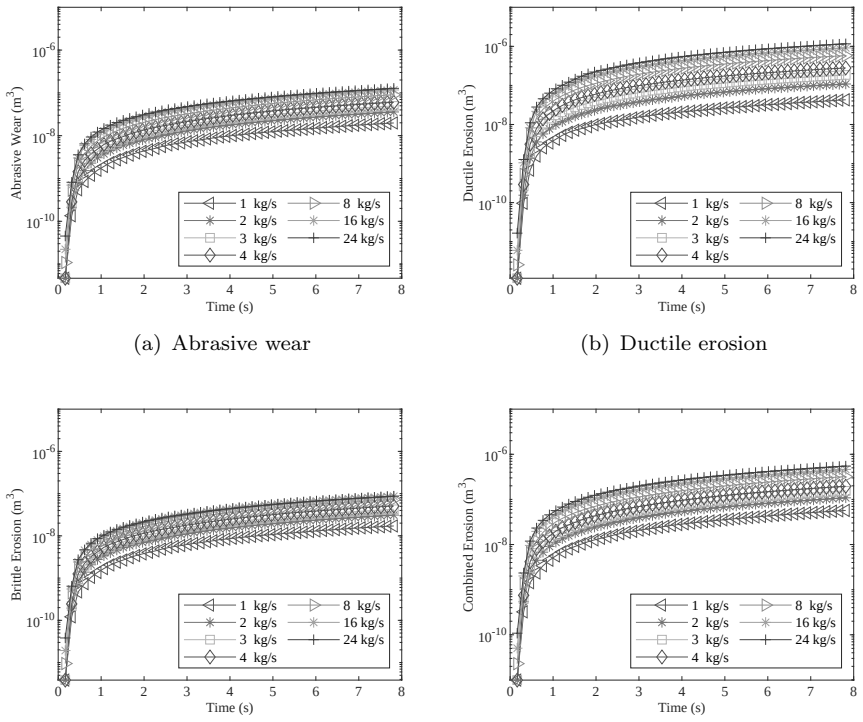

(a) Abrasive wear

(b) Ductile erosion

(c) Brittle erosion

(d) Combined erosion

FIGURE 8.7: Total wear predicted over time using established wear models with varying mass flow rate

As can be seen in Figure 8.2, the number of collisions in the domain is not approaching a constant during any mass flow simulation, therefore it is not a reduction in the number of collisions. It must be concluded from this each individual collision is becoming less severe, a fact which can be seen through the normalisation of the total wear values with the total collisions shown in Figure 8.10. This is true for abrasion, brittle erosion and combined erosion. However, it is not true for ductile erosion which shows an initially increased wear per collision across the plate before reducing after the 4 kg/s simulation as seen in Figure 8.10(b). Ductile erosion shows a slightly different behaviour where initial increases in mass flow show an increased wear per collision until a point at which the trend switches to reducing per collision in similar fashion to other mechanisms. For this model a constant total wear value is expected to be achieved however a higher mass flow is expected to be necessary to achieve this. This can be seen visually through the wear pattern development shown in Figure 8.4 where as the mass flow is increased the wear on the lip of the plate is seen to become more severe with the eventual development of two distinct zones. The cause of this wear in two distinct zone is not known for certain, however, it is suggested this arises from an excess of material in the centre of the plate dropping from the spawn and impact zone. At this point particles are effectively pushed outwards (positive and negative x) causing two distinct zones.

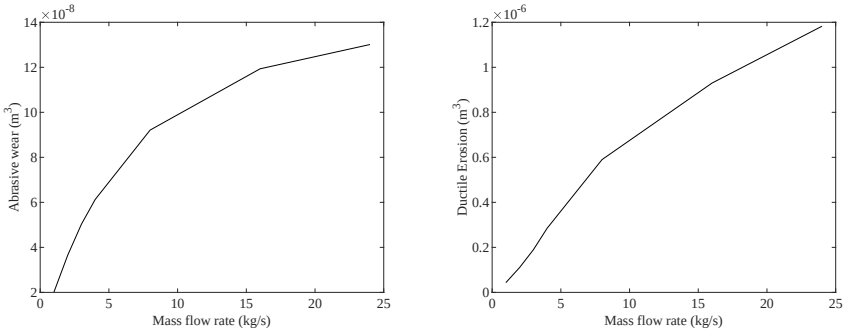

(a) Abrasion model (b) Ductile erosion model

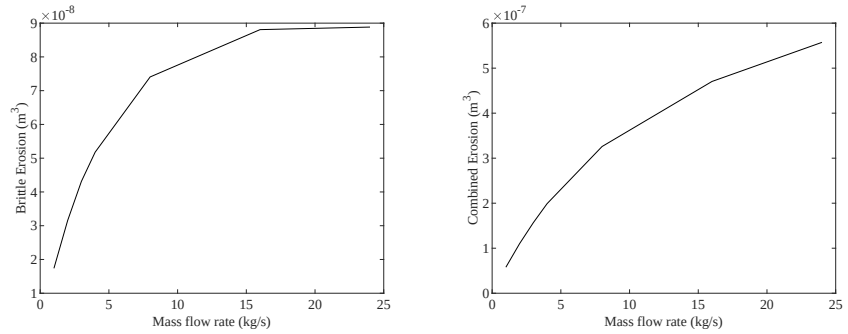

(c) Brittle erosion model (d) Combined erosion model

FIGURE 8.8: Total wear predicted plotted against the mass flow rate using established wear models

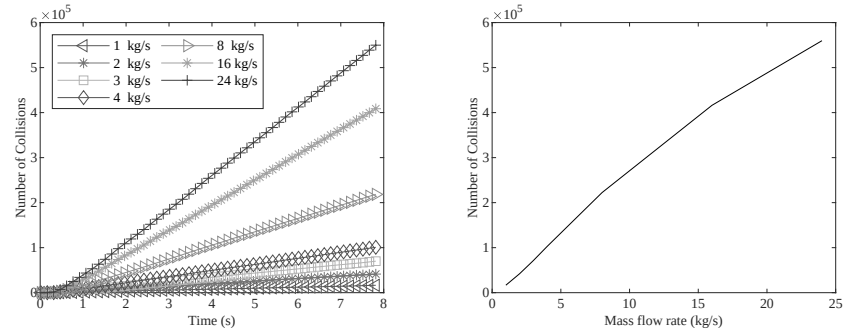

(a) Time (b) Mass flow rate

FIGURE 8.9: Number of collisions across the plate for varying mass flow rate plotted over time and plotted against the mass flow rate of the simulation

Generally, it is shown that for abrasion and brittle erosion mechanisms the wear is expected to decrease in severity per collision as mass flow is increased, however the increased number of collisions is expected to cause an overall increase to the volume of wear. A point will be reached where the total wear is expected to become constant. Physically, inside the system, this can be rationalised by noting that the particles are landing and impacting on each other. This can also be seen in Figures 8.3 and 8.5 for abrasion and brittle erosion respectively. Wear is initially seen to occur for both models

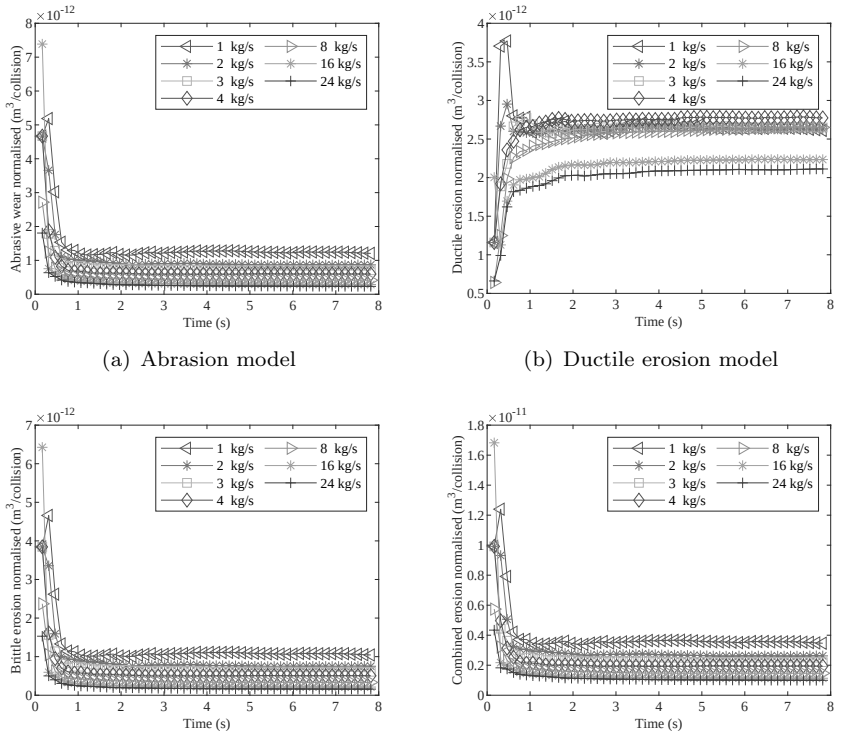

(a) Abrasion model

(b) Ductile erosion model

(c) Brittle erosion model

(d) Combined erosion model

FIGURE 8.10: Normalised wear plotted against time for the established wear models with varying mass flow rate

in the 1 - 4 kg/s ((a) - (d)) in the centre of the impact zone. At this point there is change where wear shift upwards (positive y), this represents the point at which particles are now landing on each other. This is seen to cause an arc in the wear pattern. This arc could possibly indicate a point at which the total wear on the plate becoming constant for abrasion and brittle erosion mechanisms.

The combined erosion model, unsurprisingly, shows a combination of both wear patterns. With the lower flows of 1 - 4 kg/s showing wear only in the impact zone, Figures 8.6(a) - (d). When the flow is increased a pattern similar to that seen in the ductile erosion model begins to develop, however the arc shown in abrasion and brittle erosion models is still more significant, Figure 8.6(f) and (g). For this model plate properties were set to be equivilant (i.e. speccific energy values for brittle and ductile erosion, ε and Φ respectively, are equal in equation 4.6), therefore the wear situation according to the model used would show a preference to wearing in the impact zone first.

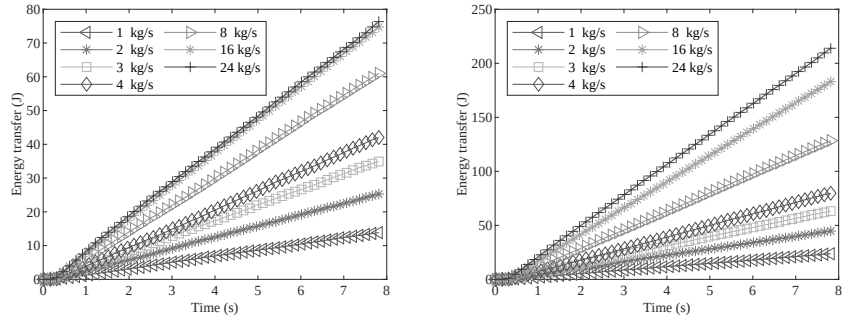

(a) E_1 (b) E_2

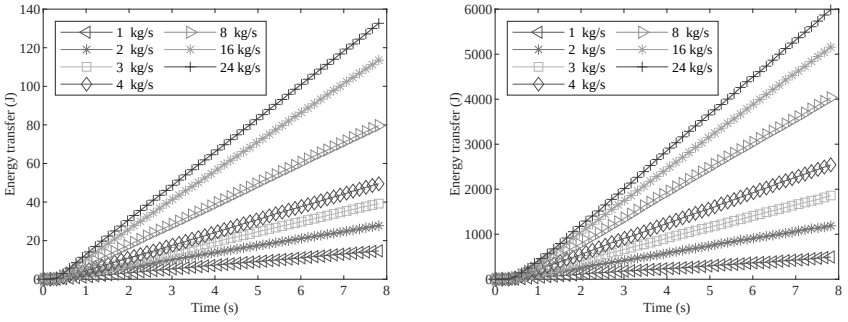

(c) E_3 (d) E_4

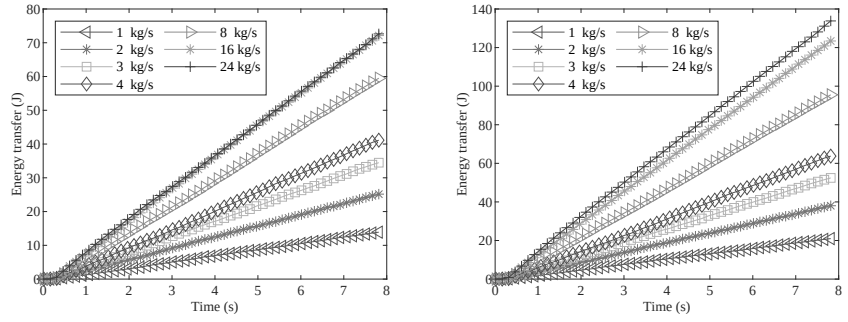

(e) E_5 (f) E_6

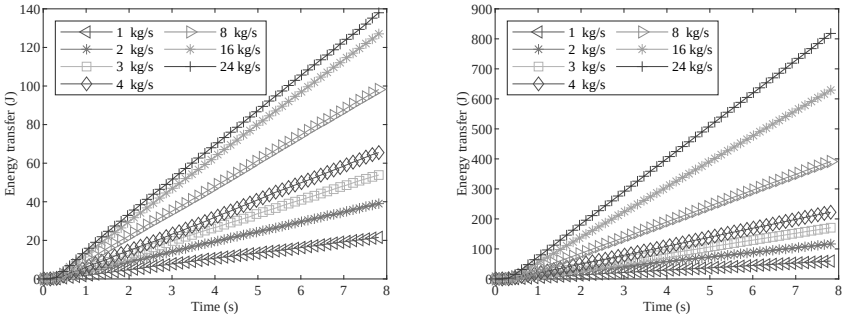

(g) E_7 (h) E_8

FIGURE 8.11: Total energy transfer predicted over time with varying mass flow rate

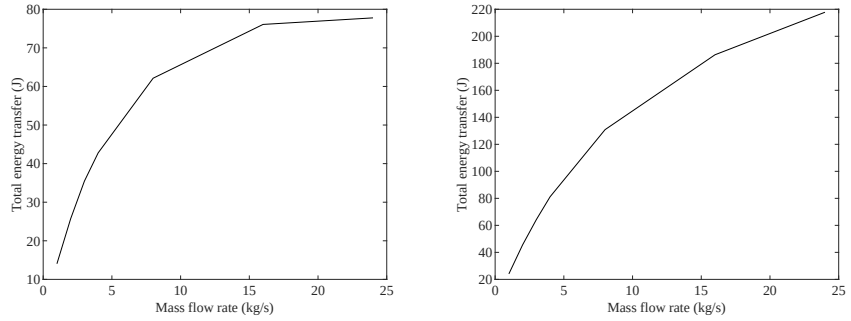

(a) E_1

(b) E_2

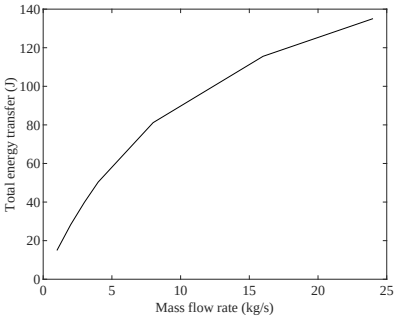

(c) E_3

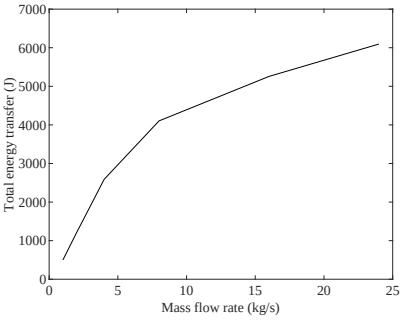

(d) E_4

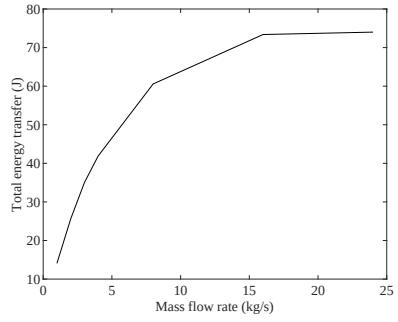

(e) E_5

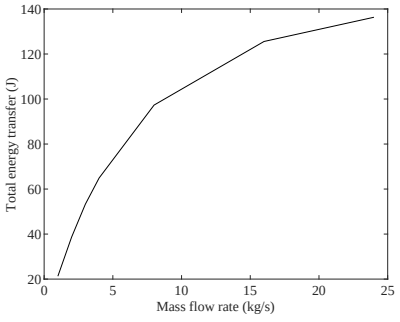

(f) E_6

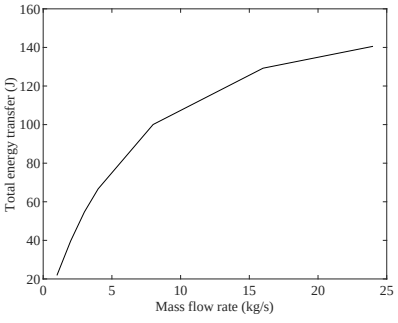

(g) E_7

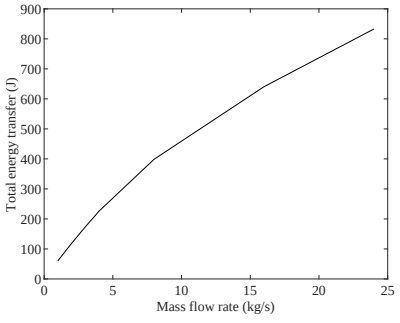

(h) E_8

FIGURE 8.12: Total energy transfer plotted against mass flow rate

8.2 Coefficient of Restitution

One of the key parameters when studying the effect of wear modelling is the coefficient of restitution of the system. It is important because it represents the energy dissipation

inside a system and therefore it would be expected to have a large influence on the wear and energy transfer calculations. For example, the energy dissipated through damping is explored in Chapter 4 and has been the basis of work carried out in the literature with specific application to ball milling [114][115].

The damping component is intrinsically linked to the coefficient of restitution as shown in equation 2.28. It could be reasonably assumed it would have an effect on the total wear and energy transfer calculated. The question posed here is, how much?

8.2.1 Methodology

This was investigated using the same setup as the previous mass flow rate simulations studied in this chapter. However, in this case the mass flow rate is kept at a constant 1 kg/s whilst the coefficient of restitution, e, is varied instead. The values of coefficient of restitution used are 0.1, 0.2, 0.3, 0.4, 0.5, 0.6, 0.7, 0.8, 0.9 and 1. The simulations parameters can be found in Table 8.2.

TABLE 8.2: DEM parameters used for studying the variation of the coefficient of restitution

Parameter	Values
Spring stiffness	8000 N/m
Mass flow rate	1 kg/s
Particle radius	0.005 m
Particle density	8000 kg/s
Sliding Friction Coefficient	0.8
Twisting Friction Coefficient	0.3
Twisting Damping	1.5
Rolling Friction Coefficient	0.3
Rolling Damping	1.5

8.2.2 Results

Figure 8.13 shows the wear patterns predicted by the abrasion model with varying coefficients of restitution. Wear is seen to occur at a maximum in the impact zone for the particles. This does not change with increases in coefficient of restitution. The wear pattern is seen to spread out with increases in coefficient of restitution due to how the particles behave post impact. Low coefficient particles do not bounce as much and rolling is seen across the plate. With higher coefficient values particles begin to bounce more, and re-impact the plate. With a high coefficient value $e = 1$ particles are perfectly elastic and at this point they bounce straight off the plate.

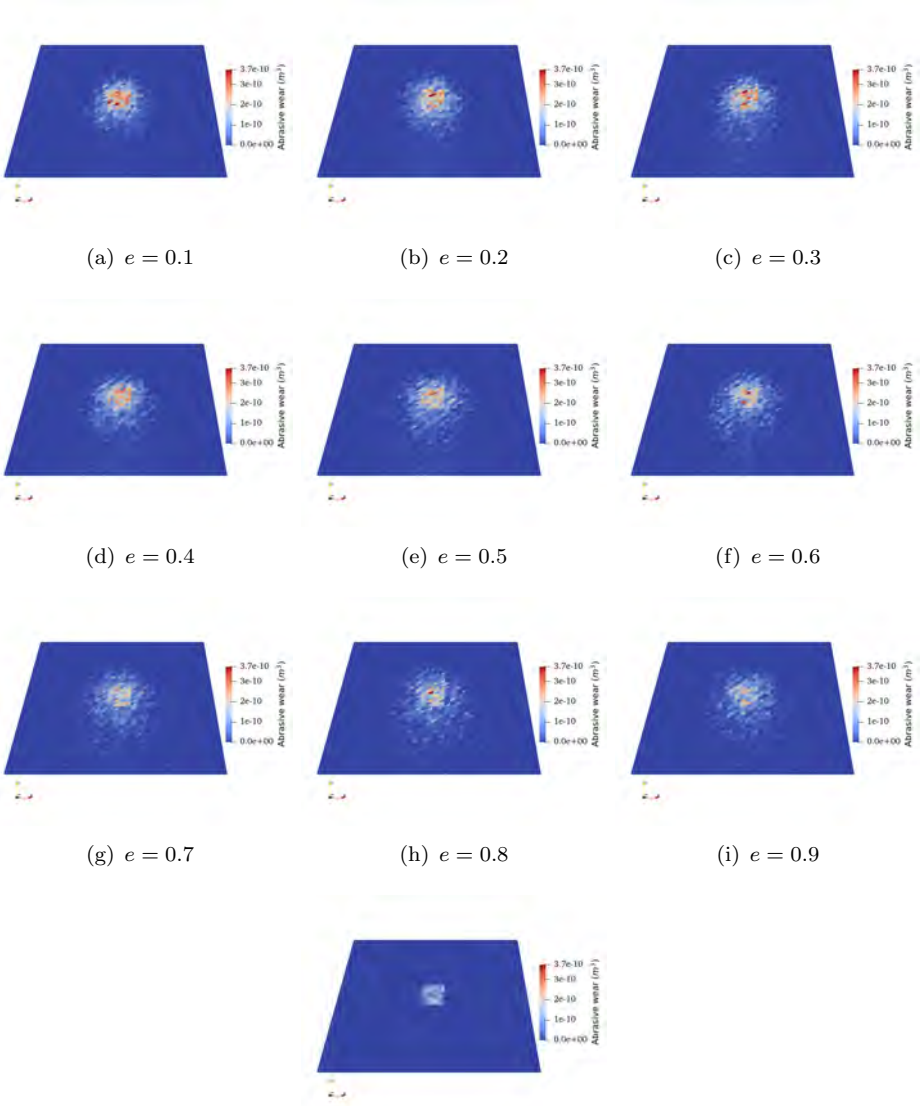

(a) $e = 0.1$ (b) $e = 0.2$ (c) $e = 0.3$

(d) $e = 0.4$ (e) $e = 0.5$ (f) $e = 0.6$

(g) $e = 0.7$ (h) $e = 0.8$ (i) $e = 0.9$

(j) $e = 1$

FIGURE 8.13: Wear pattern predicted using the abrasion model with varying coefficient of restitution

Figure 8.14 shows the wear patterns created by the ductile erosion model. High wear is predicted at lower value of the coefficient, with the wear pattern established in the run off area of the plate, Figures 8.14(a) - (e). The pattern is seen to decrease in severity with increases in the coefficient up to the simulation with perfectly elastic particles, $e = 1$, where particles immediately bounce off the plate producing very little wear.

Figure 8.15 shows the wear patterns created by the brittle erosion model. Wear is predicted in the impact zone, initially for a low coefficient value the wear zone is narrow as shown in Figures 8.15(a) and (b). As the coefficient value increases the wear zone begins to spread out from the point of impact until the final simulation using perfectly elastic spheres.

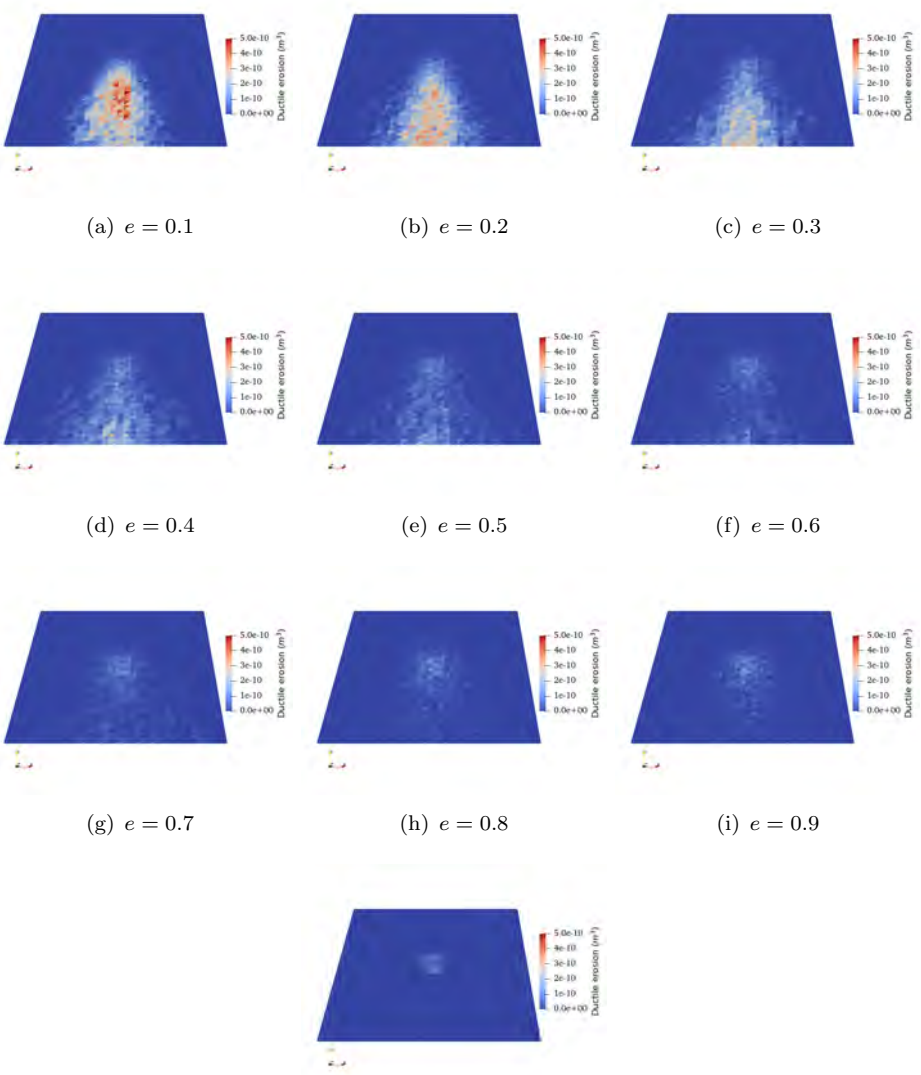

(a) $e = 0.1$ (b) $e = 0.2$ (c) $e = 0.3$

(d) $e = 0.4$ (e) $e = 0.5$ (f) $e = 0.6$

(g) $e = 0.7$ (h) $e = 0.8$ (i) $e = 0.9$

(j) $e = 1$

FIGURE 8.14: Wear pattern predicted using the ductile erosion model with varying coefficient of restitution

Figure 8.16 shows the wear patterns predicted by the combined erosion model. A similar pattern is shown for the combined erosion model as was predicted by the brittle erosion model. There is an initial narrow wear pattern, which spreads out with increased coefficient up to the point of using perfectly elastic particles which bounce of the plate and cause wear only on the initial impact.

Figure 8.17 shows the total wear calculated over the plate for the wear models. For the abrasion model, Figure 8.17(a) shows a peak at low values, $e = 0.1$ to $e = 0.5$ during which the total wear on the plate does not vary considerably. After $e = 0.5$ an approximately linear decrease is seen until $e = 0.9$ at which point wear remains constant at this value and the perfectly elastic particle $e = 1$. Figure 8.17(b) shows the total

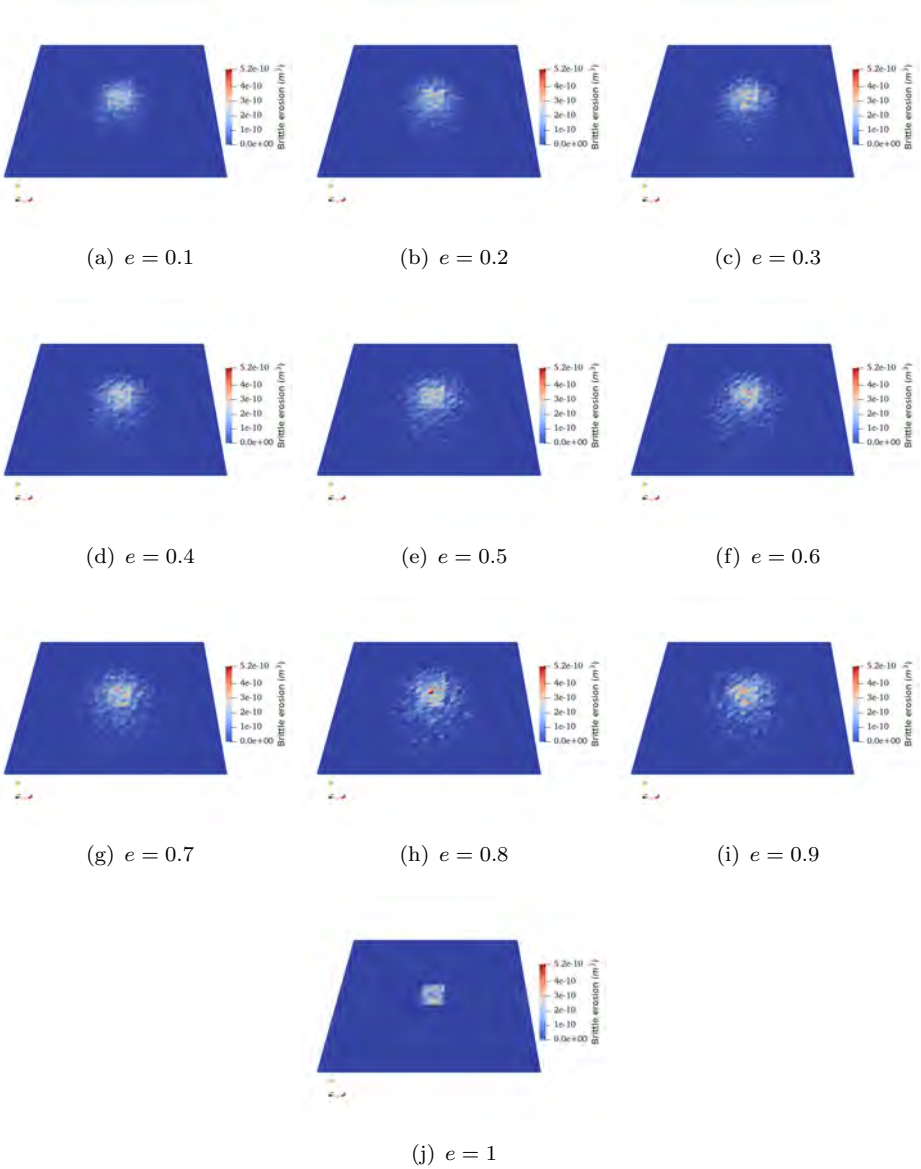

(a) $e = 0.1$ (b) $e = 0.2$ (c) $e = 0.3$

(d) $e = 0.4$ (e) $e = 0.5$ (f) $e = 0.6$

(g) $e = 0.7$ (h) $e = 0.8$ (i) $e = 0.9$

(j) $e = 1$

FIGURE 8.15: Wear pattern predicted using the brittle erosion model with varying coefficient of restitution

wear predicted using the ductile erosion model. A peak is seen at low values, $e = 0.1$ being the maximum, with a generally linear decrease until $e = 0.6$. At which point it becomes approximately constant for all further increases in coefficient until $e = 1$. For the brittle erosion model, Figure 8.17(c), the total wear is found to have a lowest value at $e = 0.1$, with an approximately linear increase until approximately $e = 0.8$. At which point the total wear becomes approximately constant until $e = 1$. Figure 8.17(d) shows the combined erosion model. An initial sharp increase is seen from $e = 0.1$ to $e = 0.3$. A lesser increase is seen from $e = 0.3$ to 0.7 at which point a final sharp increase is seen to $e = 0.8$ and thereafter it remains constant as per all other wear models.

Figure 8.18 shows the total number of collisions across the plate. It is shown to be a

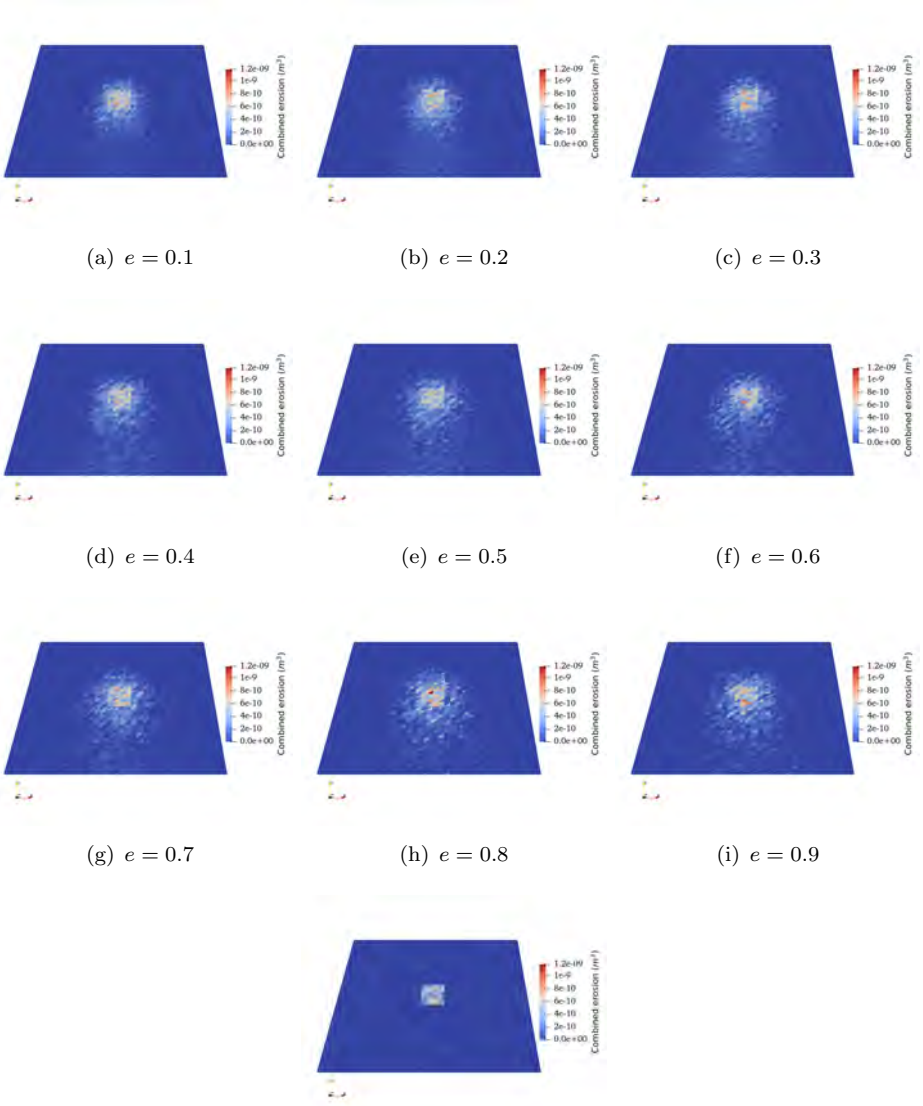

(a) $e = 0.1$ (b) $e = 0.2$ (c) $e = 0.3$

(d) $e = 0.4$ (e) $e = 0.5$ (f) $e = 0.6$

(g) $e = 0.7$ (h) $e = 0.8$ (i) $e = 0.9$

(j) $e = 1$

FIGURE 8.16: Wear pattern predicted using the combined erosion model with varying coefficient of restitution

maximum at low values, $e = 0.1$ being the maximum, after which point it begins to decrease until approximately $= 0.6$. After this point it remains approximately constant.

Figure 8.19 shows the total wear, Figure 8.17 normalised using the total number of collisions, Figure 8.18, on the plate. The normalised abrasion model, Figure 8.19(a), shows a general increase in wear per collision with increasing coefficient from $e = 0.1$ to $e = 0.6$. Between $e = 0.7$ to $e = 1$ shows a slight variation, however, this variation is generally quite small. Figure 8.19(b) shows the normalised ductile erosion model. All normalised values are much closer and show less overall variation. A lowest wear per collision is found at the lowest coefficient value $e = 0.1$, at which point there is a general increase until $e = 0.5$ at which point the normalised wear becomes approximately

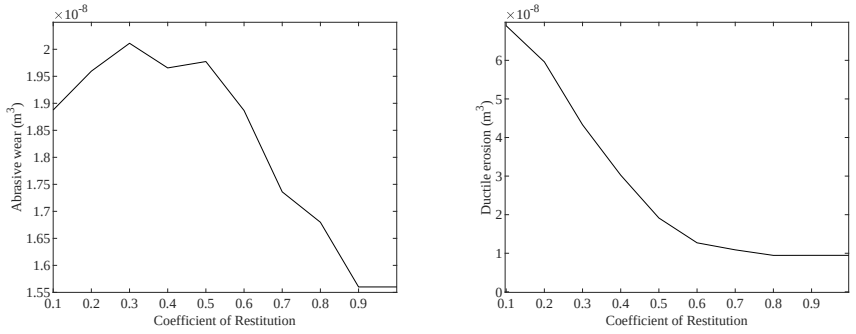

(a) Abrasion model

(b) Ductile erosion model

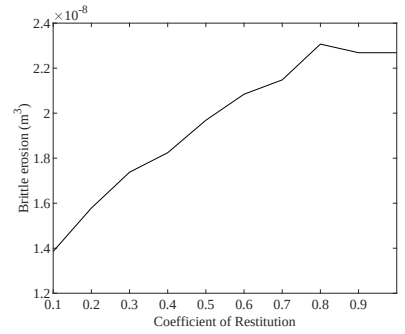

(c) Brittle erosion model

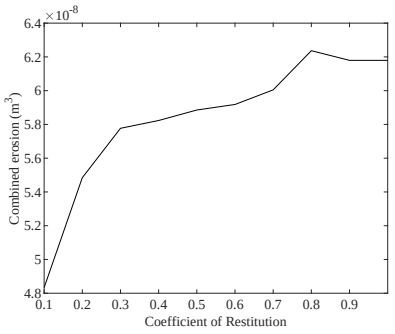

(d) Combined erosion model

FIGURE 8.17: Total wear predicted with respect to the coefficient of restitution

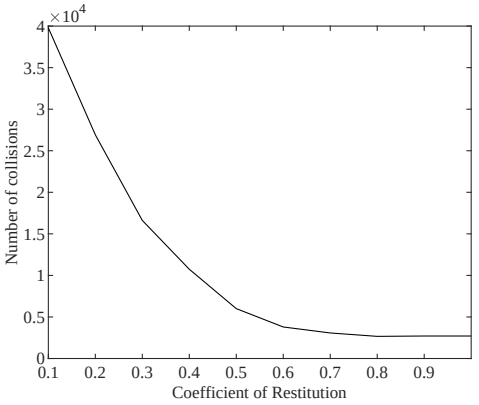

FIGURE 8.18: Number of collisions across the plate with respect to the coefficient of restitution

constant for all further increases. The normalised brittle erosion model, Figure 8.19(c), shows a general increase for all values from a minimum of $e = 0.1$ to $e = 0.8$, at which point it remains constant for all further increases. The combined erosion models, Figure 8.19(d), shows a general increase in wear per collision from a minimum value of $e = 0.1$ to $e = 0.8$ at which point it remains constant for further increases.

Figure 8.20 shows the totals for the first 8 energy transfer models. The final 6 can be found in appendix B. Figures 8.20(a) - (d) show a similar behaviour to the ductile erosion

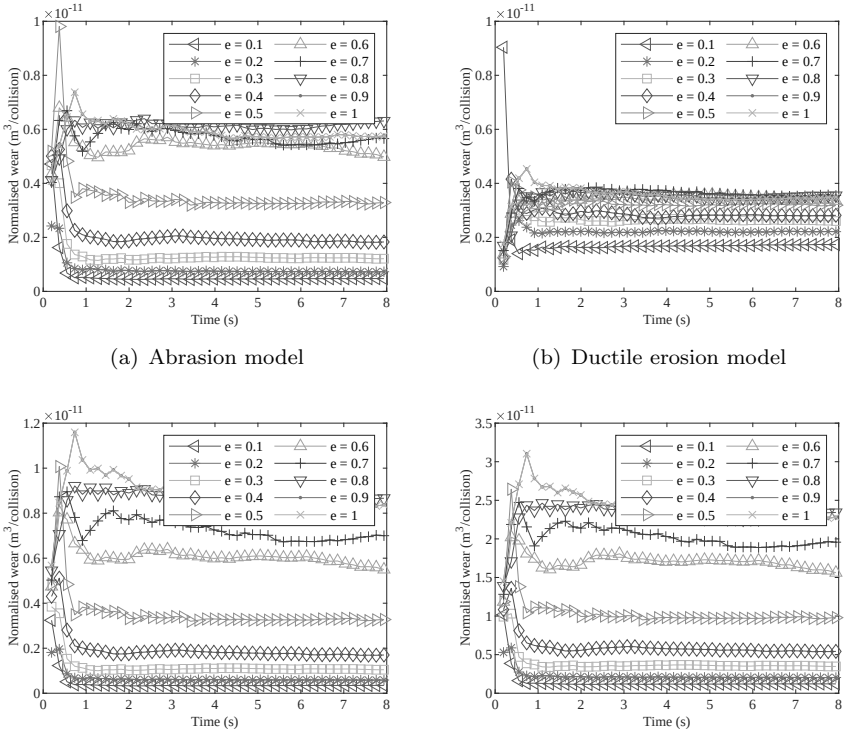

(a) Abrasion model

(b) Ductile erosion model

(c) Brittle erosion model

(d) Combined erosion model

FIGURE 8.19: Normalised wear plotted over time for the established wear models with varying coefficient of restitution

model with varying coefficient of restitution. A maximum value is seen at $e = 0.1$ and then a decrease is seen. For E_1, E_2 and E_3 this is seen to continue until approximately $e = 0.9$ at which point it becomes constant for the final simulation. E_4 decreased at a quicker rate than the others becoming constant at approximately $e = 0.6$, very similar to the trend seen for the ductile erosion model. E_5, shown in Figure 8.20, shows a peak at $e = 0.5$, with approximately constant values for $e = 0.9$ and $e = 1$. Figures 8.20(e) and (f), E_6 and E_7 all show a similar behaviour. A general increase from $e = 0.1$, until becoming approximately constant for a values between $e = 0.3$ and $e = 0.5$. A decrease is then seen from this point onwards until $e = 0.9$ at which point it remains constant. E_8, shown in Figure 8.20(h), shows a linear increase with increasing coefficient becoming constant at $e = 0.8$ onwards.

Figure 8.21 shows the normalised energy transfer per collision using the total energy transfer values shown in Figure 8.20 and the number of collisions shown in Figure 8.18. E_1 to E_3, Figure s 8.21(a) - (c), show similar trends starting with a lowest energy transfer per collision at $e = 0.1$ and increasing until $e = 0.6$. At this point it decreases back to its minimum normalised value at $e = 0.9$ and $e = 1$. E_4 shows a highest value for energy transfer at $e = 0.1$, at which point it decreases until $e = 0.6$ at which point it becomes approximately constant. Figures 8.21(e) - (h) shows E_5 to E_8 and they show similar

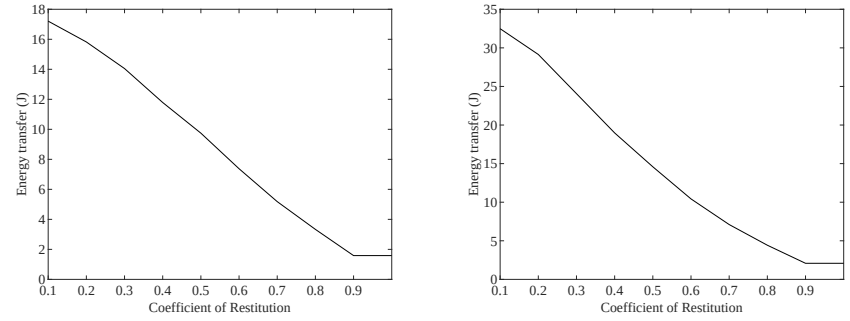

(a) E_1

(b) E_2

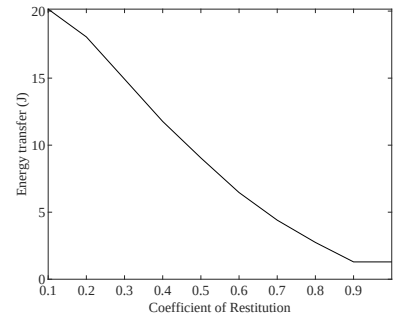

(c) E_3

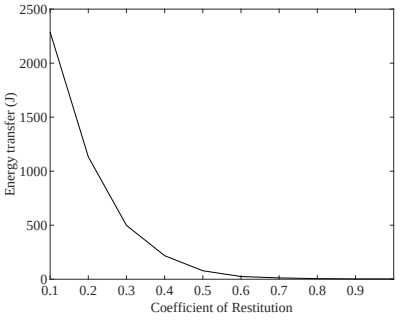

(d) E_4

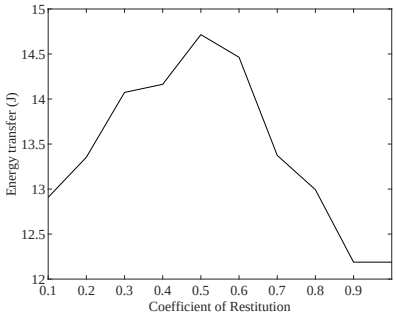

(e) E_5

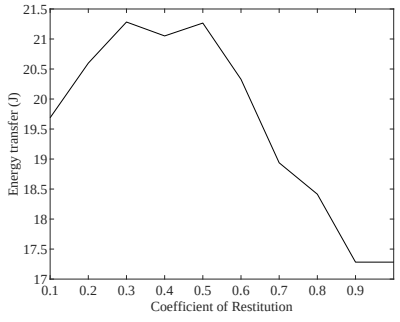

(f) E_6

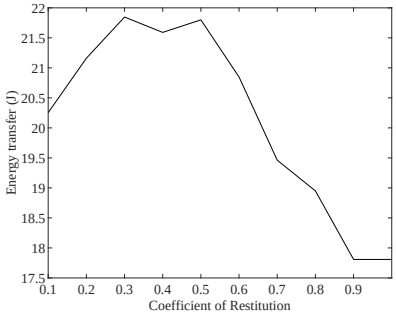

(g) E_7

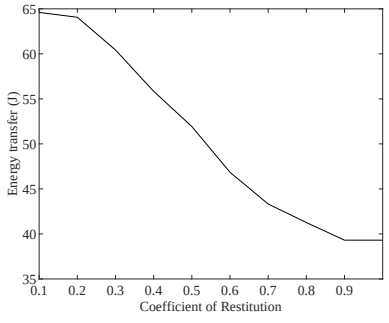

(h) E_8

FIGURE 8.20: Total energy transfer predicted with respect to the coefficient of restitution

trends. A minimum value is found at $e = 0.1$, which increases to $e = 0.6$ at which point

it becomes constant for each further increase.

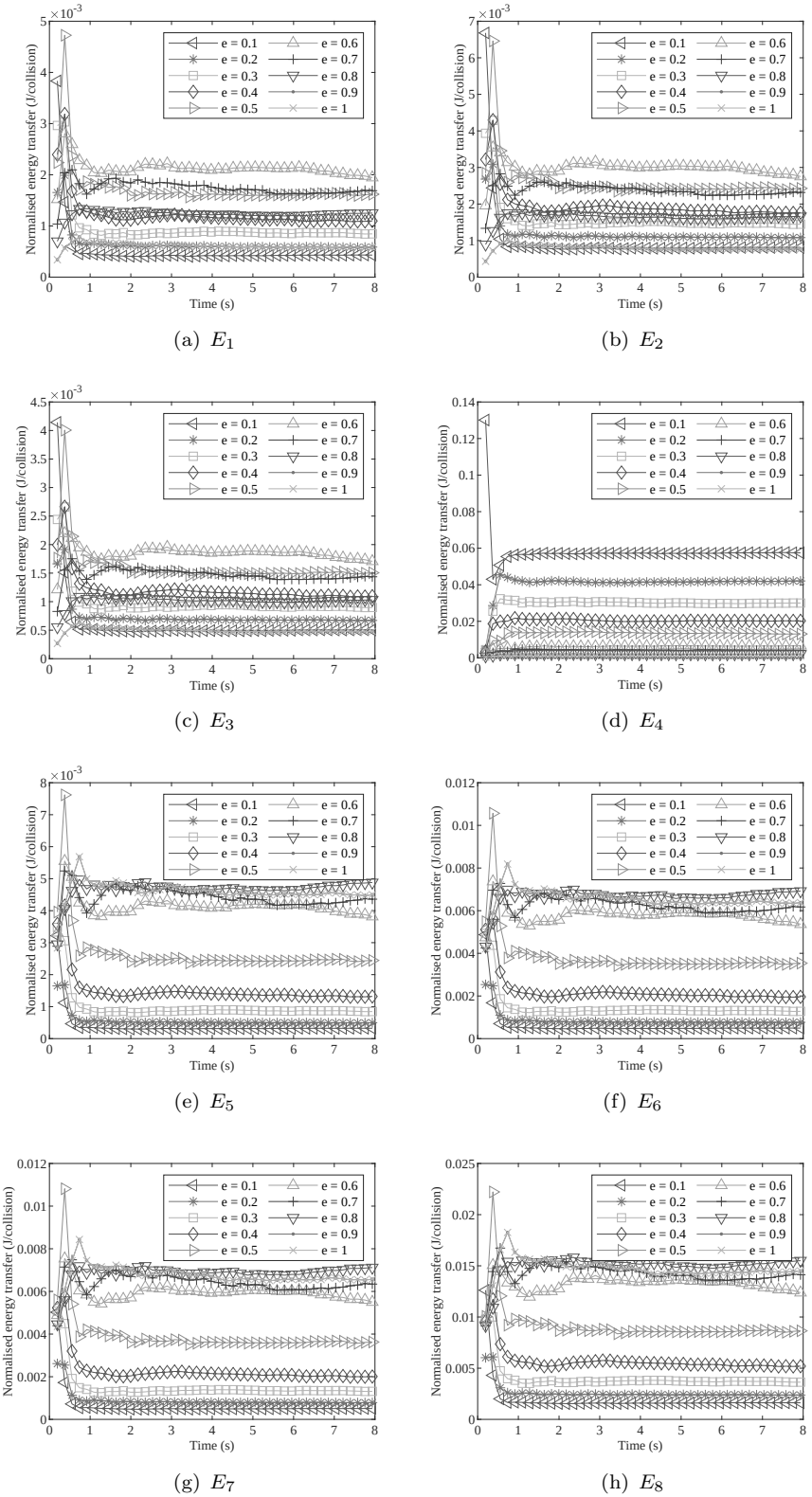

(a) E_1 (b) E_2

(c) E_3 (d) E_4

(e) E_5 (f) E_6

(g) E_7 (h) E_8

FIGURE 8.21: Normalised energy transfer plotted over time for the first 8 energy models with varying coefficient of restitution

8.2.3 Findings

In general there are 3 distinct behaviours shown with the variation of coefficient. The first type of behaviour is displayed using the abrasion model, shown in Figures 8.17(a), where an initially approximately constant value is seen between $e = 0.1$ and $e = 0.5$. This occurs while the pattern on the plate is not showing a great deal of variation either, however, it can be the seen that the number of collisions is decreasing a large amount as shown in Figure 8.18. This is caused by the particle kinetics as the particles using low coefficient of restitution values generally roll post impact and do not cause a large amount further impacts. Therefore, at this point the total amount of wear remains approximately constant for the abrasion calculation until a large change in particle kinetics is seen. This begins to occur at approximately $e = 0.5$ where the total wear decreases, on the plate this can be seen in a slight decrease in severity from Figures 8.13(f) - (i). Using perfectly elastic particles no rebounds impact the plate, causing a significant reduction in the total wear. Energy models, E_5, E_6 and E_7, show a similar behaviour. For E_5 a peak is seen for the simulations using $e = 0.1$ to $e = 0.5$, Figure 8.20(e). This is theorised to be due to this model's preference for the normal component in its force/distance calculation as shown in Table 4.2. With the plate at an angle a reduction in the normal component is to be expected.

The second type of behaviour is shown by the ductile erosion model and energy transfer models E_1 to E_4 and E_8. These show the highest wear and energy transfer value at $e = 0.1$ decreasing from this maximum in two different ways. The first is a rapid decrease until a constant value is reached at approximately $e = 0.5$ onwards which is shown for the ductile erosion model, Figure 8.17(b), and the E_4, Figure 8.20(d) model. The second is a more gradual linear decrease to $e = 0.9$ at which point it becomes constant.

The third type of behaviour is the inverse of the second type where a general increase in total wear and energy transfer is found with increasing coefficient of restitution. This is found in the brittle erosion model and the combined erosion model 8.17(c) and (d). This is the most unique behaviour of all the models. With each model thus far, increases in coefficient of restitution generally led to an overall reduction with a minimum value at $e = 1$ (i.e. a perfectly elastic particle), a result which is logical. However in the case of the brittle model, the opposite occurs.

8.3 Hole Creation: The effect of damage coefficient and particle radius

8.3.1 Coke Screener

The first case study, Chapter 6, assessed the failure times of the coke screener using the abrasion model. For this it made a simplification regarding the particle radius and when studying damage used a damage coefficient, C_d to obtain time to failure predictions. The study found the predictions to be accurate however it was noted at the time that the effect of varying particle sizing and the damage coefficient value was unknown. The section below investigates this.

8.3.2 Methodology

The same simulation setup used for the original case study is used here. The properties are given in Table 8.3. A number of variations are carried out changing both particle radius, r, and damage coefficient, C_d. The failure criteria for the simulation is set using the particle dependent MEF criterion where a value of 6 times the particle area is used as a failure point. Figure 8.22 shows the simulation running for the various particles radii studied.

TABLE 8.3: DEM coke material parameters used for the parameter case study

Parameter	Value
Spring Stiffness	16000 N/m
Particle Density	1150 kg/m^3
Coefficient of resititution	0.01
Sliding friction coefficient	0.8
Rolling friction coefficient	0.3
Rolling damping coefficient	1.5
Twisting friction coefficient	0.3
Twisting damping coefficient	1.5

The damage coefficient is set at $C_d = 1000000$, 2000000, 4000000, 8000000 and 16000000. The particle radius used is 0.015 m, 0.03 m and 0.045 m. Each variation is carried out individually creating a total of 15 simulations. Failure times for both the SEF and MEF criteria are considered.

8.3.3 Results

Tables 8.4 and 8.5 show the results from the coke screener simulations utilising the Single Element and Multiple Element failure criteria and including the hole creation method.

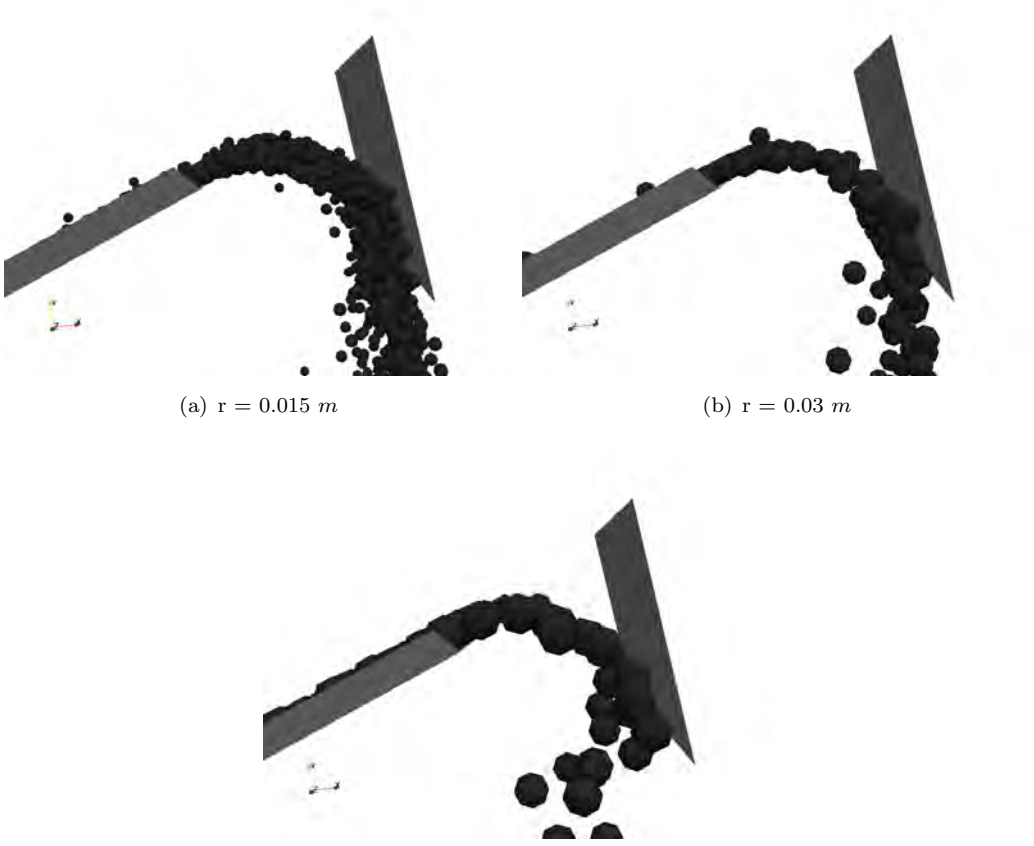

(a) r = 0.015 m

(b) r = 0.03 m

(c) r = 0.045 m

FIGURE 8.22: Images of the coke screener simulation impact zone running with varying particle radii

The results show the varying particle radius, r, particle to element ratio, R (as calculated using equation 4.7), the damage coefficient, C_d, used in the simulation to generate the hole in a reasonable amount of time, the number of global collisions, G_k, the hole area, A_h and the time to failure, t_f (i.e. the time taken to reach the required hole area in a given scenario).

Table 8.4: Single Element Failure (SEF) criterion results

Particle Radius (m)	Particle to Element Ratio	Damage Coefficient	Global Collisions	Worn Area (m^2)	Time to failure (s)
0.015	0.723909	1000000	978588	0.000977	62.745
0.015	0.723909	2000000	509008	0.000977	32.925
0.015	0.723909	4000000	267922	0.000977	18.45
0.015	0.723909	8000000	125518	0.000977	9.72
0.015	0.723909	16000000	59904	0.000977	5.775
0.03	2.895635	1000000	346380	0.000977	22.605
0.03	2.895635	2000000	213786	0.000977	15
0.03	2.895635	4000000	107579	0.000977	9.03
0.03	2.895635	8000000	62878	0.000977	6.345
0.03	2.895635	16000000	6552	0.000977	4.11
0.045	6.515178	1000000	88448	0.000977	10.38
0.045	6.515178	2000000	49504	0.000977	7.155
0.045	6.515178	4000000	24017	0.000977	4.95
0.045	6.515178	8000000	13865	0.000977	4.44
0.045	6.515178	16000000	3654	0.000977	3.93

Table 8.5: Multiple Element Failure (MEF) criterion results

Particle Radius (m)	Particle to Element ratio	Damage Coefficient	Global Collisions	Worn Area (m^2)	Time to failure (s)
0.015	0.723909	1000000	1051806	0.003906	66.585
0.015	0.723909	2000000	550602	0.003906	35.31
0.015	0.723909	4000000	286234	0.003906	19.71
0.015	0.723909	8000000	151905	0.003906	11.13
0.015	0.723909	16000000	98362	0.003906	7.89
0.03	2.895635	1000000	616100	0.016602	37.875
0.03	2.895635	2000000	316572	0.016602	21.405
0.03	2.895635	4000000	170649	0.016602	12.75
0.03	2.895635	8000000	98208	0.016602	8.37
0.03	2.895635	16000000	58320	0.016602	6.09
0.045	6.515178	1000000	263802	0.03711	26
0.045	6.515178	2000000	142285	0.03711	14.91
0.045	6.515178	4000000	80470	0.03711	9.255
0.045	6.515178	8000000	46958	0.03711	6.66
0.045	6.515178	16000000	39270	0.03711	5.28

Figures 8.23 show the failure times calculated for the damage coefficient used and for varying particle radii for the SEF and MEF criterion. This shows a decrease in the time to failure with increase in damage coefficient, i.e. they are inversely proportional. The relationship between them is also shown to be non-linear. A decrease in failure time with an increase in particle radius is also observed.

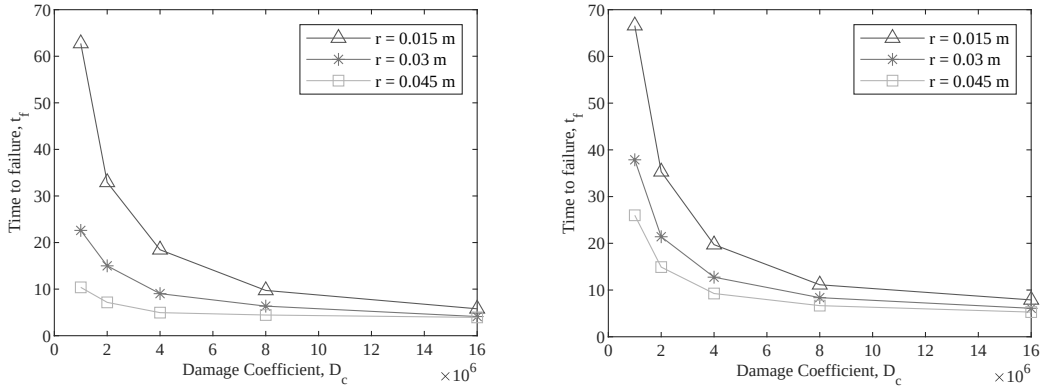

(a) SEF criterion (b) MEF criterion

FIGURE 8.23: Plots of failure time determined by the size of the hole created against the damage coefficient used for varying particle radius

Figure 8.24 shows the global collisions, (i.e. total number of particle collisions with the surrounding structure in the simulation) plotted against the damage coefficient. Global collisions are shown to decrease non-linearly with increasing damage coefficient. Global collisions also decrease with decreasing particle radius.

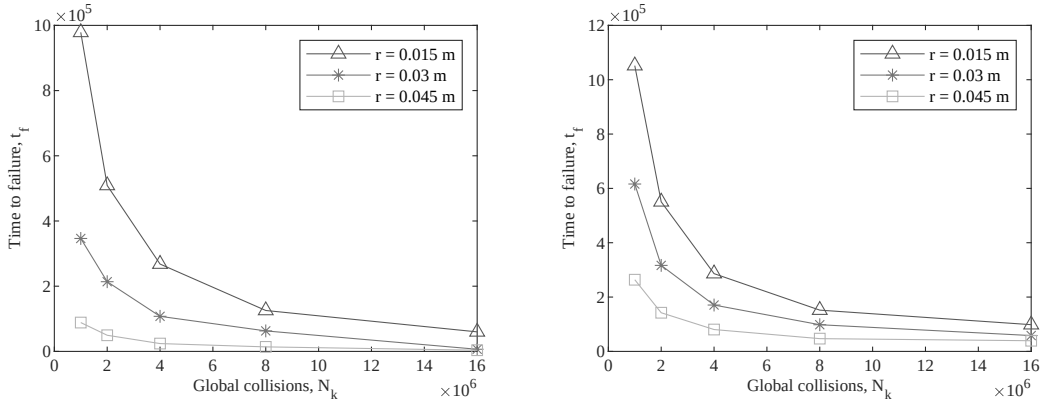

(a) SEF criterion (b) MEF criterion

FIGURE 8.24: Plots of failure time determined by the size of the hole created against the global collisions for varying particle radius

$$t_{f,norm} = \frac{t_f}{G_k} \tag{8.1}$$

Figure 8.25 shows the normalised failure time using equation 8.1. For the SEF criterion, the normalised failure time is approximately constant for the particle radius $r = 0.015$ m. It then shows that for both particle radii $r = 0.03$ m and $r = 0.045$ m the normalised failure time is approximately constant up to $C_d = 8,000,000$ at which point it begins to increase.

For the MEF criterion the normalised failure time does vary but it is effectively constant as the variation is small in comparison to the failure times in Figure 8.23.

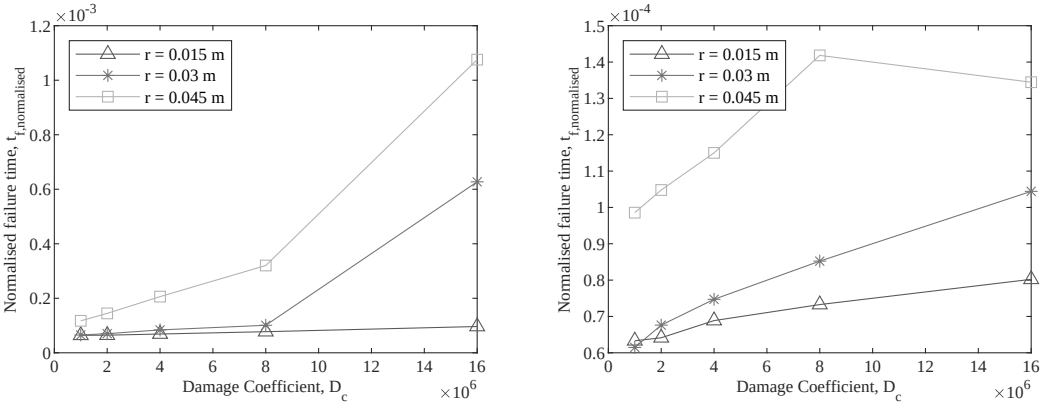

(a) SEF criterion

(b) MEF criterion

FIGURE 8.25: Plots of normalised failure time determined by the size of the hole created against the damage coefficient used for varying particle radius

8.3.4 Findings

Previously Section 4.4.4 discussed the variation of the damage parameter with respect to the mesh and, in combination with Section 4.3.4, established a starting point for damage and time to failure predictions. This section keeps the mesh consistent and looks at the effect of particle size and damage acceleration parameter on the calculation of time to failure. The initial expectation was that time to failure is inversely proportional to the particle/element size ratio as was suggested in Chapter 4. Here follows an attempt to create a model of how predicted failure times vary with respect to the mesh, damage coefficient and particle size based on equation 8.2 below.

$$F_t = F_{SEF} + H_t \tag{8.2}$$

Where F_{SEF} is the time to failure (SEF criterion), and H_t is the accumulation time of the hole.

The first term on the rhs in equation 8.2 is a combination of the varying parameters throughout the simulation and a constant C_1 is introduced. The equation below predicts the time to failure of the model using the SEF criterion, equation 8.3.

$$F_{SEF} = \frac{C_1}{C_d r R^{1/3}} \tag{8.3}$$

The second term on the rhs in equation 8.2 is the hole accumulation time, H_t. This is a function of particle mass, m, impact velocity, v, damage coefficient, C_d, hole area, A_h, particle/element ratio, R, and a coefficient C_2.

$$H_t = \frac{C_2}{C_d} . \frac{A_h R^{1/2}}{m v^{1/2}} \tag{8.4}$$

Coefficients C_1 and C_2 are both found by using a least squares regression to fit the F_{SEF} and H_t respectively from the results of a single simulation. The results of this are plotted for varying particle sizes in Figure 8.26. The simulation parameters used to create the prediction were $r = 0.03m$ and $C_d = 1,000,000$.

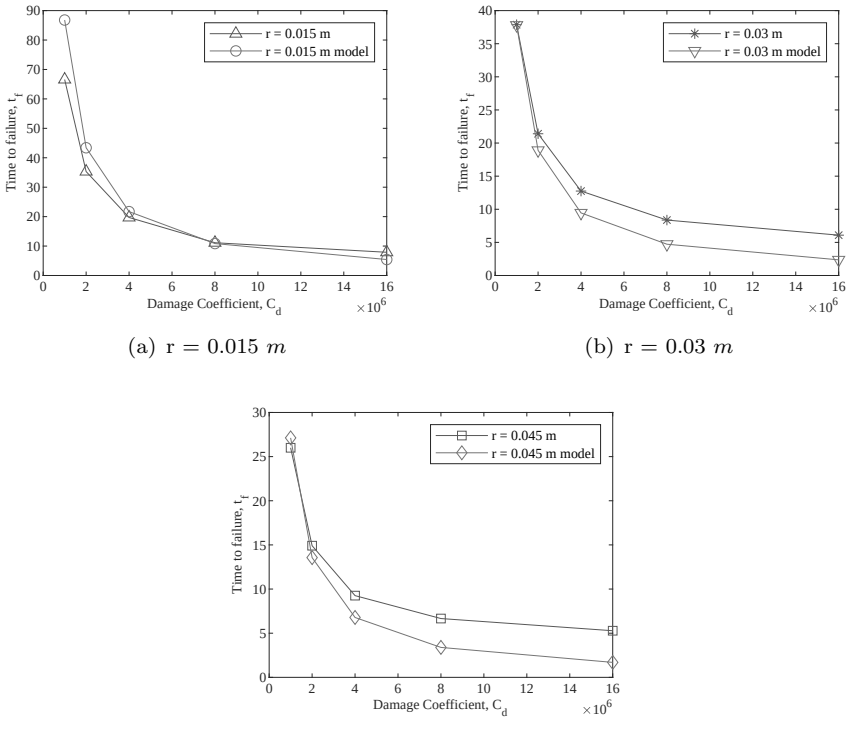

(a) r = 0.015 m

(b) r = 0.03 m

(c) r = 0.045 m

FIGURE 8.26: Predictions of the multiple element failure time prediction model against damage coefficient for varying particle radius

Figure 8.26(a) shows good agreement for large variations in damage coefficient and a halving of particle size. For an increase in particle radius, shown in 8.26(c), an initially

accurate prediction at a low damage coefficient value is obtained. However, this becomes less accurate as the damage coefficient increases. This is suggested to be a function of the relatively short failure time predicted for both the F_{SEF} and H_t values probably causing a larger error. At larger particle sizes and high damage coefficients this is possibly an indication of the simulation itself becoming less reliable. Therefore, these values should be avoided when using DEM simulations to predict failure times.

Part IV

Final Thoughts

Chapter 9

Discussion

Chapter 1 outlined a series of objectives for this work which the previous chapters have worked towards. For convenience, these have been reproduced here as follows:

- Investigate the application of the Discrete Element Method in relation to impact and wear modelling.
- Implement a method of assessing wear in industrial system into DEM for both possible material and design changes.
- Compare the predictions from DEM to known real-world wear found on-site at TATA steel, and complete this within a reasonable timeframe.

This chapter will highlight each of these original aims and discuss how these have been approached and achieved. It will conclude with the author's own thoughts regarding wear modelling in DEM based on their experience working on this project.

9.1 Wear Modelling in DEM

The work carried out in this thesis is by no means exhaustive; variations and different applications are always going to exist. This is especially true when considering the assumptions which DEM is inherently bound by which were covered in Chapter 2. These assumptions are necessary for two main reasons: (1) is their requirement for the simulation of granular materials and the complicated behaviours which they display and (2) is the limitation associated with the computational time required for simulating granular materials and their interactions with structures.

Analysing wear itself adds varitey as no single wear model is able to sufficiently represent all wear causeded by granular material impacts found in industry due to the sheer number of different applications granular materials are used in. Whether it be the pnuematic conveyance of coal through a coal injection lance, the relatively slow impact of coke on a wear plate or a slurry travelling through a pipeline. As such this is readily reflected in the literature reviewed in Chapter 3. With wear generally being divided up into multiple categories.

In applying wear modelling methods throughout this works as shown in, Chapters 4, 6, 7 and 8. It was found that DEM contained a unique benefit. Multiple wear models could be computed at once. Which, due to the already significant computational cost, has negligible impact on the calculation. Therefore, it was possible to model multiple wear mechanisms in one simulation and assess them all.

Throughout this thesis, four established wear models were used: Archard's abrasion model, Finnie's ductile erosion model, Bitter's brittle erosion model and Clark and Wong's combined erosion model. However, regarding established models, DEM is by no means limited to these [55][67][75][76][83]. A promising expansion is Oka's wear model, but this would require a large amount of material characterisation which is a limitation to the solely computational nature of the work carried out here.

During the applications, it was found using single wear models were generally not sufficient to replicate real-world industrial failures where material and/or design changes can take place. This arises from both, how a material wears in relation to the particles impacting it as was discussed in Chapter 3, and how the particle kinematics inside an industrial system change with changes in design. This was considered for an industrial coke screener in this work in Chapter 6. In this it was shown that for a considerable design change, a curved plate instead of a flat plate for example, a considerable increase in ductile erosion could be expected as shown in Section 6.8.3. Therefore, if a material was known to be susceptible to ductile erosion this would possibly result in a more rapid

failure through increased wear. Engineering judgement can therefore be excercised to limit this risk of this possible outcome.

To replicate a wider range of wear mechanisms, and assess if secondary wear mechanisms become more prominent with changes in operation/design of a system, an approach of investigating wear through a DEM perspective was used. Instead of applying individual wear models. Ultimately, this results in a wear being reduced to an energy calculation. These formulation have been stated in Table 9.1, and it includes comparisons to known wear mechanisms which have been seen throughout. Naturally, these formulations also appear in the literature for wear modelling and these have been referenced where appropriate.

TABLE 9.1: DEM energy models and the established models which they are comparable to

Equation	**References**	**Comparable to**
$E_1 = c_n v_n v_n dt$		Abrasion/Brittle erosion
$E_2 = c_n v_n v_t dt$		Combined erosion
$E_3 = c_t v_t v_n dt$		Combined erosion
$E_4 = c_t v_t v_t dt$	[115]	Ductile erosion
$E_5 = F_n v_n dt$		Brittle erosion
$E_6 = F_n v_t dt$	[55]	Abrasion
$E_7 = F_t v_n dt$		Abrasion
$E_8 = F_t v_t dt$	[88]	Combined erosion
$E_9 = \frac{1}{2} k_n \delta^2$		Brittle erosion
$E_{10} = \frac{1}{2} k_t \delta^2$		Combined erosion
$E_{11} = \frac{1}{2} k_{eff} \delta^2$		Combined erosion
$E_{12} = \frac{1}{2} m v_n^2$		Abrasion
$E_{13} = \frac{1}{2} m v_t^2$		Ductile erosion
$E_{14} = \frac{1}{2} m v^2$		Ductile erosion

The formulations can take multiple approaches, a trend which is analagous to analytical and experimental models found in Chapter 3. The models shown in Table 9.1 however, are all formulated using the information available inside a DEM simulation. Which overcomes an issue which arises when using experimental models inside a DEM environment, as not all information required for wear models is available inside DEM.

Using a variety of wear modelling methods which DEM is capable of producing allows the generation of a large amount data about of possible wear mechanisms, at which point the user may use their own experience to determine possible issues and applications with their engineering judgement.

9.2 Damage and wear assessment in industrial systems

After modelling wear through DEM, it becomes apparent that using a wear energy is not always enough. There are two components to using a wear model and applying it to an industrial system. The first is understanding the mechanisms of wear. This allows the prediction of where wear occurs, how it occurs and why it occurs. The second is the method of assessing a time to failure. This addresses how much wear occurs, which must be established through material properties.

The main material property used throughout this work to quantify the amount of 'wear' is hardness. Which, whilst not an all encompassing material property for wear, has proved effective in creating damage predictions. Likely due to the nature of the applications being highly focussed on the abrasive wear mechanism. Further material properties which can affect wear and which were considered are shown in Chapter 3. In summary, these are: yield strength, fracture toughness and young's modulus. Understanding how these interact and affect a particular scenario is the most important aspect of applying a wear model in industry (and academia).

The second component is once a wear mechanism is selected and the material property is chosen. How is a time value actually determine? This for the DEM application, becomes a function of the mesh. This thesis, used the unique approach of creating a quasi-volume from the mesh by utilising the element area and a known thickness of plate. This is laid out in detail in Chapter 4.

This allowed two methods of creating a time to failure prediction. These were named the Single Element Failure and Multiple Element Failure. The first was used successfully in the assessment of trial materials and informing engineers the extent to which a material could improve the life of their system, Chapter 6. Which, in combination with the energy formulations, allows a range of wear mechanisms and materials to be assessed rapidly from a single simulation.

The Multiple Element Failure, allowed the assessment of hole development and would allow an understanding to be developed of the possible effect of design changes on hole and subsequent material behaviour. The behaviour of both these methods was investigated in Chapter 8.

9.3 Industrial Application

The final objective of this thesis was to apply a model and use it at TATA Steel. This was done through Chapters 6 and 7. The first application was to the Coke Screener. Through this, a material trial was set up using the known wear plate material, stainless steel, and the trial material, ColWear 62-1 provided by Wall Colmonoy. Through this, the methods set out for assessing wear and damage in DEM were tested and models were validated. In this process, Archard's abrasion model, or the E_6 model shown in Table 9.1 was used to assess the trial material and provide lifetime extenstion predictions. This was then tested in a trial and found to be conservative.

The benefits of using multiple wear models inside a DEM model were seen first hand as numerous different wear possibilities could be presented to the user and operator. From this, appropriate wear models could be selected and the analysis run accordingly.

A second application was the coal injection lances on the blast furnace which pnuematically convey small particles of coal. These had known wear issues, and was an extremely different challenge to the first application. This was also successfully replicated after a method of applying a steady-state CFD velocity profile was developed for use in DEM, Chapter 5, without incurring any additional computational cost to the DEM solver.

9.4 Author's Thoughts

Modelling anything with DEM is tricky. To the author's knowledge it is perhaps one of the most involved computational methods there is as it is inherently a method which does not physically represent a system through a 'real' assumption. For example it allows overlaps between particles which is ultimately not true. However, it does allow for the modelling of particles, and the interactions between them and it does so relatively accurately at the cost of high computational time as each individual particle behaviour and collision must be calculated individually. While it may use assumptions which are not true, such as overlaps, the use of springs, assumptions regarding slip and friction etc., the bulk behaviour does replicate reality effectively which is ultimately the purpose of any computational model.

DEM seems to lie at this odd intersection between replicating the physical behaviour of a material through science and via observation. Having visual data to compare simulations to is the main method through which models are validated, however, validating the exact quantities of material worn from an industrial material handling surface is very challenging. Accurate laboratory replication is also difficult for these types of systems.

The difficulty and complexity of wear modelling also poses considerable issues. The large number of wear models available in the literature range from the early works by Archard and Finnie which were relatively simple in nature to the more complex and intricate works carried out by Hutchings, Oka and others. In recent years the author believes wear modelling has generally drifted back towards the simpler models in terms of predictions, as though they are often limited in accuracy they are more user friendly and generally more widely applicable. This has been seen in this thesis where 'simple' wear/energy models accurately predict industrial failures. Numerous authors have highlighted the fact wear models often require specific equipment to be used and standards are not generally available. Often researchers make their own versions of testing equipment which is not following standardised testing procedures and makes comparisons difficult. Authors of wear models also do not tend to stay in the field long, and therefore their models remain unused and undeveloped.

The author hopes the work in this thesis has shed some light on the potential for modelling wear and damage in a general sense. The ideal case, the author believes, would be the use of DEM to create a force profile upon a system to which then an FEM program can be used to calculate the wear transiently. However, the computational intensity and time required for this makes the results it would obtain practically useless, and the ability to model on an industrial scale is likely decades away if not longer.

DEM is itself a somewhat flawed tool, but as long as the user remembers that fact, it can be used effectively.

Chapter 10

Conclusion

10.1 General Conclusions

- Known wear models have been presented for application in the Discrete Element Method for modelling impact and wear.
- The effect of the mesh has been investigated and it was found the discretisation of the mesh has a very small effect on the global wear calculation with a variation of 0 - 5 %.
- A linear damage model, which can utilise any wear model, has been presented for calculation of failure times. The damage model variation with respect to mesh discretisation was found to create a divergent behaviour based on the mesh discretisation either refining or coarsening. Therefore the mesh must be carefully considered for wear prediction in DEM, a method to asses this is suggested in Chapter 4.
- Failure times in an industrial setting have been discussed using industrial scale testing. Two methods were developed to assess this in Chapter 4. The first method presented was the Single Element Failure (SEF) criterion for use in rapid gauging of material performance. The second was the Multiple Element Failure (MEF) criterion, demonstrated and assessed in respect to variation of damage coefficient and particle size.

10.2 Industrial Case Study Conclusions

10.2.1 Coke Screener

- Initial industrial failure times were provided anecdotally at 2 - 4 weeks using stainless steel wear plates. An industrial trial was run using Wall Colmonoy's ColWear 62-1 coated wear plate. DEM predicted a 3.5x - 4.5x life improvement through the use of this new material. The plate remained in service for 23 weeks (or a 5.3x life improvement). The DEM model proved to be pessimistic, however, it gave a good indication as to the possible improvement of using this new material.
- Variations in the operatioanl parameters of the coke screener were investigated and the effects of the subsequent wear discussed.

10.2.2 Coal Injection Lance

- A Finite Difference Method (FDM) based velocity profile was developed and applied inside DEM. Using this known industrial failure modes were recreated and the causes investigated. It was predicted the diameter restriction and gaps created due to threading were causing an internal disturbance moving particles into the free stream. This in turn was reducing collisions with the surrounding structure and was therefore reducing the wear in the lance.
- A failure area due to a bend in the lance was also accurately predicted using the velocity profile method.

10.3 Future Work

- Further investigations surrounding the effectiveness of the proposed DEM failure analysis methodology is required for further use. This would involve validating against a known system where the design is alterable. Finding such a suitable industrial system is thought to be unlikely and for a large scale system it would be costly.
- Looking forward an ideal case would utilise both DEM and FEM in a combined model whereby the stresses and strain can be calculated for the material as a continuum as opposed to the element based wear used in this work. There is research in this area regarding single particle impacts. However, work to expand this to multiple particle systems is needed to account for particle kinematics.
- A link between the simulation and wear based experimental work needs to be explored in relation to replicating industrial issues with regards to wear resulting from impacts of materials.
- The implementation of a more efficient search algorithm for structural elements (in similar fashion to the use of the Octree for particles) is needed. This could provide considerable speed up of the program and be a major step forwards to reduce the computational time currently spent searching through structural elements. However, careful consideration would be required, as the search would cover a volume created by an element instead of a point created by the particle.
- Inclusion of the effects of non-spherical drag coefficients for use within the program would be an interesting step forward for the velocity profile application.

Appendix A

Mathematical Derivations

The purpose of this appendix is to show the derivations used for all equations presented in the thesis.

A.1 Taylor Expansions of Energy Calculations

The general form of the Taylor expansion is expressed as follows where $f(a)$ is the function being considered where a is a point defined in some function $f(x)$.

$$f(a) + \frac{f'(a)}{1!}(x-a) + \frac{f''(a)}{2!}(x-a)^2 + \frac{f'''(a)}{3!}(x-a)^3 + ... \tag{A.1}$$

Detailed here are all the Taylor Expansions used to predict the summation of the energy equations. Of the equations derived there are 5 general versions which can be considered. The general forms of this are shown in equations A.2, A.3, A.4, A.5 and A.6.

For consistency throughout the derivation v_1 and v_2 represent a component of the impact velocity v. In use these can be substituted by either the normal and/or tangential components, except where otherwise stated.

$$f(a) = cv_1^2 dt \tag{A.2}$$

$$f(a) = c_1 v_1 v_2 dt \tag{A.3}$$

$$f(a) = F v_1 dt \tag{A.4}$$

$$f(a) = k_1 x^2 \tag{A.5}$$

$$f(a) = mv^2 \tag{A.6}$$

In this case of equation A.6 v can be replaced with v_1 also as it could be considered as the kinetic energy of a specific component of the equation.

A.1.1 Method 1

Method 1 calculates the Taylor expansion for general form 1 reproduced in equation A.7

$$f(a) = c_1 v_1^2 dt \tag{A.7}$$

A general form of the multivariable chain rule is as shown in equation A.8. Where D_i represents the relevant partial derivative.

$$\frac{d}{dt}f(a_1(t),...,a_k(t)) = \sum_{i=1}^{k}\left(\frac{d}{dt}a_i(t)\right)D_i f(a_1(t),...,a_k(t)) \tag{A.8}$$

Where E_1 is taken to represent $f(a)$ in equation A.1. This gives the first derivative as equation A.9 using the multivariable chain rule. Remembering $dt = t_0 - t_1$ and $v_1 = a_1 dt$.

$$f'(a) = 2c_1 v_1 a_1 dt \tag{A.9}$$

The second derivative is as follows in equation A.10.

$$f''(a) = 4c_1 v_1 a_1 \tag{A.10}$$

The third derivative is as shown in equation A.11.

$$f'''(a) = 4c_1(v_1 J_1 + a_1^2) \tag{A.11}$$

Where J represents jerk i.e., the derivative of acceleration.

These equations combined gives the Taylor expansion for method 1 as shown in equation A.12.

$$f(a + \Delta t) = f(t) + 2c_1 v_1^2 dt + 2c_1 v_1 a_1 dt^2 + \frac{4}{6}c_1(v_1 J_1 + a_1^2)dt^3 \tag{A.12}$$

A.1.2 Method 2

Method 2 focusses on the form where both the normal and tangential components are used. One is used in the damping force component of the equation and the other is used in the projected slide distance for a single timestep. The general form is reproduced here as shown in equation A.13.

$$f(a) = cv_1 v_2 dt \tag{A.13}$$

The first derivative if the second method is as shown in equation A.14.

$$f'(a) = c_1(a_1 v_2 dt + a_2 v_1 dt) \tag{A.14}$$

It should be noted $v_1 = a_1 dt$ therefore equation A.14 can be simplified to A.15.

$$f'(a) = 2c_1 v_1 v_2 \tag{A.15}$$

The second derivative can then be found as shown in equation A.16

$$f''(a) = 2c_1(a_1 v_2 + a_2 v_1) \tag{A.16}$$

The third derivative can then be found as shown equation A.17.

$$f'''(a) = 2c_1(2a_1 a_2 + v_1 J_2 + v_2 J_1) \tag{A.17}$$

Using equations A.13, A.15, A.16 and A.17 the Taylor expansion can be found as shown in equation A.18.

$$f(t+\Delta t) = f(t) + 2c_1 v_1 v_2 dt + c_1(a_1 v_2 + a_2 v_1)dt^2 + \frac{1}{3}c_1(2a_1 a_2 + v_1 J_2 + v_2 J_1)dt^3 \tag{A.18}$$

A.1.3 Method 3

The third method is used to calculate the Taylor expansion when the equation used the already calculated force, F_1, and the projected slide distance $v_1 dt$. These can be combined with the tangential and normal components to create the relative equations shown in table 4.2, in chapter 4.

$$f(a) = F_1 v_1 dt \tag{A.19}$$

An assumption is made regarding the force component of the equation. It is assumed to remain constant throughout and is therefore treated as a constant as it has already been calculated using a Taylor expansion.

The first derivative of equation A.19 is shown in equation A.20.

$$f'(a) = F_1 a_1 dt \tag{A.20}$$

Using $v_1 = a_1 dt$, equation A.20 can be simplified to equation A.21.

$$f'(a) = F_1 v_1 \tag{A.21}$$

The second derivative can then be found as shown in equation A.22.

$$f''(a) = F_1 a_1 \tag{A.22}$$

The third derivative can then be found as shown in equation A.23.

$$f'''(a) = F_1 J_1 \tag{A.23}$$

Using equations A.19, A.20, A.22 and A.23 the Taylor expansion can found as shown in equation A.24.

$$f(t + \Delta t) = f(t) + F_1 v_1 dt + \frac{F_1 a_1}{2} dt^2 + \frac{F_1 J_1}{6} dt^3 \tag{A.24}$$

A.1.4 Method 4

The fourth method uses the spring constant, k, and overlap value to calculate the spring energy of the collision. The equation in question is reproduced in equation A.25.

$$f(a) = \frac{1}{2} k_1 x_1^2 \tag{A.25}$$

The first derivative of equation A.25 is calculated and is shown in equation A.26.

$$f'(a) = k_1 x_1 v_1 \tag{A.26}$$

From equation A.26, the second derivative is calculated as shown in equation A.27.

$$f''(a) = k_1 (x_1 a_1 + v_1^2) \tag{A.27}$$

The third derivative can then be found as shown in equation A.28.

$$f'''(a) = k_1(x_1 J_1 + 3a_1 v_1) \tag{A.28}$$

Combing equations A.25, A.26, A.27 and A.28, the Taylor expansion can be found as shown in equation A.29.

$$f(t + \Delta t) = f(t) + k_1 x_1 v_1 dt + \frac{k_1(x_1 a_1 + v_1^2)}{2} dt^2 + \frac{k_1(x_1 J_1 + 3a_1 v_1)}{6} dt^3 \tag{A.29}$$

A.1.5 Method 5

The fifth method uses the kinetic energy of the collision. The general form for this is reproduced in equation A.30.

$$f(a) = m v_1^2 \tag{A.30}$$

Using equation A.30 the first derivative can be found and is shown in equation A.31.

$$f'(a) = m a_1 v_1 \tag{A.31}$$

Equation A.31 can be simplified using $F_1 = m a_1$ to equation A.32.

$$f'(a) = F_1 v_1 \tag{A.32}$$

The second derivative can then be found and is shown in equation A.33.

$$f''(a) = F_1 a_1 \tag{A.33}$$

The third derivative can then be found and is shown in equation A.34.

$$f'''(a) = F_1 J_1 \tag{A.34}$$

Using equations A.30, A.32, A.33 and A.34 the Taylor expansion can be found as shown equation A.35.

$$f(t+\Delta t) = f(t) + F_1 v_1 dt + \frac{F_1 a_1}{2} dt^2 + \frac{F_1 J_1}{6} dt^3 \tag{A.35}$$

Appendix B

Further Sections

This appendix contains further sections and images which were not included in the thesis which were removed from the main text but may be of interest to the reader. Certain sections of this appendix include relevant discussion and explanation where appropriate.

B.1 Repetitive Impact Rig

As part of the plan for this project the design, development and build of an experimental rig which would characterise the wear resistance of materials with respect to angle of impact. The intent was then to develop models based on the material to assess its wear resistance on a machine, with the knowledge of wear resistance at various angles giving insight to the effects.

Planning and design initially proceeded well. A motor driven flywheel design was selected, which would strike a plate repeatedly using a linear motion. It was to consist of multiple parts, the first was the motor and flywheel which was drive the rotary movement. This was then converted into linear motion for the striker. Finally, the plate holder and angle adjustor had angle increments of 10° allowing experimentation between 10 - 90°. However during the build, an unfortunate event occurred which meant progress on the build became delayed considerably, eventually taking approximately 1.5 years. Figure B.1 shows the rig built in the workshop once the initial delay was overcome.

FIGURE B.1: Repetitive Impact Rig build in workshop

Later in the setup process an issue was found with the rig as the motor initially selected was not strong enough to drive the flywheel and impactor. This was a function of the mass which the motor was required to move which was underestimated. Therefore, a second motor was purchased, however it also became delayed which became catastrophic to an already extremely delayed project. With this it was decided to move forward on the project without the rig. This created the main drawback with this work, as no experimental link was ultimately created.

B.2 Chapter 6: Coke Screener

Figure B.2 shows the energy transfer pattern predictions for the remaining energy models E_9 through E_{14} for the curved plate studied in the coke screener case study. Here it can be seen from figures B.2(b), (e) and (f), E_{10}, E_{13} and E_{14} respectively all predict similar patterns to the ductile erosion models and E_4 which was discussed in chapter 6. This is due to their heavy dependence on the tangential component in their equations, as E_{10} represents the tangential component of the spring energy, and E_{13} and E_{14} represent the tangential velocity and total velocity respectively. It brings forward a conclusion the velocity at run off is mostly dominated by the tangential component.

Figure B.2(d) shows energy transfer models, E_{12}, formulated through the use of the normal component of kinetic energy. It shows a similar wear pattern in appearance to the abrasion models presented in the main text.

B.3 Chapter 7: Coal Injection Lance

Figures B.3 - B.16 shows the transfer patterns predicted created for the energy models created. The majority of which displayed the focus of wear on the threaded end of lance for case 1 which worsens moving into case 2. Case 3 shows a general increase in wear across the entirety of the lance.

B.4 Chapter 8: Parameters

B.4.1 Mass flow rate

This section contains the mass flow rate plots against time generated using energy models E_9 to E_{14} as shown in figure B.17. Figure B.18 shows the total energy transfer plotted against the mass flow rate of the simulation.

Figures B.19 - B.32 shows the transfer patterns predicted for the energy models E_1 to E_{14}.

B.4.2 Coefficient of restitution

Figure B.33 shows the total energy transfer for the energy models E_9 to E_{14}.

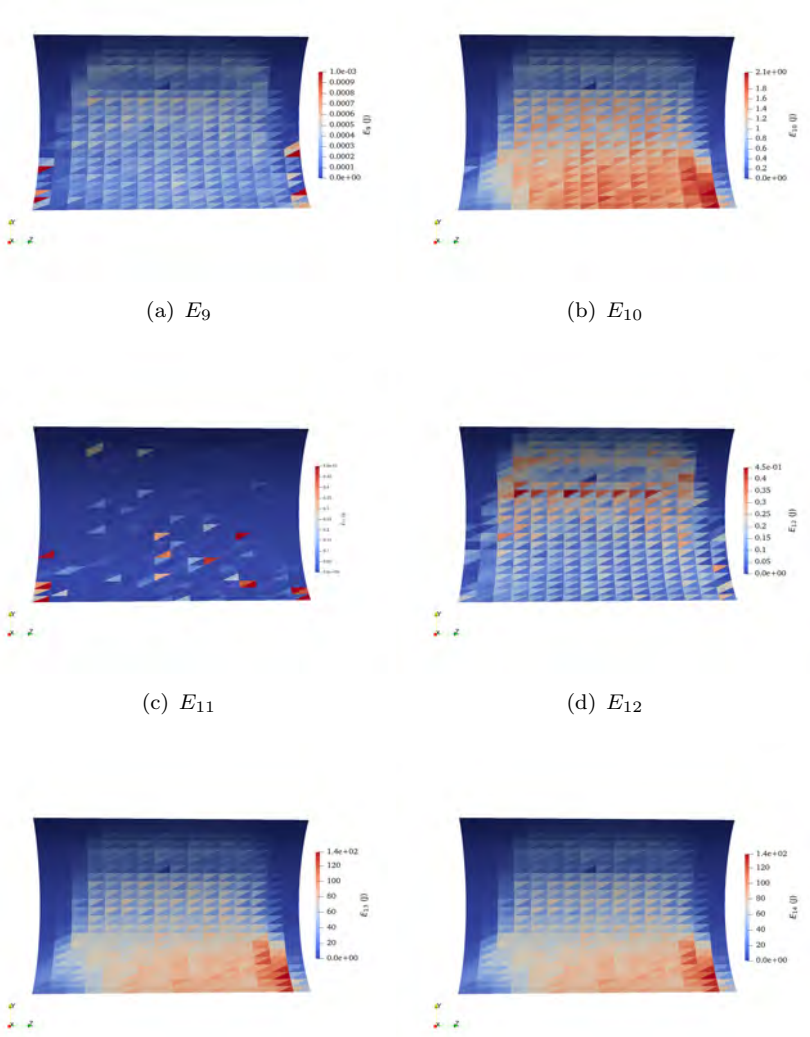

(a) E_9 (b) E_{10}

(c) E_{11} (d) E_{12}

(e) E_{13} (f) E_{14}

FIGURE B.2: Predicted energy transfer model patterns on the curved plate design

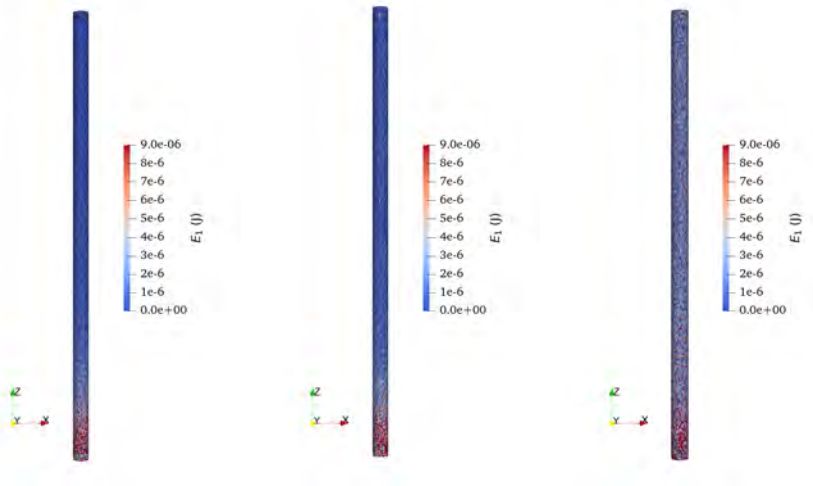

(a) Case 1 (b) Case 2 (c) Case 3

FIGURE B.3: Energy transfer model E_1 pattern prediction for the coal injection lance cases

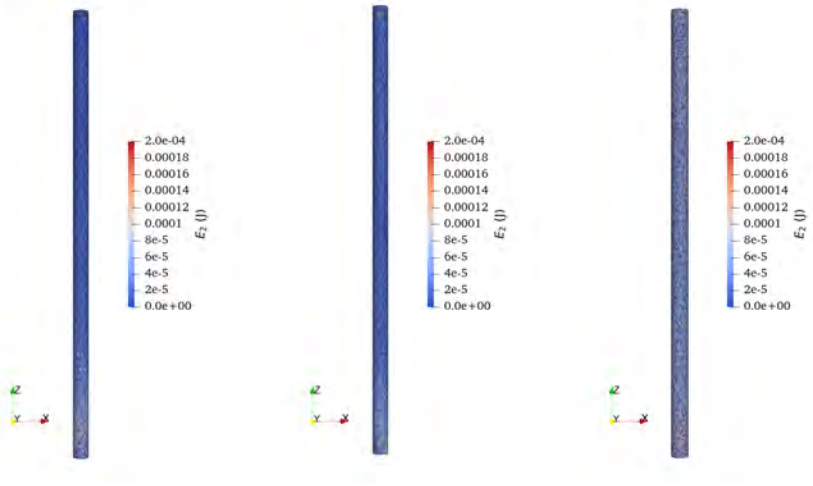

(a) Case 1 (b) Case 2 (c) Case 3

FIGURE B.4: Energy transfer model E_2 pattern prediction for the coal injection lance cases

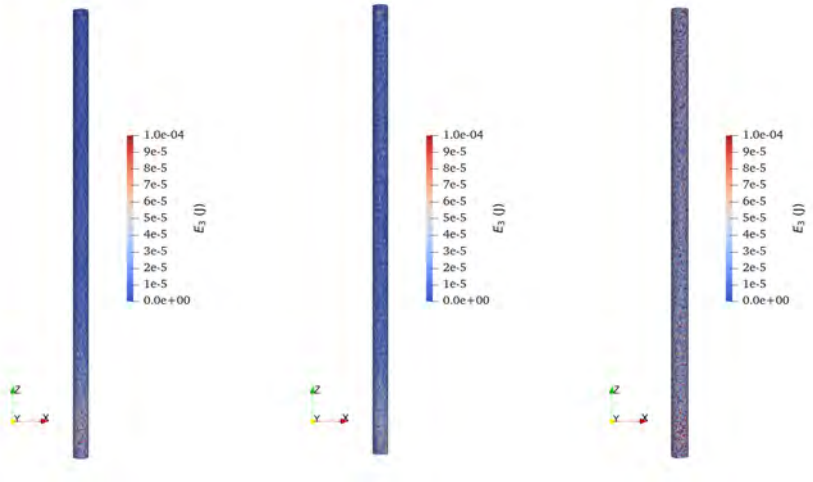

(a) Case 1 (b) Case 2 (c) Case 3

FIGURE B.5: Energy transfer model E_3 pattern prediction for the coal injection lance cases

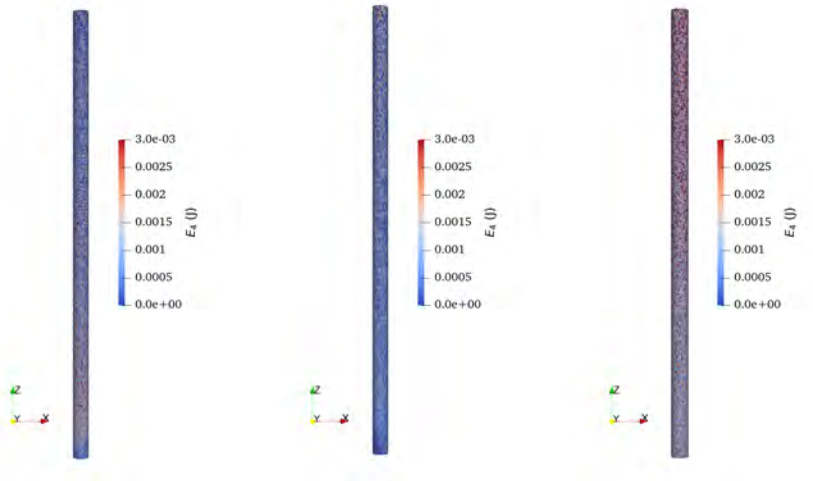

(a) Case 1 (b) Case 2 (c) Case 3

FIGURE B.6: Energy transfer model E_4 pattern prediction for the coal injection lance cases

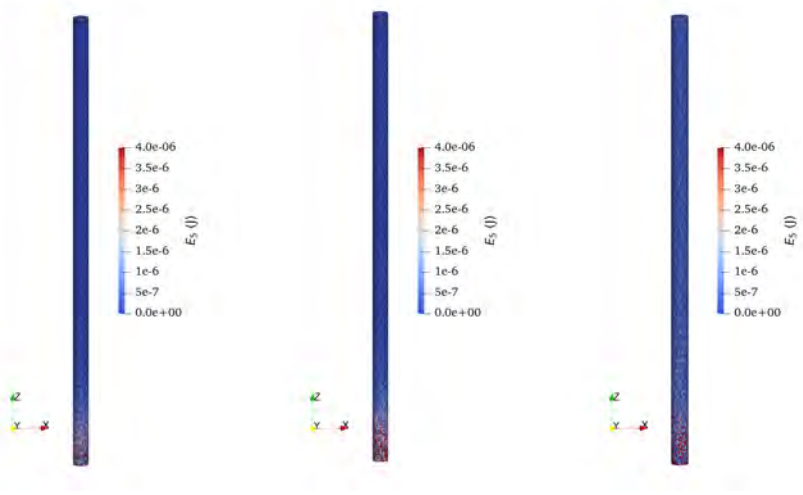

(a) Case 1 (b) Case 2 (c) Case 3

FIGURE B.7: Energy transfer model E_5 pattern prediction for the coal injection lance cases

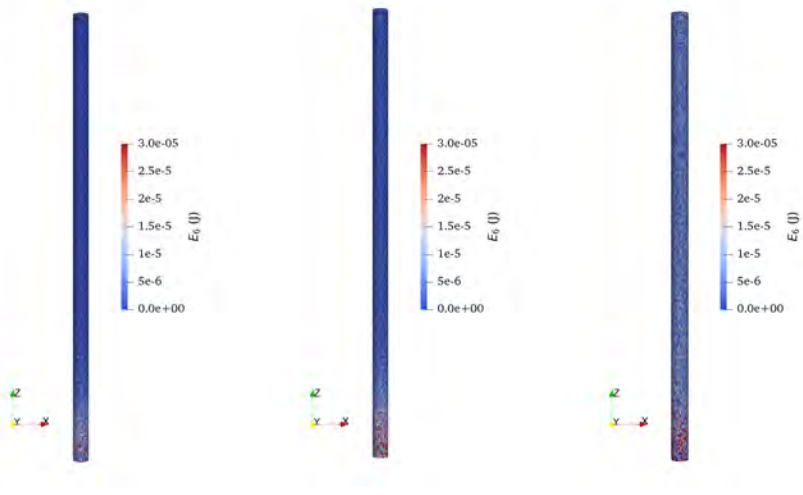

(a) Case 1 (b) Case 2 (c) Case 3

FIGURE B.8: Energy transfer model E_6 pattern prediction for the coal injection lance cases

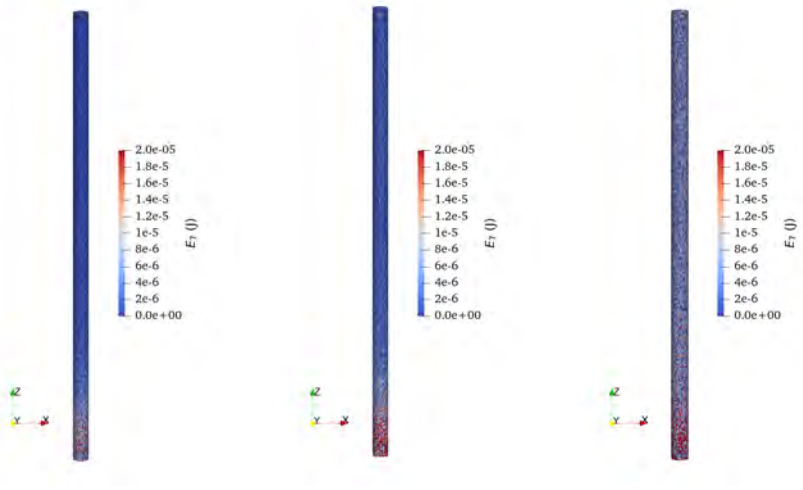

(a) Case 1 (b) Case 2 (c) Case 3

FIGURE B.9: Energy transfer model E_7 pattern prediction for the coal injection lance cases

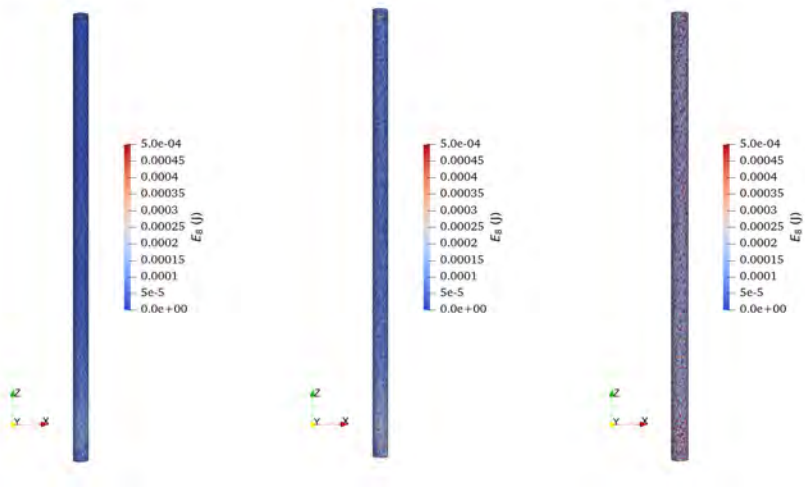

(a) Case 1 (b) Case 2 (c) Case 3

FIGURE B.10: Energy transfer model E_8 pattern prediction for the coal injection lance cases

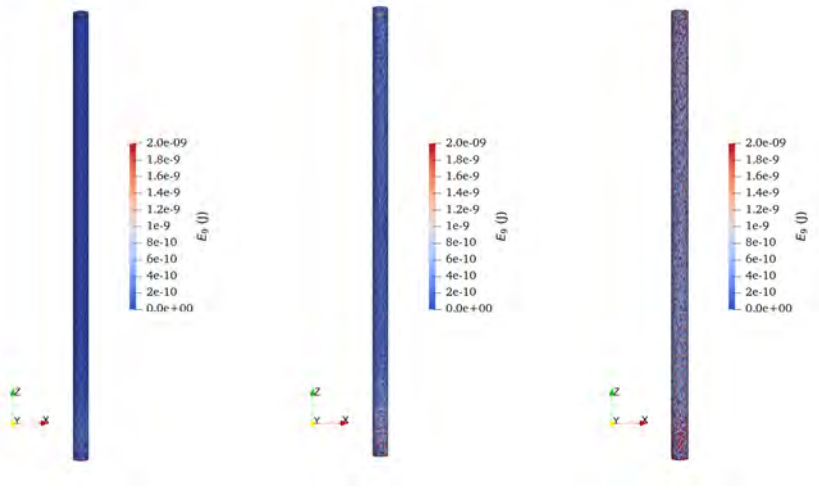

(a) Case 1 (b) Case 2 (c) Case 3

FIGURE B.11: Energy transfer model E_9 pattern prediction for the coal injection lance cases

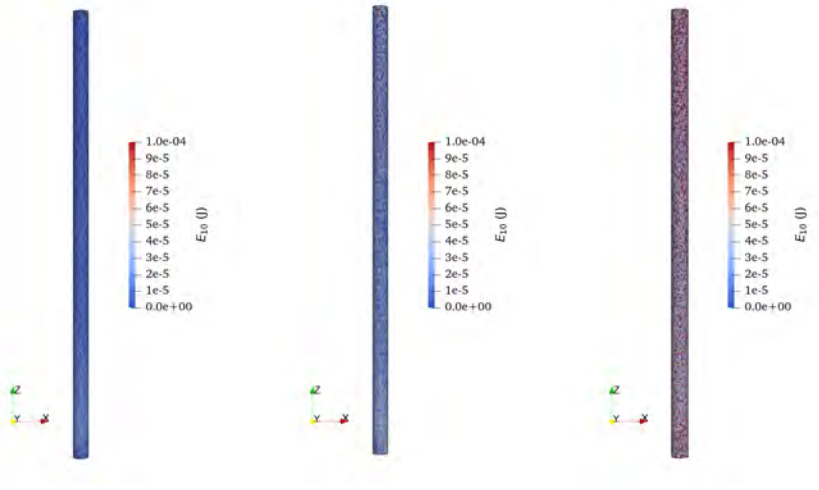

(a) Case 1 (b) Case 2 (c) Case 3

FIGURE B.12: Energy transfer model E_{10} pattern prediction for the coal injection lance cases

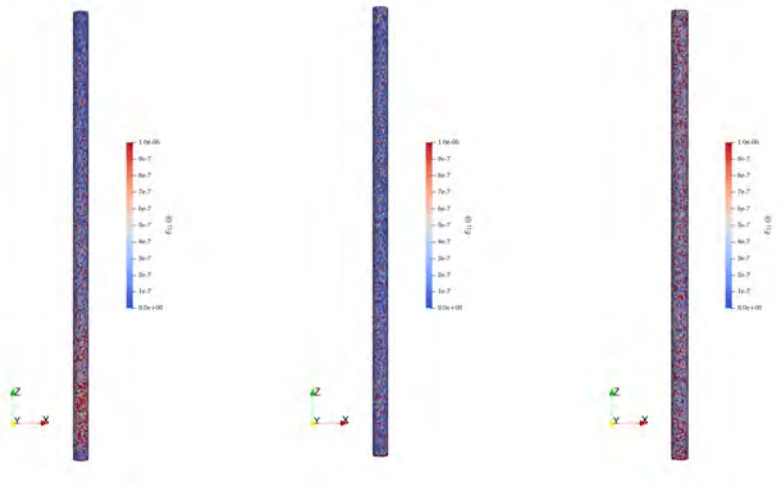

(a) Case 1 (b) Case 2 (c) Case 3

FIGURE B.13: Energy transfer model E_{11} pattern prediction for the coal injection lance cases

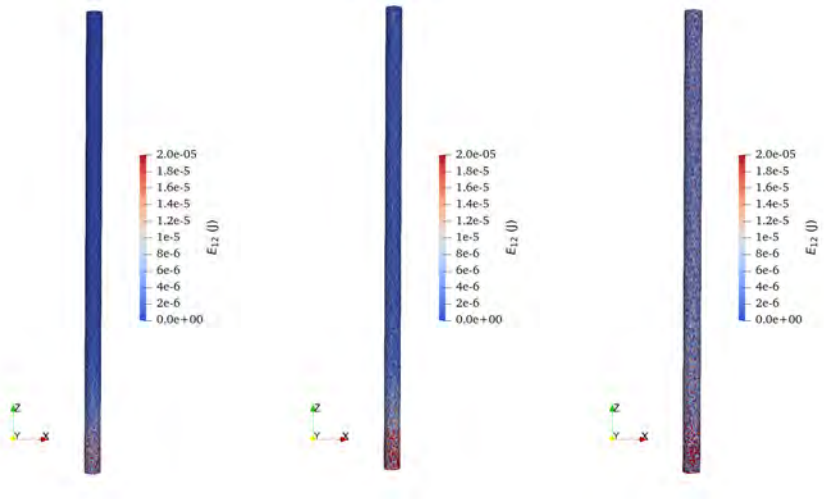

(a) Case 1 (b) Case 2 (c) Case 3

FIGURE B.14: Energy transfer model E_{12} pattern prediction for the coal injection lance cases

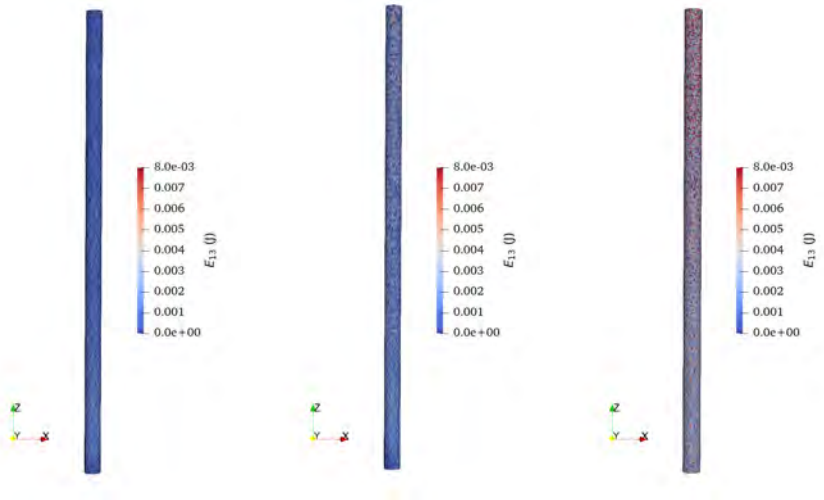

(a) Case 1 (b) Case 2 (c) Case 3

FIGURE B.15: Energy transfer model E_{13} pattern prediction for the coal injection lance cases

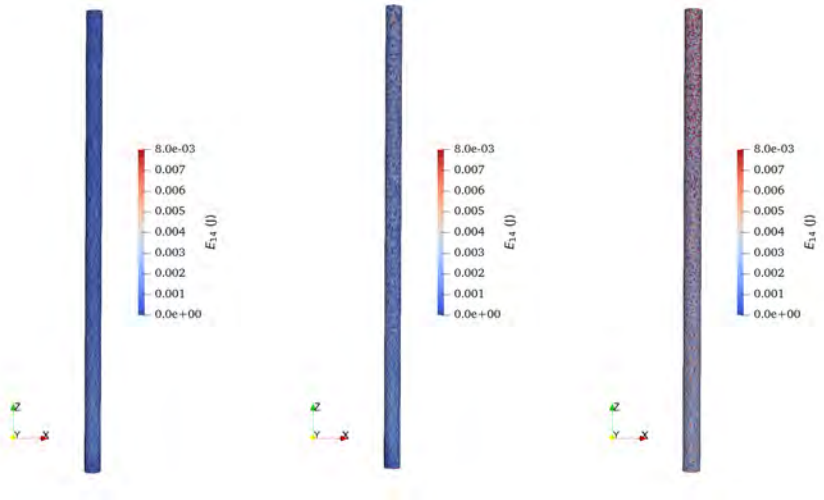

(a) Case 1 (b) Case 2 (c) Case 3

FIGURE B.16: Energy transfer model E_{14} pattern prediction for the coal injection lance cases

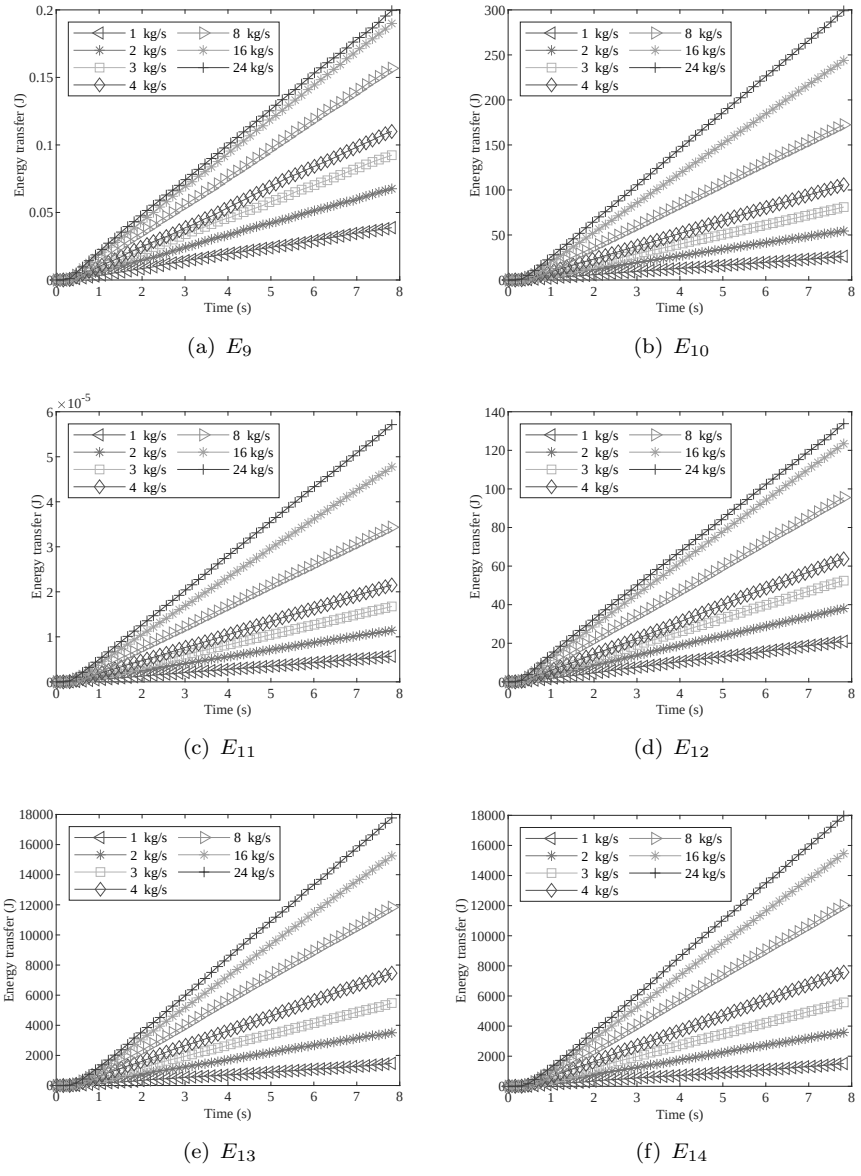

(a) E_9 (b) E_{10}

(c) E_{11} (d) E_{12}

(e) E_{13} (f) E_{14}

FIGURE B.17: Total energy transfer predicted over time with varying mass flow rate

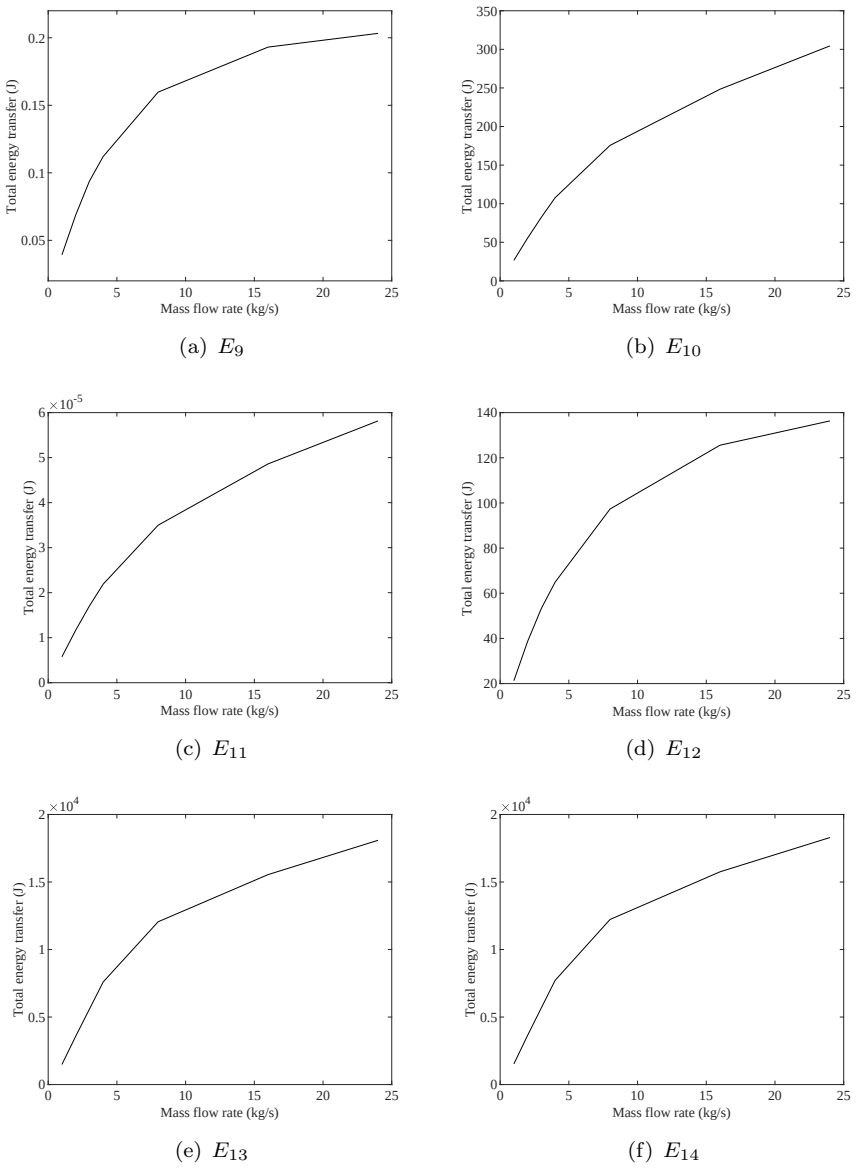

(a) E_9 (b) E_{10}

(c) E_{11} (d) E_{12}

(e) E_{13} (f) E_{14}

FIGURE B.18: Total energy transfer plotted against mass flow rate

(a) 1 kg/s

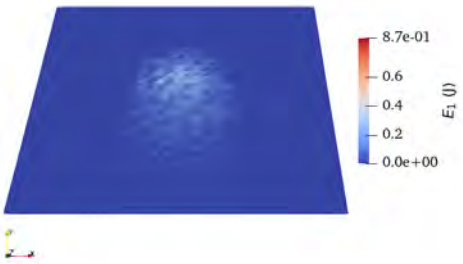

(b) 2 kg/s

(c) 3 kg/s

(d) 4 kg/s

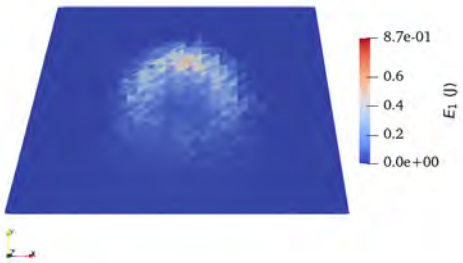

(e) 8 kg/s

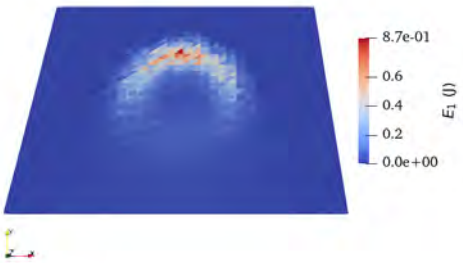

(f) 16 kg/s

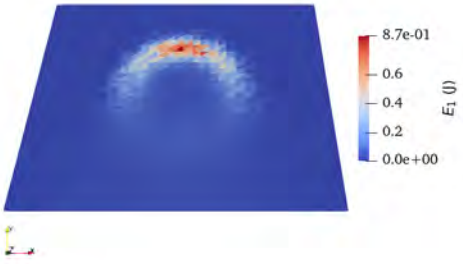

(g) 24 kg/s

FIGURE B.19: Energy transfer patterns predicted using the E_1 model for varying mass flow rate

(a) 1 kg/s

(b) 2 kg/s

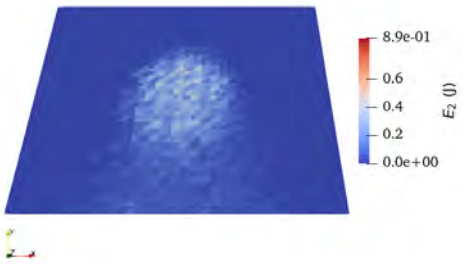

(c) 3 kg/s

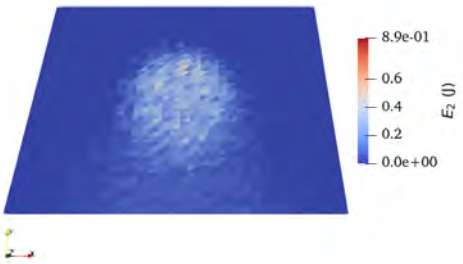

(d) 4 kg/s

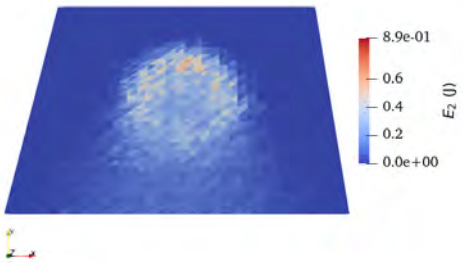

(e) 8 kg/s

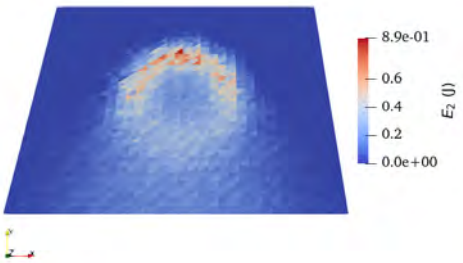

(f) 16 kg/s

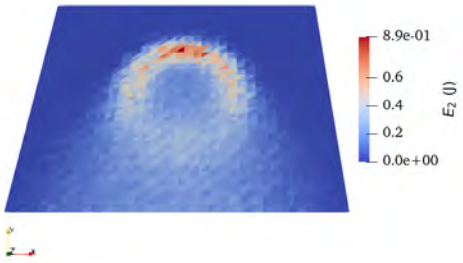

(g) 24 kg/s

FIGURE B.20: Energy transfer patterns predicted using the E_2 model for varying mass flow rate

(a) 1 kg/s

(b) 2 kg/s

(c) 3 kg/s

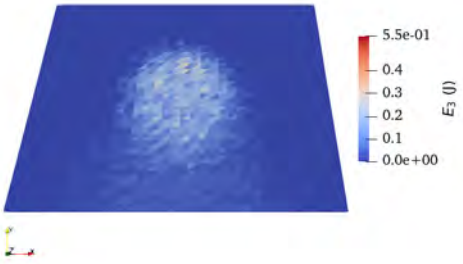

(d) 4 kg/s

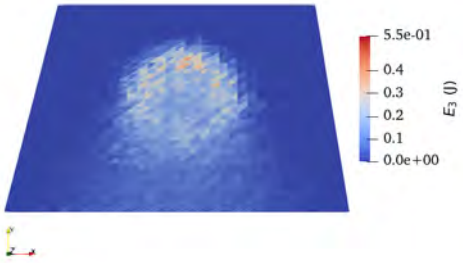

(e) 8 kg/s

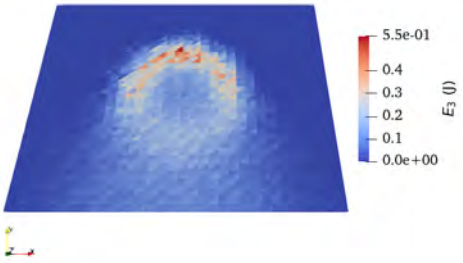

(f) 16 kg/s

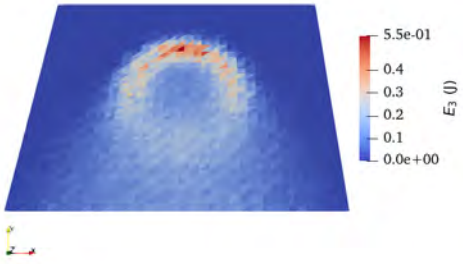

(g) 24 kg/s

FIGURE B.21: Energy transfer patterns predicted using the E_3 model for varying mass flow rate

(a) 1 kg/s

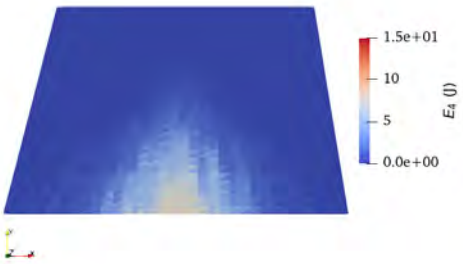

(b) 2 kg/s

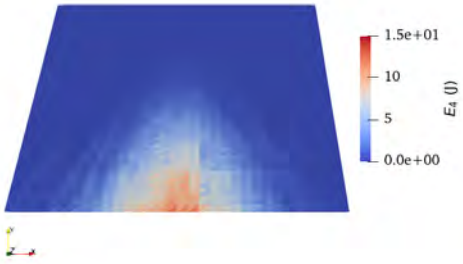

(c) 3 kg/s

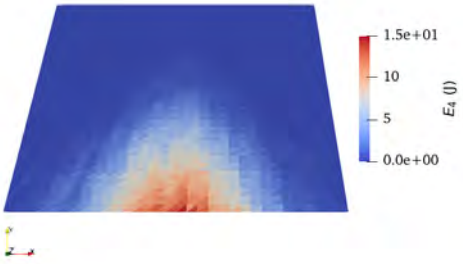

(d) 4 kg/s

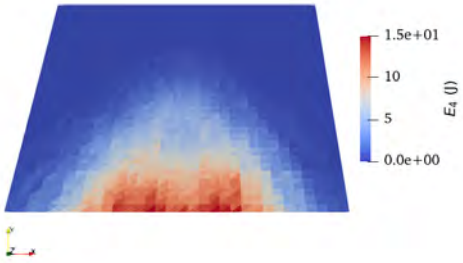

(e) 8 kg/s

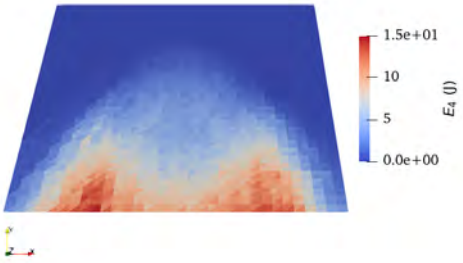

(f) 16 kg/s

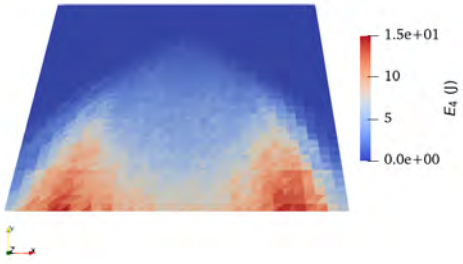

(g) 24 kg/s

FIGURE B.22: Energy transfer patterns predicted using the E_4 model for varying mass flow rate

(a) 1 kg/s

(b) 2 kg/s

(c) 3 kg/s

(d) 4 kg/s

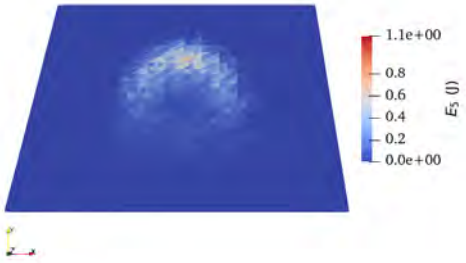

(e) 8 kg/s

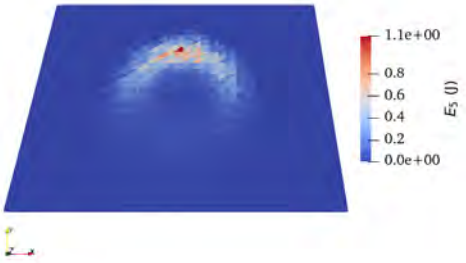

(f) 16 kg/s

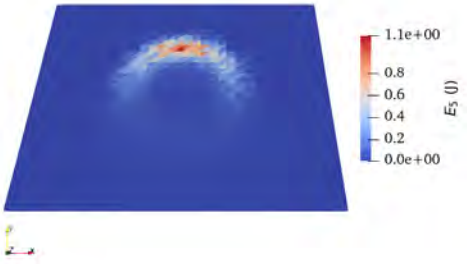

(g) 24 kg/s

FIGURE B.23: Energy transfer patterns predicted using the E_5 model for varying mass flow rate

(a) 1 kg/s

(b) 2 kg/s

(c) 3 kg/s

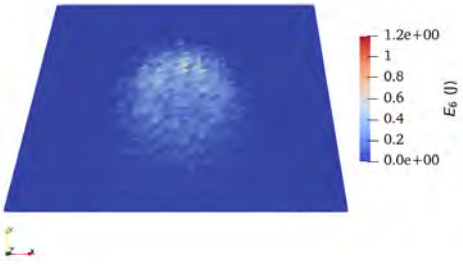

(d) 4 kg/s

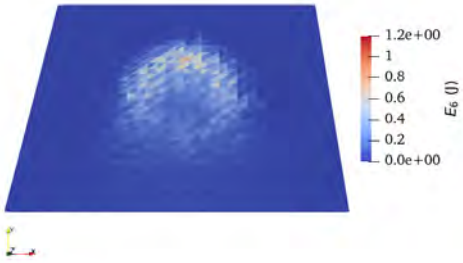

(e) 8 kg/s

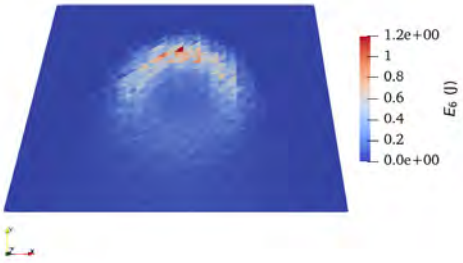

(f) 16 kg/s

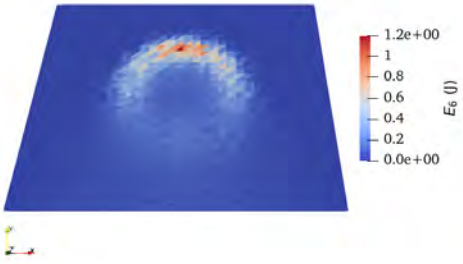

(g) 24 kg/s

FIGURE B.24: Energy transfer patterns predicted using the E_6 model for varying mass flow rate

(a) 1 kg/s

(b) 2 kg/s

(c) 3 kg/s

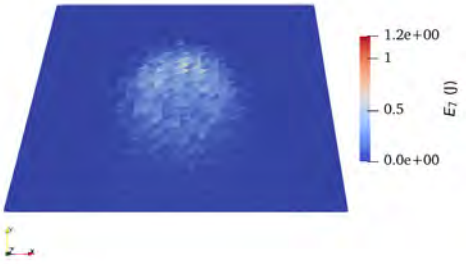

(d) 4 kg/s

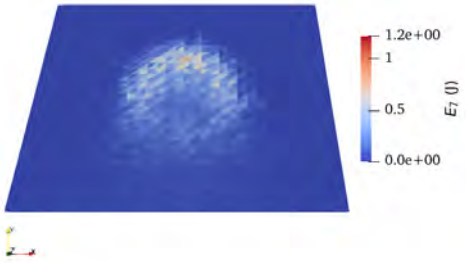

(e) 8 kg/s

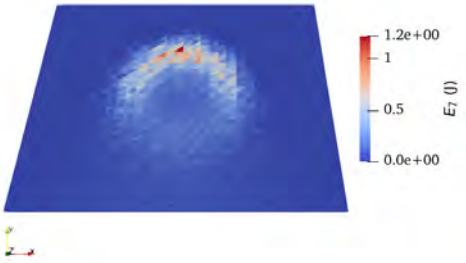

(f) 16 kg/s

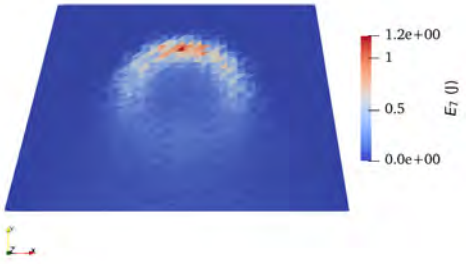

(g) 24 kg/s

FIGURE B.25: Energy transfer patterns predicted using the E_7 model for varying mass flow rate

(a) 1 kg/s

(b) 2 kg/s

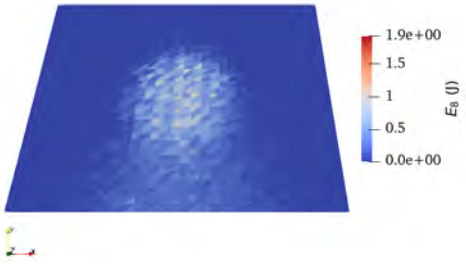

(c) 3 kg/s

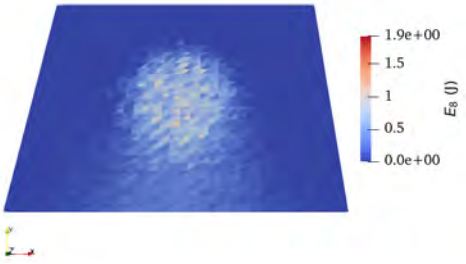

(d) 4 kg/s

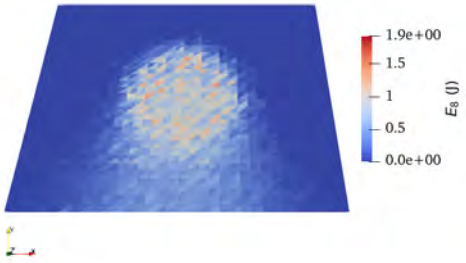

(e) 8 kg/s

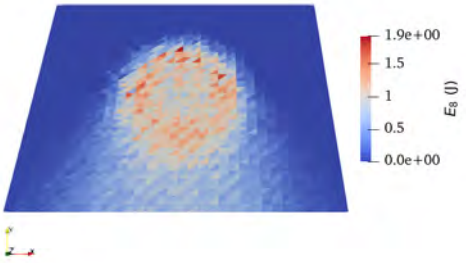

(f) 16 kg/s

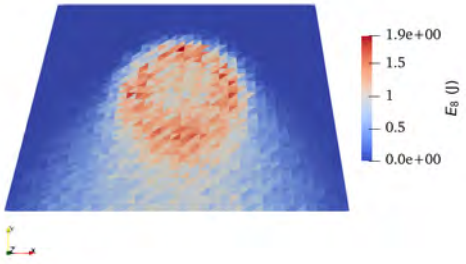

(g) 24 kg/s

FIGURE B.26: Energy transfer patterns predicted using the E_8 model for varying mass flow rate

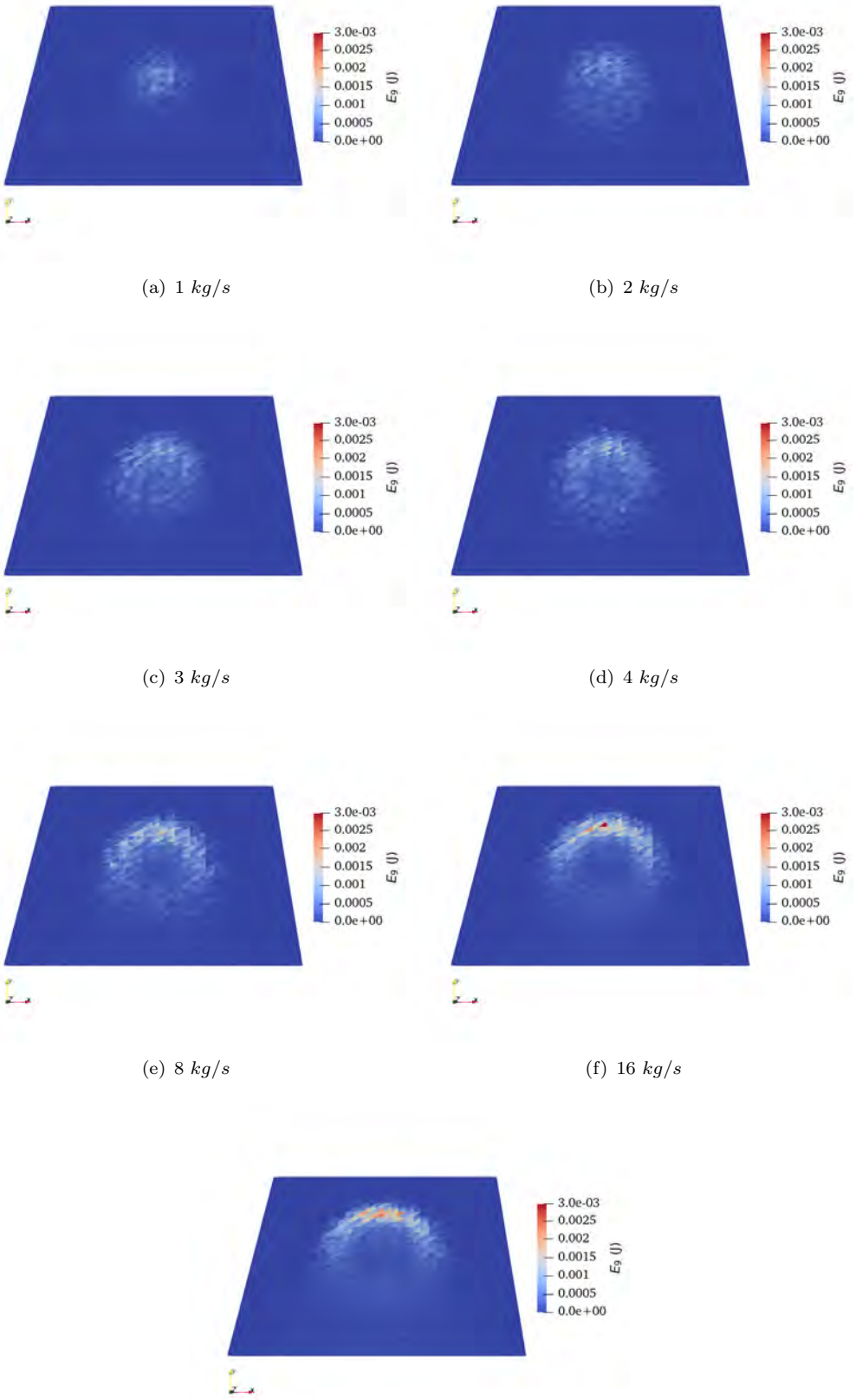

(a) 1 kg/s

(b) 2 kg/s

(c) 3 kg/s

(d) 4 kg/s

(e) 8 kg/s

(f) 16 kg/s

(g) 24 kg/s

FIGURE B.27: Energy transfer patterns predicted using the E_9 model for varying mass flow rate

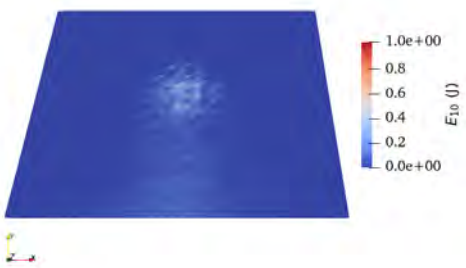

(a) 1 kg/s

(b) 2 kg/s

(c) 3 kg/s

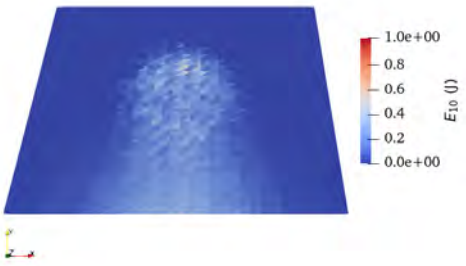

(d) 4 kg/s

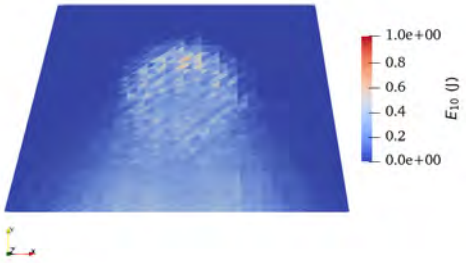

(e) 8 kg/s

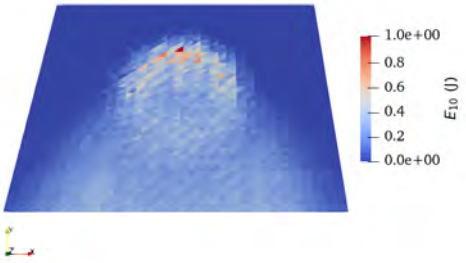

(f) 16 kg/s

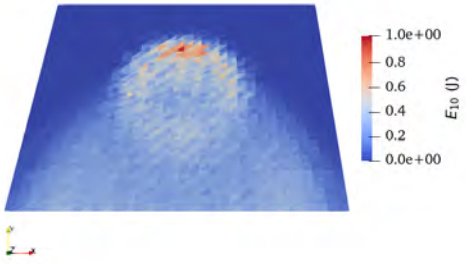

(g) 24 kg/s

FIGURE B.28: Energy transfer patterns predicted using the E_{10} model for varying mass flow rate

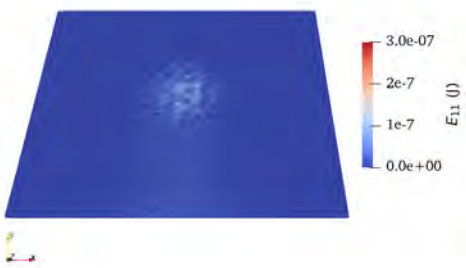

(a) 1 kg/s

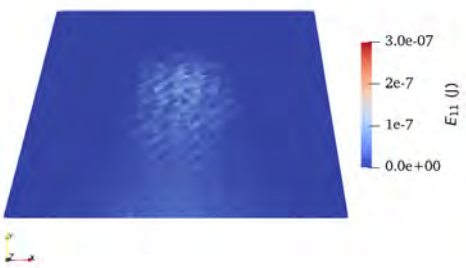

(b) 2 kg/s

(c) 3 kg/s

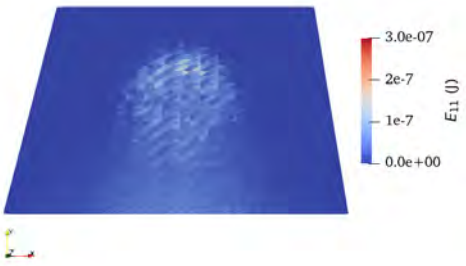

(d) 4 kg/s

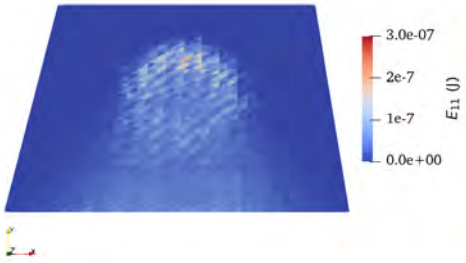

(e) 8 kg/s

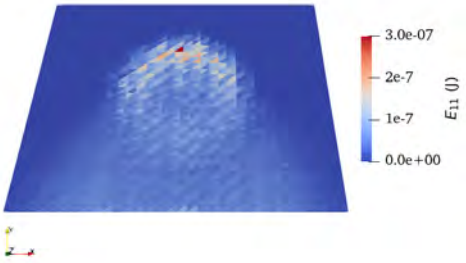

(f) 16 kg/s

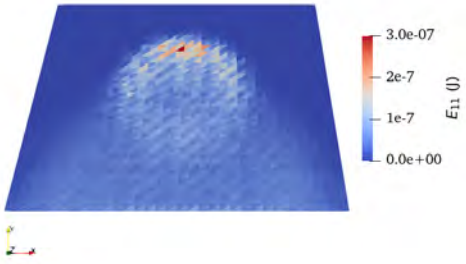

(g) 24 kg/s

FIGURE B.29: Energy transfer patterns predicted using the E_{11} model for varying mass flow rate

(a) 1 kg/s

(b) 2 kg/s

(c) 3 kg/s

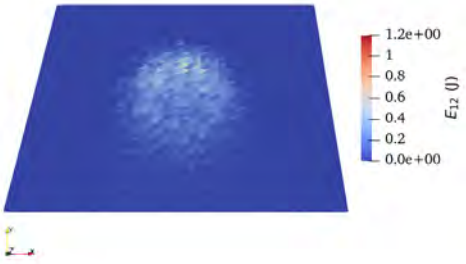

(d) 4 kg/s

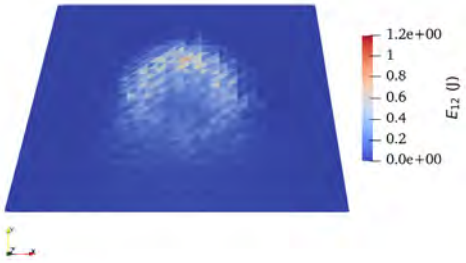

(e) 8 kg/s

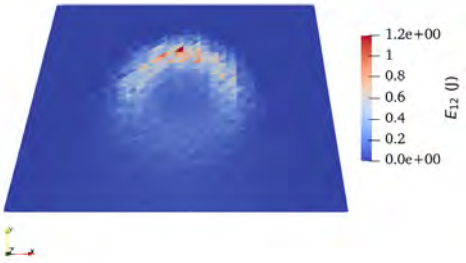

(f) 16 kg/s

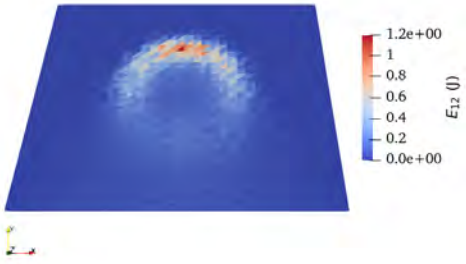

(g) 24 kg/s

FIGURE B.30: Energy transfer patterns predicted using the E_{12} model for varying mass flow rate

(a) 1 kg/s

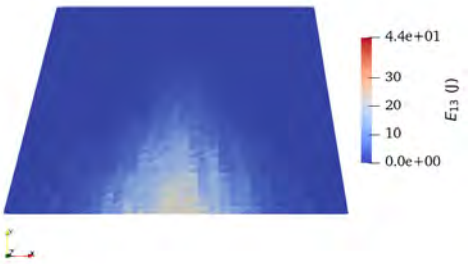

(b) 2 kg/s

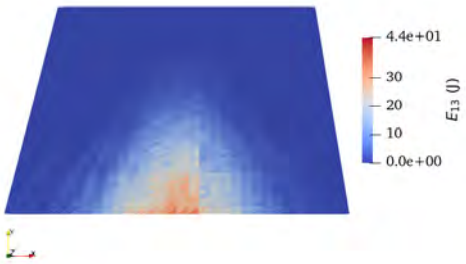

(c) 3 kg/s

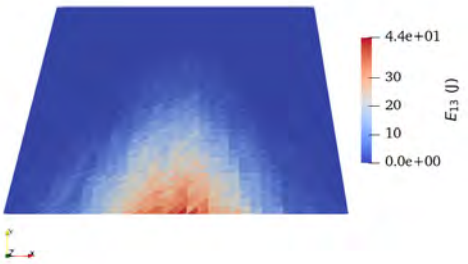

(d) 4 kg/s

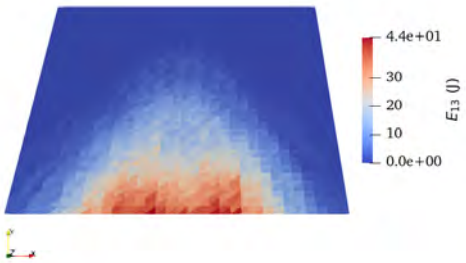

(e) 8 kg/s

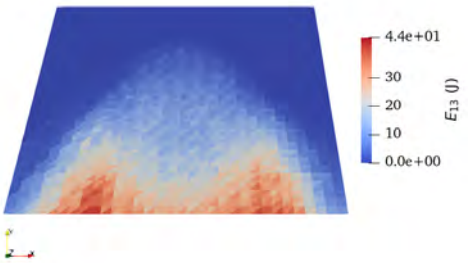

(f) 16 kg/s

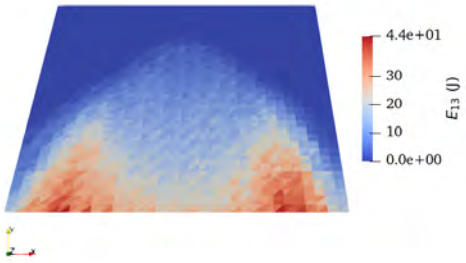

(g) 24 kg/s

FIGURE B.31: Energy transfer patterns predicted using the E_{13} model for varying mass flow rate

(a) 1 kg/s

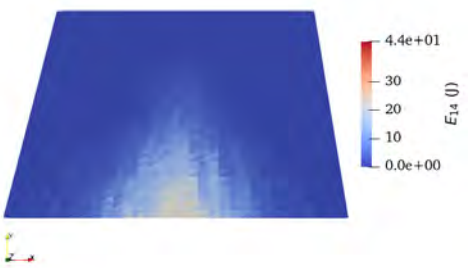

(b) 2 kg/s

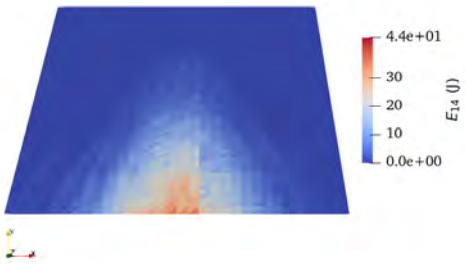

(c) 3 kg/s

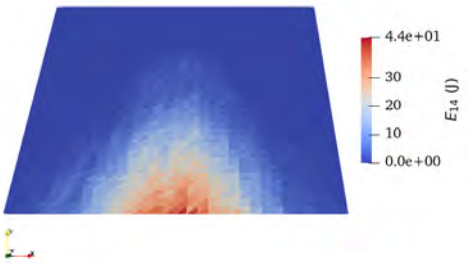

(d) 4 kg/s

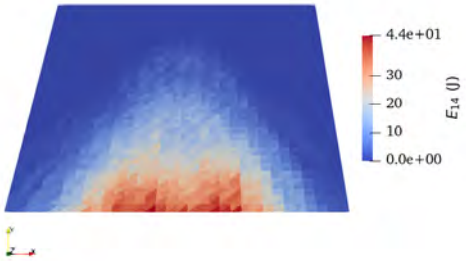

(e) 8 kg/s

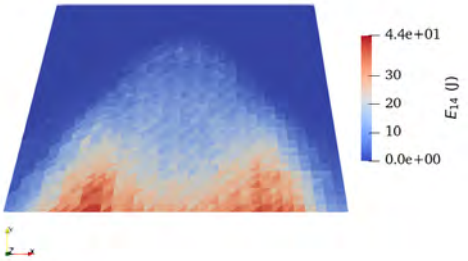

(f) 16 kg/s

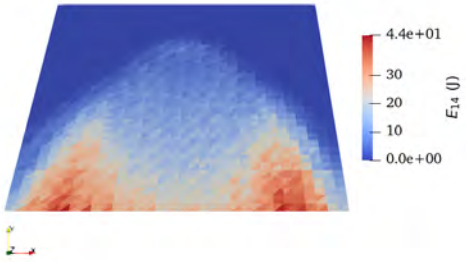

(g) 24 kg/s

FIGURE B.32: Energy transfer patterns predicted using the E_{14} model for varying mass flow rate

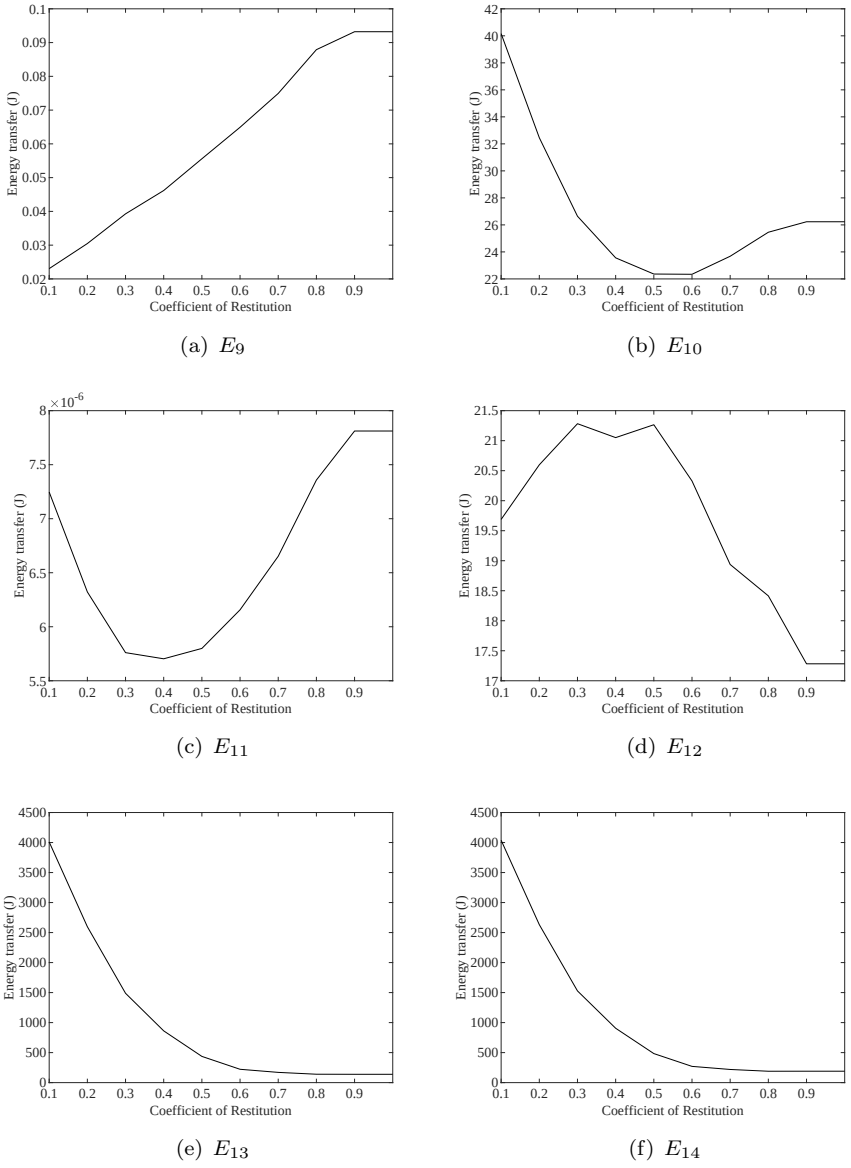

(a) E_9 (b) E_{10}

(c) E_{11} (d) E_{12}

(e) E_{13} (f) E_{14}

FIGURE B.33: Total energy transfer predicted with respect to the coefficient of restitution

Bibliography

[1] Steel University, Blast Furnace: Blast Furnace Iron Making: Introduction (2011).

[2] M. A. J. Holmes, A numerical simulation of particulate distribution of the blast furnace raw material burden through Paul Worth Bell-Less Top apparatus, Thesis, Swansea University (2015).

[3] A. Carr, The Application of Non-Spherical Discrete Element Methods to the Blast Furnace, Ph.D. thesis, Swansea University (2021).

[4] K.-H. Zum Gahr, Wear by hard particles, Tribology International 31 (10) (1998) 587 – 596.

[5] L. Bridgeman, Simulation of Industrial Granular Flow and its Effects On the Sinter Plant Operation, Thesis, Swansea University (2010).

[6] P. A. Cundall, O. Strack, A discrete numerical model for granular assemblies, Gèotechnique 29 (1) (1979) 47–65.

[7] M. A. Holmes, R. Brown, P. A. Wauters, N. P. Lavery, S. G. Brown, Bending and twisting friction models in soft-sphere discrete element simulations for static and dynamic problems, Applied Mathematical Modelling 40 (5-6) (2016) 3655–3670. doi:10.1016/j.apm.2015.10.026.

[8] W. K. Walls, Size Control in Pelletisation, Ph.D. thesis, Swansea University (2022).

[9] W. K. Walls, J. A. Thompson, S. G. R. Brown, Towards a unified theory of wet agglomeration, Powder Technology (2022) 117519doi:10.1016/j.powtec.2022.117519.

[10] J. Duran, Sands, Powders and Grains: An Introduction to the Physics of Granular Materials, Springer-Verlag, New York, 1997.

[11] P. Richard, M. Nicodemi, R. Delannay, P. Ribière, D. Bideau, Slow relaxation and compaction of granular systems, Nature Materials 4 (2) (2005) 121–128. doi:10.1038/nmat1300.

[12] M. Rhodes, Introduction to Particle Technology, 1st Edition, John Wiley and Sons, Inc., New York, 2008.

[13] G. Mortimer, The Men Who Made The SAS: The History of The Long Range Desert Group, 1st Edition, Constable, 2015.

[14] R. A. Bagnold, Libyan Sands: Travel in a Dead World, Hodder and Stoughton, London, 1935.

[15] B. Macintyre, SAS: Rogue Heroes - the authorized wartime history, 1st Edition, Crown Publishing Group, New York, 2016.

[16] O. Gonzalez, A. M. Stuart, A First Course in Continuum Mechanics, 1st Edition, Cambridge University Press, Cambridge, 2008.

[17] M. R. Kuhn, Granular Geomechanics, 1st Edition, ISTE Press Ltd and Elsevier Ltd, London, 2017.

[18] H. Zhu, M. M. Mehrabadi, M. Massoudi, The frictional flow of a dense granular material based on the dilatant double shearing model, Computers and Mathematics with Applications 53 (2) (2007) 244–259. doi:10.1016/j.camwa.2006.02.054.

[19] H. M. Jaeger, S. R. Nagel, R. P. Behringer, The physics of granular materials, Physics Today 49 (4) (1996) 32–38. doi:10.1063/1.881494.

[20] R. Brown, J. Richards, Principles of Powder Mechanics: Essays on the Packing and Flow of Powders and Bulk Solids, Pergamon Press, Oxford, 1970.

[21] J. C. Burton, J. M. Amundson, R. Cassotto, C. C. Kuo, M. Dennin, Quantifying flow and stress in ice mélange, the world's largest granular material, Proceedings of the National Academy of Sciences of the United States of America 115 (20) (2018) 5105–5110. doi:10.1073/pnas.1715136115.

[22] A. Maksuwan, Janssen's effect in mechanical behavior and fracture of granular materials, Materials Science Forum 883 (2017) 7–11. doi:10.4028/www.scientific.net/MSF.883.7.

[23] W. Goldsmith, Impact: The theory and physical behaviour of colliding solids, Edward Arnold, London, 1960.

[24] K. Johnson, Contact Mechanics, Cambridge University Press, Cambridge, 1985.

[25] N. V. Brilliantov, T. Pöschel, Granular Gases with Impact-Velocity Dependent Restitution Coefficient, Lecture note in physics (564) (2001) 100 – 124.

[26] A. Ghanbarzadeh, A. Hassanpour, A. Neville, A numerical model for calculation of the restitution coefficient of elastic-perfectly plastic and adhesive bodies with rough surfaces, Powder Technology 345 (2019) 203–212. doi:10.1016/j.powtec.2018.12.079.
URL https://doi.org/10.1016/j.powtec.2018.12.079

[27] R. L. Jackson, I. Green, D. B. Marghitu, Predicting the coefficient of restitution of impacting elastic-perfectly plastic spheres, Nonlinear Dynamics 60 (3) (2010) 217–229. doi:10.1007/s11071-009-9591-z.

[28] E. Willert, Stoßprobleme in Physik, Technik und Medizin, 2020. doi:10.1007/978-3-662-60296-6.

[29] F. Froiio, G. Tomassetti, I. Vardoulakis, Mechanics of granular materials: The discrete and the continuum descriptions juxtaposed, International Journal of Solids and Structures 43 (25-26) (2006) 7684–7720. doi:10.1016/j.ijsolstr.2006.03.023.

[30] F. Gabrieli, F. Ceccato, Impact of Dry Granular Flows on a Rigid Wall: Discrete and Continuum Approach, Procedia Engineering 158 (2016) 152–157. doi:10.1016/j.proeng.2016.08.421.

[31] T. Pöschel, T. Schwager, Computational Granular Dynamics: Models and Algorithms, Springer, Berlin, 2005. doi:10.1007/3-540-27720-x.

[32] J. Butcher, Numerical Methods for Ordinary Differential Equations, John Wiley and Sons, Inc., 2003.

[33] Y. Tsuji, T. Tanaka, T. Ishida, Lagrangian numerical simulation of plug flow of cohesionless particles in a horizontal pipe, Powder Technology 71 (3) (1992) 239–250.

[34] K. F. Malone, B. H. Xu, Determination of contact parameters for discrete element method simulations of granular systems, Particuology 6 (6) (2008) 521–528. doi:10.1016/j.partic.2008.07.012.

[35] C. O'Sullivan, J. D. Bray, Selecting a suitable time step for discrete element simulations that use the central difference time integration scheme, Engineering Computations (Swansea, Wales) 21 (2-4) (2004) 278–303. doi:10.1108/02644400410519794.

[36] G. Adams, M. Nosonovsky, Contact modeling - forces, Tribology International 33 (2000) 431–442.

[37] H. Hertz, On the contact of elastic solids, Journal für die reine und angewandte Mathematik 92 (1881) 156 – 171.

[38] R. Mindlin, H. Deresiewicz, Elastic Spheres in Contact Under Varying Oblique Forces, Journal of Applied Mechanics 20 (1953) 327–344.

[39] A. Di Renzo, F. P. Di Maio, Comparison of contact-force models for the simulation of collisions in DEM-based granular flow codes, Chemical Engineering Science 59 (3) (2004) 525–541. doi:10.1016/j.ces.2003.09.037.

[40] B. K. Mishra, C. V. Murty, On the determination of contact parameters for realistic DEM simulations of ball mills, Powder Technology 115 (3) (2001) 290–297. doi:10.1016/S0032-5910(00)00347-8.

[41] A. P. Grima, P. W. Wypych, Investigation into calibration of discrete element model parameters for scale-up and validation of particle-structure interactions under impact conditions, Powder Technology 212 (1) (2011) 198–209. doi:10.1016/j.powtec.2011.05.017.
URL http://dx.doi.org/10.1016/j.powtec.2011.05.017

[42] N. Naito, K. Maeda, H. Konno, Y. Ushiwatari, ScienceDirect Rockfall impacts on sand cushions with different soil mechanical characteristics using discrete element method 60 (2020) 384–397. doi:10.1016/j.sandf.2020.02.008.

[43] J. Ting, Discrete Numerical Model for Soil Mechanics, Journal of Geotechnical Engineering 115 (3) (1989). doi:10.1061/(ASCE)0733-9410(1989)115.

[44] J. Ting, B. Corkum, Discrete Numerical Modeling of Soil : Validation and Application, Vol. 1, Department of Civil Engineering, University of Toronto, Toronto, 1987.

[45] C. Moliner, F. Marchelli, N. Spanachi, A. Martinez-Felipe, B. Bosio, E. Arato, CFD simulation of a spouted bed: Comparison between the Discrete Element Method (DEM) and the Two Fluid Model (TFM), Chemical Engineering Journal 377 (2019). doi:10.1016/j.cej.2018.11.164.
URL https://doi.org/10.1016/j.cej.2018.11.164

[46] Blender, blender (2022).
URL https://www.blender.org/

[47] C. Ericson, Real-Time Collision Detection, Elsevier, New York, 2013.

[48] J. A. Williams, Wear and wear particles - Some fundamentals, Tribology International 38 (10) (2005) 863–870. doi:10.1016/j.triboint.2005.03.007.

[49] P. Jost, Lubrication (Tribology) - A report on the present position and industry's needs, Tech. rep., Her Majesty's Stationary Office, London (1966).

[50] K. Holmberg, A. Erdemir, Influence of tribology on global energy consumption, costs and emissions, Friction 5 (3) (2017) 263–284. doi:10.1007/s40544-017-0183-5.

[51] R. G. Bayer, Mechanical wear fundamentals and testing, 2nd Edition, Marcel Dekker, Inc., New York, 2004.

[52] J. T. Burwell, Survey of possible wear mechanisms, Wear 1 (2) (1957) 119–141. doi:10.1016/0043-1648(57)90005-4.

[53] E. Rabinowicz, Friction and wear of materials, John Wiley and Sons, Inc., New York, 1965.

[54] K. Kato, K. Adachi, Wear Mechanisms, in: B. Bhushan (Ed.), Modern Tribology Handbook, 1st Edition, CRC Press, 2000, Ch. 7, pp. 273 – 300.

[55] J. F. Archard, Contact and rubbing of flat surfaces, Journal of Applied Physics 24 (8) (1953) 981–988. doi:10.1063/1.1721448.

[56] T. Reye, Zur Theorie der Zapfenreibung [On the theory of pivot friction], Der Civilingenieur 4 (1860) 235 – 255.

[57] E. Rojas, V. Vergara, R. Soto, Case study: Discrete element modeling of wear in mining hoppers, Wear (2019). doi:10.1016/j.wear.2019.04.020.

[58] R. Xia, X. Wang, B. Li, X. Wei, Z. Yang, Discrete Element Method-(DEM-) Based Study on the Wear Mechanism and Wear Regularity in Scraper Conveyor Chutes, Mathematical Problems in Engineering 2019 (2019). doi:10.1155/2019/4191570.

[59] D. Forsström, P. Jonsén, Calibration and validation of a large scale abrasive wear model by coupling DEM-FEM: Local failure prediction from abrasive wear of tipper bodies during unloading of granular material, Engineering Failure Analysis 66 (2016) 274–283. doi:10.1016/j.engfailanal.2016.04.007.

[60] I. Hutchings, Transitions, Threshold Effects and Erosion Maps, Key Engineering Materials 71 (1992) 75–92. doi:10.4028/www.scientific.net/kem.71.75.

[61] M. Barge, G. Kermouche, P. Gilles, J. M. Bergheau, Experimental and numerical study of th ploughing part of abrasive wear, Wear 255 (1-6) (2003) 30–37. doi:10.1016/S0043-1648(03)00159-5.

[62] V. Javaheri, D. Porter, V. T. Kuokkala, Slurry erosion of steel – Review of tests, mechanisms and materials, Wear 408-409 (July 2017) (2018) 248–273. doi:10.1016/j.wear.2018.05.010.

[63] Y. Ben-Ami, A. Uzi, A. Levy, Modelling the particles impingement angle to produce maximum erosion, Powder Technology 301 (2016) 1032–1043. doi:10.1016/j.powtec.2016.07.041.

[64] R. G. Bayer, Fundamentals of wear failure, Failure Analysis and Prevention 11 (2002).

[65] G. Sundararajan, M. Roy, B. Venkataraman, Erosion efficieny - a new parameter to characterize the dominant erosion mechanism, Wear 140 (1990) 369 – 381.

[66] M. A. Islam, Z. N. Farhat, Effect of impact angle and velocity on erosion of API X42 pipeline steel under high abrasive feed rate, Wear 311 (1-2) (2014) 180–190. doi:10.1016/j.wear.2014.01.005.

[67] I. Finnie, Erosion of surfaces by solid particles, Wear 3 (1960) 87 – 103.

[68] P. A. Engel, Impact Wear of Materials, Elsevier Scientific Publishing Company, Amsterdam, 1978.

[69] P. Shewmon, G. Sundararajan, The erosion of metals, Annual Review of Material Sceince 13 (1983) 301–318.

[70] R. W. Lyczkowski, J. X. Bouillard, State-of-the-art review of erosion modeling in fluid/solids systems, Progress in Energy and Combustion Science 28 (6) (2002) 543–602. doi:10.1016/S0360-1285(02)00022-9.

[71] I. Finnie, Some observations on the erosion of ductile metals, Wear 19 (1972) 81 – 90.

[72] I. Finnie, Some reflections on the past and future of erosion, Wear 186-187 (PART 1) (1995) 1–10. doi:10.1016/0043-1648(95)07188-1.

[73] E. Bousser, L. Martinu, J. E. Klemberg-Sapieha, Solid particle erosion mechanisms of protective coatings for aerospace applications, Surface and Coatings Technology 257 (2014) 165–181. doi:10.1016/j.surfcoat.2014.08.037.
URL http://dx.doi.org/10.1016/j.surfcoat.2014.08.037

[74] G. L. Sheldon, A. Kanhere, An investigation of impingement erosion using single particles, Wear 21 (1972) 195–209.

[75] J. G. A. Bitter, A study of erosion phenomena: part 1, Wear 6 (1963) 5 – 21.

[76] J. G. A. Bitter, A study of erosion phenomena: part 2, Wear 6 (1963) 169 – 190.

[77] H. M. I. Clark, J. Tuzson, K. K. Wong, Measurements of specific energies for erosive wear using a Coriolis erosion tester, Wear 241 (1) (2000) 1–9. doi:10.1016/S0043-1648(00)00327-6.

[78] H. Arabnejad, A. Mansouri, S. A. Shirazi, B. S. McLaury, Development of mechanistic erosion equation for solid particles, Wear 332-333 (2015) 1044–1050. doi:10.1016/j.wear.2015.01.031.

[79] D. Tabor, A simple theory of static and dynamic hardness, Proceedings of the Royal Society A 192 (1947) 247–274.

[80] J. Neilson, A. Gilchrist, Erosion by a stream of solid particles, Wear 11 (1968) 111 – 122.

[81] L. Zhang, Z. Huang, W. Jie, Z. Cao, Y. Liu, L. Zhou, Effect of impact angle on wear behavior of Mo2NiB2–Ni cermets with different Ni content, Ceramics International 48 (12) (2022) 16944–16955. doi:10.1016/j.ceramint.2022.02.249.
URL https://doi.org/10.1016/j.ceramint.2022.02.249

[82] D. R. Andrews, An analysis of solid particle erosion mechanisms, Journal of Physics D: Applied Physics 14 (11) (1981) 1979–1991. doi:10.1088/0022-3727/14/11/006.

[83] K. K. Wong, H. M. Clark, Impact angle, particle energy and mass loss in erosion by dilute slurries, Wear 186-871 (1995) 454–464.

[84] Y. I. Oka, K. Okamura, T. Yoshida, Practical estimation of erosion damage caused by solid particle impact: Part 1: Effects of impact parameters on a predictive equation, Wear 259 (1-6) (2005) 95–101. doi:10.1016/j.wear.2005.01.039.

[85] Y. I. Oka, T. Yoshida, Practical estimation of erosion damage caused by solid particle impact: Part 2: Mechanical properties of materials directly associated with erosion damage, Wear 259 (1-6) (2005) 102–109. doi:10.1016/j.wear.2005.01.040.

[86] G. C. Pereira, F. J. de Souza, D. A. de Moro Martins, Numerical prediction of the erosion due to particles in elbows, Powder Technology 261 (2014) 105–117. doi:10.1016/j.powtec.2014.04.033.

[87] Y. I. Oka, M. Nishimura, K. Nagahashi, M. Matsumura, Control and evaluation of particle impact conditions in a sand erosion test facility, Wear 250-251 (PART 1) (2001) 736–743. doi:10.1016/S0043-1648(01)00710-4.

[88] Y. Zhao, H. Ma, L. Xu, J. Zheng, An erosion model for the discrete element method, Particuology 34 (2017) 81–88. doi:10.1016/j.partic.2016.12.005.
URL http://dx.doi.org/10.1016/j.partic.2016.12.005

[89] H. Sun, H. Ma, Y. Zhao, DEM investigation on conveying of non-spherical particles in a screw conveyor, Particuology 65 (2022) 17–31. doi:10.1016/j.partic.2021.06.009.

[90] L. Xu, K. Luo, Y. Zhao, J. Fan, K. Cen, Multiscale investigation of tube erosion in fluidized bed based on CFD-DEM simulation, Chemical Engineering Science 183 (2018) 60–74. doi:10.1016/j.ces.2018.02.050.
URL https://doi.org/10.1016/j.ces.2018.02.050

[91] LIGGGHTS, LIGGGHTS(R) - PUBLIC Documentation (2022).
URL https://www.cfdem.com/media/DEM/docu/Manual.html

[92] X. Chen, B. S. McLaury, S. A. Shirazi, Application and experimental validation of a computational fluid dynamics (CFD)-based erosion prediction model in elbows and plugged tees, Computers and Fluids 33 (10) (2004) 1251–1272. doi:10.1016/j.compfluid.2004.02.003.

[93] X. Chen, B. S. McLaury, S. A. Shirazi, Numerical and experimental investigation of the relative erosion severity between plugged tees and elbows in dilute gas/solid two-phase flow, Wear 261 (7-8) (2006) 715–729. doi:10.1016/j.wear.2006.01.022.

[94] C. Redondo, M. Chávez–Modena, J. Manzanero, G. Rubio, E. Valero, S. Gómez–Álvarez, A. Rivero–Jiménez, CFD–based erosion and corrosion modeling in pipelines using a high–order discontinuous Galerkin multiphase solver, Wear 478-479 (January) (2021). doi:10.1016/j.wear.2021.203882.

[95] H. C. Meng, K. C. Ludema, Wear models and predictive equations: their form and content, Wear 183 (1995) 443–457. doi:doi:10.1016/0043-1648(95)90158-2.

[96] M. Parsi, K. Najmi, F. Najafifard, S. Hassani, B. S. McLaury, S. A. Shirazi, A comprehensive review of solid particle erosion modeling for oil and gas wells and pipelines applications, Journal of Natural Gas Science and Engineering 21 (2014) 850–873. doi:10.1016/j.jngse.2014.10.001.

[97] A. W. Ruff, S. M. Wiederhorn, Erosion by solid particle impact., in: Treatise on Materials Science and Technology 16 , Erosi (1979) 69–126.

[98] I. M. Hutchings, A model for the erosion of metals by spherical particles at normal incidence, Wear 70 (1981) 269 – 281.

[99] P. H. Shipway, I. M. Hutchings, The role of particle properties in the erosion of brittle materials, Wear 193 (1) (1996) 105–113. doi:10.1016/0043-1648(95)06694-2.

[100] A. W. Roberts, Chute performance and design for rapid flow conditions, Chemical Engineering and Technology 26 (2) (2003) 163–170. doi:10.1002/ceat.200390024.

[101] W. D. Callister Jr, Materials Science and Engineering: An Introduction, 7th Edition, John Wiley and Sons, Inc., New York, 2007.

[102] Y. I. Oka, M. Matsumura, T. Kawabata, Relationship between surface hardness and erosion damage caused by solid particle impact, Wear 162-164 (PART B) (1993) 688–695. doi:10.1016/0043-1648(93)90067-V.

[103] I. Finnie, D. H. McFadden, On the velocity dependence of the erosion of ductile metals by solid particles at low angles of incidence, Wear 48 (1978) 181 – 190.

[104] A. Leyland, A. Matthews, On the significance of the H/E ratio in wear control: A nanocomposite coating approach to optimised tribological behaviour, Wear 246 (1-2) (2000) 1–11. doi:10.1016/S0043-1648(00)00488-9.

[105] M. A. Moore, F. S. King, Abrasive wear of brittle solids, Wear 60 (1) (1980) 123–140. doi:10.1016/0043-1648(80)90253-7.

[106] M. Neale, M. Gee, Guide to Wear Problems and Testing for Industry, Professional Engineering Publishing Limited, UK, 2000.

[107] American Society for Testing and Materials (ASTM), Standard Test Method for Measuring Abrasion Using the Wet Sand/Rubber Wheel Apparatus, ASTM G105-20(2020) (2020).

[108] American Society for Testing and Materials (ASTM), Standard Test Method for Measuring Abrasion Using the Dry Sand/Rubber Wheel Apparatus, ASTM G65-16(2021) (2021).

[109] American Society for Testing and Materials (ASTM), Standard Test Methods for Abrasion Resistance of Organic Coatings by Falling Abrasive, ASTM D968-22(2022) (2022).

[110] M. Zalzalah, R. Lewis, T. Slatter, A new predictive model for normal and compound impact wear, Wear 480-481 (December 2020) (2021) 203954. doi:10.1016/j.wear.2021.203954.
URL https://doi.org/10.1016/j.wear.2021.203954

[111] J. A. Thompson, L. Berry, S. Southern, W. K. Walls, M. A. Holmes, S. G. Brown, The effect of mesh discretisation on damage and wear predictions using the Discrete Element Method, Applied Mathematical Modelling 105 (2022) 690–710. doi:10.1016/j.apm.2022.01.005.
URL https://doi.org/10.1016/j.apm.2022.01.005

[112] M. Miner, Cumulative damage in fatigue, Journal of Applied Mechanics 12 (1945) 149–164.

[113] A. C. Fischer-Cripps, Introduction to Contact Mechanics, 2nd Edition, Springer Science, New York, 2007.

[114] D. Boemer, Discrete Element Method Modeling of Ball Mills - Liner Wear Evolution, Ph.D. thesis, University of Liège (2015).

[115] D. Boemer, J. P. Ponthot, A generic wear prediction procedure based on the discrete element method for ball mill liners in the cement industry, Minerals Engineering 109 (2017) 55–79. doi:10.1016/j.mineng.2017.02.014.
URL http://dx.doi.org/10.1016/j.mineng.2017.02.014

[116] G. G. Stokes, On the effect of the Internal Friction of Fluids on the Motion of Pendulums, Transactions of the Cambridge philosophical society 9 (1850).

[117] C. E. Brennen, Fundamentals of Multiphase Flows, 1st Edition, Cambridge University Press, Cambridge, 2005.

[118] A. Haider, O. Levenspiel, Drag Coefficient and Terminal Velocity of Spherical and Nonspherical Particles, Powder Technology 58 (1989) 63–70.

[119] C. Grossmann, H. Roos, Numerical treatment of Partial Differential equations, Springer-Verlag Berlin Heidelberg, Berlin, 2007.

[120] B. S. Massey, Mechanics of Fluids, 5th Edition, Van Nostrand Reinhold Co. Ltd, 1984.

[121] Y. A. Çengel, J. M. Cimbala, Fluid Mechanics: Fundamental and applications, 1st Edition, McGraw-Hill, New York, 2006.

[122] B. W. McCormick, Aerodynamics, Aeronautics and Flight Mechanics, 2nd Edition, Wiley, New York, 1994.

[123] L. Schiller, A. Naumann, A drag coefficient correlation, Zeitschrift des Vereines Deutsches Ingenieure (77) (1935) 318–320.

[124] T. Niemi, Particle Size Distribution in CFD Simulation of Gas-Particle Flows, Ph.D. thesis, Aalto University (2012).

[125] T. R. Jayawickrama, N. E. L. Haugen, M. U. Babler, M. A. Chishty, K. Umeki, The effect of Stefan flow on Nusselt number and drag coefficient of spherical particles in non-isothermal gas flow, International Journal of Multiphase Flow 140 (2021) 103650. doi:10.1016/j.ijmultiphaseflow.2021.103650.
URL https://doi.org/10.1016/j.ijmultiphaseflow.2021.103650

[126] B. J. Connolly, E. Loth, C. F. Smith, Shape and drag of irregular angular particles and test dust, Powder Technology 363 (2020) 275–285. doi:10.1016/j.powtec.2019.12.045.
URL https://doi.org/10.1016/j.powtec.2019.12.045

[127] H. Versteeg, W. Malalasekera, An Introduction to Computational Fluid Dynamics, 2nd Edition, Pearson Education Ltd, 2007.

[128] McColskey, Specification: McColskey S190 3-Deck, 4th Edition, McColskey International, 2012.

[129] McColskey, S190: High Production Screener [brochure] (2020).

[130] W. Hutny, G. Lee, J. Price, Fundamentals of coal vcombustion during injection into a blast furnce, Progress in Energy and Combustion Science 17 (1991) 373–395.

[131] D. C. Wilcox, Reassessment of the scale-determining equation for advanced turbulence models, AIAA Journal 26 (11) (1988) 1299–1310. doi:10.2514/3.10041.

[132] D. C. Wilcox, Formulation of the k-ω turbulence model revisited, AIAA Journal 46 (11) (2008) 2823–2838. doi:10.2514/1.36541.